Vortex dynamics in nanostructured systems superconductor-superconductor and superconductor-metal of one and two bands

MSc. Jesús David González Acosta

+

Vortex dynamics in nanostructured systems superconductor-superconductor and superconductor-metal of one and two bands

MSc. Jesús David González Acosta

Dissertation submitted at the Universidad Nacional de Colombia to obtain the degree:
Doctor in Sciences-Physics

Advisor:
José José Barba Ortega, Prof. Ph.D.
Universidad Nacional de Colombia-Sede Bogotá

Research field: Theory of superconductivity
Research group: Mesoscopic physics (UNAL)

Universidad Nacional de Colombia
Facultad de Ciencias, Departamento de Física
Bogotá, Colombia
2018

A Dios el dador de todas las cosas;
a mi madre amada, valiente y esforzada, Aura;
a mi esposa amada, Laury de Jesús;
a mis hijas Helena y Emma;
a mi hermano Estiffer y sobrinos Stiffer, Jesús
y Andrés;
a mis tías Ena, María, Luz, Chave y tío Gabriel;
y a las memorias de mi tía Maura y abuela
amada Baldomera, te llevo en mi vida siempre
…

Acknowledgments

Al Doctor José José Barba Ortega por darme la oportunidad de investigar el importante fenómeno de la superconductividad y por su dedicación a contribuir a mi formación doctoral.

Al Doctor Milorad V. Milošević, por su orientación recibida durante mi pasantía de investigación y la oportunidad de ser estudiante de doctorado en Ciencias-Física de la Universidad de Amberes, Bélgica bajo su dirección.

Al Doctor José Sierra por su valiosa ayuda y consejos cuando más lo he necesitado durante mi pregrado, maestría y doctorado.

Al Doctor Ruthber Escorcia por su apoyo durante mi formación profesional y personal.

Al Profesor Alberto García por creer y apoyar mi idea de iniciar mis estudios doctorales comprometiendo su patrimonio.

A mi madre por ser una mujer esforzada y valiente trabajando día a día sola por el bienestar de tus hijos.

A mi esposa Laury, por su dedicación a nuestras hijas Helena y Emma para fundamentarlas en el amor y su apoyo en el camino recorrido durante mi doctorado.

A mi hermano, Estiffer por asumir la responsabilidad de la familia mientras estudiaba para poder ser el primer doctor en la familia.

A mis amigos, Eduardo, José Luis, Jader, Antonio, Andrés y José José por sus voces de aliento cuando más lo necesitaba en este duro camino.

A mis amigos en la Universidad de Amberes, Victor, Rebeca, Miša, Jonas, Hossein, Sara y Jagger por brindarme una familia lejos de casa.

A mi amigos, Željko y Slavisa por los grandes momentos compratidos y contribuciones a mi tesis.

A los profesores Juan Carlos De La Rosa y Omar Rodríguez por su valiosa gestión en la Universidad del Magdalena para poder inicial mis estudios doctorales.

A la Universidad del Magdalena por otorgar mi entrada al programa de formación avanzada hacia la consecusión del doctorado.

Al Departamento Administrativo de Ciencia, Tecnología e Investigación (COLCIENCIAS), por la beca otorgada mediante convocatoria doctorado nacional 567. Esta fue vital para alcanzar los resultados obtenidos durante mis estudios.

A todos los que olvido en este momento y merecen ser citados aquí.

Preface

The overarching theme of the thesis are the emergent novel phenomena in two-component superconductors. My advisor in Colombia, Prof. Barba Ortega, has directed my research on two-component superconductors made of one same material, with properties spatially changed by either localized heating or nanostructuring. My advisor in Belgium, Prof. Milosevic, directed my research on samples made of two distinct superconducting materials, related to very recent experiments, with accompanying development of the theoretical model and the numerical implementation suited for high-performance computing.

The principal objective of this thesis is to investigate the behavior of vortex matter under the effect of several configurations of pinning landscape with the inclusion of the enhanced surface, in several cases in this research, by using De Gennes' boundary condition phenomenological parameter. Its effect is studied upon the vorticity, magnetic induction, Cooper pair density, magnetization and phase of the order parameter as functions of the external applied magnetic field.

A particular case of spatial manipulation of the landscape of the superconducting condensate in thin films via local changes of the thermal properties is considered, but also, including the variations of anisotropy through a variations of critical temperature T_c and the spatially localized heating of the superconductor T. This simple approach provides the perfect alternative for modulation of vortex collective, emerging in the type-II superconductors as a natural response to the applied magnetic field, which was, up to now, controlled purely via nanofabricated static pinning centers, whose intensity and distribution cannot be changed once the landscape is defined.

Also it is considered in this research the modulation of the superconducting condensate at nanoscale via control of the thickness over the surface, yields an landscape for magnetic flux quanta due to the selected symmetry that allow to impose creation of vortex configurations, but also tune the critical parameters of the superconductor that can be effectively controlled. Our result suggests the possibility of modifying superconductivity of a thin film by exploiting well-controlled and thickness-dependent quantum size effects. Two manuscripts published in the Journal of low temperature physcis included in this chapter, in colaboration wit Professor Edson Sardella (Universidade Estadual Paulista) and Professor José Barba, were referenced later in the review Physical Review B by Baek, et al. [REF. [1]]

Finally, a study of two-component superconductivity is presented, where the sample is a combination of different superconductors in a hybrid heterostructure. We cover a multitude of possible two-component superconducting hybrids, realized either by combining two different materials, or using one same material with different levels of disorder and/or different

thickness in two regions, where we hope that our findings will improve understanding of the involved processes and offer new pathways to superconducting quantum devices.

Prefacio

El tema general de la tesis son los nuevos fenómenos emergentes en superconductores de dos componentes. Mi asesor en Colombia, el Prof. Barba Ortega, ha dirigido mi investigación sobre superconductores de dos componentes hechos de un mismo material, con propiedades modificadas espacialmente por calentamiento localizado o nanoestructuración. Mi asesor en Bélgica, el Prof. Milošević, dirigió mi investigación sobre muestras hechas de dos materiales superconductores distintos, relacionados con experimentos muy recientes, junto con el desarrollo del modelo teórico y la implementación numérica adecuada para la computación de alto rendimiento.

El objetivo principal de esta tesis es investigar el comportamiento de los vórtices bajo el efecto de varias configuraciones de puntos de anclaje con la inclusión de una superficie mejorada, considerada en varios casos en esta investigación, usando la condición de frontera de De Gennes, parámetro fenomenológico $b < 0$. Se estudia su efecto sobre la vorticidad, la inducción magnética, la densidad de pares de Cooper, la magnetización y la fase del parámetro de orden como funciones del campo magnético externo aplicado.

Se considera un caso particular de manipulación espacial de la distribución del condensado superconductor en películas delgadas mediante cambios locales de las propiedades térmicas, pero también, incluyendo las variaciones de anisotropía a través de variaciones de T_c y el calentamiento localizado del superconductor T. Este enfoque simple proporciona la alternativa perfecta para la modulaciń del colectivo de vórtices, emergiendo en los superconductores tipo II como una respuesta natural al campo magnético aplicado, que hasta ahora estaba controlada puramente a través de centros de anclaje estáticos nanofabricados, cuya la intensidad y distribución no se pueden cambiar una vez que se define su distribución.

También se considera en esta investigación la modulación del condensado superconductor a nanoescala a través del control del espesor sobre la superficie, el cual produce una distribución del quantum de flujo magnético debido a la simetría seleccionada que permite imponer la creación de configuraciones de vórtice, pero también ajustar los parámetros críticos del superconductor que puede ser controlado. Nuestro resultado sugiere la posibilidad de modificar la superconductividad de una película delgada explotando efectos de tamaño cuántico dependientes del grosor. Dos manuscritos publicados en la Journal of low temperature physcis incluidos en este capítulo, en colaboración con el Profesor Edson Sardella (Universidade Estadual Paulista) y el Profesor José Barba, fueron citados más adelante en la revista Physical Review B por Baek, et al. [REF. [1]].

Finalmente, se presenta un estudio de la superconductividad de dos componentes, donde la

muestra es una combinación de diferentes superconductores en una heteroestructura híbrida. Cubrimos una multitud de posibles híbridos superconductores de dos componentes, ya sea combinando dos materiales diferentes, o usando un mismo material con diferentes niveles de desorden y/o grosor diferente en dos regiones, donde esperamos que nuestros hallazgos mejoren la comprensión del procesos involucrados y ofrecer nuevas opciones para dispositivos cuánticos superconductores.

Contents

1 Introduction

I first reviewed historic events related to superconductivity. Further, different theoretical frameworks are presented, starting from phenomenological models of London brothers and Ginzburg and Landau, up to more sophisticated microscopic approaches, namely Bardeen-Cooper-Schrieffer model. In addition, The intrinsic properties of the superconductors and response to the applied magnetic field, as well as the behavior of the vortices are included in this thesis.

1.1 Introduction to superconductivity

The history about superconductivity began when some scientists predicted a steady decrease in resistance with falling temperature until reaching a minimum value at 0 K and the current could flow with little or no resistance depending on purity. At that time, people had known that the resistance of metals decreased with falling temperature but people did not know what would happen at temperature approaching absolute zero (0 K). A lot of metals show zero electrical resistance to direct current (DC) when they are cooled below a characteristic critical temperature, T_c. This phenomenon was discovered in 1911 at Leiden University when Dutch physicist Heike Kamerlingh Onnes observed the disappearance of the electrical resistance in mercury [2]. Onnes was the first to liquefy helium by cooling it to 4,2 K in 1908 and study the electrical properties of metals at extremely low temperatures. Then, he studied mercury since very pure samples could be easily prepared by distillation. The experimental results for mercury is shown in Fig. **1-1**. The resistance of the mercury sample suddenly disappeared at 4,2 K. Due to its extraordinary electrical properties, Onnes believed that mercury had passed into a new state. He called it superconductivity and the phase transition temperature is the T_c. Other materials were found to exhibit superconductivity such as lead and tin. Due to his research, Onnes was awarded the Nobel Prize in Physics in 1913. All attempts to find at least to traces of resistance in bulk superconductor were no avail. On the basis of the sensitivity of modern equipment, we can argue that the resistivity of superconductors is zero, at least at level of $10^{-29}\Omega$.m. For comparison, we note that the resistivity of high-purity copper at 4.2K is $10^{-12}\Omega$.m [3].
In addition to the perfect conductivity, the material in the superconducting state display another important characteristic which is the perfect diamagnetism, where sample expels from within the magnetic field that is less intense a certain value known as critical field H_c and when cooled below T_c [4] Fig. **1-2**. It is also called Meissner effect since it was
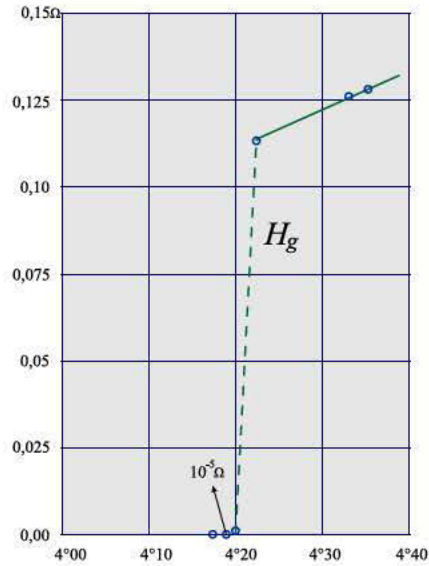
Figure 1-1: Plots of resistance versus temperature for mercury. The resistance of mercury follows the path of a normal metal above the critical temperature T_c, and then suddenly drops to zero at the critical temperature, which is 4,2 K for mercury.

discovered by Meissner and Ochsenfeld in 1933. Moreover, such expulsion of magnetic field is independent of the history of cooling below T_c and applying a magnetic field. This effect distinguishes superconductivity from perfect conductivity and it indicates that a new theory should be made. The superconductors can be separated into two types taking into account how the destruction of Meissner effect occurs. The Meissner effect is obtained only through weak magnetic fields. The first type (type-I superconductor), superconductivity is abruptly destroyed when the magnetic exceeds a certain temperature-dependent critical field, $H_c(T)$ while for the second type (type-II superconductor) the flux partially penetrates the superconductor and the penetration gradually increases with increasing of the field. The H-T phase diagram only shows two states, Meissner state and normal state [see Fig. **1-3** (a)] for type-I superconductors. For the Type-II superconductors there are two critical fields $H_{c1}(T)$ and $H_{c2}(T)$ [see Fig. **1-3** (b)], when $H < H_{c1}(T)$ the superconductor shows the Meissner effect, but when $H_{c1}(T) < H < H_{c2}(T)$ the vortex state is reached, later when $H > H_{c2}(T)$ take place in the superconductor, the flux totally penetrates which becomes the normal state. In this case, the density of vortices increases with field, when vortex core is in normal state, overlap with another, and the material is now a normal metal. In 1957 Abrikosov proved to that the way the magnetic flux penetrated in the type-II superconductor was in the form of quantum of vortices with a core in the normal state and a mixture of a normal-superconducting state is reached which is called vortex state or mixed state. Most materials of practical interest are of type-II due to the large H_{c2}. In 1935, the brothers Fritz and Heinz London developed the first theory of superconductivity in order to explain the
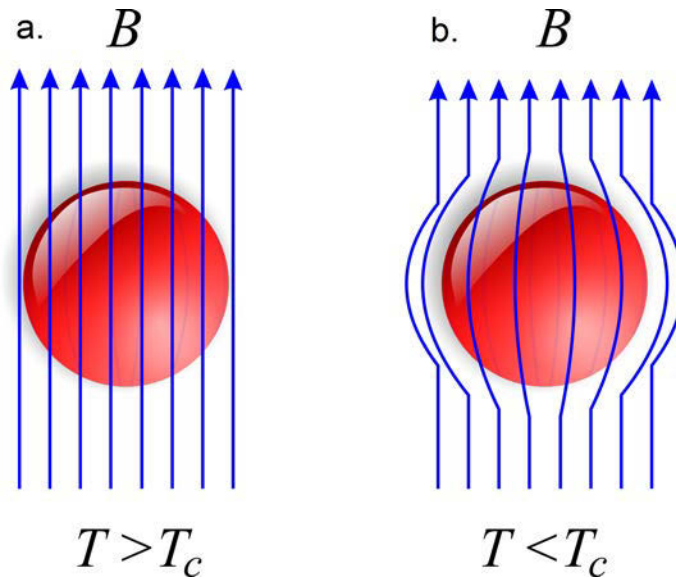
Figure 1-2: Illustration of the Meissner effect of a superconducting sphere, subject to a uniform magnetic field. (a) The magnetic field penetrates completely the material in the normal state, i.e., when $T > T_c$. (b) Keeping on the field, the material is cooled to reach the superconducting state $(T < T_c)$ where the magnetic flux is expelled from inside the material.
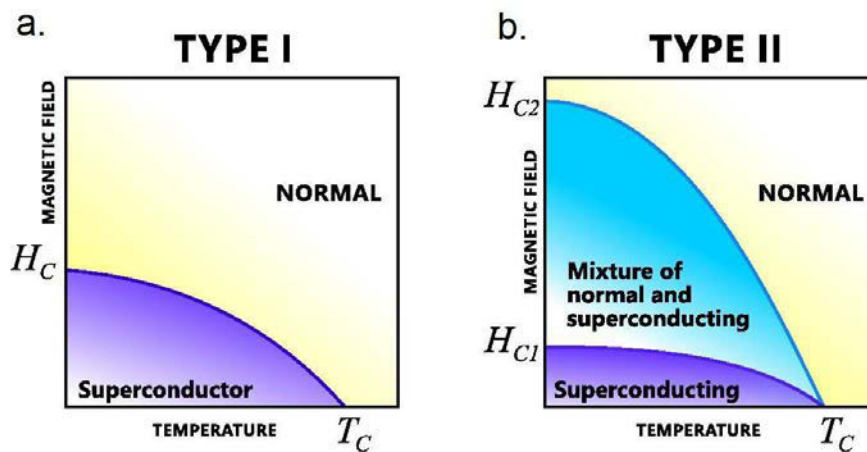
Figure 1-3: (a) A plot of H-T phase diagram for a type-I superconductor and (b) for a type-II superconductor.
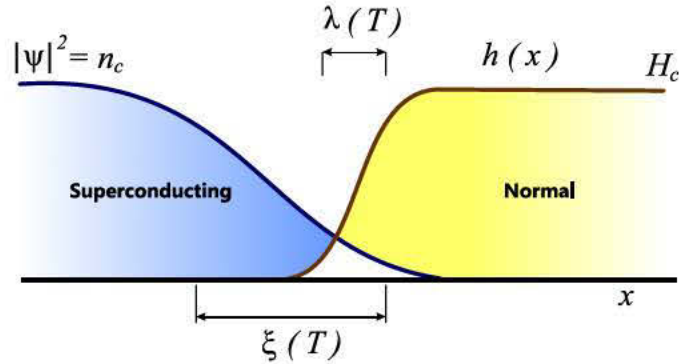
Figure 1-4: Variations of the square of the superconducting order parameter $\Psi(x)$ and the external magnetic field $h(x)$ in the interface between the normal and superconducting domains. $\xi(T)$ and $\lambda(T)$ are the temperature dependent coherence length and magnetic field penetration depth, respectively.

Meissner effect. They started from the Drude-Lorentz equation of motion for electrons in a metal, and by incorporating Maxwell equations and imposing the condition $B = 0$ inside the superconductor. These equations successfully describe both perfect conductors and perfect diamagnetism by the screening supercurrent which flows to cancel the magnetic flux inside the superconductor. In consequence, the value of magnetic field is not zero at the boundary of the superconductor while it decays exponentially. The London penetration dept λ is the distance over which a magnetic field can penetrate into a superconductor and exponentially decay from the boundary of the superconductor. In 1953, Pippard proposed the non-local generalization of the London equations, He introduced the coherence length ξ_0 in his theory, over which the supercurrent j_s and the super-electrons n_s do not change significantly. It is a intrinsic length scale for superconductor and the dimensionless parameter λ/ξ_0 decides if the superconductor is of type-I or type-II. It is worth to mention that the coherence length was also introduced independently by Ginzburg and Landau, but there are differences in both length scales. The Pippard coherence length is related to the BCS coherence length and it is independent from the temperature while the Ginzburg-Landau length depends on temperature.

The first quantum (phenomenological) theory of superconductivity was the Ginzburg-Landau (G-L) theory postulated by Vitaly Lazarevich Ginzburg and Lev Landau, in 1950 [5]. The theory was later proven to be a very powerful theory for superconductivity. This quantum theory should be taken into account, firstly, that the superconducting state is more ordered than normal one and, secondly, that the transition from one state to another (without magnetic field) is a second order phase transition. This implies the existence of an order parameter for a superconductor which is nonzero at $T < T_c$ and vanishes at $T \geq T_c$. As originally proposed, this theory was a triumph of a physical intuition, in which a pseudowavefunction $\Psi(\mathbf{r})$ was introduced as a complex order parameter. $|\Psi(\mathbf{r})|^2$ was supposed to represent the
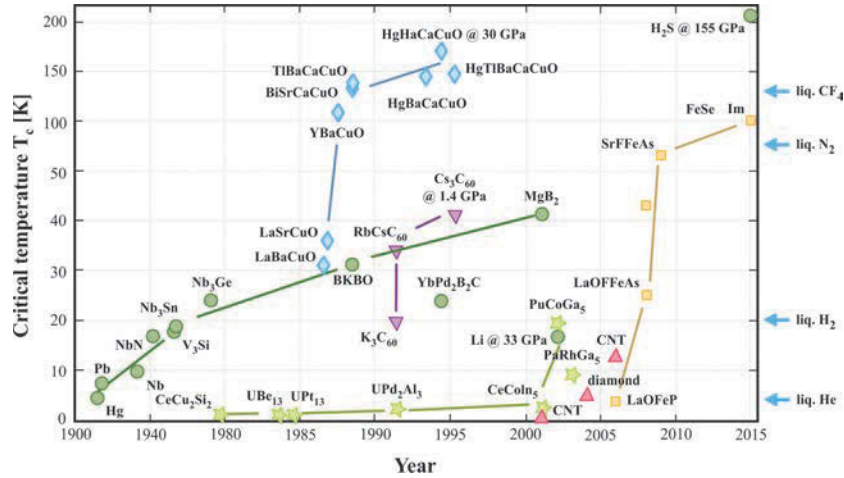
Figure 1-5: The chronology of discoveries of superconductors, and their critical tempera-
tures. Credit: Wikipedia.

local density of superconducting electrons, $n_s(\mathbf{r})$. This theory correctly features both char-
acteristic lengths for the superconductor, i.e. the magnetic penetration depth λ and the
coherence length ξ as shown in Fig. **1-4**. This theory is also able to describe the destruction
of superconductivity by temperature, magnetic field and current. Finally, the surface energy
between the normal and superconducting phases depends on the dimensionless material con-
stant $\kappa = \lambda/\xi$, which is also called the GL parameter. When $\kappa < 1/\sqrt{2}$ ($\kappa > 1/\sqrt{2}$), the
surface energy is positive (negative) leading to type-I (type-II) superconductors.

This theory was initially given limited attention in the western literature because of its
phenomenological foundation until: 1) in 1957 Abrikosov predicted the vortex states in
type-II superconductors by solving the GL equations [6] and 2) in 1959 Gor'kov showed
that the GL theory was, in fact, derivable as a rigorous limiting case of the microscopic
theory [7], suitably reformulated in terms of Green functions to allow specially treating
inhomogeneous regime. The conditions for validity of the GL theory were shown to be a
restriction to temperatures sufficiently near T_c and to spatial variations of Ψ and $\mathbf{A}$ which
were not too rapid. Nowadays, the GL theory is widely used for studying e.g. vortices in
superconductors. Due to the pioneering contributions to the theory of superconductors and
super fluids, Ginzburg and Abrikosov shared the Nobel Prize in Physics in 2003.

In 1957, the physical mechanism of superconductivity became clear only 46 years after
the phenomenon had been discovered, when Bardeen, Cooper and Shrieffer published their
theory (the BCS theory) [8]. The decisive step in understanding the microscopic mechanism
of superconductivity is due to L. Cooper (1956). The fundamental element in this theory
is the pairing of electrons close to the Fermi level into Cooper pairs through an attractive
interaction mediated by phonons. The pairs do not break, unless a certain minimum energy
is provided. This energy provides the band gap. At low temperature, the pairs condensate
into a boson-like state so that they move collectively and unperturbed through the crystal

lattice since they cannot absorb energies smaller than the Cooper-pair binding energy. For this contribution, the authors were awarded the Nobel Prize in Physics in 1972.

In 1987 Johannes Georg Bednorz and Karl Alexander Müller discovered the first high-T_c superconductor, the layered copper oxide BaLaCuO with a T_c of about 40 K [9] (the highest known critical temperature at the time for Nb_3Ge, 23K). They were awarded the Nobel Prize in Physics "for their important breakthrough in the discovery of superconductivity in ceramic materials". Subsequently, shortly after it was found that replacing lanthanum with yttrium, i.e. making YBCO, raised the critical temperature to 92 K, which was important because of liquid nitrogen could then be used as a refrigerant. By 1993, cuprate with a T_c of 133 K at atmospheric pressure was found ($HgBa_2Ca_2Cu_3O_8$) [10] and BSCCO with T_c equal to 105 K [11]. After this discovery further efforts to find cuprates with higher T_c failed until 2000, when a slight increase in the transition temperature was detected for fluorinated Ha-1223 samples (T_c =138 K) [12], but until now, the higher values of T_c are reached under high pressure such as Hg-1223 (at 164 K) [13] and HgBaCaCuO cuprates under 30 GPa pressure. High-T_c superconductors are type-II superconductors. However, they can not be accounted for the conventional BCS theory. The mechanism that causes superconductivity in high-T_c superconductors is one of the major unsolved problems of the theoretical condensed matter physics. In 1994, Sr_2RuO_4 was found to display superconductivity with $T_c \approx 1$ K [14]. It has received considerable attentions because it is an unconventional p-wave spin-triplet superconductor [15], due to the superconductors until this time were spin-singlet paired including conventional or unconventional superconductors. The electronic structures of Sr_2RuO_4 are consistent with the quasi-two-dimensional Fermi liquid at low temperatures ($T < 40K$). The theoretical study of this material can be done by using the BCS theory and GL theory.

Superconductivity in magnesium diboride (MgB_2) was discovered as late as 2001 [16], with T_c at 39 K, a record by far in ordinary metallic compounds and it is considered another important event in the history of superconductivity. The remarkable properties of MgB_2 open a new window in superconductivity for fundamental as well as applied research. The main disadvantage of early MgB_2 samples is their low critical magnetic field H_{c2} . But H_{c2} can be increased up to more than 40T in bulk and up to near 60T in oriented thin films by Carbon doping. MgB_2 was found to be a two-band BCS superconductor with a much higher critical temperature and a significantly smaller isotope effect [17]. The critical temperature of MgB_2 of 39 K enables the realization of electronic circuits based on this material which gives a significant advantage for this material as compared to the low-temperature superconductors. Compared to the High-T_c superconductors, MgB_2 is simpler, cheaper, and more stable over time. This material is expected to be very promising for applications. In addition, in Tokyo Institute of Technology, Japan [18], was discovered a new superconductor based in iron (LaFeOP). However, the critical temperature was to stay at 4-6 K irrespective of hole/electron-doping. A large increase in the T_c to 26K was then found in $LaFe[O_{1-x}F_x]As$ [19], but under pressure this material can reach T_c =43K. The chronology of dicoveries of
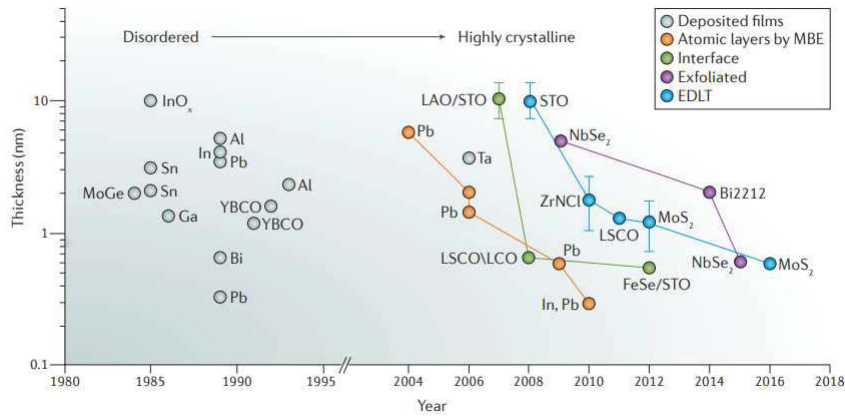
Figure 1-6: Evolution of the thickness of 2D superconductors. (figure taken from Ref. [218])

superconductors and their critical temperature can be followed in Fig. **1-5**.

In the past century, most 2D superconductors were fabricated by deposition of metallic thin films (see Fig. **1-6**), which led to strongly disordered, amorphous or granular samples (grey) [20, 21, 22, 23]. More recently, atomic layers grown by molecular beam epitaxy (MBE; orange) [16, 24, 25, 26, 70], interfacial superconductors (green) [28, 29, 30], exfoliated atomic layers (purple) [31, 32, 33, 34] and electric double-layer transistors (EDLT; blue) [35, 36] have been fabricated. These systems are highly crystalline, in marked contrast with older samples. The deposited films are of three kinds: InO_x, MoGe and Ta are sputtered thin films; Sn, Ga, Al, In, Pb and Bi are MBE-grown thin films; and $YBa_2Cu_3O_y$ (YBCO) was deposited by reactive evaporation. Bi2212, $Bi_2Sr_2CaCu_2O_{8+x}$; LAO, $LaAlO_3$; LCO, La_2CuO_4; LSCO, $La_{2-x}Sr_xCuO_4$; STO, $SrTiO_3$.

1.2 Theories of superconductivity

1.2.1 London approach

In order to understand the behavior of a superconductor in an external magnetic field this theory contains several assumptions. First the two-fluid model, where the all the free electrons of the superconductor are divided into two groups: superconducting electrons of density n_s and normal electrons of density n_n. Second, a homogeneous distribution of superconducting electrons is assumed, i.e. n_s is taken identical everywhere. Finally, assume that both the electric and magnetic fields are so weak that they do not have any apreciable influence on the superconducting electron density. London equations were deduced to describe the relation between the current, electric field and magnetic field [37]. The first London equation describes the connection between supercurrent density and applied electric field, thus the equation of motion for superconducting electrons in an electric field is

$$n_s m \frac{d\mathbf{v}_s}{dt} = n_s e \mathbf{E} \tag{1-1}$$

Where m is the electron mass, e is the electron charge, $\mathbf{v}_s$ is the super fluid velocity, and n_s is the number density of super fluid. Taking into account that the supercurrent density is $\mathbf{j}_s = n_s e \mathbf{v}_s$, we have

$$\mathbf{E} = \frac{d}{dt}(\Lambda \mathbf{j}_s) \tag{1-2}$$

where

$$\Lambda = m/n_s e^2$$

simply follows Newton's second law for the superconducting electrons.
The second London equation describes how the applied magnetic field penetrates into the superconductor, and gives the relation between the supercurrent and the magnetic field.

$$\mathbf{H} + \lambda^2 \nabla \times \nabla \times \mathbf{H} = 0 \tag{1-3}$$

When the London gauge is implemented for the vector potential as

$$\nabla \cdot \mathbf{A} = 0 \tag{1-4}$$

with Maxwell equation $\nabla \times \mathbf{H} = 4\pi/c \mathbf{j}_s$, $\nabla \times \mathbf{E} + 1/c(\partial \mathbf{H}/\partial t)$ and $\mathbf{H} = \nabla \times \mathbf{A}$, one obtains

$$\mathbf{j}_s = -\frac{c}{4\pi\lambda^2}\mathbf{A} \tag{1-5}$$

Let us consider a semi-infinite superconductor for $x > 0$, where the surface coincides with $x = 0$ plane, under applied magnetic field H_0. We solve the second London equation (1-3) with boundary conditions $H(0) = H_0$, $H(\infty) = 0$. The solution is

$$H = H_0 e^{-x/\lambda} \tag{1-6}$$

which means that the magnetic field decreases by increasing the distance from the surface of the superconductor. The characteristic length of decay is λ, called the London magnetic field penetration length:

$$\lambda = \left(\frac{mc^2}{4\pi n_s e^2}\right)^{1/2} \tag{1-7}$$

It indicates that the screening (Meissner) supercurrent at the surface decreases over the same length. Following the two fluid model, λ is also temperature dependent, as possible to control the energy gaps, critical temperature and critical magnetic field in selected region as a result of

$$\lambda(T) = \frac{\lambda(0)}{[1 - (T/T_c)^4]^{1/2}} \tag{1-8}$$

1.2.2 BCS theory

The phenomenological theory had surprising success in explaining many of the principal properties of superconductors but it does not explain the microscopic origins of superconductivity. In 1957 Bardeen, Cooper and Schrieffer proposed microscopic theory which is more complicated than the GL theory that predicts quantitatively many of the properties of elemental superconductors [8]. The vortex structure and the critical parameters can be precisely calculated by using the GL theory and the microscopic level is not necessary for the purpose of this thesis. Therefore, the discussion of the BCS theory will be limited to the basics.

One year before the publication of the BCS theory, Cooper demonstrated that the normal ground state of an electron gas is unstable with respect to the formation of "bound" electron pairs. The quotation marks is used due to these pair electron are not bounded in the ordinary sense, and the presence of the filled Fermi sea is essential for this state to exist. Therefore this is properly a many-electron state. In consequence, BCS theory starts from the assumption that there is an attraction between electrons, which overcome the Coulomb repulsion, and pairs of electrons, called Cooper-pairs [38], are formed. The electrons interact attractively indirectly in the following way: one electron slightly disturbs the lattice in its neighborhood. The resulting phonon interacts quickly with another electron, which takes advantage of the deformation and lowers its energy. The second electron emits a phonon by itself which interacts with the first electron and so on. It is that passing back and forth of phonons which couples the two electrons together and brings them into a lower energy state. Electrons in such a Cooper-pair are situated on the Fermi surface and have opposite momentum and opposite spin. These electrons form a cloud of Cooper-pairs which drift cooperatively through the crystal. In order to destroy one Cooper-pair, it is necessary to destroy all Cooper-pairs in a macroscopic region of the superconductor. It requires much energy and, consequently, the probability of the process is very small.

Since the electrons of a Cooper-pair have a lower energy than two unpaired electrons, the Fermi energy of the superconducting state may be considered to be lower than that for the non-superconducting state. The lower state is separated from the normal state by an energy gap E_g. The energy gap stabilizes the Cooper-pairs and prevents them from breaking apart. In 1959 Gor'kov showed that the Ginzburg-Landau theory follows form of the BCS theory, valid near T_c and suitable to deal with spatially varying situations [7]. He showed that the order parameter Ψ can be seen as the wave-function of the center-of-mass motion of the Cooper-pairs. This work provided a solid theoretical foundation for the GL theory.

1.2.3 Ginzburg-Landau (GL) theory

The London theory did not consider quantum effects, contrary to the Ginzburg-Landau theory [5]. This theory is based on the theory of second-order phase transitions developed by Landau [39], in which a phase transition of second order occurs when the state of a body

change gradually while its symmetry change discontinuously at the transition temperature. Furthermore, the low-temperature phase is the one of reduced symmetry, i.e., it is more ordered. This theory introduced a complex-order parameter $\psi(\mathbf{r})$ as a pseudowavefunction of the superconducting electrons, where $|\psi(\mathbf{r})|^2$ is to represent the local density of super-conducting electrons, $n_s(\mathbf{r})$. The free energy is expanded in powers of the order parameter, which is small near the transition temperature and it is valid to temperature region close to the critical temperature, $T_c - T \ll T_c$. The variational method is applied to this assumed expansion of the free-energy density in powers of $|\psi(\mathbf{r})|^2$ and $|\nabla\psi(r)|^2$, bringing about two coupled GL equations, for $\psi(\mathbf{r})$ and for the vector potential $A(\mathbf{r})$ respectively, capable of dealing with an inhomogeneous distribution of $\psi(\mathbf{r})$ and a nonlinear response to fields. In the following sections, the main principles of GL theory will be covered.

1.2.3.1 Free energy density

The wave function of superconducting electrons $\Psi(\mathbf{r})$ is the order parameter and its normal-ization such that $|\Psi(\mathbf{r})|^2$ gives the density of Cooper pairs:

$$|\Psi(\mathbf{r})|^2 = n_s \tag{1-9}$$

The simplest case to be considered with GL theory is a homogeneous superconductor without external magnetic field. In this case $\Psi(\mathbf{r})$ does not depend on $\mathbf{r}$ and the expansion of free energy in power of $|\Psi|^2$ near T_c becomes

$$G_{0s} = G_n + \alpha|\Psi|^2 + \frac{\beta}{2}|\Psi|^4 \tag{1-10}$$

G_n is the free energy density of the normal state, α and β are phenomenological expansion coefficients depending on the superconducting material. The temperature dependence of α is $\alpha \propto (T - T_c)$ Fig. **1-7**. While β is positive and temperature independent. Minimization of the free energy with respect to $|\Psi|^2$, leads to $|\Psi_0|^2 = -\alpha/\beta$.

Now, the general case of a inhomogeneous superconductor in a uniform external magnetic field near T_c the Gibbs free energy can be expanded in powers of Ψ as

$$G_{sH} = G_n + \alpha|\Psi|^2 + \frac{\beta}{2}|\Psi|^4 + \frac{1}{2m^*}\left|\left(-i\hbar\nabla - \frac{e^*}{c}\mathbf{A}\right)\Psi\right|^2 - \frac{(\mathbf{H} - \mathbf{H}_0)^2}{8\pi} \tag{1-11}$$

where $\mathbf{H}_0$ is the external magnetic field and $\mathbf{H}$ is the exact microscopic field at a given point of the superconductor. Thus the last term describes the magnetic energy of the magnetic field generated by the supercurrents. The term before is the kinetic energy density of the superconducting electrons.

The total energy of the superconducting system can be obtained from the volume integration of Eq. 1-11, and the equilibrium state is reached when the variations of this total energy with respect to Ψ^* and $\mathbf{A}$ become zero.
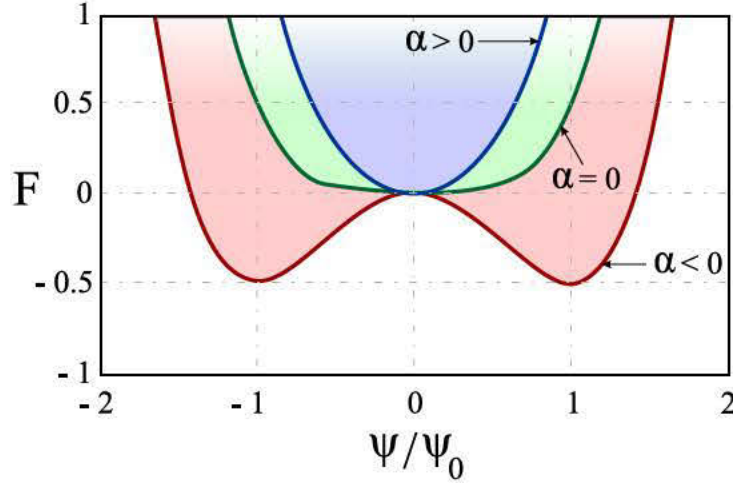
Figure 1-7: Ginzburg-Landau free-energy functions for describing spontaneous symmetry breaking through a second order phase transition.

$$\int \left\{ \alpha\Psi\delta\Psi^* + \beta|\Psi|^2\Psi\delta\Psi^* + \frac{1}{2m^*}\left[(-i\hbar\nabla\Psi - \frac{e^*}{c}\mathbf{A}\Psi)\cdot(i\hbar\nabla\delta\Psi^* - \frac{e^*}{c}\mathbf{A}\delta\Psi^*)\right]\right\} dV_s = 0$$

$$(1\text{-}12)$$

Let $\varphi = (-i\hbar\nabla - \frac{e^*}{c}\mathbf{A})\Psi$. By using relationship $\nabla(c\nu) = \nu\nabla c + c\nabla\nu$, where c is a scalar, the second term in Eq. 1-12 can be written as

$$\frac{1}{2m^*}\varphi(i\hbar\nabla - \frac{e^*}{c}\mathbf{A})\delta\Psi^* = \frac{1}{2m^*}i\hbar\left[\nabla(\delta\Psi^*\varphi) - \delta\Psi^*\nabla\varphi\right] - \frac{1}{2m^*}\varphi\frac{e^*}{c}\mathbf{A}\delta\Psi^* \qquad (1\text{-}13)$$

By Gauss's theorem,

$$\int \nabla(\delta\Psi^*\varphi)dV_s = \oint \delta\Psi^*\varphi dS_s$$

We obtain

$$\int dV_s\frac{1}{2m^*}\varphi(i\hbar\nabla - \frac{e^*}{c}\mathbf{A})\delta\Psi^* = \int dV_s\frac{1}{2m^*}(-i\hbar\nabla - \frac{e^*}{c}\mathbf{A})^2\Psi\delta\Psi^* + \oint i\hbar\frac{1}{2m^*}\mathbf{n}\cdot\varphi\delta\Psi^*dS_c \quad (1\text{-}14)$$

Eq. 1-12 can only be satisfied if

$$\alpha\Psi + \beta|\Psi|^2\Psi + \frac{1}{2m^*}\mathbf{\Pi}^2\Psi = 0 \tag{1-15}$$

$$\oint \mathbf{n}\cdot\left(\frac{i\hbar}{2m^*}\mathbf{\Pi}\Psi\delta\Psi^*\right)dS_s = 0 \Rightarrow \mathbf{n}\cdot\mathbf{\Pi}\Psi|_{boundary} = 0 \tag{1-16}$$

Finally, the Eq.1-15 and Eq.1-16 are the first Ginzburg-Landau equation and the boundary condition, respectively, with $\mathbf{\Pi} = (-i\hbar\nabla - \frac{e^*}{c}\mathbf{A})$.

The variation of Eq. 1-11 with respect to the vector potential $\mathbf{A}$ is

$$\int \left\{ \left(-i\hbar\nabla - \frac{e^*}{c}\mathbf{A}\right)\Psi\frac{-e^*}{c}\delta\mathbf{A}\Psi^* + \frac{-e^*}{c}\delta\mathbf{A}\Psi\left(i\hbar\nabla - \frac{e^*}{c}\mathbf{A}\right)\Psi^* \right\} dV \tag{1-17}$$

$$+\frac{1}{4\pi}\int (\nabla \times \mathbf{A} - \mathbf{H}) \cdot \nabla \times \delta\mathbf{A} dV = 0$$

The first integral can be written as

$$\int \left[\frac{i\hbar e}{m^*c}(\Psi^*\nabla\Psi - \Psi\nabla\Psi^*) + \frac{4e^2}{m^*c^2}|\Psi|^2\mathbf{A} \right] \cdot \delta\mathbf{A} dV = 0 \tag{1-18}$$

Using the identity

$$\mathbf{a} \cdot (\nabla \times \mathbf{b}) = \mathbf{b} \cdot (\nabla \times \mathbf{a}) - \nabla \cdot [\mathbf{a} \times \mathbf{b}] \tag{1-19}$$

we can carry out the integration in the last term of (1-17):

$$\frac{1}{4\pi}\int \left\{ \delta\mathbf{A} \cdot \nabla \times \nabla \times \mathbf{A} + \nabla \cdot [\delta\mathbf{A} \times (\nabla \times \mathbf{A} - \mathbf{H}_0)] \right\} dV = 0 \tag{1-20}$$

By using Gauss's theorem to convert the volume integral into a surface integral:

$$\int \nabla \cdot [\delta\mathbf{A} \times (\nabla \times \mathbf{A} - \mathbf{H}_0)] dV = \oint_s d\mathbf{S}[\delta\mathbf{A} \times (\nabla \times \mathbf{A} - \mathbf{H}_0)], \tag{1-21}$$

The surface integral is zero because the magnetic field at the surface of the superconductor is fixed; hence $\delta\mathbf{A}|_S = 0$.

Finally, after some elementary modifications Eq. 1-17 takes the form

$$\int \left[\frac{i\hbar e}{m^*c}(\Psi^*\nabla\Psi - \Psi\nabla\Psi^*) + \frac{4e^2}{m^*c^2}|\Psi|^2\mathbf{A} + \frac{1}{4\pi}\nabla \times \nabla \times \mathbf{A} \right] \cdot \delta\mathbf{A} dV = 0 \tag{1-22}$$

For arbitrary $\delta\mathbf{A}$, the integral 1-22 can be zero only if the expression in square braquets is zero. This condition determines the second equation of GL theory, for the vector potential $\mathbf{A}$:

$$\mathbf{j}_s = -\frac{i\hbar e}{m^*}(\Psi^*\nabla\Psi - \Psi\nabla\Psi^*) - \frac{4e^2}{m^*c}|\Psi|^2\mathbf{A} \tag{1-23}$$

where, by Maxwell's equation, the current density $\mathbf{j}_s$ in the superconductor is

$$\mathbf{j}_s = \frac{c}{4\pi}\nabla \times \nabla \times \mathbf{A}, \qquad \mathbf{H} = \nabla \times \mathbf{A}. \tag{1-24}$$

To summarize, the two coupled non-linear GL equations are:
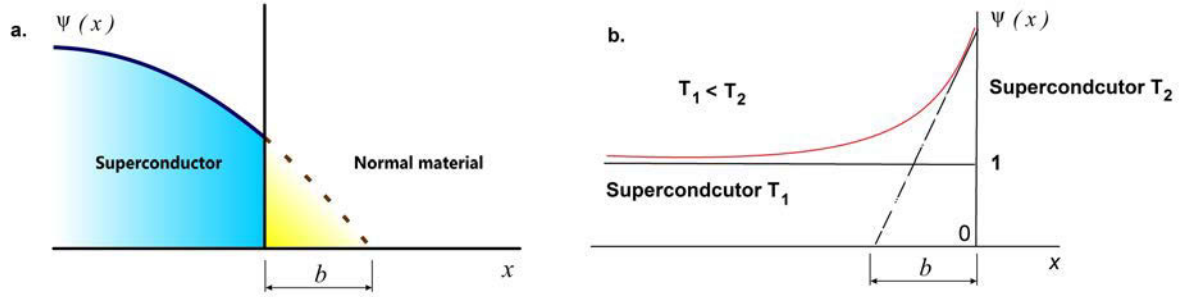
Figure 1-8: Schematic representation of the spatial dependence of the order with the extrapolation length of De Gennes b at the interface between (a) superconductor and normal metal, and (b) superconductor of $T_c = T_1$, and a superconductor at $T_c = T_2$, with $T_1 < T_2$

$$\alpha\Psi + \beta|\Psi|^2\Psi + \frac{1}{2m^*}\left(-i\hbar\nabla - \frac{e^*}{c}\right)^2\Psi = 0 \tag{1-25}$$

$$\mathbf{j}_s = -\frac{i\hbar e}{m^*}(\Psi^*\nabla\Psi - \Psi\nabla\Psi^*) - \frac{4e^2}{m^*c}|\Psi|^2\mathbf{A} \tag{1-26}$$

The first equation is similar to the usual quantum-mechanical Schrödinger's equation for a particle of mass $2m$, charge $2e$, energy $-\alpha$ and wave function $\Psi(\mathbf{r})$ in a potential $\beta|\Psi|^2$. These Ginzburg-Landau equations allow us to determine the spatial variation of the order parameter and the current distributions. In the limiting case of $|\Psi|$=const. from the GL equations, the London approach appears as a result of a rigid Ψ.

1.2.4 Boundary conditions

When applying the GL equations to a finite sample it is necessary to introduce some conditions. The boundary condition for the potential vector $\mathbf{A}$ is that at which the magnetic field at the surface of the superconductor must be equal to the applied external magnetic field H_0:

$$(\nabla \times \mathbf{A}) \times \hat{\mathbf{n}}|_s = \mathbf{H_0} \times \hat{\mathbf{n}} \tag{1-27}$$

where $\hat{\mathbf{n}}$ denotes the normal component to the surface of the superconductor.
If the superconductor has an interface with vacuum or an insulator, the condition will be

$$\left(-i\hbar\nabla - \frac{e^*}{c}\mathbf{A}\right)\Psi\bigg|_n = 0 \tag{1-28}$$

It is easy with the help of (1-26) to verify that (1-23) satisfies a very natural physical requirement, as it is to assure that no supercurrent passes through the superconductor-dielectric interface.

However, De Gennes, using the BCS microscopic theory , generalized this condition to superconducting/metal or superconducting/superconducting interfaces to higher T_c [40] (see Fig.**1-8**) introducing a more general condition:

$$\left(-i\hbar\nabla - \frac{e^*}{c}\mathbf{A}\right)\Psi\bigg|_n = \frac{i\hbar}{b}\Psi \tag{1-29}$$

where b is the extrapolation length which is an arbitrary real number.

The value of extrapolation length is determined by the medium adjacent to the superconductor:

1. for vacuum or an insulator: $b \to \infty$,
2. for normal metals: $b > 0$, and for ferromagnets: $b \to 0$,
3. for superconducting layer with a higher T_c: $b < 0$.

The latter case is of theoretical interest because the order parameter near the surface will increase, which will lead to higher critical fields and critical temperatures.

1.2.5 Characteristic length scales

The GL theory introduces two important characteristic length scales: the coherence length ξ and the penetration depth λ. A simplified case in which no fields are applied is considered. Then $\mathbf{A} = 0$, and Ψ is real since the differential equation (1-25) has only real coefficients.

$$-\frac{\hbar^2}{2m^*}\nabla^2\Psi + \alpha\Psi + \beta\Psi|\Psi|^2 = 0 \;, \tag{1-30}$$

If a normalized wavefunction $f = \Psi/\Psi_\infty$, where $\Psi_\infty^2 = -\alpha/\beta > 0$, the equation becomes

$$-\frac{\hbar^2}{2m^*|\alpha|}\nabla^2 f - f + f|f|^2 = 0 \;, \tag{1-31}$$

The constant $\xi^2(T) = \frac{\hbar^2}{2m^*|\alpha(T)|}$ has dimension of length square; $\xi(T)$ is known as the coherence length and corresponds to the distance over which the order parameter varies. The temperature dependence of the coherence length is given by

$$\xi(T) = \xi_0(1 - T/T_{c0})^{1/2} \tag{1-32}$$

where the length ξ_0 is $\hbar/(2m^*\alpha_0)^2$.

The typical length scale λ over which the magnetic field can vary is the penetration depth and can be obtained from the second GL equation. Neglecting the gradient of Ψ, Eq. (1-26) can be written in the following form

$$\nabla \times \mathbf{j} = -\frac{4e^2}{m^*c}|\Psi|^2\nabla \times \mathbf{A}. \tag{1-33}$$
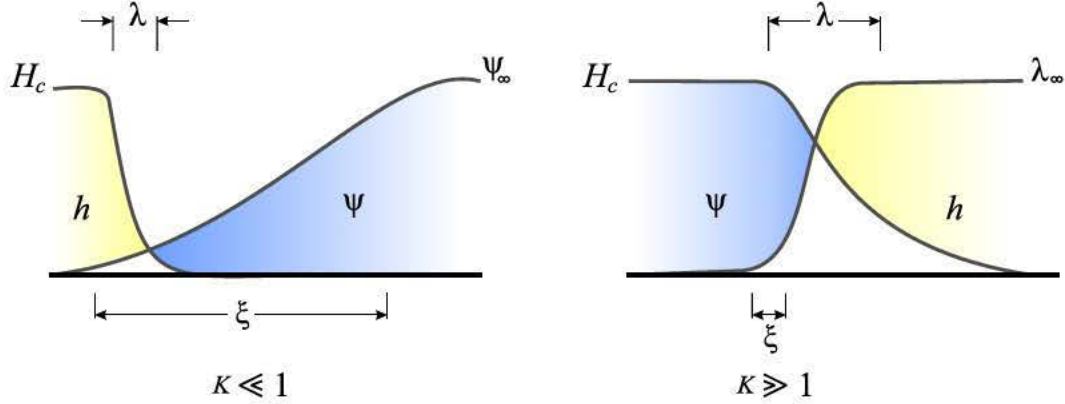
Figure 1-9: Schematic diagram of variation of H and Ψ

Using the Maxwell equation it is possible to rewrite this as

$$\mathbf{H} + \lambda^2 \nabla \times \nabla \times \mathbf{H} = 0 \tag{1-34}$$

and the penetration depth λ is given by

$$\lambda(T) = \left(\frac{m^* c^2 \beta}{16 \pi \alpha(T) e^2} \right)^{1/2} \propto (1 - T/T_{c0})^{-1/2} \tag{1-35}$$

The exact temperature dependence of ξ and λ is related to the purity of the superconductor, defined by the electron mean free path l_{el} [40, 41]

$$\xi(T) = 0.74\xi_0(1 - T/T_{c0})^{-1/2} \quad \text{when} \quad l_{el} \gg \xi_0 (\text{pure}), \tag{1-36}$$

$$\xi(T) = 0.855\sqrt{\xi_0 l_{el}}(1 - T/T_{c0})^{-1/2} \quad \text{when} \quad l_{el} \ll \xi_0 (\text{dirty}), \tag{1-37}$$

and

$$\lambda(T) = \frac{\lambda_L(0)}{\sqrt{2}}(1 - T/T_{c0})^{-1/2} \quad \text{when} \quad l_{el} \gg \xi_0 (\text{pure}), \tag{1-38}$$

$$\lambda(T) = \frac{\lambda_L(0)}{\sqrt{2}}\sqrt{\frac{\xi_0}{1.33 l_{el}}}(1 - T/T_{c0})^{-1/2} \quad \text{when} \quad l_{el} \ll \xi_0 (\text{dirty}), \tag{1-39}$$

where ξ_0 and $\lambda_L(0)$ are the BCS coherence length and the London penetration depth at zero temperature, respectively.

In principle the validity of the GL theory is limited to the vicinity of the critical temperature T_c [41]. In the series expansion (1-11) of the Gibbs free energy density G_{sH} in powers of $|i\hbar\nabla\Psi - (2e/c)\mathbf{A}\Psi|^2$, only the first term has been kept. Therefore, only slow changes of Ψ and $\mathbf{A}$ are assumed over distances comparable with the characteristic size of an inhomogeneity

in the superconductor. In practice, and especially if the Gibbs free energy is expanded to higher order terms of $t = 1 - T/T_c$ [42], the validity of GL formalism can be reached further below T_c. Early work shows that the GL model was valid for any temperature bellow T_c in strong magnetic fields [40]. In the studies of mesoscopic superconductors the GL theory has been successfully used deep into the superconducting phase [43, 44, 45]. In the case of a clean superconductor ($l_{el} \gg \xi_0$), the GL theory is valid if $\xi(T), \lambda(T) \gg \xi_0$. Since $\xi(T) \sim \xi(0)(1 - T/T_c)^{-1/2}$, the temperature must be close to T_c, the critical temperature at zero field and the first condition of validity is satisfied automatically. The second condition, $\lambda(T) \gg \xi_0$, represents the requirement that local electrodynamics is applicable, or, in other words, that the superconductor is of the London type. Since $\lambda(T) \sim \lambda(0)(1 - T/T_c)^{-1/2}$ and $\kappa \sim \lambda(0)/\xi(0)$, the condition $\lambda(T) \gg \xi_0$ expresses again that temperature must be close to T_c.

1.2.6 Ginzburg-Landau parameter κ

The Ginzburg-Landau parameter κ is defined in terms of the two important characteristic length scales, the magnetic field penetration depth and the Ginzburg-Landau coherence length

$$\kappa = \frac{\lambda}{\xi} \tag{1-40}$$

where both lengths show the same temperature dependence within the GL theory, κ is typically considered a material constant with negligible temperature dependence. In the following section, it is possible to confirm that a superconductor in the applied magnetic field depends on whether the value of κ is less or larger than $1/\sqrt{2}$.

1.3 Properties of superconductors

1.3.1 The lower critical field H_{c1}

The formation of vortices in type-II superconductor becomes thermodynamically favorable at the lower critical fiel H_{c1}. In the case of a typical London superconductor the variation of Ψ is neglected. The London expression for the free energy can be written as

$$\epsilon = \frac{1}{8\pi} \int [\mathbf{H}^2 + \lambda^2 (\nabla \times \mathbf{H})^2] dV \tag{1-41}$$

where this equation is simply the sum of the magnetic and kinetic energies of the supercon-ducting electrons contained in the vortex. By using the formula

$$(\nabla \times \mathbf{H})^2 = \mathbf{H} \cdot \nabla \times \nabla \times \mathbf{H} - \nabla \cdot [(\nabla \times \mathbf{H}) \times \mathbf{H}], \tag{1-42}$$

and

$$\int \nabla \cdot [(\nabla \times \mathbf{H}) \times \mathbf{H}]dV = \oint [(\nabla \times \mathbf{H}) \times \mathbf{H}] \cdot d\mathbf{S} \tag{1-43}$$

we obtain

$$\epsilon = \frac{1}{8\pi} \int \mathbf{H} \cdot (\mathbf{H} + \lambda^2 \nabla \times \nabla \times \mathbf{H})dV \tag{1-44}$$

Since we have the relation of Eq.(1-3), the equation above can be written as

$$\epsilon = \frac{\Phi_0}{8\pi} H(0) = \left(\frac{\Phi_0}{4\pi\lambda}\right)^2 \ln\kappa. \tag{1-45}$$

We already know that, for a superconductor in an external magnetic field, the energy that is a minimum at equilibrium is the Gibbs free energy G. Per unit length of the vortex, this energy is

$$\mathcal{G} = \epsilon - \int \frac{\mathbf{B} \cdot \mathbf{H_0}}{4\pi} dV \tag{1-46}$$

Thus in the case of a vortex which carries one magnetic flux quantum Φ_0, we have

$$\mathcal{G} = \epsilon - \frac{\Phi_0 H_0}{4\pi} \tag{1-47}$$

$\mathcal{G} < 0$ determines the field where the formation of vortex starts to be favored, i.e.,

$$H_{c1} = \frac{4\pi\epsilon}{\Phi_0} = \frac{\Phi_0}{4\pi\lambda^2}\ln\kappa \tag{1-48}$$

1.3.2 The upper critical field H_{c2}

The type-II superconductor is characterized by a regular vortex lattice, in which period decreases and it becomes of the order of the coherence length ξ as the magnetic field is increased. Then a second-order phase transition occurs from the mixed to the normal state. This happens when the external field reaches the value of the upper critical field. Thus, when the magnetic field has reduced Ψ to a value much smaller than Ψ_∞ a linearized GL theory will be appropriate. Then, using the Eq. (1-25) and the definition for ξ the coherence length, the corresponding equation is

$$\left(\frac{\nabla}{i} - \frac{2\pi\mathbf{A}}{\Phi_0}\right)^2 \Psi = -\frac{2m^*\alpha}{\hbar^2}\Psi \equiv \frac{\Psi}{\xi(T)^2} \tag{1-49}$$

The convenient gauge choice to solve the problem of the nucleation of superconductivity in a bulk sample is $\mathbf{A}_y = Hx$ considering the presence of a field $\mathbf{H}$ along the z axis. By expanding left member of the equation above, we have

$$\left[-\nabla^2 + \frac{4\pi i}{\Phi_0}Hx\frac{\partial}{\partial y} + \left(\frac{2\pi H}{\Phi}\right)^2 x^2\right]\Psi = \frac{1}{\xi^2}\Psi \tag{1-50}$$

Now, it is possible to choose a solution of the form $\Psi = e^{ik_y y} e^{ik_z z} f(x)$. Then, by working on Eq.1-50, we obtain

$$-f''(x) + \left(\frac{2\pi H}{\Phi_0}\right)^2 (x - x_0)^2 f = \left(\frac{1}{\xi^2} - k_z^2\right) f \tag{1-51}$$

with $x_0 = k_y \Phi_0 / 2\pi H$. Multiplying Eq. 1-51 by $\hbar/2m^*$, we obtain the Schrödinger equation of a harmonic oscillator and the problem becomes as that of finding the quantized states of a normal charged particle in a magnetic field (Landau levels). The equation of eigenvalues are

$$\epsilon_n = \left(n + \frac{1}{2}\right) \hbar \omega_c = \left(n + \frac{1}{2}\right) \hbar \left(\frac{2eH}{m^* c}\right) \tag{1-52}$$

finally, considering the lowest value of $k_z = 0$ and n_0. The corresponding value for upper critical field is

$$H_{c2} = \frac{\Phi_0}{2\pi \xi^2(T)} \tag{1-53}$$

1.3.3 Surface superconductivity and the third critical field H_{c3}

The state of a type-II superconductor immersed in an external magnetic field H_0 slightly lower than H_{c2} (the upper critical field) shows a tightly packed vortex lattice forms, in which the order parameter at this field is small, $\Psi \to 0$. The finite size of superconducting samples can influence on the nucleation of superconductivity as it was demonstrated by Saint-James and de Gennes [47]. For a metal-insulator interface the parallel field H_{c3} is larger than H_{c2} by a factor of 1.695. At H_{c3} the superconducting sheath of thickness $\sim \xi(T)$ is formed at the surface called surface superconductivity.

A good approximation was suggested by C. Kittel by using a variational method. By working with the GL theory to explain the surface superconductivity, the trial function was taken to be

$$\Psi = f(x) e^{ik_y y} = e^{-\alpha x^2} e^{ik_y y} \tag{1-54}$$

with x measured from the sample surface. This choice automatically satisfies the boundary condition

$$\left. \frac{\partial \Psi}{\partial x} \right|_{surface} = 0 \tag{1-55}$$

The gauge choice of $\mathbf{A}$ is along $\mathbf{e}_y$. The parameters a and k_y are then determined variationally. In the linearized approximation, the Gibbs free energy per unit surface area can be written as

$$G - G_n = \frac{\hbar^2}{2m^*} \int_0^\infty \left[-\frac{1}{\xi^2} |\Psi|^2 + \left| \left(\frac{\nabla}{i} - \frac{2\pi}{\Phi_0} \mathbf{A}\right) \Psi \right|^2 \right] dx \tag{1-56}$$

The linearized theory is valid only at the transition, where $G = G_n$. The final result is

$$H_{c3} \approx \left(\frac{\pi}{\pi - 2}\right)^{1/2} \frac{\Phi_0}{2\pi\xi^2} = 1.66 H_{c2} \tag{1-57}$$

Therefore, in a magnetic field parallel to the surface, superconductivity nucleates in a surface layer of thickness $\sim \xi$ at a field almost 70 percent higher than the nucleation field of superconductivity in the bulk of the material.

1.3.4 Magnetization of type-II superconductor

Let us consider a cylinder of type-II superconductor in a longitudinal magnetic field H_0, with coherence length ξ which depends only on x coordinate and increases monotonically with x, but the penetration depth λ is independent of x. The current exerts a Lorentz force on each vortex f_L:

$$f_L = \frac{1}{c} j \Phi_0 = \Phi_0 \frac{dM}{dx} \tag{1-58}$$

considering $B = H_0 + 4\pi M$ and $j = c[dM/dx]$. Since the system of vortices is in equilibrium, the other force can be obtained by differentiating 1-45 which depends on ξ. Now, comparing with (1-58), the condition for equilibrium can be written as:

$$\Phi_0 \frac{dM}{dx} = \left(\frac{\Phi_0}{4\pi\lambda}\right)^2 \frac{1}{\xi} \frac{d\xi}{dx} \tag{1-59}$$

where

$$M = \frac{\Phi_0}{16\pi^2\lambda^2} \ln\frac{\xi}{l} \tag{1-60}$$

where l corresponds to the integration constant and has dimensions of length. We can use the relation for upper critical field $\Phi_0 = 2\pi\xi^2 H_{c2}$ and apply it to a particular point x_0. We have $\Phi_0 = 2\pi l^2 H_0$, therefore

$$\frac{\xi}{l} = \left(\frac{H_0}{H_{c2}}\right)^{1/2} \tag{1-61}$$

Finally, substituting Eq.(1-61) in Eq.(1-60), we obtain

$$M = -\frac{\Phi_0}{32\pi^2\lambda^2} \ln\frac{H_{c2}}{H_0} \tag{1-62}$$

By considering a dependence $M(H_0)$ at fields H_0 close to H_{c2} and after some calculations, we have

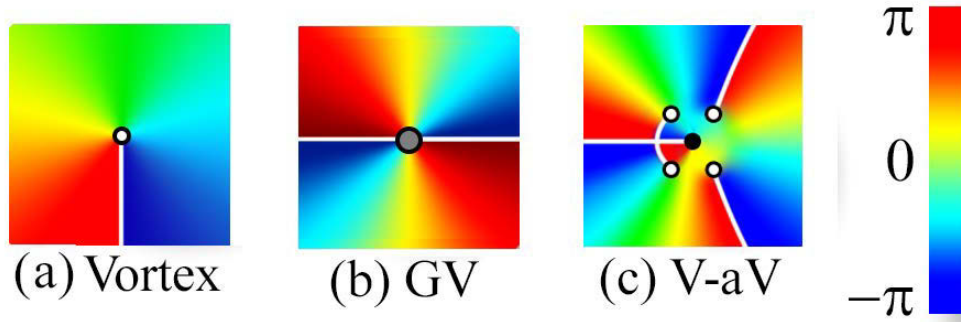$$-4\pi M = \frac{H_{c2} - H_0}{4\kappa^2} \tag{1-63}$$

Figure 1-10: The phase plot for the single-vortex (a), a giant vortex with vorticity $L = 2$ (b) and the $L = 4 - 1$ vortex-antivortex structure with total vorticity $L = 3$ (c).

This equation is correct to logarithmic accuracy, provided that $\kappa \gg 1$. We can see that $|M|$ decreases linearly as $H_0 \to H_{c2}$.

In mesoscopic samples, whose size is comparable to the coherence length ξ and penetration depth λ, the properties of a superconductor are considerable influenced by the confinement effects. Therefore, vortex states in mesoscopic superconductors depends strongly on the boundary conditions imposed by the sample shape, i.e., on the topology of the system, which makes the behavior of mesoscopic samples significantly different from the bulk ones. The distinction between type-I and type-II superconductors is determined not only by κ and thickness of the sample d, but also by the lateral dimensions of the sample (see e.g. Ref. [46]). Consequently, the vortex state is very different from the Abrikosov triangular lattice in bulk, where only the vortex-vortex interaction plays a role, whereas, in mesoscopic system the sample boundary tries to impose its geometry on the vortex distribution [46, 47]. During the last two decades, numerous works have shown this behavior. It was shown that [48] vortices form shell structures in superconducting disks and for large radius of the disks the influence of the boundary diminishes and the triangular lattice may reappear [49]. Moreover, Some peculiar vortices such as the giant vortex and the anti-vortex states were unveiled. The total number of vortices in the sample in which the configuration vortex consisting of vortices, giant vortex and antivortices can be determined by going around a closed path in the plane around a given point anticlockwise, the phase of the order parameter will change L times 2π. L is related with the vorticity. The anticlockwise direction is just to make sure that L for a vortex is always positive. The vortex at the center of the sample shows a vorticity $L = 1$. It is due to the phase of the order parameter which changes by 2π (See Fig. **1-10**(a)). The Fig.**1-10**(b) shows the phase around the vortex center changing twice by 2π indicating that this giant vortex has vorticity $L = 2$. Fig. **1-10**(c) shows the vortex-antivortex structure. The antivortex is at the center and the four vortices surround it. This antivortex has vorticity $L = -1$ so that the total vorticity of this sample is $L = 4 - 1 = 3$.

1.3.5 Types of superconductors

A classification of superconductors depends on their behavior in in the presence of an external applied magnetic field. This division is based on the fact that the surface energy α_{ns}, of an interface between a normal and a superconducting region has a different sign, which is proportional to the difference between the two characteristics length of a superconductor $(\xi - \lambda)$. Therefore, the Ginzburg-Landau parameter $\kappa = \lambda/\xi$ reach a relevant importance. If $\kappa < 1/\sqrt{2}$ the superconductor is classified as type-I and its surface energy is positive. On the other hand, the condition $\kappa > 1/\sqrt{2}$ (type-II superconductors) implies in a negative surface energy, favoring the formation of superconducting-normal boundaries and the flux penetrates in small tubes (vortices), each one carrying a quantized amount of flux. However, types I and II conventional single-band superconductors interchange at the Ginzburg-Landau parameter $\kappa = 1/\sqrt{2}$ close of the critical temperature. At lower temperatures an intertype (transitional) domain in the (κ,T) plane can be found in a finite intervals of κ by using the extended Ginzburg-Landau formalism, but also two standard types with the transitional domain in between applies also to multiband superconductors, such as recently discovered borides and iron-based materials, can belong to the intertype regime [50].

1.3.5.1 Type-I superconductors

Type-I superconductors include all superconducting elements except niobium. Niobium, superconducting alloys and chemical compounds make up the second group, type-II. The Meissner effect is of more remarkable phenomenon of Type-I superconductors, in which not only a magnetic field is *excluded* from entering a superconductor, but also that a field in a originally normal state is *expelled* as it is cooled bellow T_c. The existence of such a reversible Meissner effect implies that superconductivity will be destroied by a critical magnetic field H_c, which is related thermodynamically to the free-energy difference between the normal and superconducting state in zero field. H_c can be determined by equating the energy $H^2/8\pi$ per unit volume, associated with holding the field out against the magnetic pressure with the condensate energy. That is

$$\frac{H_c^2(T)}{8\pi} = f_n(T) - f_s(T) \tag{1-64}$$

where $f_n(T)$ and $f_s(T)$ are the Helmholtz free energy densities in the normal and superconducting state respectively. It can be shown that the normal phase and the superconducting phase have equal thermodynamic potential G (and therefore can coexist) only at applied field $H_0 = H_c$. This is true for the samples with zero demagnetizing factors, i.e., for long, thin cylinder or sheet parallel to the applied magnetic field.
In Fig. **1-9** are sketched the one-dimensional variations of Ψ and $H(x)$ in the domain wall, contrasting the cases with $\kappa \ll 1$ and $\kappa \gg 1$. For $\kappa \ll 1$ it is possible to notice that the surface energy is positive since there is a region of thickness $\sim (\xi - \lambda)$ from which the

magnetic field is held out. The argument is reversed for $\kappa \gg 1$, leading to a negative surface energy. This argument can be justified by using the GL theory.

The solutions of the GL differential equations are subject to the boundary conditions for the order parameter and magnetic field $\mathbf{H}$, when $x \to -\infty$ then $\Psi = 0$ and $H = H_0$, while if $x \to +\infty$ then $\Psi = \Psi_\infty$ and $H = 0$. The appropriate quantity to calculate is the Gibbs free energy, since $H = H_c$, while B depends on the locations of the domain wall. We calculated the SN interface energy γ as:

$$\gamma = \int_{-\infty}^{\infty} (g_{sH_a} - f_{s0})dx = \int_{-\infty}^{\infty} \left(f_{sH_a} - \frac{HH_c}{4\pi} - f_{s0} \right) dx \tag{1-65}$$

$$= \int_{-\infty}^{\infty} \left[\alpha|\Psi|^2 + \frac{\beta}{2}|\Psi|^4 + \frac{1}{2m^*} \left| \left(-i\hbar\nabla - \frac{e^*}{c}\mathbf{A} \right) \Psi \right|^2 + \frac{(H - H_c)^2}{4\pi} \right] dx \tag{1-66}$$

where we used Eq. 1-64. This can be simplified if the first GL equation is multiply by Ψ^* and integrate over x by parts. Then the following identity is obtained

$$0 = \int_{-\infty}^{\infty} \left[\alpha|\Psi|^2 + \frac{\beta}{2}|\Psi|^4 + \frac{1}{2m^*} \left| \left(-i\hbar\nabla - \frac{e^*}{c}\mathbf{A} \right) \Psi \right|^2 \right] dx \tag{1-67}$$

As a consequence, our expression for the surface energy simplifies to

$$\gamma = \int_{-\infty}^{\infty} \left[-\frac{\beta}{2}|\Psi|^4 + \frac{(H - H_c)^2}{4\pi} \right] dx \tag{1-68}$$

This equation shows that the surface energy is the balance of the negative condensation energy (first term) and the positive energy cost of screening the magnetic field (second term). In general γ is approximately proportional to $\xi - \lambda$. Therefore, for type-I superconductors where $\lambda < \xi$ the surface energy is positive, while in the opposite case the surface energy is negative.

1.3.5.2 Type-II superconductors

The energy of an interface between a normal and a superconducting region is $\alpha_{ns} < 0$ for type-II superconductors. Under some circumstances, it is energetically favorable for these materials, immersed in a magnetic field, to become subdivided into alternating normal and superconducting domains. As long as the applied magnetic field is $H_0 < H_{c1}$ a type-II superconductor exhibit Meissner effect, the average field in the interior of the specimen is $B = 0$. However, at $H_{c1} < H_0 < H_{c2}$ the magnetic field penetrates into this materials as quantized vortex filaments with normal core, axis parallel to $\mathbf{H}_0$ and order parameter equal to zero. Finally, at certain field $H_0 = H_{c2}$, the average field in the interior, B, becomes equal to H_0 and the bulk superconductivity disappears. Once inside the superconductor,
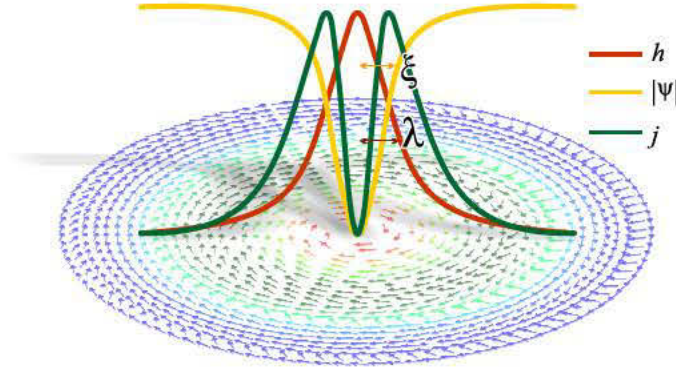
Figure 1-11: Cross section and vector plot of the super-currents of an isolated vortex in a type-II superconductor. The modulus of the order parameter $|\Psi|$, the local magnetic field H and the the circulating screening currents j are shown as a function of the radial distance from the center of the vortex

the vortices arrange themselves at distance $\sim \lambda$ from each other so that in cross-section form a regular triangular lattice. The vortex current circulates within an area of radius $\sim \lambda$, the penetration depth. The size of this area can be well in excess of ξ because $\lambda \gg \xi$ for type-II superconductors (See Fig. **1-11**). At the field $H_0 = H_{c2}$, the vortex lattice grows so dense that the distance of the lattice period, becomes of the order ξ. In this order, the normal cores of the vortices come into contact with each other and the order parameter Ψ becomes zero over the entire volume of the superconductor. In other words, a second-order phase transition occurs.

The different phases (Meissner, mixed and normal) can be easily identified by the equilibrium magnetization

$$\mathbf{M} = \frac{\mathbf{B} - \mathbf{H}}{4\pi} \tag{1-69}$$

where, B is magnetic induction and can be obtained by averaging the local magnetic field over the sample volume. Eq. 1-69 shows the magnetization $-M$ plotted as a function of the applied field H_0 for bulk type-I and type-II superconductors. The incoming magnetic flux causes a smooth decrease of the magnetization $|M|$ down to zero at the second critical field H_{c2}, where superconductivity is suppressed (see Fig.**1-12**).

1.3.5.3 Characteristics of interchange of types I-II

The superconductivity types are determined to the way the magnetic field penetrates the bulk superconductor to create a nonuniform configuration of the flux/condensate. However, the situation for a superconductor with $\kappa \approx 1$ and $T < T_c$ offers different scenarios of interchange
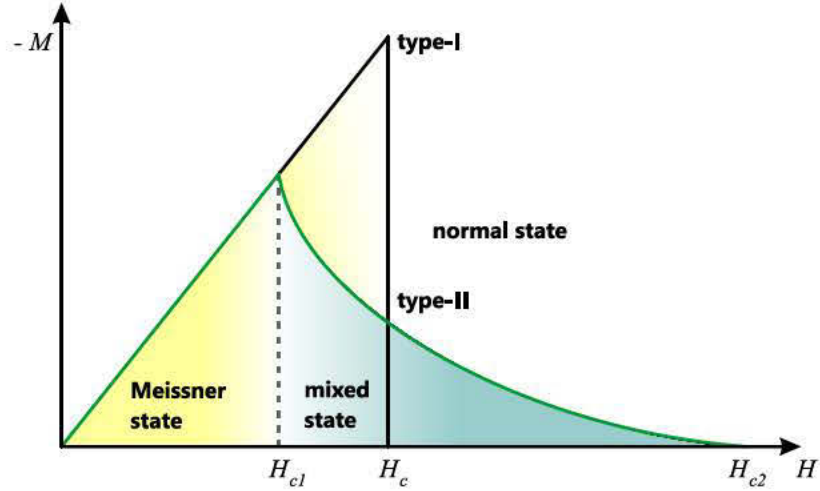
Figure 1-12: The magnetization as a function of the applied magnetic field for bulk type-I and type-II superconductor.

between types I and II. The interchange takes place when the surface energy associated with the domain wall becomes zero. Most common crtiterion of the type interchange is the domain wall (interface) between superconductive (S) and normal (N) phases. But also, another criterion is obtained by considering the superconductivity nucleation at the upper critical field H_{c2}: here types I and II interchange when $H_{c2} = H_c$. The stability of a single Abrikosov vortex is also useful, resulting in the interchange condition $H_{c1} = H_c$. In the context of the unconventional vortex states, the interaction of two Abrikosov vortices is repulsive in type II and attractive in type I [3,4]. The corresponding criterion is a change of the sign of the vortex-vortex interaction or, more precisely, of its long-range asymptote.

1.4 Vortices in superconductors

1.4.1 Fluxoid quantization

By using the second GL equation we can easily obtain the quantization condition which can be written in the following form by introducing the magnitude $|\Psi|$ and the phase ϕ of the order parameter:

$$\mathbf{j} = \frac{2e\hbar}{m}|\Psi|^2\nabla\phi - \frac{4e^2}{mc}|\Psi|^2\mathbf{A}. \tag{1-70}$$

The line integral of Eq.(1-70) around a closed circuit gives

$$\oint \mathbf{j} \cdot \mathbf{dl} = \frac{2e}{m}|\Psi|^2 \oint (\hbar\nabla\phi - \frac{2e}{c}\mathbf{A}) \cdot dl. \tag{1-71}$$

By using Stokes'theorem and the definition of vector potential $\mathbf{A}$, $\oint \mathbf{A} \cdot d\mathbf{l} = \int (\nabla \times \mathbf{A}) \cdot d\mathbf{S} = \int \mathbf{h} \cdot d\mathbf{S} = \Phi$ leads to

$$\frac{mc}{4e^2|\Psi|^2} \oint \mathbf{j} \cdot d\mathbf{l} + \frac{2e}{c}\Phi = \oint \hbar \nabla \phi \cdot d\mathbf{l}. \tag{1-72}$$

Since the complex superconducting order parameter phase ϕ is single-valued, this requires that the phase must change by integral multiples of 2π in a closed circuit:

$$\frac{mc}{4e^2|\Psi|^2} \oint \mathbf{j} \cdot d\mathbf{l} + \Phi = n\frac{hc}{2e} = n\Phi_0. \tag{1-73}$$

with $\Phi_0 = 2.07 \cdot 10^{-15} \text{Tm}^2$ the so called superconducting quantum flux. This equation expresses the condition where the sum of the enclosed flux Φ and the line integral involving the current density $\mathbf{j}$ is quantized.

1.4.2 Isolated vortex line

An isolated vortex in an infinite superconductor comprises a normal core of radius $\sim \xi$ and currents circulating within an area $\sim \pi\lambda^2$. It is possible to assume that GL parameter is $\kappa \gg 1$. Then $\lambda \gg \xi$ at distance $r \gg \xi$ (i.e.$|\Psi|^2 = 1$). From the second GL equation (Eq.(1-26)), where we took curl of both sides, we obtain

$$\mathbf{H} + \lambda^2 \nabla \times \nabla \mathbf{H} = \frac{\Phi_0}{2\pi}\nabla \times \nabla\theta. \tag{1-74}$$

Which is valid every where. We have $\nabla \times \nabla\theta = 0$, since $\nabla \times \nabla\varphi = 0$, where φ is an arbitrary function. But at center of the vortex $|\nabla\theta| \to \infty$ which represents a singularity. The integral over the surface of a small circle centered on the center of the vortex:

$$\int \nabla \times \nabla\theta \cdot d\mathbf{S} = \oint \nabla\theta \cdot d\mathbf{l} = 2\pi \tag{1-75}$$

Where the phase changes by 2π. Thus $\nabla \times \nabla\theta$ is zero everywhere except for the center of the vortex. This corresponds to the behavior of the δ-function

$$\nabla \times \nabla\theta = 2\pi\delta(\mathbf{r})\mathbf{e}_v \tag{1-76}$$

where $\mathbf{e}_v$ is the unit vector along the vortex. As a result, Eq. 1-74 can be replaced by

$$\mathbf{H} + \lambda^2 \nabla \times \nabla \times \mathbf{H} = \Phi_0\delta(\mathbf{r})\mathbf{e}_v \tag{1-77}$$

subject to the boundary condition $H(\infty) = 0$. The solution of Eq. (1-77) is

$$H = \frac{\Phi_0}{2\pi\lambda^2}K_0(r/\lambda), \tag{1-78}$$

where K_0 is the Bessel function with imaginary argument. By setting a cut-off at $r = \xi \ll \lambda$, one obtains an approximate field in the center of a vortex as

$$H(0) \approx \frac{\Phi_0}{2\pi\lambda^2}\ln\kappa, \tag{1-79}$$

More accurate value of $H(0)$ can be obtained by considering the variation of $\Psi(r)$ inside the vortex core and carrying out numerical integration of the GL equations [6] as:

$$H(0) = \frac{\Phi_0}{2\pi\lambda^2}(\ln\kappa - 0.18), \tag{1-80}$$

The above correction is not essential since all the calculations are effectuated on the assumption that $\kappa \gg 1$.

1.4.3 Interaction between vortex lines

Consider two vortices positioned at $\mathbf{r}_1$ and $\mathbf{r}_2$. The energy without vortices is

$$\mathcal{F} = \frac{1}{8\pi}\int[\mathbf{H}^2 + \lambda^2(\nabla \times \mathbf{H})^2] \tag{1-81}$$

The total magnetic field generated by the two vortices must satisfy an equation constructed by analogy with Eq.(1-77)

$$\mathbf{H} + \lambda^2\nabla \times \nabla \times \mathbf{H} = \Phi_0[\delta(\mathbf{r} - \mathbf{r}_1) + \delta(\mathbf{r} - \mathbf{r}_2)]\mathbf{e}_v \tag{1-82}$$

After a series of transformation, it is possible to obtain from Eq.(1-81) and Eq.(1-82)

$$\mathcal{F} = \frac{\Phi_0}{8\pi}[H(\mathbf{r}_1) + H(\mathbf{r}_2)] \tag{1-83}$$

Here $H(\mathbf{r}_1)$ and $H(\mathbf{r}_2)$ are the field of vortex 1 and vortex 2, respectively. The field $H_{12}(x)$ due to vortex 2 separated from vortex 1 by the distance $x = |\mathbf{r}_1 - \mathbf{r}_2|$. Then from equation above

$$\mathcal{F} = 2\epsilon + \frac{\Phi_0}{8\pi}2H_{12}(x) \tag{1-84}$$

The first term is the energy of two single vortices and the second term is the energy of their interaction. Force per unit length acting on the vortex is

$$f = -\frac{dU}{dx} = -\frac{\Phi_0}{4\pi}\frac{dH_{12}}{dx} \tag{1-85}$$

According to Maxwell's equations for two parallel vortices

$$|f| = \frac{1}{c}j_{12}(x)\Phi_0 \tag{1-86}$$

where j_{12} is the current density induced by vortex 1 at the core of vortex 2 (or vice versa). Putting this in vector form, we obtain

$$\mathbf{f} = \mathbf{j} \times \frac{\Phi_0}{c}\mathbf{e}_v \tag{1-87}$$

1.4.4 Interaction of a vortex with the surface of a superconductor

The entry of vortices into superconductors suggests more detailed analysis by considering that penetrations of vortices into a type-II superconductors are energetically favorable only at H_{c1}, vortices must first overcome an energy barrier surface. To explain interaction of vortices with the surface, we can consider a smooth surface of a superconductor and an isolated vortex in the interior. An external field H_0 applied parallel to the surface will induce a Meissner current circulating near the surface which will take the vortex away from the barrier. This can be described by assuming an antivortex is present outside the superconductor at the image position with respect to the vortex. The vortex and such an imaged antivortex attract each other while the mirror surface currents arises from the applied field repealing the vortex. This is the so-called Bean-Livingston barrier [51]. The Gibbs free energy of an isolated vortex can be found as a function of the distance from the surface for different values of H_0. We assume that the vortex center is at x_0. The force exerted on the vortex towards the surface is due to the interaction with vortex image. Using Eq. (1-87) we have

$$f_{\text{image}} = \frac{1}{c} \frac{c}{4\pi} \frac{dH_{\text{v}}}{dx} \Phi_0, \tag{1-88}$$

Where H_{v} is the field generated by the image vortex. The interaction force between the vortex and Meissner current is

$$f_M = \frac{1}{c} \frac{c}{4\pi} \frac{H_{\text{v}}}{\lambda} e^{-x/\lambda} \Phi_0, \tag{1-89}$$

The Gibbs free energy can be obtained effectuating the integration of the total force $f = f_M + f_{\text{image}}$ exerted on vortex we find:

$$\mathcal{G} = \frac{\Phi_0}{4\pi} \left[H_0 e^{-x/\lambda} - H_{\text{v}}(2x_0) + H_{c1} - H_0 \right] \tag{1-90}$$

We can see that (1-90) gives different curves of $\mathcal{G}(x_0)$ for a superconductor under several values of applied magnetic field H_0 which is shown in Fig. **1-13**. It is possible to see that the field $H_0 = H_{c1}$ is the lowest field at which the vortex entry is thermodynamically favorable. However, the vortex penetration is prevented by the Bean-Livingston barrier. As we continue to increasing the field H_0 , the barrier shrinks but does not disappear and the vortex is still unable to penetrate the superconductor. In other words the superconductor remains in the Meissner state which is now metastable. The barrier finally vanishes at field $H_0 = H_p$, which is often referred to as the super heating field for the Meissner state, or the flux penetration field. The Bean-Livingston barrier causes a small hysteresis in the magnetization curve of a homogeneous type-II superconductor near H_{c1} , for magnetic field (or energy) swept up and down [52]. It is present even if the sample is made ideally homogeneous.

1.4.5 Interaction of a vortex with defects in a superconductor

We assume that the dimension of the cylindrical defect is $d > \xi(T)$. The interaction energy of an isolated vortex (of diameter $\sim 2\xi$) can be determined. The normal core of vortex store
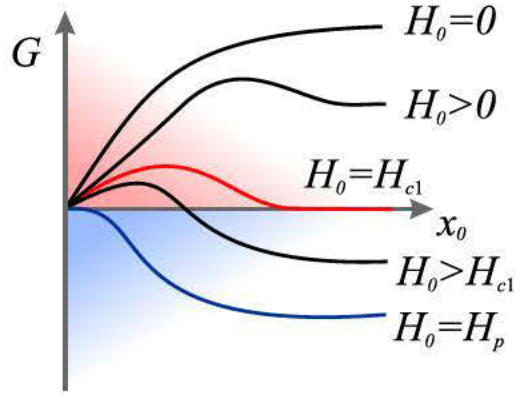
Figure 1-13: Gibbs free energy of an isolated vortex as a function of its distance from the surface for different values of H_0

a positive energy per unit of length, which is

$$\frac{H_{\mathrm{cm}}^2}{8\pi}\pi\xi^2 \tag{1-91}$$

This value is relative to the energy of superconductor without the vortex and it is far away from the defect. When vortex is inside of defect the energy of the system is reduced . As a consequence, the vortex is attracted to the defect. The interaction force per unit of length f_{p} is [53]:

$$f_{\mathrm{pd}} \approx H_{\mathrm{cm}}^2\xi/8 \tag{1-92}$$

as the vortex changes its position near the edge of defect $\sim \xi$. If the defect is a spherical one, then the pinning force varies with the diameter d of the defect as

$$f_{\mathrm{pd}} \approx H_{\mathrm{cm}}^2\xi d/8 \tag{1-93}$$

Another pinning centers in superconductors are dislocations, dislocation walls, grain boundaries, and interfaces between superconductors with different parameters.

1.4.6 Vortex lattices

The flux line lattice was for the first time visualized by using magnetic decoration consisting in the evaporation of ferromagnetic powder which is attracted by the stray field of the vortices [54]. It is important to stress that there is a small energy difference between a triangular and square flux line lattice in a homogeneous superconductor. As noted by Abrikosov, the
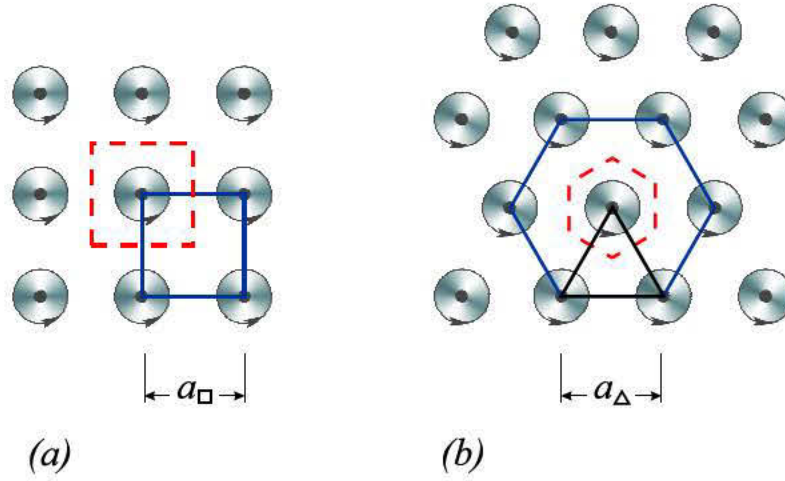
Figure 1-14: Schematic diagram of square and triangular vortex arrays. The dashed lines outline the basic unit cell.

parameter determining the relative stability of various possible periodic vortex configurations is

$$\beta_A \equiv \frac{\langle \Psi_L^4 \rangle}{\langle \Psi_L^2 \rangle^2} \tag{1-94}$$

This parameter is obviously independent of the normalization of Ψ. Numerical calculations show that for square lattice [6], $\beta_A = 1.18$. Later this value was rectified and shown that the triangular array had, in fact, the most favorable value of $\beta_A = 1.16$ of all possible periodic solution [55]. The triangular array exhibits each vortex surrounded by hexagonal array (See Fig. **1-14**) of other vortices in which the nearest neighbor distance is

$$a_\triangle = \left(\frac{4}{3} \right)^{1/4} \left(\frac{\Psi_0}{B} \right)^{1/2} = 1.075 \left(\frac{\Psi_0}{B} \right)^{1/2} \tag{1-95}$$

whereas for the four neighbors in a square array

$$a_\square = \left(\frac{\Psi_0}{B} \right)^{1/2} \tag{1-96}$$

Thus, for a given flux density in a homogeneous superconductor, $a_\triangle > a_\square$. Taking into account the repulsion of the vortices, it is reasonable that the vortex configuration with the greatest separation of the nearest neighbors would be favored. Nevertheless, defects in the material may introduce sufficient inhomogeneity to destroy the regular array entirely. Abrikosov vortex lattice in superconductors can be visualized using scanning tunneling microscopy, scanning probe magnetometry, Bitter decoration, magneto-optical imaging etc.

2 Theoretical models and numerical approach

The Ginzburg-Landau equations are a set of nonlinear partial differential equations that need to be solved self-consistently. In the presence of the applied magnetic field, the order parameter is obtained through the first equation (1-25). The variation of vector potential $\delta\mathbf{A}$ induced by the current is calculated using Fourier transformation, and the new vector potential is brought in turn into the first equation (1-25) to solve the new order parameter. The whole process as described above runs iteratively until the system reaches the equilibrium state. Hereby, we introduce the numerical processes used to solve both GL equations.

2.1 Solving the first GL equation

We use the finite-difference representation of the GL equations, i.e., we solve them on a regular two-dimensional Cartesian space grid (x, y). This is sufficient because all the problems which we solved numerically in this thesis are effectively two-dimensional.

We solve the first equation iteratively for a given applied magnetic field. This is done by first approximating (initializing) both ψ and $\mathbf{A}$. For the exact solution of this quantities, Eq. (1-25) will be exactly zero, for non exacts solutions it gives a finite value. Therefore, we can use it to guide the iterative process in this way:

$$\eta(\Psi - \Psi_0) = -[(-i\nabla - \mathbf{A})^2\Psi_0 - (1 - T)\Psi_0 + |\Psi_0|^2\Psi_0] \tag{2-1}$$

where Ψ_0 is the currently found best approximation to the solution of the GL equations, and we are looking for the improved estimate Ψ in the next iteration. It should be noted that the form of Eq. (2-1) mimics the one of the time-dependent single-gap GL theory.

η is a finite real coefficient used to improve the numerical stability of the iterative procedure having the sense of inverse time-step and it is real in our case. For the time-dependent GL it it would be given by microscopic parameters. (Eq. 2-1) can alternatively be written in the form of the time-dependent single gap Ginzburg-Landau theory [56].

All the terms on the right hand side should in principle be evaluated with the current approximation to the solution Ψ_0, save for the cubic term which requires appropriate linearization, as will be explained below.

The complex link variables are introduced by using the vector potential $\mathbf{A}$ as a link between two computational lattice points $\mathbf{r_1}$ and $\mathbf{r_2}$

$$U_\mu^{\mathbf{r_1},\mathbf{r_2}} = \exp\left(-i \int_{\mathbf{r_1}}^{\mathbf{r_2}} \mathbf{A}\mu(\mathbf{r})d\mu\right) \tag{2-2}$$

where, $\mu = x, y$. These link variable are used to discretized the first term in Eq. (2-1) (index j denotes the lattice point of interest).

We divide our simulation region of size $L_x \times L_y$ into a discrete lattice with spacings $a_x \equiv L_x/M$ and $a_y \equiv L_y/M$, where $M(N)$ are the number of points in the $x(y)$ direction. We can then write (for example for $\mu = x$)

$$\begin{aligned}
(\quad -i\nabla_x - A_x)^2\Psi(x_0, y_0) &= -\frac{1}{U_x}\nabla(\nabla_x(U_x\Psi)) \\
&= -\frac{1}{U_x}\nabla_x\left[\frac{U_x^{x_0+1,y_0}\Psi(x_0+1,y_0) - U_x^{x_0,y_0}\Psi(x_0,y_0)}{a_x}\right] \\
&= -\frac{1}{U_x a_x^2}\left[U_x^{x_0+1,y_0}\Psi(x_0+1,y_0) - 2U_x^{x_0,y_0}\Psi(x_0,y_0) + U_x^{x_0-1,y_0}\Psi(x_0-1,y_0)\right] \\
&= -\frac{1}{a_x^2}\left[U^{Ej}\Psi_E - 2\Psi + U^{Wj}\Psi_W\right].
\end{aligned} \tag{2-3}$$

This is written for the lattice point $j = (x_0, y_0)$ and the neighboring lattice points are referred to by the corresponding cardinal direction denoted by its initial: (N)orth, (E)ast, (S)outh, (W)est. We also introduced $U^{Ej} \equiv U_x^{x_0+1,y_0}/U_x^{x_0,y_0} = exp(-i\int_{x_0,y_0}^{x_0+1,y_0} A_x(r)dx) \approx exp(-iA_x a_x)$ and analogous expressions for U^{Wj}, U^{Nj}, U^{Sj} in other directions.

With this discretization the first GL equation becomes:

$$\begin{aligned}
\eta(\Psi_j - \Psi_{j0}) = \Big[&\frac{U^{Ej}\Psi_E}{a_x^2} + \frac{U^{Wj}\Psi_W}{a_x^2} + \frac{U^{Nj}\Psi_N}{a_y^2} + \frac{U^{Sj}\Psi_S}{a_y^2} - \frac{2\Psi_j}{a_x^2} - \frac{2\Psi_j}{a_y^2} \\
&+(1-T)\Psi_j - |\Psi|^2\Psi_j\Big]
\end{aligned} \tag{2-4}$$

The key numerical trick is to choose terms to associate with the new solution for Ψ and ones to evaluate based on Ψ_0. Moreover, the nonlinear term can be linearized as follows, to facilitate the convergence:

$$\begin{aligned}
|\Psi|^2\Psi = \Psi^2\Psi^* &= [\Psi_0 + (\Psi - \Psi_0)]^2[\Psi_0^* + (\Psi^* - \Psi_0^*)] \\
&\approx |\Psi_0|^2\Psi_0 + 2|\Psi_0|^2(\Psi - \Psi_0) + \Psi_0^2(\Psi^* - \Psi_0^*) \\
&= 2|\Psi_0|^2\Psi - 2|\Psi_0|^2\Psi_0 + \Psi_0^2\Psi^*
\end{aligned} \tag{2-5}$$

With our assignment of different terms to Ψ or Ψ_0 and the above expansion of the cubic term, Eq. 2-4 can be rewritten as:

$$\eta(\Psi - \Psi_0) = \tilde{U}\Psi_0 - \frac{4}{a^2}\Psi + (1-T)\Psi - 2|\Psi_0|^2\Psi_0 - \Psi_0^2\Psi^* \tag{2-6}$$

where $\tilde{U}\Psi_0$ is a shorthand notation for the first four terms on the right side of Eq. 2-4, and $a_x = a_y = a$ as taken for simplicity. This choice of terms containing Ψ_0. terms containing Ψ is not unique, but the shown one has demonstrated stability in a vast number of simulations. We rearrange the first GL equation by conveniently grouping the terms multiplying the Ψ, Ψ_0 and constant terms, as:

$$[\eta - (1-T) + 4/a^2 + 2|\Psi_0|^2]\Psi = \tilde{U}\Psi_0 + \eta\Psi_0 + 2\Psi_0|\Psi_0|^2 - \Psi_0^2\Psi^* \tag{2-7}$$

Equation 2-7 is of the form

$$c\Psi - a + e\Psi^* = 0, \tag{2-8}$$

with

$$\begin{aligned}
c &= \eta - (1-T) + 4/a^2 + 2|\Psi_0|^2 \\
e &= \Psi_0^2 \\
a &= \tilde{U}\Psi_0 + \eta\Psi_0 + 2\Psi_0|\Psi_0|^2
\end{aligned} \tag{2-9}$$

and solution

$$\Psi = \frac{a^*e - ac^*}{|e|^2 - |c|^2}, \tag{2-10}$$

where right side depends only on Ψ_0. After going through several hundred iterations of the first GL equation in the above form, we use its (approximate) solution Ψ to compute the supercurrent given by

$$j_x = \frac{1}{2}\left[\Psi^*\left(\frac{1}{i}\frac{\partial}{\partial x} - A_x\right)\Psi + \Psi\left(\frac{1}{i}\frac{\partial}{\partial x} - A_x\right)^*\Psi^*\right], \tag{2-11}$$

with the same expression for y component with x replaced by y. These expressions are again easy to express using the link variables:

$$\left(\frac{1}{i}\frac{\partial}{\partial x} - A_x\right)\Psi_j = -i\frac{U_x^{Ej}\Psi_E - \Psi_j}{a_x}, \tag{2-12}$$

and

$$\left(\frac{1}{i}\frac{\partial}{\partial y} - A_y\right)\Psi_j = -i\frac{U_y^{Nj}\Psi_N - \Psi_j}{a_y}, \tag{2-13}$$

Subsequently one uses the Maxwell equation to calculate the new value of the vector potential as explained in the next section and the process is iteratively repeated until convergence is reached.

2.2 Solving the second GL equation

The second GL equation $\mathbf{j} = -\kappa^2 \nabla^2 \mathbf{A}$ will be solved to find the new value for the vector potential in every iteration. A Fourier transformation is used to solve this partial differential equation. The problem considered is two dimensional, since the sample is infinitely thick in the z-direction. Spatial variation of the current in the z-direction will be neglected. Due to this fact, a discrete Fourier transformation will be used for the x- and y-direction and a continuous one for the z-direction. An exponential Fourier series is chosen because this guarantees to satisfy the periodic boundary conditions $\mathbf{A}(x + L_x, y, z) = \mathbf{A}(x, y + L_y, z) = \mathbf{A}(x, y, z)$, where $\mathbf{A}$ is the magnetic field induced by the superconductor, not the applied magnetic field. When $A(na_x, ma_y, z) = A_{nm}(z)$ with $a_x \equiv L_x/N$ and $a_y \equiv L_y/M$, this leads to an expression

$$A_{nm}(z) = \frac{1}{NM} \int_{-\infty}^{\infty} \sum_{\alpha=0}^{N-1} \sum_{\beta=0}^{M-1} \tilde{A}_{\alpha\beta}(k) \exp(-2\pi izk) \exp\left(-2\pi i \frac{n\alpha}{N}\right) \exp\left(-2\pi i \frac{m\beta}{M}\right) dk \quad (2\text{-}14)$$

The inverse Fourier transformation is:

$$\tilde{A}_{\alpha\beta}(k) = \int_{-\infty}^{\infty} \sum_{n=0}^{N-1} \sum_{m=0}^{M-1} A_{mn}(z) \exp(-2\pi izk) \exp\left(-2\pi i \frac{n\alpha}{N}\right) \exp\left(-2\pi i \frac{m\beta}{M}\right) dz \quad (2\text{-}15)$$

The Laplacian of the vector potential is then calculated according to $\nabla^2 A \equiv \frac{\partial^2 A}{\partial x^2} + \frac{\partial^2 A}{\partial y^2} + \frac{\partial^2 A}{\partial z^2}$, hereby taking into account the $\frac{n\alpha}{N} = \frac{na_x\alpha}{a_x N} = \frac{x\alpha}{L_x}$, and analogous for y:

$$\nabla^2 A_{nm}(z) = \frac{1}{NM} \int_{-\infty}^{\infty} \sum_{\alpha=0}^{N-1} \sum_{\beta=0}^{M-1} \left[-(2\pi ik)^2 - \left(2\pi i \frac{\alpha}{L_x}\right)^2 - \left(2\pi i \frac{\beta}{L_y}\right)^2 \right]$$
$$\times \tilde{A}_{\alpha\beta}(k) \exp(-2\pi izk) \exp\left(-2\pi i \frac{n\alpha}{N}\right) \exp\left(-2\pi i \frac{m\beta}{M}\right) dk \quad (2\text{-}16)$$

The current density will also be expressed as a Fourier series:

$$j_{nm}(z) = \frac{1}{NM} \int_{-\infty}^{\infty} \sum_{\alpha=0}^{N-1} \sum_{\beta=0}^{M-1} \tilde{j}_{\alpha\beta}(k) \exp(-2\pi izk) \exp\left(-2\pi i \frac{n\alpha}{N}\right) \exp\left(-2\pi i \frac{m\beta}{M}\right) dk \quad (2\text{-}17)$$

with coefficients

$$\tilde{j}_{\alpha\beta}(k) = \int_{-\infty}^{\infty} \sum_{\alpha=0}^{N-1} \sum_{\beta=0}^{M-1} j_{nm}(z) \exp(2\pi izk) \exp\left(2\pi i \frac{n\alpha}{N}\right) \exp\left(2\pi i \frac{m\beta}{M}\right) dz \quad (2\text{-}18)$$

To take the integral over the entire z domain, a mathematical transformation will be used to simplify the calculation. Since the current density is uniform a long the z-direction, we use $j_{nm}(z) = j_{nm} \prod(z, -d/2, d/2)$ in which $\prod$ is a step-like function that is 1 inside the interval $[-d/2, d/2]$ and 0 outside, with d the thickness of the material. Later, the limit $d \to \infty$ will be taken to correctly consider the bulk behavior along the z-direction. The Fourier transform of this step-function is:

$$\int_{-\infty}^{\infty} \prod(z, -d/2, d/2) \exp(2\pi izk) dz = \int_{-d/2}^{d/2} \exp(2\pi izk) dz = \frac{sin(\pi kd)}{\pi k}, \tag{2-19}$$

which leads to the simplification of Eq. 2-18 as

$$\tilde{j}_{\alpha\beta}(k) = \tilde{j}_{\alpha\beta} \frac{sin(\pi kd)}{\pi k} \tag{2-20}$$

Next, Eq.2-16 and Eq. 2-17 are substituted into the equation $j = -\kappa^2 \nabla^2 \mathbf{A}$, to obtain

$$\tilde{A}_{\alpha\beta}(k) = \frac{1}{\kappa^2} \frac{\tilde{j}_{\alpha\beta}(k)}{(2\pi i \kappa)^2 + q_{\alpha\beta}^2}, \tag{2-21}$$

with $q_{\alpha\beta}^2 = \left(2\pi\frac{\alpha}{L_x}\right)^2 + \left(2\pi\frac{\beta}{L_y}\right)^2$. Eq. 2-21 gives the vector potential in reciprocal space. Substitution into Eq. 2-14 brings it back to real space:

$$A_{nm}(z) = \frac{1}{NM} \int_{-\infty}^{\infty} \sum_{\alpha=0}^{N-1} \sum_{\beta=0}^{M-1} \frac{1}{\kappa^2} \frac{\tilde{j}_{\alpha\beta}(k)}{(2\pi i\kappa)^2 + q_{\alpha\beta}^2} \frac{sin(\pi kd)}{\pi k}$$
$$\times \exp(-2\pi izk)\exp\left(-2\pi i\frac{n\alpha}{N}\right) \exp\left(-2\pi i\frac{m\beta}{M}\right) dk \tag{2-22}$$

The integral over k:

$$I = \int_{-\infty}^{\infty} \frac{1}{(2\pi ik)^2 + q_{\alpha\beta}^2} \frac{sin(\pi kd)}{\pi k} dk, \tag{2-23}$$

can be done analytically with the result:

$$I = \begin{cases} [1 - cosh(q_{\alpha\beta}z)\exp(-dq_{\alpha\beta}/2)]/q_{\alpha\beta}^2, z < d/2 \\ sinh(dq_{\alpha\beta}^2)\exp(-q_{\alpha\beta}/2)/q_{\alpha\beta}^2, z > d/2 \end{cases} \tag{2-24}$$

We are interested in the field behavior in the plane $z = 0$. where $I = [1 - exp(-dq_{\alpha\beta}/2)]/q_{\alpha\beta}^2$. For considering bulk behavior along the z-direction, the limit $d \to \infty$ should be taken.

This reduces the integral further to $I = 1/q_{\alpha\beta}^2$, and finally gives

$$A_{nm}(0) = \frac{1}{NM} \int_{-\infty}^{\infty} \sum_{\alpha=0}^{N-1} \sum_{\beta=0}^{M-1} \frac{1}{\kappa^2} \frac{\tilde{j}_{\alpha\beta}}{q_{\alpha\beta}^2} \exp\left(-2\pi i \frac{n\alpha}{N}\right) \exp\left(-2\pi i \frac{m\beta}{M}\right) dk \tag{2-25}$$

The vector potential is thus obtained by Fourier transformation of the current density in the xy-plane to obtain their coefficients $\tilde{j}_{\alpha\beta}$. These coefficients are then substituted into Eq. to obtain the value for the vector potential.

Now, In order to calculate the Gibbs free energy of the system, we start from the expression (1-11), which can be written in dimensionless form as follows:

$$F = \frac{\mathcal{G}_s - \mathcal{G}_n}{H_c^2 V/8\pi} = \int [-2|\Psi|^2 + |\Psi|^4 + 2|(-i\nabla - \mathbf{A})\Psi|^2 + 2\kappa^2(\mathbf{H} - \mathbf{H_0})]dV \tag{2-26}$$

where the integration is carried out over the entire space. Using mathematical transformations and the Gauss theorem $\int \nabla \cdot \mathbf{A} dV = \oint \mathbf{n} \cdot \mathbf{A} dS$, the third term of the integrand in Eq. 2-26 can be written as

$$\int |(-i\nabla - \mathbf{A})\Psi|^2 dV = \oint \mathbf{n} \cdot [\Psi^*(-i\nabla - \mathbf{A})\Psi]dS + \int \Psi^*(-i\nabla - \mathbf{A})^2 \Psi dV. \tag{2-27}$$

The first term on the right side equals to zero due to the boundary conditions of (Eq. 1-28). The second term is rewritten with the help of the first GL equation and finally we have

$$\int |(-i\nabla - \mathbf{A})\Psi|^2 dV = \int (|\Psi|^2 - |\Psi|^4)dV. \tag{2-28}$$

Therefore,

$$F = \int [(\mathbf{H} - \mathbf{H_0})^2 \kappa^2 - 1/2|\Psi|^4)dV] \tag{2-29}$$

where $\mathbf{H} = \nabla \times \mathbf{A}$. Using the vector relations $\nabla \cdot (\mathbf{a} \times \mathbf{b}) = \mathbf{b} \cdot (\nabla \times \mathbf{a}) - \mathbf{a} \cdot (\nabla \times \mathbf{b})$ and $\mathbf{a} \times (\nabla \times \mathbf{a}) = 0$, and the London gauge $\nabla \cdot \mathbf{A} = 0$, the free energy becomes

$$F = V^{-1} \int [2(\mathbf{A} - \mathbf{A_0}) \cdot \mathbf{j} - |\Psi|^4)]d\mathbf{r}, \tag{2-30}$$

where $\mathbf{A_0}$ denotes the vector potential of the applied magnetic field $\mathbf{H_0}$ the supercurrent is given by Eq. (1-26).

2.3 Numerical algorithm

2.3.1 Cartesian coordinates

In this thesis, we investigate the dynamics of vortices in a thin square mesoscopic superconductor. we show how the vortices are nucleated into the sample to form a multivortex, single vortex, and giant vortex states. We also calculate the magnetization and the free energy as functions of the applied magnetic field. Thus, we are allowed to take the order parameter and the local magnetic field invariant along the z direction. The vortex configurations at the equilibrium can be obtained from generalized the GL equations which account for the time evolution of the vortices until the most stable configuration is accomplished [57]. The time evolution was incorporated to the GL equations in such a manner that their gauge invariance is preserved. The Time Dependent Ginzburg-Landau (TDGL) equations for the complex order parameter Ψ the vector potential $\mathbf{A}$, and the scalar electrical potential Φ are given by

$$\frac{\hbar^2}{4mD}\left(\frac{\partial}{\partial t} + \frac{ie}{\hbar}\Phi\right)\Psi = -\frac{1}{4m}\left(-i\hbar\nabla - \frac{2e}{c}\mathbf{A}\right)^2\Psi + \alpha\Psi - \beta|\Psi|^2\Psi$$

$$\sigma\left(\frac{1}{c}\frac{\partial\mathbf{A}}{\partial t} + \nabla\Phi\right) = \mathbf{J}_s - \frac{c}{4\pi}\nabla\times\mathbf{A} \tag{2-31}$$

where the supercurrent density is

$$\mathbf{J_s} = \frac{e}{m}\mathfrak{R}\left[\bar{\Psi}\left(-i\hbar\nabla - \frac{2e}{c}\mathbf{A}\right)\Psi\right], \tag{2-32}$$

where $\mathfrak{R}$ indicates the real part and the overbar the complex conjugation. Also in Eq. 2-32 D is the diffusion coefficient, σ is the electrical conductivity, and α are the two phenomenological constants. The temperature dependence of α can be expressed as $\alpha(T) = \alpha_0(T_c - T)$, for all temperatures $T \leqslant T_c$, where T_c is the critical temperature. We consider the zero-electrical potential gauge at all times $\Phi = 0$, whereas, $|\Psi|^2$ represents the local density of Cooper pairs and the local magnetic field is given by $\mathbf{h} = \nabla\times\mathbf{A}$. The boundary conditions to solve the TDGL normal to the sample surfaces is $(-i\hbar\nabla - \frac{2e}{c}\mathbf{A})\cdot\hat{n} = 0$ and $h_z = H$ parallel to the sample surfaces, where H is the external field uniformly applied along the z direction. The TDGL equations can be written in dimensionless units as:

$$\frac{\partial\Psi}{\partial t} = -(-i\nabla - \mathbf{A})^2\Psi + (1-T)\Psi(1-|\Psi|^2),$$

$$\beta\frac{\partial\mathbf{A}}{\partial t} = \mathbf{J}_s - \kappa^2\nabla\times\mathbf{A},$$

$$\mathbf{J}_s = (1-T)\mathfrak{R}[\bar{\Psi}\left(-i\hbar\nabla - \frac{2e}{c}\mathbf{A}\right)\Psi] \tag{2-33}$$

where $\kappa = \lambda(T)/\xi(T) = \lambda(0)/\xi(0)$ is the GL parameter, $\tau = \xi^2(0)/D$ is the characteristic time, magnetic field $H_{c2}(0) = \Phi_0/2\pi\xi^2(0)$ and $\beta = 4\pi\sigma D/c^2\xi^2$.
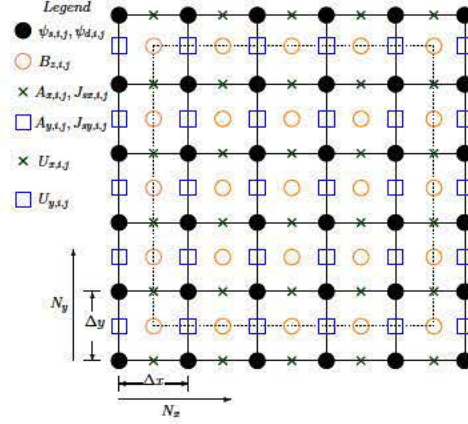
Figure 2-1: The computational mesh in rectangular coordinates used for evaluation of $\Psi_{i,j}$ ($\bullet$, vertex variable); $h_{z,i,j}$ and $L_{i,j}$($\bigcirc$, cell variable); $A_{x,i,j}$ and $U_{x,i,j}$ ($\blacksquare$, link variable in x-direction); $A_{y,i,j}$ and $U_{y,i,j}$($\square$, link variable in y-direction). The superconducting domain is delimited by the dashed line, and superconducting layer is surrounded by the solid line.

In order to discretized the TDGL equations we use the $\Psi - U$ method [58]. This method has the important characteristic of preserving the gauge invariance of the TDGL equations. This is accomplished by introducing the auxiliary fields

$$U_x(x,y,t) = \exp\left(-i\int_{x_0}^{x} A_x(s,y,t)ds\right),$$

$$U_y(x,y,t) = \exp\left(-i\int_{y_0}^{y} A_y(x,s,t)ds\right). \tag{2-34}$$

where (x_0, y_0) is an arbitrary point. Thus, the first of the TDGL equations and the supercurrent density can be written in the following form:

$$\frac{\partial \Psi}{\partial t} = U_x\frac{\partial^2(U_x\Psi)}{\partial x^2} + U_y\frac{\partial^2(U_y\Psi)}{\partial y^2} + (1-T)\Psi(1-|\Psi|^2),$$

$$
\begin{aligned}
J_{s\alpha} &= \frac{(1-T)}{2i}\left[U_\alpha\bar{\Psi}\frac{\partial(U_\alpha\Psi)}{\partial\alpha} - U_\alpha\Psi\frac{\partial(U_\alpha\bar{\Psi})}{\partial\alpha}\right] \\
&= (1-T)\Im\left[U_\alpha\bar{\Psi}\frac{\partial(U_\alpha\Psi)}{\partial\alpha}\right],
\end{aligned}
\tag{2-35}
$$

where $\alpha = (x,y)$, and $\Im$ indicates the imaginary part.

Here, we only show the results. The discretization are carried out in a rectangular mesh consisting of $N_x \times N_y$ cell points. We denote by Δt the incremental time, by (a_x, a_y) the lattice spacing between adjacent cell points, and by (x_i, y_j) an arbitrary vertex point in the mesh (See Fig. **2-1**). Let us define

$$t_n\Delta t, \; n = 1, 2, 3, ...,$$

$$x_i = (i-1)a_x, \ i = 1, 2, 3, ..., N_x + 1,$$

$$y_j = (j-1)a_y, \ j = 1, 2, 3, ..., N_y + 1,$$

$$\Psi_{i,j}^n = \Psi(x_i, y_j, t_n),$$

$$U_{x,i,j}^n = U_x(x_{i+1}, y_j, t_n)\bar{U}_x(x_i, y_j, t_n) = \exp\left(-i\int_{x_i}^{x_{i+1}} A_x(s, y, t)ds\right),$$

$$U_{y,i,j}^n = U_y(x_i, y_{i+1}, t_n)\bar{U}_y(x_i, y_j, t_n) = \exp\left(-i\int_{y_i}^{y_{i+1}} A_y(x, s, t)ds\right),$$

$$h_{z,i,j}^n = h_z\left(x_i + \frac{a_x}{2}, y_j + \frac{a_y}{2}, t_n\right). \tag{2-36}$$

According to these definitions, it can be easily seen that Ψ is a vertex variable, h_z is a cell variable, and U is a link variable.

$$
\begin{aligned}
\Psi_{i,j}^{n+1} &= \Psi_{i,j}^n + \Delta t\frac{U_{x,i,j}^n\Psi_{i+1,j}^n - 2\Psi_{i,j}^n + \bar{U}_{x,i-1,j}^n\Psi_{i-1,j}^n}{a_x^2} \\
&+ \Delta t\frac{U_{y,i,j}^n\Psi_{i,j+1}^n - 2\Psi_{i,j}^n + \bar{U}_{y,i,j-1}^n\Psi_{i,j-1}^n}{a_y^2} \\
&+ \Delta t(1-T)\Psi_{i,j}^n(1 - |\Psi_{i,j}^n|^2),
\end{aligned}
$$

$$
\begin{aligned}
U_{x,i,j}^{n+1} &= U_{x,i,j}^n + \Delta t\frac{(1-T)}{i\beta}U_{x,i,j}^n\mathfrak{J}[\bar{\Psi}_{i,j}^n U_{x,i,j}^n\Psi_{i+1,j}^n] \\
&- \Delta t\frac{\kappa^2}{\beta a_y^2}U_{x,i,j}^n(\bar{L}_{i,j-1}^n L_{i,j}^n - 1),
\end{aligned}
$$

$$
\begin{aligned}
U_{y,i,j}^{n+1} &= U_{y,i,j}^n + \Delta t\frac{(1-T)}{i\beta}U_{y,i,j}^n\mathfrak{J}[\bar{\Psi}_{i,j}^n U_{y,i,j}^n\Psi_{i,j+1}^n] \\
&- \Delta t\frac{\kappa^2}{\beta a_x^2}U_{y,i,j}^n(\bar{L}_{i,j}^n L_{i-1,j}^n - 1),
\end{aligned} \tag{2-37}
$$

Where

$$L_{i,j}^n = U_{x,i,j}^n\bar{U}_{x,i,j+1}^n U_{y,i+1,j}^n\bar{U}_{y,i,j}^n = exp(-ia_x a_y h_{z,i,j}^n) \tag{2-38}$$

The discretized boundary conditions are

$$
\Psi_{1,j}^n = U_{x,1,j}^n \Psi_{2,j}^n, \ \Psi_{N_x+1,j}^n = \bar{U}_{x,N_x,j}^n \Psi_{N_x,j}^n,
$$
$$
\Psi_{i,1}^n = U_{y,i,1}^n \Psi_{i,2}^n, \ \Psi_{i,N_y+1}^n = \bar{U}_{y,i,N_y}^n \Psi_{i,N_y}^n, \tag{2-39}
$$

The link variables U and L are updated at any (i, j) surface cell point by using the boundary condition $L_{i,j}^n = exp(-i a_x a_y H)$, whatever the instant n.

Starting from some initial conditions for and the link variable U, and upon using the TDGL Eqs. 2-37 and the boundary conditions (2-39), the new order parameter and the local magnetic field are determined. This process is repeated until a stationary state is achieved. The applied magnetic field H is ramped up in small intervals of ΔH. The stationary state found for a fixed value of H is then used as the initial condition for $H + \Delta H$. For the first value of H, the system is initialized at the Meissner state where $\Psi_{i,j}^0 = 1$, $U_{x,i,j}^0 = 1$, $U_{y,i,j}^0 = 1$. At each fixed applied field we follow the time evolution of the local magnetic field and the superconducting order parameter until we obtain a steady state solution. Then, this stationary solution is used as the initial condition for the next applied field. Thus, as the applied magnetic field increases and the time changes, we preserve the magnetic history of the system. That is, we study the time evolution of the system at each fixed applied magnetic field by assuming that there is already some penetrated magnetic flux inside the sample.

The TDGL equations describe the gradient flow for the Gibbs free energy. Thus, in principle, the output of the TDGL should correspond to the global minimum of the energy of the system. The energy, in units of $\mathcal{G}_0 = a_0^2 T_c^2 / b$, is given by

$$
\begin{aligned}
\mathcal{G} \ = \ & \frac{1}{V} \int \left[(1-T)|(-i\nabla - \mathbf{A})\Psi|^2 + (1-T)^2 |\Psi|^2 \left(\frac{1}{2}|\Psi|^2 - 1 \right) \right. \\
& \left. + \ \kappa^2 ((\nabla \times \mathbf{A})_z - H)^2 \right] dV
\end{aligned} \tag{2-40}
$$

This equation can be discretized as follow

$$
\begin{aligned}
\mathcal{G}_n \ = \ & \frac{1}{N_x} \frac{1}{N_y} \sum_{i=1}^{N_x} \sum_{j=1}^{N_y} \left\{ \frac{(1-T)}{2} \left[\frac{|U_{x,i,j}^n \Psi_{i+1,j}^n - \Psi_{i,j}^n|^2}{a_x^2} \right. \right. \\
& + \ \frac{|U_{x,i,j+1}^n \Psi_{i+1,j+1}^n - \Psi_{i,j+1}^n|^2}{a_x^2} + \frac{|U_{y,i,j}^n \Psi_{i,j+1}^n - \Psi_{i,j}^n|^2}{a_y^2} \\
& + \ \left. \frac{|U_{y,i+1,j}^n \Psi_{i+1,j+1}^n - \Psi_{i+1,j}^n|^2}{a_y^2} \right] \\
& + \ \frac{(1-T)^2}{4} \left[|\Psi_{i,j}^n|^2 \left(\frac{1}{2}|\Psi_{i,j}^n|^2 - 1 \right) + |\Psi_{i+1,j}^n|^2 \left(\frac{1}{2}|\Psi_{i+1,j}^n|^2 - 1 \right) \right. \\
& + \ \left. \left. |\Psi_{i+1,j+1}^n|^2 \left(\frac{1}{2}|\Psi_{i+1,j+1}^n|^2 - 1 \right) + |\Psi_{i,j+1}^n|^2 \left(\frac{1}{2}|\Psi_{i,j+1}^n|^2 - 1 \right) \right] + (h_{z,i,j}^n - H)^2 \right\} \tag{2-41}
\end{aligned}
$$

The magnetization $4\pi M = B - H$, where B is the induction (the spatial average of the local magnetic field), is

$$-4\pi M_n = \frac{1}{N_x N_y} \sum_{i=1}^{N_x} \sum_{j=1}^{N_y} h_{z,i,j}^n - H \tag{2-42}$$

The stationary state is accepted when the absolute value of the order parameter does not change within a certain precision, the difference $||\Psi_{i,j}^{n+1}| - |\Psi_{i,j}^n||$. The effective manner of of counting the number of vortices can be found by integrating Eq. 2-33 along a rectangle containing the superconducting square. This leads us to

$$\oint \frac{1}{|\Psi|^2} \Re[\bar{\Psi}(-i\nabla - \mathbf{A})\Psi] \cdot d\mathbf{r} = (2\pi N - \Phi), \tag{2-43}$$

where N is the number of vortices vorticity and Φ is the total penetrated flux. The discrete counterpart of this equation is

$$N_n = \frac{\Phi_n}{2\pi} + \frac{1}{2\pi} \sum_{i=1}^{N_x} \left\{ \frac{1}{|\mathbf{\Psi}_{i,1}^n|^2} \Im[\bar{\Psi}_{i,1}^n U_{x,i,1}^n \Psi_{i+1,1}^n] - \frac{1}{|\mathbf{\Psi}_{i,N_y+1}^n|^2} \Im[\bar{\Psi}_{i,N_y+1}^n U_{x,i,N_y+1}^n \Psi_{i+1,N_y+1}^n] \right\}$$
$$+ \frac{1}{2\pi} \sum_{j=1}^{N_y} \left\{ \frac{1}{|\mathbf{\Psi}_{N_x+1,j}^n|^2} \Im[\bar{\Psi}_{N_x+1,j}^n U_{y,N_x+1,j}^n \Psi_{N_x+1,j+1}^n] - \frac{1}{|\mathbf{\Psi}_{1,j}^n|^2} \Im[\bar{\Psi}_{1,j}^n U_{y,1,j}^n \Psi_{1,j+1}^n] \right\} \tag{2-44}$$

where, for instance,

$$|\mathbf{\Psi}_{i,1}^n|^2 = \frac{1}{2}(|\Psi_{N_x+1,1}^n|^2 + |\Psi_{i+1,1}^n|^2) \tag{2-45}$$

2.3.2 Polar coordinates

The algorithm to solve the time dependent Ginzburg-Landau equations for superconductor samples with circular geometries,by using the link variables technique in polar coordinates. Here, we will reproduce some steps of the algorithm developed in this reference at a minimum level and introduce what is new with respect to the boundary conditions. This procedure will help us to present the results in a more comprehensible manner. At this point, it is convenient to introduce the auxiliary vector field $U = (U_\rho, U_\theta)$ in polar coordinates, which is defined by

$$U_\rho(\rho, \theta) = \exp\left(-i \int_{\rho_0}^{\rho} A_\rho(\theta, \xi) d\xi\right),$$

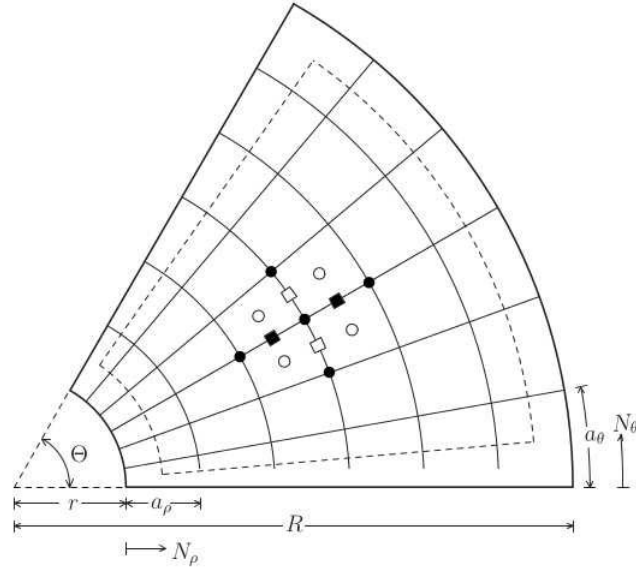$$U_\theta(\rho, \theta) = \exp\left(-i \int_{\theta_0}^{y} A_\theta(\xi, \theta) d\xi\right). \tag{2-46}$$

Figure 2-2: The computational mesh in polar coordinates used for evaluation of $\Psi_{i,j}$ ($\bullet$, vertex point); $h_{z,i,j}$ and $L_{i,j}$ ($\bigcirc$, cell point); $A_{\rho,i,j}$ and $U_{\rho,i,j}$ ($\blacksquare$, link point); $A_{\theta,i,j}$ and $U_{\theta,i,j}$ ($\square$, link point). The superconducting domain is delimited by the dashed line, and superconducting layer is surrounded by the solid line.

where (ρ_0, θ_0) is an arbitrary reference point. Thus, the TDGL equations can be rewritten as

$$\frac{\partial \Psi}{\partial t} = \frac{\bar{U}_\rho}{\rho} \frac{\partial}{\partial \rho} \left[\rho \frac{\partial (U_\rho \Psi)}{\partial \rho} \right] + \frac{\bar{U}_\theta}{\rho^2} \frac{\partial^2 (U_\theta \Psi)}{\partial \theta^2}$$
$$+ \ (1-T)\Psi(1 - |\Psi|^2),$$

$$\beta \frac{\partial A_\rho}{\partial t} = (1-T)\Im \left[\bar{U}_\rho \bar{\Psi} \frac{\partial (U_\rho \Psi)}{\partial \rho} \right] - \kappa^2 \frac{1}{\rho} \frac{\partial h_z}{\partial \theta},$$

$$\beta \frac{\partial A_\theta}{\partial t} = (1-T)\Im \left[\frac{\bar{U}_\theta \bar{\Psi}}{\rho} \frac{\partial (U_\theta \Psi)}{\partial \theta} \right] - \kappa^2 \frac{\partial h_z}{\partial \rho}, \tag{2-47}$$

The grid used for the discretization of the TDGL equations of 2-47 on a circular sector is illustrated in Fig. **2-2**.

The mesh consists of $N_\rho \times N_\theta$ cells with size (a_ρ, a_θ) in polar coordinates. The circular sector has internal radius r and external R; Θ is its angular width. Let (ρ_i, θ_j) be a vertex point in the mesh, where $\rho_{i+1} = \rho_i + a_\rho$, $\theta_{j+1} = \theta_j + a_\theta$, for all $1 \leqslant i \leqslant N_\rho, 1 \leqslant j \leqslant N_\theta$; $\rho_1 = r$ and $\theta_1 = 0$ this particular choice for the initial value of the angle does not imply a loss of generality since the system is invariant under any rotation.

The discrete variables for the vertex points can be written as:

$$\rho_i = r + (i-1)a_\rho, \ 1 \leqslant i \leqslant N_\rho + 1 \qquad\qquad \theta_j = (j-1)a_\theta, \ 1 \leqslant j \leqslant N_\theta + 1$$

whereas the cell points $(\rho_{i+1/2} = \rho_i + a_\rho/2, \ \theta_{j+1/2} = \theta_i + a_\theta/2)$ and the link points in the radial and transversal directions can be defined by $(\rho_{i+1/2}, \theta_j)$ and $(\rho_i, \theta_{j+1/2})$.
For the discretized vector potential, link variables and the local magnetic field, we obtain

$$A_{\rho,i,j} = A_\rho(\rho_{i+1/2}, \theta_j), \ A_{\theta,i,j} = A_\theta(\rho_i, \theta_{j+/1/2}) \tag{2-48}$$

$$\begin{aligned} U_{\rho,i,j} &= \bar{U}_\rho(\rho_i, \theta_j)U_\rho(\rho_{i+1}, \theta_j) = \exp(-ia_\rho A_{\rho,i,j}), \\ U_{\theta,i,j} &= \bar{U}_\theta(\rho_i, \theta_j)U_\theta(\rho_i, \theta_{j+1}) = \exp(-i\rho a_\theta A_{\theta,i,j}), \end{aligned} \tag{2-49}$$

$$h_{z,i,j} = h_z(\rho_{i+1/2}, \theta_{j+1/2}), \tag{2-50}$$

respectively.
The discrete variable L will be define as follow:

$$L_{i,j} = \exp\left(-i\oint_{\partial\mathcal{D}} \mathbf{A} \cdot d\mathbf{r}\right) = \exp\left(-i\int_{\mathcal{D}} h_z\rho d\rho d\theta\right) = \exp(-ia_\rho \rho_{i+1/2} a_\theta h_{z,i,j}) \tag{2-51}$$

where $\mathcal{D}$ is the domain of a unit cell limited by a closed path $\partial\mathcal{D}$, therefore

$$L_{i,j} = U_{\rho,i,j}U_{\theta,i+1,j}\bar{U}_{\rho,i,j+1}\bar{U}_{\theta,i,j}. \tag{2-52}$$

We find the following recurrence relations for the order parameter and the link variables by using the one-step forward-difference Euler scheme with time step Δt:

$$\Psi_{i,j}(t + \Delta t) = \Psi_{i,j}(t) + \mathcal{F}_{\Psi,i,j}(t)\Delta t, \qquad U_{\alpha,i,j}(t + \Delta t) = U_{\alpha,i,j}(t)\exp\left(-\frac{i}{\beta}\mathcal{F}_{U_{\alpha,i,j}}(t)\Delta t\right)$$

Where

$$\begin{aligned} \mathcal{F}_{\Psi,i,j} &= \frac{\rho_{i+1/2}(U_{\rho,i,j}\Psi_{i+1,j} - \Psi_{i,j}) + \rho_{i-1/2}(\bar{U}_{\rho,i-1,j}\Psi_{i-1,j} - \Psi_{i,j})}{\rho_i a_\rho^2} \\ &+ \frac{U_{\theta,i,j}\Psi_{i,j+1} - 2\Psi_{i,j} + \bar{U}_{\theta,i,j-1}\Psi_{i,j-1}}{\rho_i^2 a_\theta^2} + (1-T)\Psi_{i,j}(1 - |\Psi_{i,j}|^2) \end{aligned} \tag{2-53}$$

$$\mathcal{F}_{U_{\rho,i,j}} = \Im\left[(1-T)\bar{\Psi}_{i,j}U_{\rho,i,j}\Psi_{i+1,j} + \kappa_{eff}^2\left(\frac{L_{i,j} - L_{i,j-1}}{\rho_{i+1/2}^2 a_\theta^2}\right)\right], \tag{2-54}$$

$$\mathcal{F}_{U_{\theta,i,j}} = \Im\left[(1-T)\bar{\Psi}_{i,j}U_{\theta,i,j}\Psi_{i,j+1} + \kappa_{eff}^2\frac{\rho_i}{a_\rho^2}\left(\frac{L_{i-1,j}}{\rho_{i-1/2}} - \frac{L_{i,j}}{\rho_{i+1/2}}\right)\right], \tag{2-55}$$

The discretized boundary conditions are

$$\Psi_{1,j} = U_{\rho,1,j}\Psi_{2,j}, \ \Psi_{N_\rho+1,j} = \bar{U}_{\rho,N_\rho,j}\Psi{N_\rho,j},$$
$$\Psi_{i,1}^n = U_{y,i,1}^n\Psi_{i,2}^n, \ \Psi_{i,N_\theta+1} = \bar{U}_{\theta,i,N_\theta}\Psi_{i,N_\theta}, \tag{2-56}$$

The magnetization is $4\pi M = B - H$, where B is the magnetic induction which is given by the spatial average of the local magnetic field. We have

$$4\pi M = \frac{1}{\mathcal{A}}\sum_{i=1}^{N_\rho}\sum_{j=1}^{N_\theta} h_{z,i,j}\mathcal{A}_{\rho,i} - H \tag{2-57}$$

Where $\mathcal{A}$ is total area of circular sector and $\mathcal{A}_{\rho,i} = a_\rho\rho_{i+1/2}a_\theta$ which is the area of a unit cell. The vorticity can be determined by integrating the phase φ in each unit cell of the mesh. We have

$$N_{i,j} = \frac{1}{2\pi}\oint_{\mathcal{C}_{i,j}} \nabla\varphi \cdot d\mathbf{r}, \ N = \sum_{i=1}^{N_\rho}\sum_{j=1}^{N_\theta} N_{i,j} \tag{2-58}$$

where $\mathcal{C}_{i,j}$ is a closed path with the lower left and upper right corner at (i,j) and $(i+1, j+1)$ respectively. We calculated N in order to make sure that the number of vortices agrees with the map of the order parameter.

3 Vortex matter in an inhomogeneous superconducting condensate

One of the important aspects of the properties of type-II superconductors is their magnetic behavior, i.e. the way of penetration of the magnetic field into the material. In a broad interval of applied magnetic fields between the lower critical field, H_{c1}, and the upper critical field, H_{c2}. In this chapter, I will exemplify some experimental results of the studied vortex matter with direct vortex imaging techniques. Such as experiments sensitive directly to the vortex magnetic field and with sufficient spatial resolution to resolve individual vortices. In addition, different experimental setups used to manipulate the vortex behavior through external means are presented, where particular attention is given to design of a pinning landscape and individual vortex manipulation by a nearby magnetic or tunneling tip, or a laser beam.

3.1 Direct vortex imaging techniques

3.1.1 Bitter decoration

The experiments performed, by using the Bitter decoration technique provides means of direct observation of static vortex structures at the surface of the superconductor with spatial resolution of about 80 nm, and rather poor sensitivity. The sample must be cleaned before repeating the experiment. Various aspects of vortex behavior that can be studied in decoration experiments are considered, in particular vortex lattice ordering and the effects of pinning and anisotropy on the equilibrium vortex arrangement. It is used in small applied fields $H < 10$ mT. The pinning forces increase on cooling, therefore vortices get stuck at their positions at some temperature T^* in between T_c and the chamber base temperature. T^* may be as high as 0.8 - 0.9 T_c [59]. Therefore the imaged vortex positions may not correspond to the ground state at the base temperature, which is a known caveat of the Bitter decoration technique.

Some mesoscopic samples can be made from a Nb film deposited on a Si substrate by using magnetron sputtering where the Bitter decoration technique based on *in situ* evaporation of Fe particles that are attracted to regions of magnetic field created by individual vortices and thus allow their visualization which is described in detail in Ref. [60].

Figure **3-1** (a) shows a typical vortex structure in the macroscopic film. The disordered
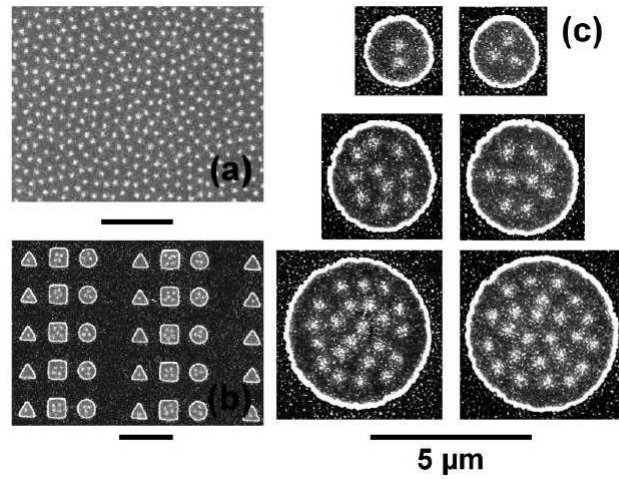
Figure 3-1: Scanning electronic microscope (SEM) images of vortex patterns obtained after field cooling (a) macroscopic film (b) part of an array containing dots, (c) vortex configurations in disks obtained in the same experiment Scale bars in all images correspond to $5\mu m$.

vortex arrangement is a signature of the presence of pinning (see, e.g., [61]), typical for sputtered Nb films. Using e-beam lithography and dry etching, the film can be made into large arrays of mesoscopic "dots" disks, triangles, and squares. This technique allow to obtain snapshots of about a hundred vortex configurations in nominally identical samples under identical conditions (field H, temperature T, etc.).

3.1.2 Magneto-optical imaging

This is another experimental tool for the direct observation of magnetic vortices in type-II superconductors. To be able to see magnetism directly with our eyes has been a very old dream, in a way by using magneto-optical imaging is possible the realization of this dream. This technique has been improved to enable single vortex observation at low flux densities. The main advantage of the new method is its high temporal resolution combined with the applicability to any superconducting sample with a flat surface. Magneto-Optical Imaging has developed rapidly over the last decade to emerge as a leading technique to directly visualise the static and dynamic magnetic behaviour of materials, capable of following magnetic processes on the scale of centimeters to sub-microns and at time scales from hours to nanoseconds. The images are direct, real-time, and give space-resolved information, such as ultrafast magnetic processes and revealing the motion of individual vortices in superconductors. The conventional magneto-optical imaging employ a plane polarized light and the Faraday effect in a ferrite garnet film (FGF) to visualize the local magnetic field over the superconductor surface (see Fig. **3-2**). For individual vortex observation it is necesary to to resolve the
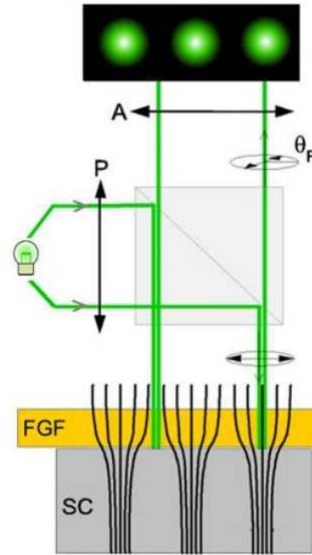
Figure 3-2: Principle of MO imaging. The maxima of the magnetic field from vortices in a superconducting sample (SC) gives maxima in the Faraday rotation θ_F of incoming plane polarized light in a ferrite garnet layer (FGF) near the sample. Vortices appear as bright spots when imaged using a crossed polarizer (P)/analyser (A) setting (from Ref. [62]).
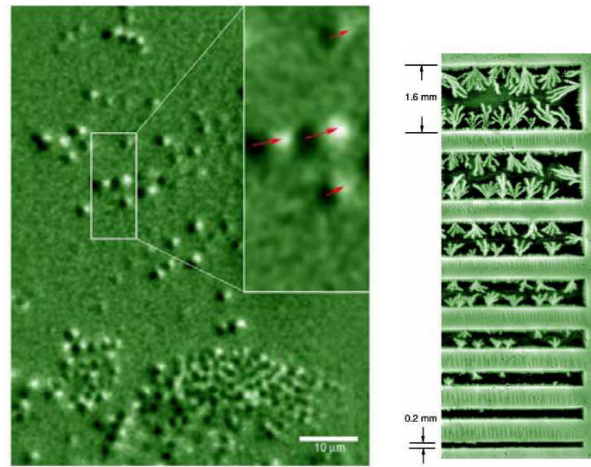
Figure 3-3: (Left) Vortex dynamics during flux penetration (from Ref. [62]). (right) MO image showing flux distribution in MgB_2 strip-shaped samples at 4 K and 15 mT applied field. The image brightness represents the local flux density. Both the number and size of the dendrites are larger for the wider samples.(from Ref. [63])

magnetic field modulation decaying rapidly with distance from the sample surface and to minimize depolarization effects in the optical system leading to loss of polarization contrast. Therefore, cryostat/MO system is combined as modular open microscope featuring a 100 W Hg lamp, an Olympus LMPlan 50 X objective mounted inside a modified Hi-Res (Oxford Instruments) He flow cryostat, a Glan-Taylor polarizer/analyser pair, a Smith beam splitter and a cooled CCD camera [62].

In Fig. **3-3** (left) we can observe the image with the change in flux distribution over a 1 s time interval after a small increase in the applied field by using MO. The dark and bright spots represent initial and final vortex positions, respectively. Medium brightness corresponds to an unchanged flux distribution, indicating stationary vortices. The insert shows a close-up of four vortex jumps. The arrows indicate the direction of vortex motion. In Fig **3-3** (rigth) also superconducting samples dominated by abrupt dendritic avalanches can be observed [63].

3.1.3 Scanning Hall probe microscopy

This technique typically uses Hall probe made of the semiconductor heterostructure $GaAs/Al_{0.3}Ga_{0.7}As$, which is a transducer that varies its output voltage in response to a magnetic field. Scanning Hall probe microscopy (SHPM) is a superior magnetic imaging technique due to many reasons. The Hall probe exerts negligible force on the underlying magnetic structure and is noninvasive. Unlike the magnetic decoration technique, the same area can be scanned over and over again. The magnetic field caused by hall probe is so minimal it has a negligible effect on, the sample it is measuring. The sample does not need to be an electrical conductor, unless using STM for height control. The measurement can be performed from 5-500 K in ultra high vacuum (UHV) and is nondestructive to the crystal lattice or structure. Tests requires no special surface preparation or coating. The detectable magnetic field sensitivity is approximately 100nT· $Hz^{-1/2}$. SHPM can be combined with other scanning methods such as scanning tunneling microscope (STM).

There are some shortcomings or difficulties when working with an SHPM. High resolution scans become difficult due to the thermal noise of extremely small hall probes. There is a minimum scanning height distance due to the construction of the hall probe. (This is especially significant with 2DEG semi-conductor probes due to their multi-layer design). The scanning (lift) height affects obtained image. Scanning large areas takes a significant amount of time. There is a relatively short practical scanning range (order of 1000's micrometer) along any direction. The housing is important to shield electromagnetic noise (Faraday cage), acoustic noise (anti-vibrating tables), air flow (air isolation cupboard), and static charge on the sample (ionizing units).

Very interesting images of trapping of single-quantum vortices by demagnetized disks were obtained by Kramer et al. [64], see Fig. **3-4** (a)-(d). The white dashed lines connect nearest-neighbor magnetic disks. (a) Individual vortices. (b) Coexistence of individual vortices and
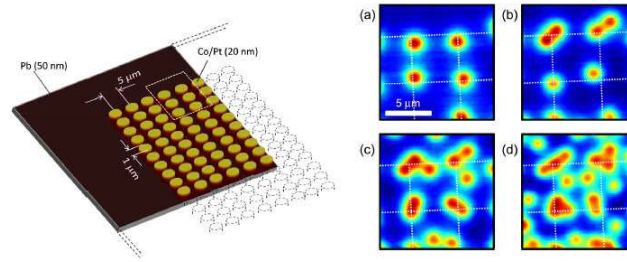
Figure 3-4: (Left) Schematic representation of the sample layout. A type-II superconducting Pb film 50 nm thick covers the whole substrate including the magnetic disks. (Right) Scanning Hall microscopy image at the border of the patterned area. (from Ref. [64])

vortex dimers. (c) Coexistence of vortex dimers and trimers. (d) Different vortex trimers at coexisting with interstitial vortices.

3.1.4 Transmission electron microscopy (TEM)

This technique requires very thin sample most often an ultrathin section less than 100 nm thick, sections for enabling the electrons to cross the sample. An image is formed from the interaction of the electrons with the sample as the beam is transmitted through the specimen. The image is then magnified and focused onto an imaging device, such as a fluorescent screen, a layer of photographic film, or a sensor such as a charge-coupled device. For superconductors [cryo-Lorentz transmission electron microscopy (cryo-LTEM)] it started to gain importance only recently as it has been implemented in Cambridge [65] and Lausanne [66] and used to image vortices in MgB_2.

3.2 Flux quanta manipulation

3.2.1 Scanning SQUID microscope

Direct observation of vortices by the scanning superconducting quantum interference device microscopy (SQUID) is an alternative and complement method to visualize vortices in the superconducting dots Fig.**3-5** (left). By scanning a small pick-up loop over the dots, one can magnetically image the vortices without damaging the samples. This allows us to study systematically how the vortex configuration evolves with magnetic field in a specific sample. In particular, scanning SQUID microscope can be used in the field of superconductivity for both imaging of the magnetic landscapes of the vortex matter and the mechanical control of individual flux quanta. Since SQUIDs are by far the most sensitive detectors of magnetic flux and thus provide the best product of spatial resolution and field sensitivity, they are a natural choice as a sensor for a magnetic microscope. In the latter case, by applying local vertical
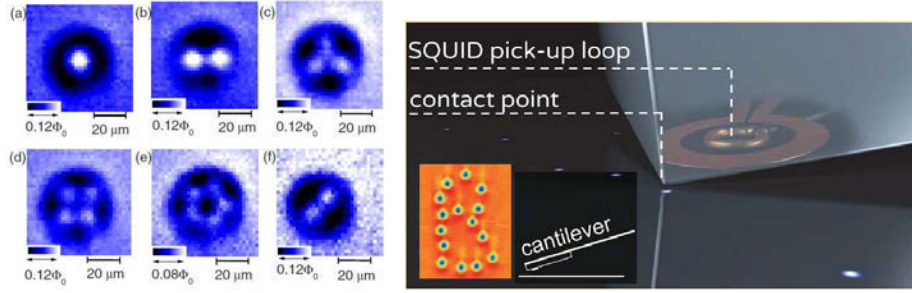
Figure 3-5: (Left) Scanning SQUID microscope images of vortices in an amorphous MoGe
disk, color bars indicate the magnitude of the magnetic flux detected in the
pick-up loop, (from Ref. [67]). (Right) Experimental configuration. Stress is
applied with the tip of the SQUID chip by pushing the cantilever (inset) into
the sample. Vortex configuration in an NbN thin film imaged at 4.2 K with no
contact area. Inset depicting vortices arranged into capital letter B, (from Ref.
[68]).

stress with the tip of the sensor, vortices can be attached to the contact point, relocated, and
stabilized at new position, Fig.**3-5** (right). In this way, mechanical manipulation of vortices
provides a local view of the interaction between strain and nanomagnetic objects as well as
controllable, effective, and reproducible manipulation technique.

3.2.2 Scanning tunneling microscopy

A scanning tunneling microscope (STM) is an instrument for imaging surfaces at the atomic
level Fig. **3-6** (a). In 1981 at IBM Zurich, Gerd Binnig and Heinrich Rohrer earned the
Nobel Prize in Physics in 1986 for STM good resolution, it is considered to be 0.1 nm lateral
resolution and 0.01 nm (10 pm) depth resolution [69], which makes scanning tunneling mi-
croscope an excellent tool for visualizing surfaces at the atomic level, where also individual
atoms at the surface of the material can be manipulated. The STM can be used not only in
ultra-high vacuum but also in air, water, and various other liquid or gas ambients, and at
temperatures ranging from near zero Kelvin to over 1000°C. STM is based on the concept
of quantum tunneling. When the sharp conducting tip, whose apex can be a single atom,
mounted on a piezoelectric tube is brought very near to the surface to be examined, a bias
(voltage difference) applied between the two can allow electrons to tunnel through the vac-
uum between them. The resulting tunneling current is a function of tip position, applied
voltage, and the local density of states (LDOS) of the sample. In superconductivity, STM
can provide high-resolution imaging of vortex matter, where the output signal displays the
contrast between normal electrons and Cooper pairs, as is shown in Fig. **3-6**(b). Addition-
ally, STM is sensitive to local density of states and through it to local gap function $|\Delta(\mathbf{r})|$,
rather than $\mathbf{B}(\mathbf{r})$. For each of the techniques there is a trade-off between field sensitivity (or
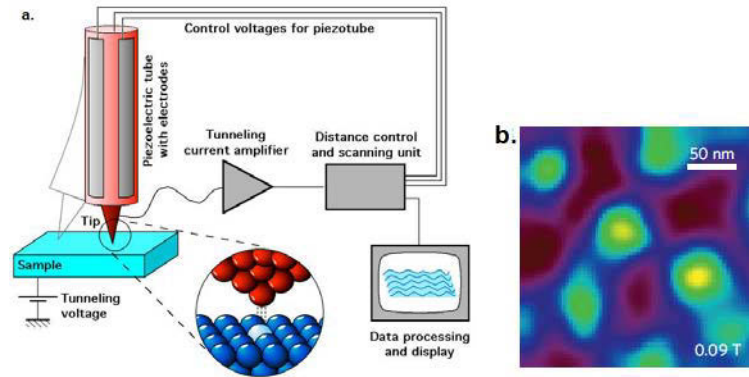
Figure 3-6: Scanning tunneling microscope (STM). (a) Schematic description of the STM. A tip with an apex of a single atom width is mounted on a piezoelectric stylus which scans the sample. Tunneling current is controlled with external voltage, and the output signal is shown on the display (credit: Wikipedia). (b) Image of the vortices in a superconducting film obtained by STM (figure taken from Ref. [70]).

more generally signal-to-noise ratio) and spatial resolution. The STM can be used to change the temperature locally, generation of quantized vortices and also creating superconducting islands how it is describe as follow:

3.2.2.1 The local pinning in a superconductor through the heating effect

Several phenomena related to vortex states have been revealed by the STM, such as the anisotropy of the Fermi surface distribution of the superconducting gap [71] , the vortex lattice melting process [72] , order-disorder transition [73].
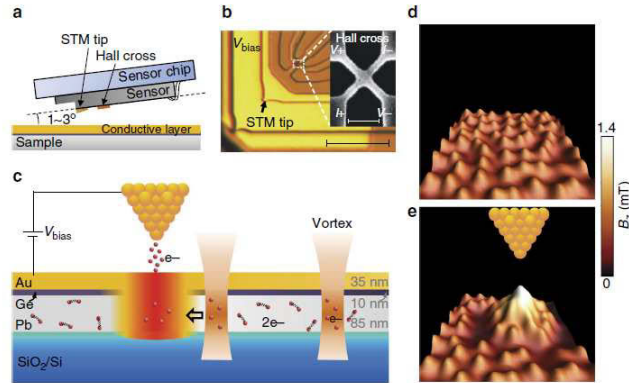
Figure 3-7: (a) Schematic view of the scanning Hall probe microscopy (SHPM), (b) An optical image of the Hall sensor, (c) Schematic representation of the local heating effect by using the STM tip. (d) SHPM image of a vortex lattice observed after field cooling and (e) SHPM image after 5 s of tunnelling at bias voltage of 0.5 V and tunnelling current of 0.5 nA. A vortex cluster forms at the tip position due to the local quench of the hot spot (figure taken from Ref. [74]).

However, despite the precise manipulation of vortices with the STM is still a open topic. Recently, a novel method to use STM controlling quenching of a hot spot in a superconducting film by using the local heating effect of the tunnelling junction on vortex states was reported, which is especially interesting at the nanoscale Fig. **3-7**. Tuning the bias voltage the heating effect of the tunneling junction can be well controlled to manipulate single-quantum vortices.

3.2.2.2 Controlled Generation of Quantized Vortex

Normally, the vortex enter in the superconducting sample in a presence of a high magnetic field in the form of quantized Abrikosov vortices with each of them carrying one flux quantum $\Phi_0 = h/2e$ (h, the Plank constant and e, the electron charge). Quantized vortices, as topological defects, play an important role in both physics and technological applications of superconductors. When a tunneling junction is established between the STM tip and the superconductor, a hot spot, playing the role of a pinning center, is created. The supercurrent, flowing in the vicinity of the hot spot, will be reoriented at the position of the hot spot thus creating a magnetic (vortex) dipole (see **3-8**). For a fixed average supercurrent density, the intensity of dipoles mainly depends on the size of the pinning center.
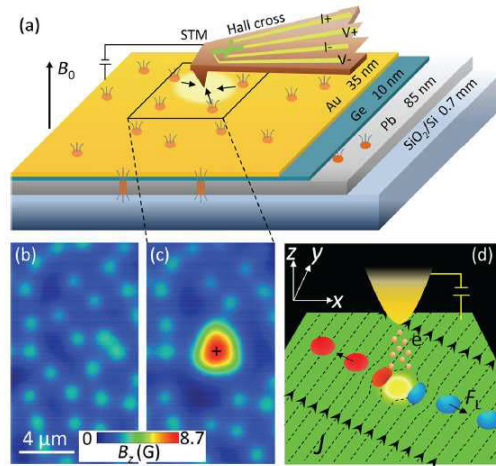
Figure 3-8: (a) Schematic view of sample geometry and the experimental setup, not drawn
to scale, (b) Scanning Hall probe microscopy image of the vortex pattern ob-
served after field cooling, (c) After applying a pulse tunneling current to the
vortex pattern in panel b, adjacent vortices around the tip are attracted to
the hot spot at the STM tip position. (d) Schematic image demonstrating the
generation mechanism of vortex-antivortex pairs. The dashed lines indicate the
supercurrent flowing direction. The solid arrows indicate the moving direction
of vortices and antivortices under the Lorentz force. (figure taken from Ref.
[75]).

3.2.2.3 Creating islands by local current annealing

The nanostructured superconductors were made from single YPtBi crystals by local current
annealing structurally amorphous YPtBi in an STM tunnel junction (see Fig. **3-9**). Strong
confinement effects with unique vortex structures has been observed and also several prop-
erties of these nanostructures were obtained from tunneling spectroscopy measurements as
a function of spatial position, temperature, and magnetic field.
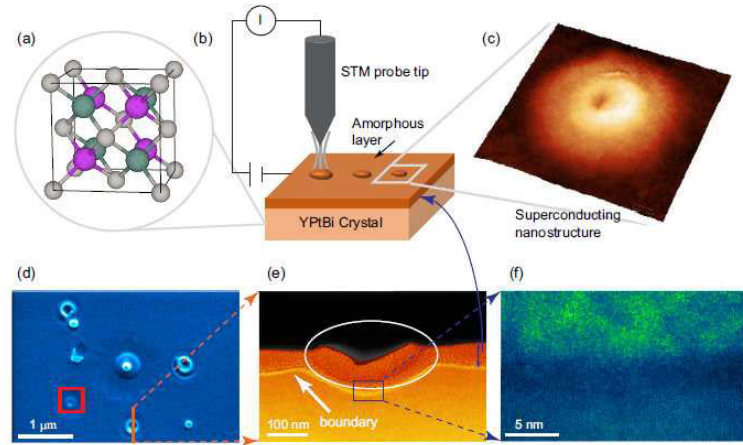
Figure 3-9: (a) C1 b crystal structure of YPtBi: Y (purple), Pt (gray), Bi (green) (b) Illustration of the process of creating superconducting islands by passing a current pulse with the STM probe tip held fixed within ≈1 nm of an amorphous YPtBi layer. (c) Three-dimensional rendered STM topographic image (200 nm x 200 nm). (d) SEM image showing seven different superconducting nanostructures created by local current annealing with the STM probe tip. (e) TEM cross section of the superconducting island in the bottom center of (d) highlighted by the orange line. The cross-sectional image shows ≈50-nm-thick amorphous layer covering the entire surface of the YPtBi crystal. (f) High-resolution TEM image of the boundary region separating the underlying YPtBi crystal and the region of the created nanostructure. (figure taken from Ref. [1]).

Different energy gaps, critical temperature, and critical magnetic fields were found in the center region versus the perimeter region of the nanostructure. Sequential addition of single vortices into the nanostructured island is observed at magnetic fields between the lower critical field H_{c1}, and the upper critical field H_{c2}. To observe the vortex formation within the superconducting island, The experiment carried out a spatial mapping of the differential conductance and extracted maps at zero bias as a function of magnetic field, as shown in Fig. **3-10**. Red represents the superconducting region with low conductance in the gap and blue corresponds to the normal state. With increasing magnetic field, the conductance maps show a single vortex sequentially added to the superconducting island. Finally, superconductivity in the center region is gradually suppressed without any vortex structure appearing. Looking toward the future, we anticipate that having the ability to induce a local structural transition to a superconducting phase with local probes will be a useful quantum nanotechnology workbench to design superconducting nanostructures for investigating both fundamental superconducting properties and practical applications of quantum electronics.
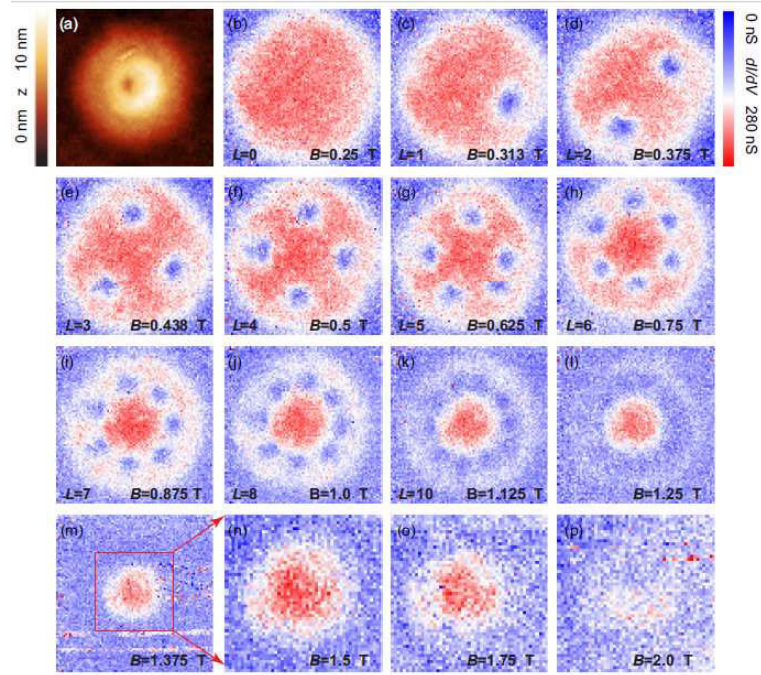
Figure 3-10: Sequential addition of vortices in a nanostructured superconducting island. (a) STM topographic image of the superconducting island. (b)-(p) Corresponding Fermi-level maps showing superconducting (red) and normal (blue) regions of the island as vortices (small blue disks) sequentially populate the nanostructure as the magnetic field is increased. The vortices are seen to distribute along the perimeter of the island and avoid the center. (figure taken from Ref. [1]).

3.2.3 Low-temperature scanning laser microscopy

The average properties of the vortex matter can be tuned with temperature, magnetic fields or electric currents. Yet, handling of individual vortices has been performed only with magnetic force, superconducting quantum interference device or strain-induced scanning local probe microscopies. Since these techniques are slow and heavy to implement in cryogenic environments, new approaches to provide a large-scale and versatile basis for sculpting the magnetic flux profile in superconductor devices are required. The most recent technique to manipulate individual vortices is the far-field optical method based on local heating of the superconductor with a focused laser beam to realize a fast and precise manipulation of individual Abrikosov vortices. Since a single vortex can induce a Josephson phase shift 10,11 , our method paves the way to fast optical drive of Josephson junctions, notably in superconducting elementary circuits with potential large parallelization of operations.
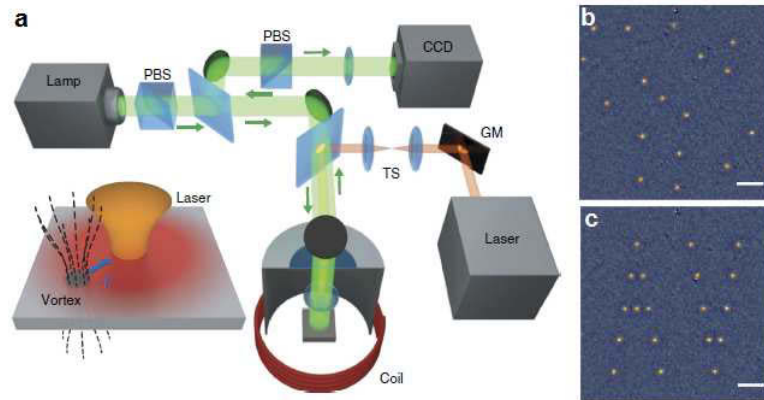
Figure 3-11: Single vortex manipulation with a focused laser beam. Sequential addition of vortices in a nanostructured superconducting island. (a) The concept of vortex attraction in a thermal gradient induced by a laser spot is illustrated. Magneto-optical imaging of individual vortices is based on the Faraday rotation of light polarization. PBS, polarizing beam-splitter. CCD, charge-coupled device. Local heating of the niobium film is performed with a tightly focused continuous wave laser (wavelength 561 nm) from which 40% of the optical power is absorbed. Vortex manipulation is performed by moving the laser beam with galvanometric mirrors (GMs) placed in a telecentric system (TS). (b) Magneto-optical image of a field-cooled vortex structure in the niobium film (c) Artificial vortex pattern engineered by single vortex repositioning from the initial vortex distribution displayed in b. The repositioning procedure is fully automatized. The laser is focused on the SC with a full-width at half-maximum diameter of 1.1 μm. The absorbed power is set to 17 μW. (figure taken from Ref. [76]).

The laser beam tightly focused induce a thermal gradient to manipulate single flux quanta. The laser locally heats the superconductor and creates a micron-sized hotspot with a temperature rise in the Kelvin range, while keeping the temperature below T_c. This thermal gradient can easily be tuned with lases power, so that the generated thermal force overcomes the pinning potential and induces a vortex motion towards the laser focus. Thus, the laser beam acts as optical tweezers that move single flux quanta to any new desired positions in the superconductor.

4 Influence of enhanced surface superconductivity in a mesoscopic sample

The possibility of surface enhancement of superconductivity represent a superconductor with a surface enhanced order parameter or negative surface extrapolation length, whose magnitud can be controlled. De Gennes' boundary condition phenomenological parameter b is used to study its effect upon the vorticity, magnetic induction, Cooper pair density, magnetization and phase of the order parameter as functions of the external applied magnetic field, including the analyses of the limit between 2D and 3D behavior of a superconducting sample by selecting certain value of b.

4.1 Introduction

The boundary condition of the superconducting order parameter at the surface of a specimen modifies the Gibbs free energy density near the surface on the scale of the coherence length. In superconducting samples with mesoscopic dimensions, the total free energy can be affected significantly via the boundary condition. The Ginzburg-Landau (GL) equations [5] are arguably the most convenient and frequently employed tool in studying the vortex matter and thermodynamic properties of superconducting materials with general boundary conditions. The surface contact energy term is added to the GL free energy in the form $\int_s (|\Psi|^2) ds$, where Ψ is the modulus of the order parameter [77]. The size of the sample contributes significantly to the total free energy. It is usually considered to be large enough such that the influence of finite dimensions on their properties are negligible along the external applied magnetic field which usually is taken as z direction. Therefore, demagnetizing effects are not assumed. However, this is not the case in many situations of interest. Examples range from quantum size effects in metallic nanoparticles [78, 79] and microfluidics [80] to cluster size effects [81]. Hallmark physical ingredients in these systems are large surface-to-volume ratio and one or more dimensions of the sample approaching a relevant fundamental scale. Technological advances have been possible to enhance critical fields, critical temperature and have a better vortex control in micro, nano and mesoscopic superconducting samples. Superconductors in a mesoscopic scale with different geometry revealed a diversity of new phenomena that are not present in other scales. Also, these systems are affected by the

medium where the sample is embedded. The possibility to control the dynamics and vortex density has made them one of the favorite experimental and theoretical system for studies of the physics of solid state [82, 83, 84, 85, 86, 87]. Furthermore, it was observed that structural defects influence strongly the vortex configuration, critical temperature, fields and currents in the sample [88, 89, 90, 91, 92, 93]. P. N. Lisboa-Filho *et al.* tested the smallest square cross section for the occurrence of vortices in a mesoscopic superconductor. They found that the limit of vortex penetration is for the square sample of size $3\xi \times 3\xi$ in which only a single vortex are allowed in the sample [94], where ξ is the coherence length. Barba-Ortega *et al.* tested the limit values of the deGennes parameter b for the occurrence of a single vortex in a mesoscopic square of area L^2. They found that the sample remain always in the single vortex state for $L \propto \ln b$ [95, 96]. B. J. Baelus *et al.* studied the effect of the enhancement of surface superconductivity and Ginzburg-Landau (GL) parameter on the critical field and critical temperature for superconducting mesoscopics cylinders. They found that increasing the confinement effects ($|b| \to 0$) the critical temperature increases and is independent of GL Parameter, the vorticity and third critical fields increase and the multi-vortex state move to the center creating a giant vortex state [96].

This chapter is organized as follows. Sec.4.1. Introduction. Addendum to the theoretical formalism is presented Sec.4.1.1. In Sec. 4.2. The the Ginzburg Landau equations are solved for a small mesoscopic superconducting square of area $S = 9\xi^2$ in the the presence of an external applied magnetic field applied perpendicular to its surface. We consider a superconducting/superconducting interface at higher critical temperature boundary condition ($b < 0$). We find that a multi-vortex state in the square is induced due to the presence of another superconductor in opposite to what occurs for the $1/b = 0$ case where only one vortex is possible [94]. We have gone further by doing some true 3D simulations in a parallelepiped of volume $V = Sd$ by using several values of d. We have determined a value of d for which there is no difference between 2D and 3D calculations.

4.1.1 Addendum to the theoretical formalism

A small superconducting square surrounded by a medium which enhances superconductivity at the edge of the sample is considered. To deal with this problem we use the GL theory and solve numerically and self-consistently the system of two GL equations (2-33). The free energy of the superconducting state can be written as a sum of two contributions, G_b and G_s. The former is the bulk energy of the sample and the latter is the surface energy. These contributions are given by:

$$G_b = \int \left[-|\Psi|^2 + \frac{1}{2}|\Psi|^4 + |(-i\nabla - \mathbf{A})\Psi|^2 + \kappa^2 \mathbf{H}^2 - 2\kappa^2 \mathbf{H} \cdot \mathbf{H_0})^2 \right] dV, \tag{4-1}$$

$$G_s = \frac{1}{b} \int |\Psi|^2 dS \tag{4-2}$$

The integration in Eqs. (4-1) and (4-2) is performed over the sample bulk and surface, respectively. We can notice that by minimization of the free energy functional $G = G_b + G_s$ with respect to the order parameter Ψ and the vector potential $\mathbf{A}$, the general boundary condition for the order parameter can be obtained phenomenologically as follows:

$$\mathbf{n} \cdot (-i\nabla - \mathbf{A})\Psi = \frac{i}{b}\Psi \qquad (4\text{-}3)$$

where $\mathbf{n}$ is the unit vector normal to the sample surface, b is the de Gennes "extrapolation length", $\mathbf{A}$ is the vector potential, and Ψ is the order parameter.

4.2 Multi-vortex state in a mesoscopic square with enhanced superconductivity at the boundary

We studied a mesoscopic superconducting square (see Fig.**4-1**) of size $3\xi \times 3\xi$ with a superconductor/superconducting at higher critical temperature external interface simulated by $b/\xi = -2.5, -12.5, -1.7, -1.25$, with $\kappa = 5.0$. The GL equations were solved by using the link variable method [58] with a mesh size $\Delta x = \Delta y = 0.1\xi$. We also considered a superconducting/vacuum interface $b \to \infty$ for comparison purposes with the b finite results. For the finite case, we solve the true $3D$ Ginzburg-Landau equations [58, 97], the size of the simulation box is taken sufficiently large to ensure that the local magnetic field equals the applied field far from the sample boundaries. The simulation box has dimensions $19\xi \times 19\xi \times 11\xi$ and the superconductor inside has the size $3\xi \times 3\xi \times d$, where d varied from 1ξ until 8ξ; the resolution of the mesh-grid was taken as $\Delta x = \Delta y = \Delta z = 0.1\xi$.

In Fig. **4-2** we illustrate the magnetization curves as functions of the external applied magnetic field. They present a typical profile of a magnetization curve of a mesoscopic superconductor. It exhibits a series of discontinuities, in which each jump signals the entrance of one or more vortices into the sample. Notice that the number of jumps and the upper thermodynamic field $H_{c3}(0)$ vary significantly with b. We can also observe that as the parameter b decreases towards negative values, $H_{c3}(0)$ decreases. In addition, Fig. **4-2** shows that it is possible to obtain novel curves of magnetization and the number of vortex in the sample only by modifying the deGennes parameter, while the dimensions are remained constant. Thus, we estimated the limit value of the b parameter for which the vorticity N is a maximum. The vorticity grows from $N = 1, 2, 3, 5, 6$, selecting limit values of deGennes parameter as $b/\xi = \infty, -12.5, -2.5, -1.7, -1.25$ respectively for a square sample with constant area $S = 9\xi^2$. In reference [94] only the $N = 1$ state (for $b/\xi = \infty$) was found.

In Fig. **4-3** (left panel) we present the magnetization as a function of the external magnetic field H_e for different sizes of the mesoscopic superconducting square sample and fixed value of b. Notice that the first transition fields H_{c1} and the number of discontinuities vary significantly with the size of the sample. In this way, the vortex configuration that we can obtain is different for each size of the square. It is seen that the upper critical field $H_{c3}(0)$ is increased
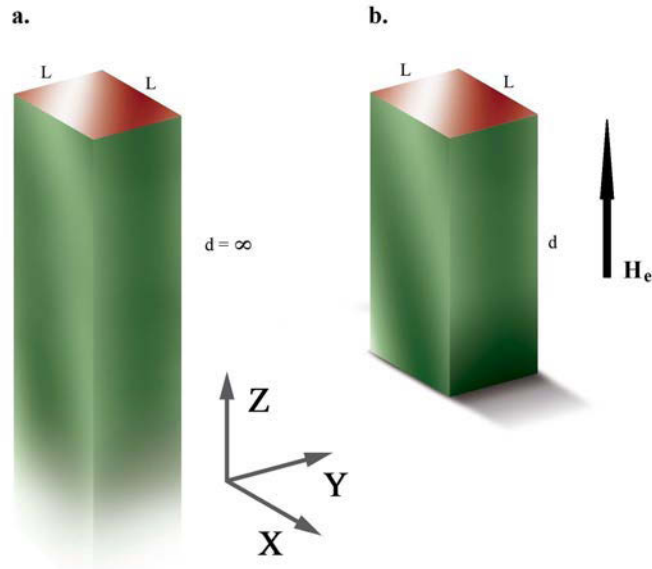
Figure 4-1: Layout of the studied sample: (Left) sample with length $d = \infty$, whereas a sample which length $d = 8\xi$ is considered (right).
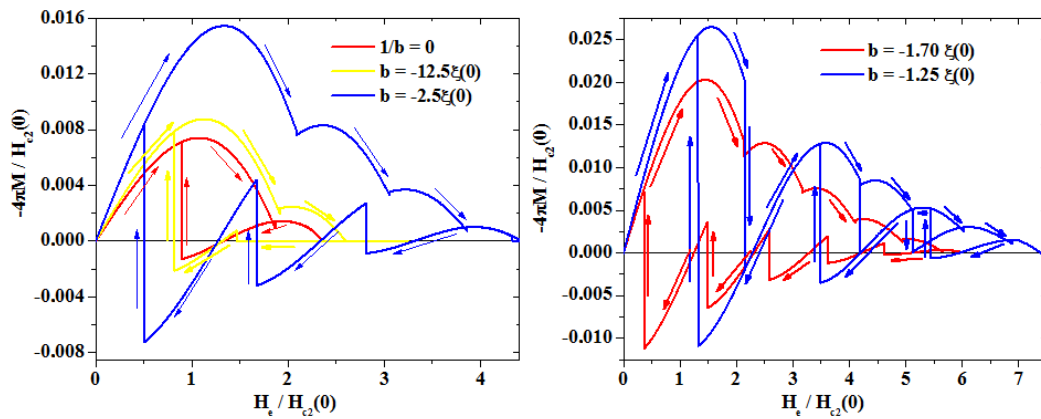

Figure 4-2: Magnetization as a function of the external applied magnetic field H_e for different negatives values of the deGennes parameter.
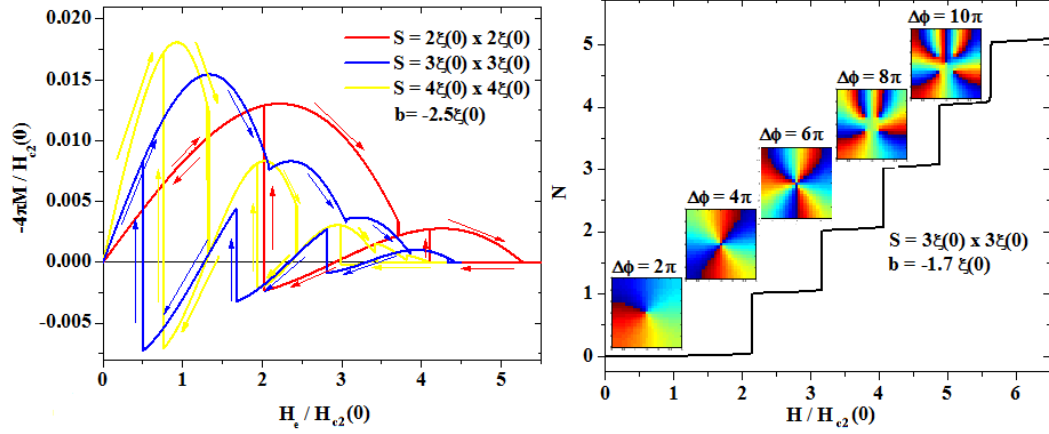
Figure 4-3: (left panel) Plot of the magnetization as a function of the external applied magnetic field for the square with different values of area for $b = -2.5\xi$. (right panel) Vorticity as a function of external magnetic field and phase of the order parameter.

when the area of the sample is reduced. In the right panel of this figure we illustrate the vorticity N as a function of of the magnetic field H_e. The magnetic fields for all N to $N + 1$ transitions are $H_e/H_{c2}(0) = 2.608, 3.618, 4.478, 5.219, 6.027$ by using $b = -1.7\xi$. The phase of the order parameter allows to determine the number of vortices in a given region. If the vorticity in this region is N, then the phase changes by $2\pi N$.

Fig. **4-4** (left panel), shows the $H_3(0)-b$ curve for a sample with $b/\xi = \infty, -12.5, -2.5, -1.7, -1.25$ and the corresponding cases $H_3(0)/H_{c2}(0) = 2.32, 2.59, 4.43, 6.02, 7.33$, respectively. As we can see, $H_3(0)$ grows quickly when $|b|$ decreases. The curve at the inset shows the linear fitting $H_3(0) \approx 51.74\gamma - 49.58$ ($\gamma = 1 - \Delta x/b$). From the experimental point of view, this is an important result, since the higher critical field, the higher critical current density can be obtained. The same behavior is observed in the right panel of this figure showing the maximum of the magnetization M_{Max} as a function of b, for which the curve at the inset has the linear fitting $M \approx 0.003H_e - 0.0009$. Therefore, from both figures we can conclude that the system becomes much more diamagnetic when H_e and b are increased. Thus, if we are interested in shielding the third penetration of magnetic field (surface flux and vortex penetration), a superconductor surrounded by another superconductor at a higher critical temperature is useful. In Fig. **4-5** (a)-(e) We show the snapshot of the order parameter $|\Psi|^2$ (upper row), the vorticity N (middle row) and the local magnetic field $\mathbf{h} = \nabla \times \mathbf{A}$ for several values of b. Following the panels from the left to the right, in this order, it shown that is possible to obtain a giant vortex configuration for low vorticity such as $N = 2, 3$. This is novel since previous configurations have been found in larger systems, bu not in such confined systems. Then, our results indicate that superconducting/superconducting interface at higher critical temperature could be a way of inducing the nucleation of giant vortex state. For $N = 4, 5$
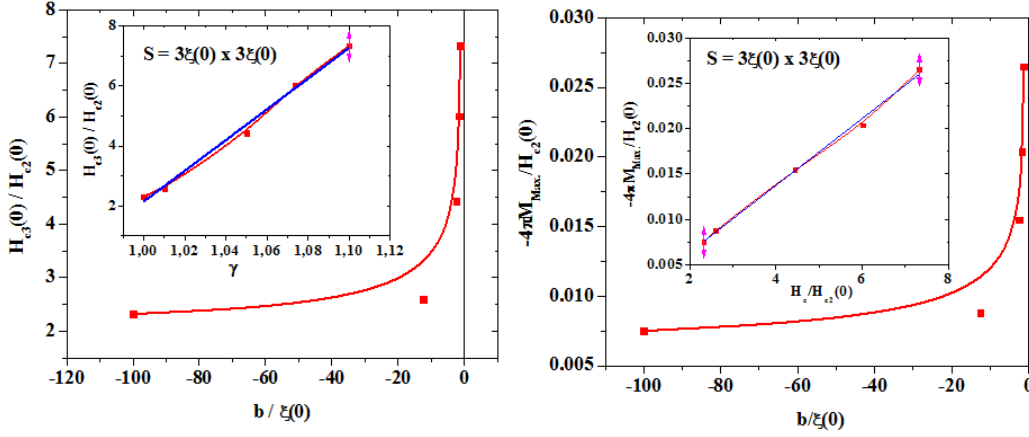
Figure 4-4: (left panel) The upper critical field $H_{c3}(0)$ field as a function of b and $\gamma = 1 - a_x/b$ parameter (inset). (right panel) Maximum of the magnetization curve M_{Max} as a function of b and H_e (inset). Theoretical results (red line) and linear fit (blue line) in inset.

we observe a multivortex state. The multi vortex state is indistinguishable in the density plot of the magnitude of the order parameter neither in the magnetic field induction, since they are so packed in a small region. However, the core center are not coincident. This kind of vortex configurations can be achieved only if the deGennes parameter values and applied magnetic field harmonize for every multi-vortex state in this confinement system.

Until now our analyses is based in the 2D TDGL equations, that is, we have assumed invariance of the system along the z direction. With the purpose of making sure that our results are nor most influenced by demagnetizing effects, so that it could be applied to a film, rather than only to a cylinder, we have done some numerical simulations for a parallelepiped of volume $V = Sd$, for $s = 9\xi^2$ and several values of d. In Fig. **4-6** we show the magnetization as a function of the external applied magnetic field H_e. As we can see through panel (a), the $d = 8\xi$ case present no significant difference to the $d = \infty$ situation. For the other values of d we can observe some difference in the magnetization, but only in the Meissner state. In the other hand, in the mixed state all curves are very close together. Then, we can assure that our discussion can be extended to superconducting films. The details of the 3D simulations can be found in [97]. Here we present a brief description of how we proceeded in order to carry out these calculations. First of all, we define a simulation box designed as a parallelepiped, which we call a domain Ω. Inside this box we consider a smaller domain $\Omega_{sc} \subset \Omega$ filled by the superconducting material. Both domains are concentric. In Ω_{sc} we solve numerically the full TDGL equations. At the superconductor-vacuum interface $\partial\Omega_{sc}$ we apply the boundary condition of vanishing superconducting current density for which $(-i\boldsymbol{\nabla} - \mathbf{A}) \cdot \mathbf{n} = \frac{i}{b}\psi$, where $\mathbf{n}$ is a normal unit vector pointing outward the surface. Outside the superconductor, we solve only second TDGL equation by neglecting the current density
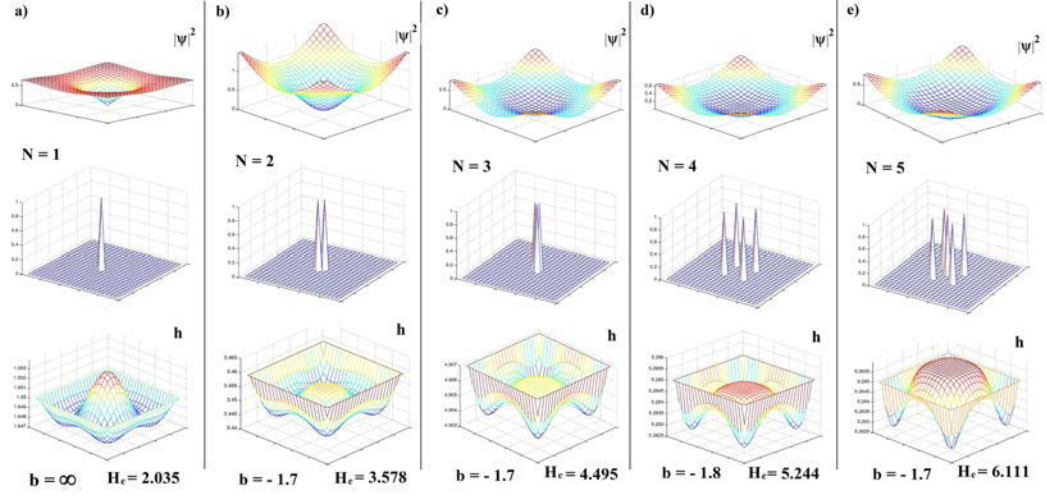
Figure 4-5: (upper row) Snapshots of the order parameter $|\Psi|^2$, the vorticity N (middle row), and the local magnetic field $\mathbf{h} = \nabla \times \mathbf{A}$ (lower row)for (a) $b = \infty$, $N = 1$, (b-c) $b = -1.7\xi$, $N = 2, 3$, (d) $b = -1.8\xi$, $N = 4$ and (e) $b = -1.7\xi$, $N = 5$.
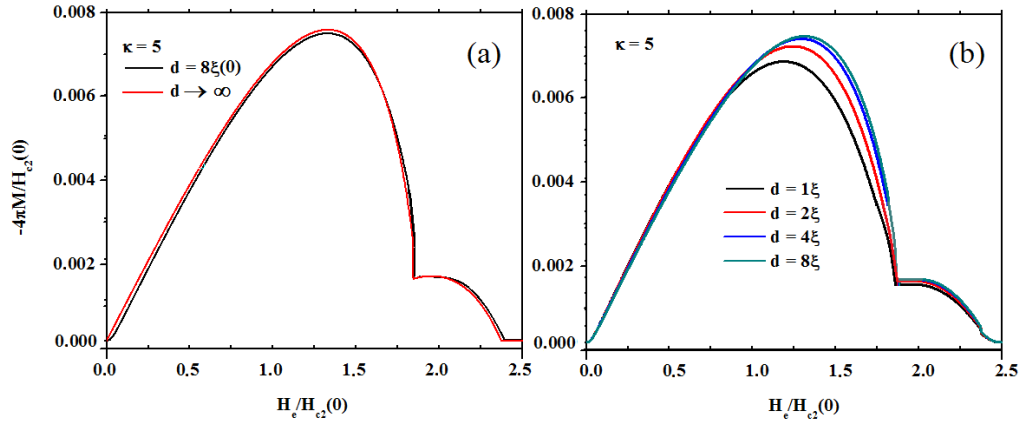
Figure 4-6: Magnetization as a function of the external applied magnetic field H_e for (a) $d = \infty, 8\xi$, $\kappa = 5.0$, (b) $d = 8\xi, 6\xi, 4\xi, 1\xi$.
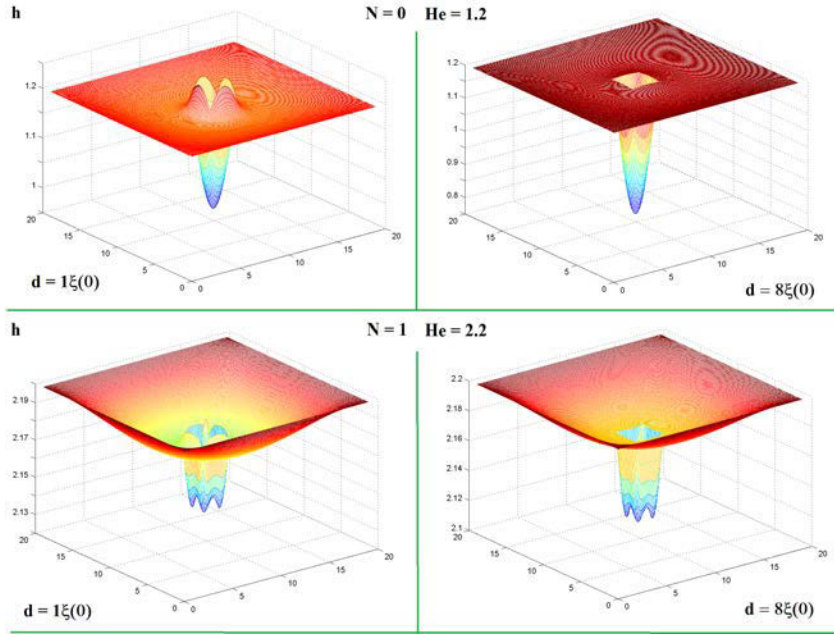
Figure 4-7: The local magnetic field at the $z = 0$ plane for $d = 1\xi$ (left column) and $d = 8\xi$ (right column) for two distinct values of the applies field.

term. At the vacuum-vacuum interface $\partial\Omega$ we suppose that the local magnetic field $\mathbf{h}$ equals the applied field $\mathbf{H}$. The surfaces $\partial\Omega_{sc}$ and $\partial\Omega$ are taken sufficiently distant from one each other until the results are unchanged by increasing the simulation box. In Fig. **4-7** we present two scenarios for the intensity of the local magnetic field at the middle plane of the superconductor ($z = 0$ plane): one is the Meissner state (upper row) and the other one is the mixed state (lower row) for two different values of d. As we can see, the demagnetization effects are more significant in the Meissner state.

4.3 Conclusion

We studied the effect of different negative values of the deGennes parameter in the thermodynamics properties for a small superconducting square of size $3\xi \times 3\xi$ in the presence of an applied external magnetic field by solving the coupled nonlinear Ginzburg-Landau equations. We considered the lateral surface of the sample in contact with a thin superconducting layer at higher critical temperature. Our results show that a giant vortex state and multi-vortex state appear in the sample choosing a convenient value of $b < 0$ parameter, even for such small system. The vorticity, the local magnetic filed, cooper pair density, magnetization and the phase of order parameter depend strongly of the chosen boundary condition. Also, the upper magnetic field H_{c3} grows when the values of the deGennes parameter decreases toward negative values. We present new results in this paper such as the analytical dependence be-

tween the third critical field, maximum of the magnetization and b-parameter and a weak dependence of the first critical field as a function of the b-parameter.

Publications.

The results presented in this chapter were published as:

- J. Barba-Ortega, J. D. González and E. Sardella, *Multi-vortex state induced by proximity effects in a small superconducting square*, Journal of Low Temp. Phys. **177**, 193 (2014).

5 Complex vortex configuration in the presence of defects with different thermal properties

We propose a way to manipulate the landscape of the superconducting condensate in thin films via local changes of the thermal properties, including in the variations of anisotropy through a variations of T_c and the spatially localized heating of the superconductor T. This simple approach provides the perfect alternative for modulation of vortex collective, emerging in the type-II superconductors as a natural response to the applied magnetic field and the transport current, which was, up to now, controlled purely via nanofabricated static pinning centers, whose intensity and distribution cannot be changed once the landscape is defined.

5.1 Introduction

The vortices (tubes of quantized magnetic flux) allows the superconducting state to survive at high applied magnetic field in type-II superconductor, making them technologically relevant. The vortices have a non-superconducting core with a radius on the scale of the coherence length ξ and a circulating super-current that generates one quantum of magnetic flux, $\Phi_0 = h/2e$, over the scale of the London penetration depth. Although the paired electrons in a superconductor carry charge without resistance, a current will exert a Magnus force on all magnetic flux, which results in dissipation, if any of them move. The vortex pinning is an opportunity to understand and reduce uncontrolled vortex motion. A vortex may be pinned by collocating its energetically costly non-superconducting core with a defect that locally suppresses superconductivity [98, 99, 100, 101, 102]. Continued reduction in uncontrolled vortex motion will open up applications both for quiet circuits in sensing and communication and for large currents in high-field magnets and power distribution. Collectively controlled vortex motion can serve as a rectifier [103], a vortex ratchet mechanism can perform clocked logic [104], and vortices can control spins in an adjacent diluted magnetic semiconductor [105], while vortices adjacent to an electron gas in a quantum-Hall state may allow the creation of exotic quantum states [106]. A proposed test of the long-standing idea that vortices may entangle like polymers requires controlled local manipulation of single vortices [107]. Vortices are of theoretical interest for their own sake [108, 109], as clues to the underlying superconductivity [110, 111], as analogues for interacting bosons [112], and

as model systems for soft condensed matter [108]. In mesoscopic samples there is a competition between the Abrikosov lattice, being the lowest-energy configuration in bulk material and films, and the boundary, which tries to impose its geometry on the vortex lattice. Experimentally, the magnetization of superconducting disks and rings has been measured as a function of the externally applied magnetic field [113, 114, 115]. In small systems vortices may overlap so strongly that it is more favorable to form one giant vortex. Experimental reports show that when the order parameter is enhanced, as a consequence, the surface contact energy has an enhancing effect upon the transition temperature T_c [116]. This could be accomplished, for example, via deposition of a superconductor with a higher intrinsic T_c or surface cold working [117, 118], or, perhaps, via disordering a thin surface film [119], or depositing a thin film of a normal metal [120, 121]. The possibility of reversible surface enhancement of superconductivity has been examined experimentally [118]. It is shown that single crystal tin samples with cold-worked surfaces represent a superconductor with a surface-enhanced order parameter or negative surface extrapolation length, whose magnitude can be controlled. Other experimental results discuss the enhancement of order parameter in two principally different ways: either as an effect of stresses induced by surface treatment [117] or as the effect of stress-free defects [122]. On the other hand, Kozhevnikov and coworkers found that a surface modification provided an enhancement of the order parameter controllable [118]. Associated with this is the prediction that surface enhancement can yield a significant increase of the critical temperature for samples. In consequence the practical applications are expanded.

The structure of the superconducting sample strongly influences its effects on the behavior of the vortices in a type-II superconductor, in which the external magnetic field can penetrate and as a consequence the superconductivity is locally depreciated [123]. Although the structure can be specifically designed with the inclusion of artificial pinning induced by magnetic dots, submicron holes, chemically grown defects, irradiation with heavy ions, permanent nanomagnets, or nanostructured perforations, the geometry of these defects is important, not only for determining equilibrium flux structures, but also for determining the critical parameters of the mesoscopic superconductor [124, 125, 126, 127, 64]. Considering the essence of a defect, the main idea has always been to create a spatial inhomogeneity in the superconducting condensate, i.e. locally suppress or enhance superconductivity on a scale comparable to the size of the vortex core. Therefore, if a surface arrangement of the geometrical defects is made, the superconductor can sustain several values of the upper critical magnetic field, where ideally the homogeneous lattice of vortices is interlocked with the increase in the anisotropy [128, 129, 130]. In complex oxides, strongly-correlated electron systems can be found in which slight variations of the charge carrier density lead to dramatic changes in their physical properties [131] and increase the potential for novel technological applications, opening up the possibility of electrostatic tuning of the carrier concentration [132], like in classical field-effect transistors [133, 134] or superconductivity [135, 136, 137, 138, 139, 140]. Oxide superconductors are an example of those in which the

critical temperature T_c can be modified via the application of an electric field [139, 140] or by using ferroelectric field effects [139], and those processes allow one to change the T_c in a reversible way.

In this thesis, the consequences of a weak-superconducting regions due to the incidence of a continuous wave laser was investigated, since it provide a locally variation of the temperature and adopt almost any kind of shape and size. We are motivated by the response of a superconductor interacting with laser light of a continuous wave laser (CWL). Due to that it offers a great opportunity to modify a will the number of defects and location in the superconducting sample, which allows to obtain new configurations of vortex and thermodynamic properties. In order to investigate the response of the system to magnetic field in which defects are created for a CWL, we apply the time-dependent Ginzburg-Landau (TDGL) theory where the change of the temperature is locally modified. The TDGL model provide excellent description for the study of this system due to working temperature of the superconducting sample as well as the local temperature imposed by CWL can be found as a coefficient on TDGL equations to be changed in the systems to be study.

This chapter is organized as follows. Sec.5.1. Introduction. Addendum to the theoretical formalism is presented Sec.5.1.1. In Sec. 5.2. We study the influence of a pentagonal/hexagonal defect at higher/lower critical temperature in a thin superconducting disk on the critical fields and vortex configuration is investigated numerically. The coupled nonlinear Ginzburg-Landau equations are solved self-consistently to calculate and compare quantities such as the magnetization, super-current, Gibbs free energy, Cooper pair density, magnetic induction, and phase of order parameter. For certain magnetic field ranges, we found a coexistence of a giant vortex state, placed in the center of the disk and a complex multi-vortex state, toward the corners of the defect. In Sec. 5.3, we study the static and dynamic properties of a superconducting condensate in a thin disk, consisting of overlapped geometrical defects. As a consequence of the selected system for numerical simulation, the parameter order in the regions is position-dependent and is decreased when a magnetic field is present. Thus the vortex structure and its mutual interactions, as well as interactions with different kinds of defects and interfaces, become very complex. In order to investigate the response of the system to a magnetic field, we applied TDGL theory, where the anisotropy is included through a spatially dependent critical temperature T_c, which is included in the functional through the coefficient α due to its intrinsic dependence on the critical temperature of superconducting materials. In Sec. 5.4. Static and dynamic properties of vortices are studied in a superconducting array of weakly-superconducting (or normal regions) created in the sample increasing the temperature T locally and by using a continuous wave laser (CWL) that emits a beam with a controlled heat output, beam duration and intensity. The time-dependent Ginzburg-Landau theory is used to describe the interaction of the light with the superconductor, where the defects are include through the spatially-dependent temperature T. Vortices penetrating into the weak-superconducting regions which are generated considering that $T > T_c$ where the CWL is pointing. Qualitative changes are observed in the

dynamics of the superconducting condensate in the presence of pinning with different shapes and sizes which are possible to be modified in the same superconducting sample without any structural changes. Our results are summarized in each Section.

5.1.1 Addendum to the theoretical formalism

As model system we consider a defect in a thin superconducting disk including a pinning which is introduced as a pentagonal and hexagonal shapes of another superconducting material with smaller (larger) critical temperature $T_{c1} < T_c$ ($T_{c1} > T_c$) [141, 142] (see Fig. **5-1**). The sample is immersed in an insulating medium in the presence of an uniform magnetic field H_0. To solve this problem we use the thin film limit, $d \ll \xi, \lambda$, (d is the thickness of the disk and R_e its radius). For this system we solved numerically the following TDGL equations:

$$\frac{\partial \psi}{\partial t} = (i\nabla - \mathbf{A})^2 \psi + \psi \left(f(\mathbf{r}) - |\psi|^2 \right) \tag{5-1}$$

$$\frac{\partial \mathbf{A}}{\partial t} = Re \left[\bar{\psi} \left(-i\nabla - \mathbf{A} \right) \psi \right] - \kappa^2 \nabla \times \nabla \times \mathbf{A} \tag{5-2}$$

where the parameter $f(\mathbf{r})$ is related with the T_c-nonhomogeneity in the system: for $f(\mathbf{r}) < 1$ superconductivity can be suppressed inside the pinning center, consequently it attracts the flux domains, whereas in the case of $f(\mathbf{r}) > 1$ the defect interacts with the flux repulsively. The equation 5-1 with the inhomogeneity coefficient $f(\mathbf{r})$ which is valid at $T = 0$. In Eqs. (5-1) and (5-2) dimensionless units were introduced as follows: $|\psi|$ is the order parameter in units of $\psi_\infty(0) = \sqrt{\alpha(0)/\beta}$, where $\alpha(0)$ and β are two phenomenological constants; lengths in units of the coherence length ξ; time in units of $t_0 = \pi\hbar/8K_BT_c \approx 10^{-12}s$; $\mathbf{A}$ in units of $H_{c2}(0)\xi$, where $H_{c2}(0)$ is the second thermodynamic critical field, the temperature in units of the critical temperature T_c, supercurrent $\mathbf{J} = Re[\bar{\psi}(-i\nabla - \mathbf{A})\psi]$ in units of $J_0 = \hbar c^2/8\pi e\xi$, $\lambda(0)$ is the penetration depth.

5.2 Complex vortex configuration in a disk with a higher/lower critical temperature superconducting geometrical central defect

We choose $d = \xi$ and $R_e = 13\xi$. Largest unit cells lengths were $a_r = R_e/N_r$ and $a_\theta = 2\pi/N_\theta$, taking $N_r = N_\theta = 64$ as the number of cells in the r and θ directions respectively. In a microscopic analysis is possible to establish a link between the microscopic theory of deGennes and the Ginzburg-Landau theory but this is not a objective of this work. Let us now turn to the presentation of the results that arise from the numerical solution of

TDGL equations. Here, we are interested only in the vortex configurations and the choice of geometrical defects is adequate for this purpose. The disk and defects areas are $A_{Disk} = 13^2\xi^2\pi \simeq 531\xi^2$, $A_{Pentagon} \simeq 116\xi^2$ and $A_{Hexagon} \simeq 127\xi^2$ respectively. We consider $f(r,\theta) = 1$ everywhere, except at defects position in the disk which are simulated by using $f(r,\theta) = 0.8$ for the superconductor at lower critical temperature and $f(r,\theta) = 1.2$ for the superconductor at higher critical temperature, see Fig. **5-1**.
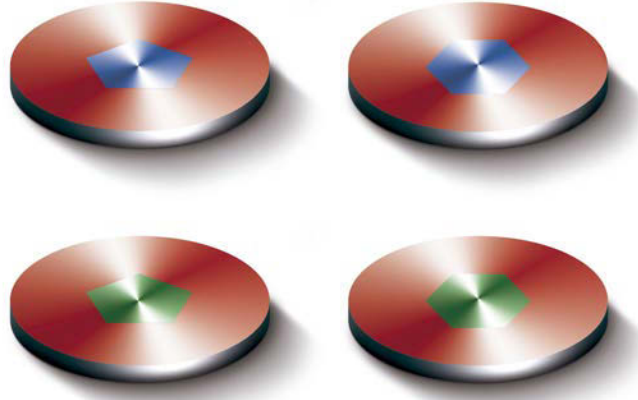
Figure 5-1: Layout of the studied sample: Superconducting disk with a central superconductor defect at higher critical temperature (green) or at lower critical temperature (blue), for pentagonal (left) or hexagonal (right) case.

5.2.1 Magnetization and vorticity

In the first step, we will compare the magnetization in Fig. **5-2** (up) and vorticity Fig. **5-2** (down) as a function of the applied magnetic field for the two geometries considered. The disk with hexagonal defect formed by a superconductor at higher critical temperature $(Sup > T_c)$ is analyzed by using the green curves in both magnetization and vorticity, and the blue one for pentagonal defect formed by a superconductor at lower critical temperature $(Sup < T_c)$. It is clear to see in the Fig. **5-2** (up) that the superconducting state is not always the Meissner state, further, for the chosen boundary condition superconductor/vacuum $b \to \infty$, the first transition field $H_1/H_{c2} = 1.0556$ is independent of the defect geometry and the kind of the superconductor used. For $1.0556 < H_0 < 1.3975$ (in the mixed state), we observe significant differences in the magnetization in the samples with a $Sup < T_c$ and a $Sup > T_c$. While for $1.3975 < H_0 < 1.38$, the magnetization curves behave similarly, increasing the magnetic field, the superconductivity is destroyed at $H_0/H_{c2} = 1.8$. Finally, in the downward branch of the magnetic field, at $H_0 = 0$, we find that the magnetization is zero

Figure 5-2: Magnetization curve (up) and vorticity N (down) as a function of the applied
magnetic field H_0. (*Sup* means superconductor)

for the hexagon case, while for pentagon defect, the magnetization is $-4\pi M = -0.2501/H_{c2}$, with obvious paramagnetism in the sample. This behavior is clearly reflected in the vorticity Fig. **5-2** (down), which confirms that the value H_0 for the first entry of vortices occurs in $H_0/H_{c2} = 1.0556$ for each defect, and additionally tha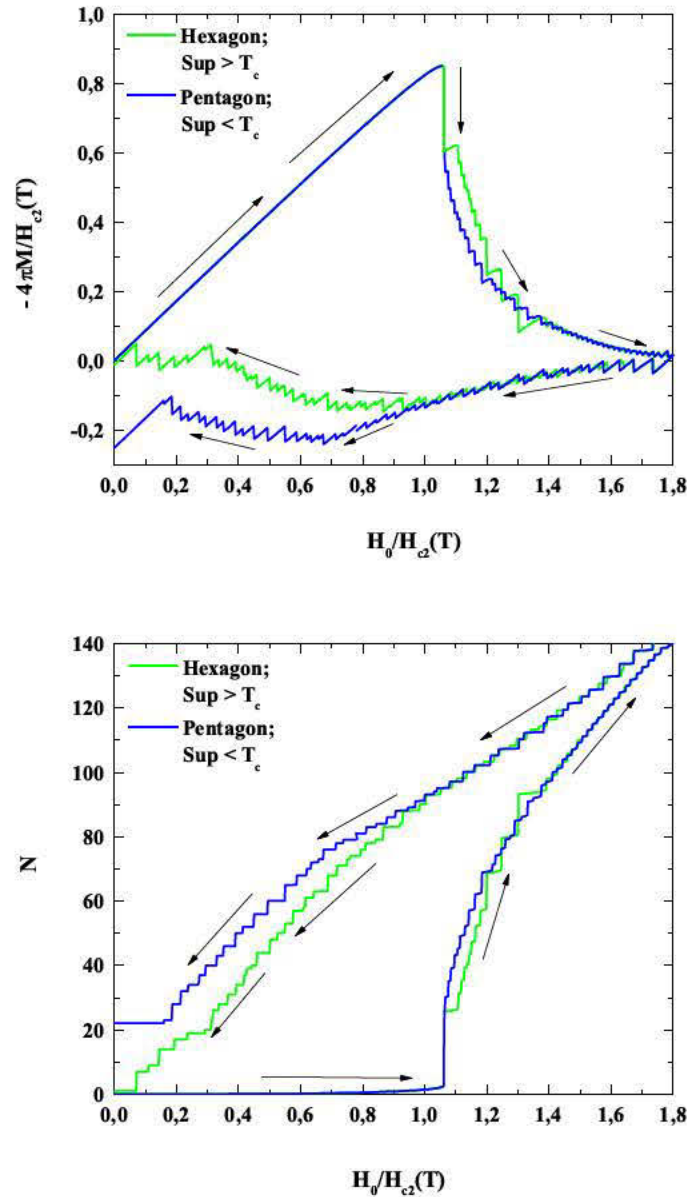t the vortices are pinned in the case of a pentagon defect at $H_0 = 0$. Now, in the interval $1.0556 > H_0/H_{c2} > 0.9542$, we can ensure that the number of vortices is similar (pentagon and hexagon cases, both in the down branch of the magnetic field) and from $H_0/H_{c2} = 0.9542$ $H_0 = 0$, the vorticity are different, as we can see in Fig. **5-2** (down), where the vorticity for the hexagon case is $N = 1$, while for the pentagon case $N = 22$ at $H_0 = 0$.

5.2.2 Cooper pair density and magnetic field distribution

Figure **5-2** is in a good agreement with Figs. **5-3**, **5-4**, **5-5** and **5-6**. It is easier to find the corresponding values in which the different transitions occurs. Additionally, it is possible to count the number of vortices in those figures, and compare it with the Fig. 2 (down). In this subsection, we analyses the vortex configuration, by using the results obtained from the numerical calculations for the Cooper pair density and the magnetic field distribution as a function of the applied magnetic field (increasing $\uparrow H_0$ to H_2 and then decreasing $\downarrow H_0$ to zero, Fig. **5-3** and **5-4**). In the two superior panels of the Fig. **5-3**, we can appreciate a multi-vortex state with $N = 24$ and $N_d = 4$ (N implies the number of vortex into the superconductor area, whereas N_d inside the defect) for $H_0/H_{c2} = 1.0619, 1.0623$ respectively. High (low) Cooper-pair density is given by red (blue) regions. Following the panels corresponding from the left to the right, the vortices adopt the form of a hexagon, remaining outside of the defect, but increasing H_0 the vortices can go into it. It can be explained due to the enhancement of the order parameter at the interface by choice the suitable superconductor with higher critical temperature to form the defect. N_d take values of $8, 10, 14$ for $H_0/H_{c2} = 1.1074, 1.1265, 1.2771$ respectively; is precisely in this last one, where we can observe a normal region outside of the defect, and when the force of vortex-vortex interaction overcomes the repulsive force exerted by the defect, the vortices can penetrate into the defect. Is interesting to analyze the behavior of the vortices when the magnetic field is decreasing, the vortices start to exit, as we can see in the second panel in Fig. **5-3**, from $H_0/H_{c2} = 0.6111$ to $H_0/H_{c2} = 0.0349$. The Fig. **5-3** indicates that the superconductor/defect interface can be easily tunneled, due to the order parameter suppression, from the defect to outside of it. The two panels in the bottom on Fig. **5-3** shows the plot of the magnetic field distribution in the sample, high (low) magnetic field is given by red (blue) regions. The red spots in the sample represent the nucleus of the vortices and the red regions at the surface of the sample, represent the compression of the magnetic field. Also is possible to find that the magnetic field distribution shown a correspondence with the cooper pair density in the same values of applied magnetic field H_0. In fact, even when only a few quanta of magnetic flux are nucleated into a mesoscopic sample, the vortex interactions
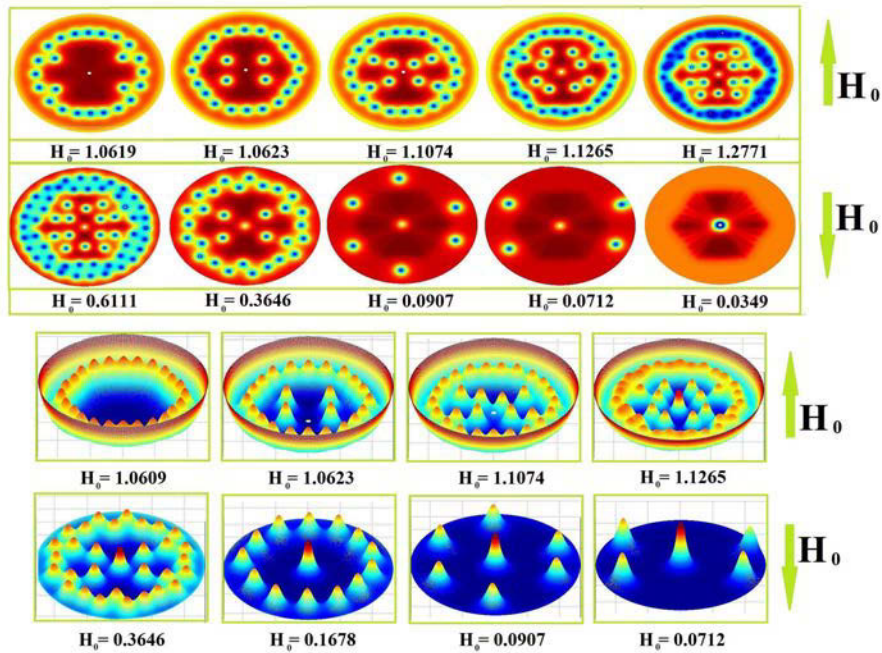
Figure 5-3: (Color online) Square modulus of the order parameter $|\psi|^2$ at the indicated applied magnetic field for a thin disk with an hexagonal defect at higher critical temperature (two superiors lines). Oblique view magnetic induction $\vec{h}$ (two inferior lines). ($\uparrow H_0$ ($\downarrow H_0$) the applied magnetic field is increasing (decreasing)

Figure 5-4: (Color on line) Square modulus of the order parameter $|\psi|^2$ at H_0 for a thin disk with a pentagonal defect at lower critical temperature (two superiors lines). Oblique view of the magnetic induction $\vec{h}$ (two inferior lines).

with other vortices and with the screening currents circulating around the boundary give rise to a variety of configurations such as multi-vortex states. These configurations are strongly influenced by both the geometry and size of the sample and defect. In the Fig. **5-4**, following the superior panel from left to right, at $H_0/H_{c2} = 1.0617$ the vortices "feel" the boundary of the pentagonal defect (at lower critical temperature), then the vortices go inside the defect at lower values of H_0, since that the order parameter in the defect frontier is suppressed, if the Figs. **5-3** and **5-4** are compared, as a consequence this region reach first the normal state than the rest of the disk (contrary than we note in Fig. **5-3**. So, the pinning effect in the down branch of the magnetic field is enhanced, see the second panel Fig. **5-4**. At $H_0/H_{c2} = 0.1419$ is possible to see the vortices caged in the defect despite the $H_0 = 0$, it can be noted also in the Fig. **5-2** (blue curve, for pentagonal defect at lower Tc) where at $H_0 = 0$ remain a negative value of the magnetization (Fig. **5-2** up) as well as a positive value of vorticity (Fig. **5-2** down). Notice that in the magnetic field distribution (two inferior panels Fig. **5-4**) the vortices move towards the center when the magnetic field is increasing. At higher magnetic field, individual vortices are no longer visible in the contour plots of the magnetic field distribution at $H_0/H_{c2} = 1.5777$. Also, at $H_0/H_{c2} = 1.5777$, the vortices are too close to each other and the spots corresponding are overlapping in the picture. How do the geometry of the defect influence in the vortex states? Fig. **5-3** and Fig. **5-6** shows,
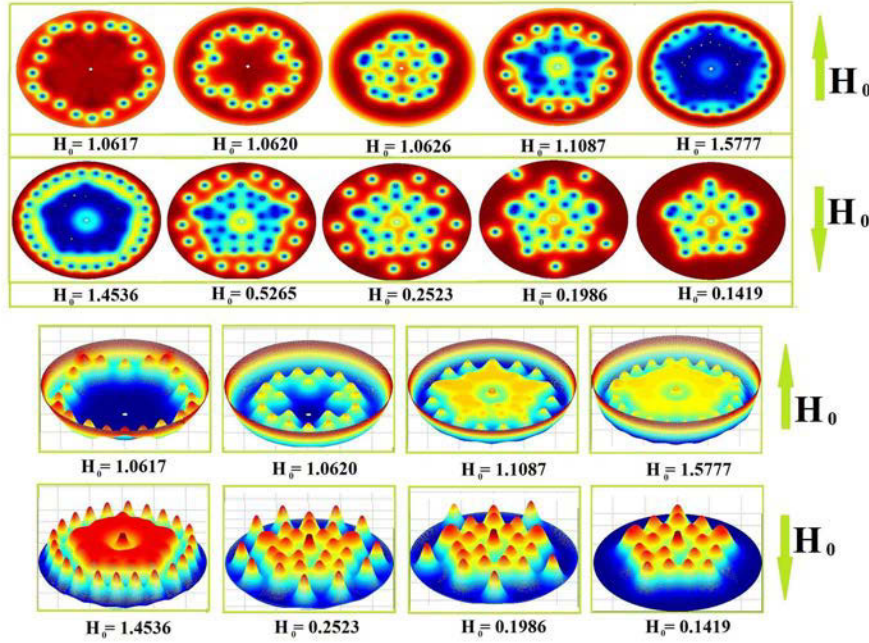
Figure 5-5: (Color online) Square modulus of the order parameter $|\psi|^2$ at H_0 for a thin disk with an hexagonal defect at lower critical temperature (two superiors lines). Phase of the order parameter (two inferior lines).

in both cases pentagonal and hexagonal defects are formed with a superconductor at higher critical temperature than the rest of the disk. We found that the number of vortices on the defect depends on its geometry. In the Fig. **5-3** (hexagonal defect) at $H_0 = 1.1256$ we see $N_d = 8$, and in the Fig. **5-6** (pentagonal defect) at $H_0 = 1.1577$, $N_d = 1$, just one vortex can penetrate the defect and this vortex remains from $H_0 = 1.1000$ to $H_0 = 1.1577$, which shown the influence of the geometric in the anti-pinning effect. The opposite situation occurs in the Figs. **5-4** and Fig. **5-5** for a defect at lower critical temperature respect of the rest of the disk, if we compared the panels at $H_0 = 1.0626$ and $H_0 = 1.0642$ the vortices entrance occurs first in the pentagonal case than the hexagonal case. It shown that the geometry of the defect has a clear effect over the force pinning in our system.

5.2.3 Phase of order parameter

In the Fig. **5-5**, we can appreciate that the vortices are caged in hexagonal disposition at $H_0 = 1.0606$ and the superficial superconductivity is reached at $H_0 = 1.3710$. Now, if we compare snapshots of two superiors panels of the Figs. **5-5** and Fig. **5-6**, for hexagonal and pentagonal case, respectively, a multi-vortex configuration can be maintained in the defect with $f(r, \theta) = 1.2$, regarding the defect where $f(r, \theta) = 0.8$, because the vortices entrance
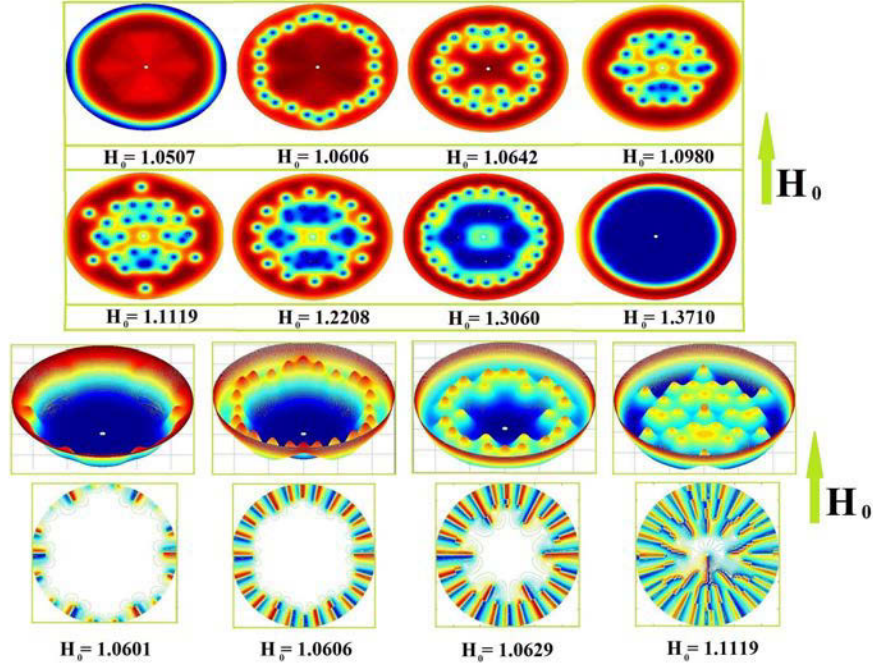
Figure 5-6: (Color online) Square modulus of the order parameter $|\psi|^2$ at H_0 for a thin disk with a pentagonal at higher critical temperature (two superiors lines). Phase of the order parameter (two inferior lines).

is more gradual in the up branch of the magnetic field, in the second case (Fig. **5-6**) that the first one (Fig. **5-5**). Is possible to note, comparing the snapshots at $H_0/H_{c2} = 1.3710$ in Fig. **5-5** that the normal state is reached in the center of the disk, whereas in Fig. **5-6** at $H_0/H_{c2} = 1.6078$ remain a multi-vortex state. This behavior can be confirmed watching the lower panels in Fig. **5-5** and Fig. **5-6**, due to that the phase of order parameter allows to determine the number of vortices in a given region and the fact that the phase of ψ varies by 2π in making a complete circuit, corresponding to the existence of a single flux quantum associated with the vortex. If the vorticity in this region is N, then the phase changes $\Delta\phi/2\pi$. The color code for values of the phase close to one are given by red regions and close to 2π by red regions. The discrete configuration of the vortices into the defect are found in pentagonal case (Fig.**5-6**) at higher values of H_0 than the hexagonal case (Fig.**5-5**) before the defect to reach the normal state.

5.2.4 Superconducting current density

When a superconducting sample is placed in an external magnetic field, the magnetic field is expelled from the superconductor due to screening currents near the sample boundary. The
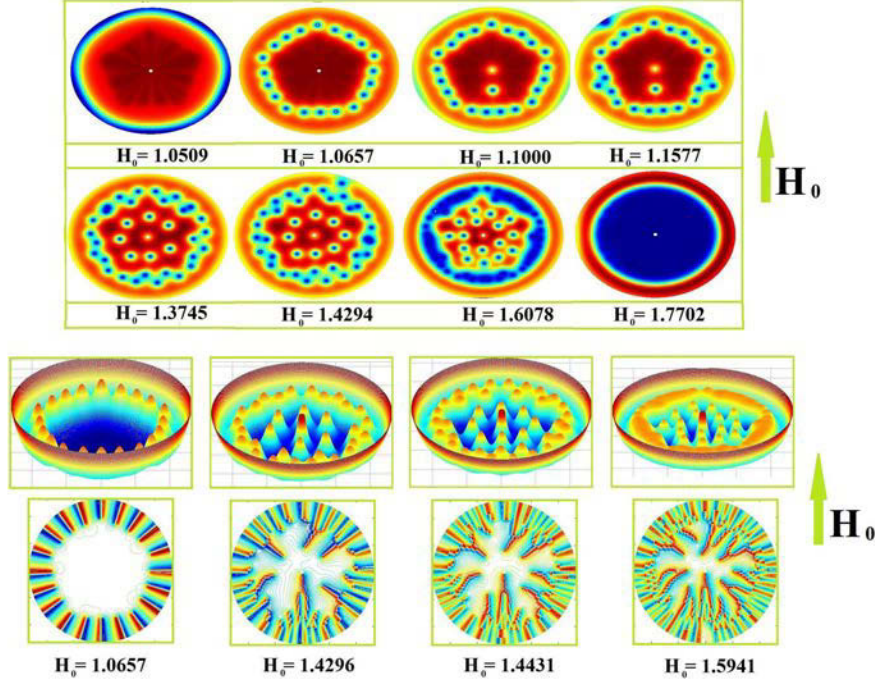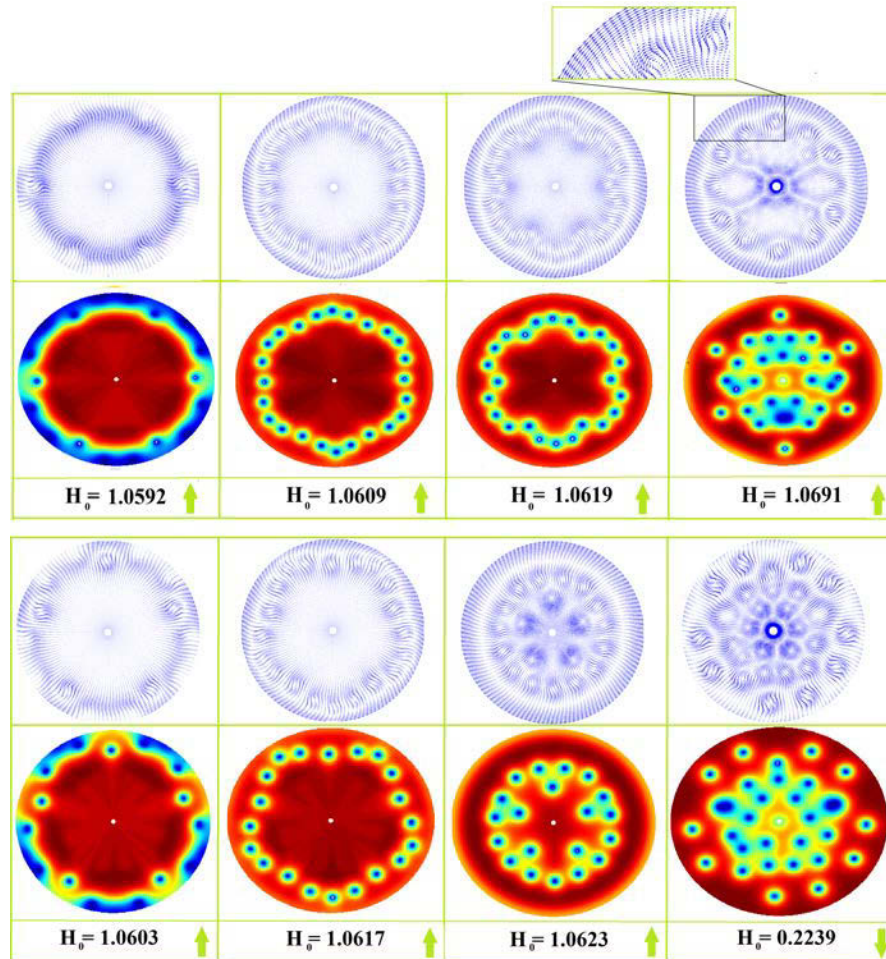
Figure 5-7: (Panel up) Square modulus of the order parameter $|\psi|^2$ at H_0 for a thin disk
with and hexagonal defect at higher critical temperature with the corresponding
simulation of the behavior of the super-current. (Panel down) Similar simula-
tion using a pentagonal defect formed by a superconductor of lower critical
temperature.
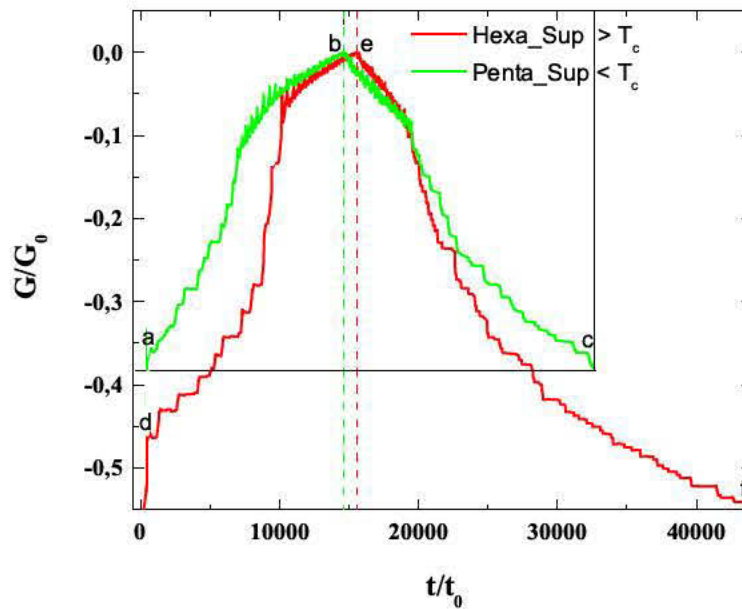
Figure 5-8: Free Gibbs energy loop as a function of the time t for a disk with hexagonal and pentagonal defect

direction of the screening currents is such that the corresponding magnetic field is opposite to the external one, which leads to a lower total field in the superconductor. The magnetic field penetrating the superconductor creates currents flowing in a direction opposite to the screening currents. The competition between these currents and the screening currents results in the existence of vortices. The Fig. **5-7** shows vector plots of the super-current in the superconducting disk with the conditions described in the caption, for selected vortex configuration (see in the panels of the Fig. **5-7**). In this figure, it is clear that the screening currents near to the boundary of the sample flow clockwise and the currents around the vortex in the center counter-clockwise. The magnitude of the current, is indicated by the length of the arrows, as we can see, it is not the same every where in the sample. We see in the superior panel of the Fig. **5-7** at $H_0/H_{c2} = 1.0691$ and in the inferior panel at $H_0/H_{c2} = 0.2239$ in the same figure, that when the vortices has entered in the respective defects, in the region between the two vortices the currents around these two vortices cancel each other out. Additional possible information one can obtain is about the presence of anti-vortices in the sample, looking for some spots in the figure, where the currents flow in clockwise direction. In order to understand the process of nucleation, we calculated the corresponding free energy for the whole system as a function of time (Fig.5-8). The results is a series of cusps as a function of time, each of which corresponding to a change in vorticity in the system. Furthermore, the magnetization curve is in agreement with the vorticity of the

superconducting system, which represents the diamagnetic variation in the sample. It is seen from Fig. **5-8** for green line that the critical fields $H_1/H_{c2} = 1.0104$ (a), $H_2/H_{c2} = 1.8000$ (b) and decreasing to $H_0 = 0$ (c) at the time $t_1/t_0 \approx 815$, $t_2/t_0 \approx 1436$ and $t_3/t_0 \approx 32544$ respectively, whereas for red line we obtain $H_1/H_{c2} = 1.0709$ (d), $H_2/H_{c2} = 1.8000$ (e) and $H_0 = 0$ (f) at the time $t_1/t_0 \approx 907$, $t_2/t_0 = 15564$ and $t_3/t_0 \approx 43776$ respectively. Additionally, the points (b) and (e) marks the peaks of the curves in which the free Gibbs energy is zero, this helps us to find the time used for the system to reach the normal state.

Conclusions

We investigated theoretically the influences of the centered geometrical defects formed by higher/lower critical temperature superconducting sample on the vortex configuration in a thin superconducting disk. We calculated the magnetization, Cooper pair density, magnetic field, super-current density and free energy as a function of time for hexagonal and pentagonal defects. The vortex lattice was different in the two geometries used due to the fact that it tries to adapt to the geometry of the sample. This influences considerably the stability range of the different vortex states. We also want to emphasize that the surface barrier generated by given $f(r, \theta)$ values, plays a crucial role for the pinning/anti-pinning effect, which not only accelerates the vortices to rush into the central area but also decelerates or even stops the vortex to escape from the defects due to the surface barrier.

5.3 Induced anisotropy by the inclusion of defects of variable T_c in a superconducting disk

5.3.1 Addendum to the theoretical formalism

We considered a mesoscopic superconducting disk with overlapped geometric defects in the presence of an applied magnetic field H (see Fig. **5-9**). The local critical temperature of the sample is changed spatially by inserting another kind of superconductor. This structure can be modeled by using a theoretical approach based on anisotropic GL formalism in the absence of external currents and the anisotropy is included in the functional through the parameter α, as $\alpha = \frac{1}{\gamma(r,\theta)}\alpha_0$, where this anisotrpy on α is effectively equivalent to T_c-anysotropy in the system. For $0 < 1/\gamma(r, \theta) < 1$ the superconductivity is strongly suppressed inside the defect and it attracts the flux domains, the function $\gamma(r, \theta) > 1$ in this case would correspond to $(1 - T/T_c)/(1 - T/T_{cw})$ with the lower critical temperature $T_{cw} < T_c$ (T_{cw} weaker critical temperature). Whereas in the case of $1/\gamma(r, \theta) > 1$ the defects interacts with the flux repulsively, the function $\gamma(r, \theta) < 1$ in this case would correspond to $(1 - T/T_c)/(1 - T/T_{cs})$ with the stronger critical temperature $T_{cs} > T_c$ (T_{cs} stronger critical temperature). The TDGL for the superconducting order parameter and vector potential is

written in the following form for a superconducting film:

$$\frac{\partial \psi}{\partial t} = -(i\nabla + \mathbf{A})^2 \psi + \psi \left(\frac{1}{\gamma(r,\theta)} - |\psi|^2 \right) \tag{5-3}$$

The Gibbs free energy and the magnetization are very sensitive to changes in the vortex configurations. Therefore, any important physical phenomenon must be manifested into this quantities. The TDGL equations describe the gradient flow for the Gibbs free energy. The energy, is given by:

$$G = \frac{1}{V} \int \left[|(-i\nabla - \vec{A})\psi|^2 + |\psi|^2 \left(\frac{|\psi|^2}{2} - \frac{1}{\gamma} \right) + \kappa^2((\nabla \times \vec{A})_z - H)^2 \right] dV \tag{5-4}$$

where the first term is the kinetic energy, the second term is the condensation energy, the third term is the field energy, and the parameter γ is the anisotropy, which only appears in the condensation term. We simulated a mesoscopic superconducting disk with two defects, one with area A_1 and another with area A_2. The pinning/anti-pinning is introduced as we illustrated in Fig. **5-9** (schematic view of the studied samples). We will assume a superconducting/vacuum external interface, and the configurations of this system are organized by cases and summarized in Table 1.
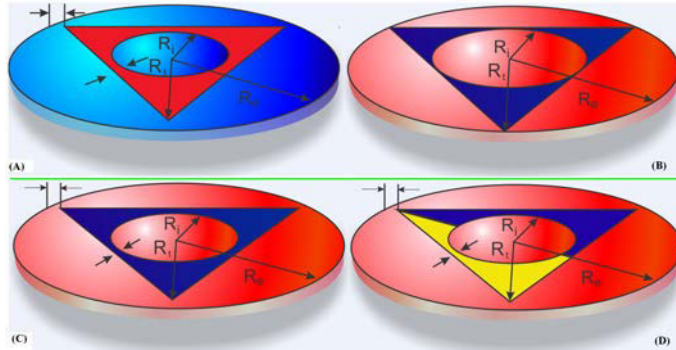
Figure 5-9: Layout of the studied sample: Type-II superconducting disk consisting of overlapped circular and triangular defects. The following lengths must be considered in order to establish the dimension of the disk and the defects: R_e (radius of the thin disk), R_t (length from the center of the disk to the vertex of the triangle), and R_i (radius of the circle inscribed on the triangle).

5.3.2 Magnetization, free energy and superconducting current density

In this section, we are interested in the behavior of the magnetization of the entire sample when the case of a circular defect overlapped onto a triangular defect with a different anisotropy is considered. This configuration creates a complex spatial disposition of the local

Tabla 5-1: Lengths and degree of anisotropy in the superconducting thin disk: Radius of disk R_e/ξ, length from the center of the disk to the vertex of the triangle R_t/ξ, radius of the circle inscribed on the triangle $R_i/\xi(0)$, and anisotropy in the triangle γ_T, in the inscribed circle γ_C, and outside of the triangle γ_{Ext}. In Case 4, two different anisotropies were selected: $1/\gamma = 0.8$ (left) and $1/\gamma = 1.2$ (right).

	R_e	R_t	R_i	$1/\gamma_T$	$1/\gamma_C$	$1/\gamma_{Ext}$
Caso 1	25.25	20.20	08.41	1.20	1.00	1.00
Caso 2	25.25	20.20	12.62	0.80	1.00	1.00
Caso 3	08.25	06.60	02.75	0.80	1.00	1.00
Caso 4	08.25	06.60	02.75	0.80-1.20	1.00	1.00
Caso 5	25.25	20.20	08.41	0.80	1.00	1.00
Caso 6	08.25	06.60	04.12	0.80	1.20	1.20

critical temperature T_c and opens up great possibilities for the control of the pinning/anti-pinning centers in order to enhance the possibilities of technological applications of this kind of superconducting sample for the design of useful devices. As is well known, the magnetization of the sample increases linearly with the applied magnetic field until $H \approx 0.90 H_{c2}(0)$, (Fig. **5-10**). It can be seen that the first entrance of the vortex occurs for different values of the magnetization. For $1/\gamma_{Ext} = 1.0$ (cases 1-5), this value is influenced by variations in the anisotropy inside the sample, as well as by its geometry [See Fig.**5-9**(B),(C) and (D)]. Furthermore, in case 6 ($1/\gamma_{Ext} = 1.2$), the magnetization appreciably shows the influence of the anisotropy of the sample (upper left). In Fig. **5-10**, the magnetization curve (blue line) shows the entrance of the vortices at $H \approx 0.925 H_{c2}(0)$, $H \approx 1.045 H_{c2}(0)$, and $H \approx 1.013 H_{c2}(0)$, which correspond to the vortex entrance to the superconducting sample, the triangle defect with anisotropy $1/\gamma_T = 1.2$, and the circle defect with $\gamma_C = 1.0$, respectively, a profile which is not typical. When the vortices enter the sample, the magnetization decreases, showing jumps, as expected in samples with anisotropy $1/\gamma = 1.0$ in the whole sample, but the result obtained with the inclusion of two defects with different critical temperature is reflected in the curves for every single case selected in this paper. Fig. **5-10** (rigth up) depicts the results of free energy as a function of the applied external field. This curve exhibited a series of discontinuities; each discontinuity signaled a vortex entrance and abrupt reductions in energy. Therefore, the number of vortices is related to the magnetization and free energy in which the system had the longest mixed state phase at zero temperature. Following this relation ($M = \frac{\partial G}{\partial H}$), the jumps of the magnetization curve show that the vortices are preferably situated inside the disk at $1/\gamma = 1.0$, as can be seen in the behavior of the blue line, until the saturation number of vortices is reached, and so the increased vortex-vortex interaction expels some of them into the defects with different values of γ. This is reflected in the curves [Fig. **5-10**(right up)] with larger jumps among smaller ones. [Fig. **5-10**(down)] depicts the values of the current density j normalized to
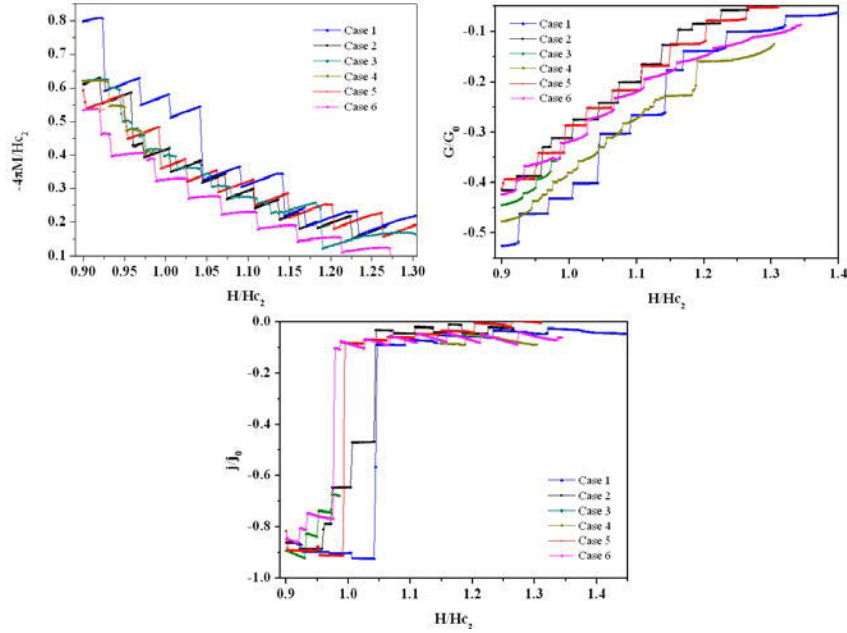
Figure 5-10: (Color online) (left up) Magnetization, (right up) free-energy and (down) su-
percurrent density, increasing the magnetic field for $A_1 \approx 214\xi^2$ cases 3,4 and
6 and for $A_2 \approx 638\xi^2$ cases 1, 2 and 5, (cases 1 - 6 in the Table 1).

its maximum value j_0, obtained by calculating for $H = 0.0$. We can infer that the negative
values of j are due to screening currents that flow clockwise around the sample and that
the variations in the curves under the same applied magnetic field show the existence of the
inhomogeneity of the superconductor. Therefore, it is possible that the current density is
larger in some regions where $1/\gamma > 1$ and the superconductivity is enhanced, but also it
is possible to find local suppressed superconductivity for $0 < 1/\gamma < 1$, which changes the
movement of every vortex and the pinning/anti-pinning center in the sample. The current
density distribution directly affects the number of vortices that first enter into the sample
as well as into the overlapped triangle and circle defects included in the superconducting
sample. In Fig. **5-11**, it is easier to find the corresponding values of the applied magnetic
field in which the different transitions occur, but also it is possible to count the number of
vortices in those figures and compare them. Nevertheless, it is easier to do in cases 3, 4, and
6 [Fig. **5-11**(right)] than in cases 1, 2, and 5 [Fig. **5-11**(left)], due to the fact that the area
is larger in these last cases.

5.3.3 Cooper pair density

Figs. **5-10** and **5-11** are in a good agreement with Figs. **5-12**-**5-17**. In this subsection, we
analyze the vortex configuration using the results obtained from the numerical calculations
for the Cooper pair density for the cases 1-6. Following the panels for each case (see Figs.

Figure 5-11: (Color online) Vorticity N as a function of the applied magnetic field H, for (left) $R_e = 25.25\xi$ (cases 1,2,5),and (right) $R_e = 8.25\xi$ (cases 3,4,6).

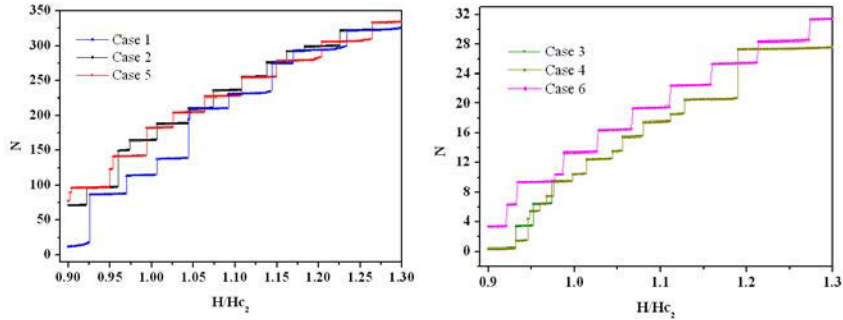**5-12** - **5-17**), at the first snapshot with $H = 0.0, N = 0$, we can see the variation of the anisotropy selected for every case, because in the simulations high Cooper pair density is depicted by red regions and low density by blue regions. Therefore, this can explain the enhancement/decrease of the order parameter spatially by choosing the suitable superconducting area with higher/lower critical temperature to form the defect using the desired entropy. In most studies of superconducting mesoscopic samples, the metastability of different vortex states results from competition between the vortex interaction with Meissner currents, which in most of the investigations represents the effect of the sample boundaries and the vortex-vortex interaction. However, when anisotropy is present in the sample, an additional, competing effect needs to be included in our analysis, taking into account the enhanced or reduced superconductivity in parts of the sample, where vortices are expelled or favorably reside, respectively. To begin with, we first consider a sample as in Fig. **5-12**, but now with $R_e = 25.25\xi$, $R_t = 0.8R_e$, $R_i = R_e/3$, $1/\gamma_T = 1.2$, $1/\gamma_C = 1.0$ and $1/\gamma_{Ext} = 1.0$. The results are summarized in the panels in Fig. **5-12**. As can be seen in these figures, the anisotropy in the circle inside the triangle is the same as outside of it. Despite the fact that the vortices penetrate the points of the boundary near the vertices of the triangular defect [according to panels (a) - (i)] until they saturate the disc outside the triangular defect, they do not penetrate the defect at the vertices, as commonly occurs in triangular superconducting samples [see panel (j)], but they do not remain inside it. There are enough vortices to expel some of them into the circle defect, owing to the lower-energy barrier for vortex entry there, considering that $1/\gamma_T > 1/\gamma_C$. Therefore, they feel that it is favorable to reside there in order to minimize energy [see panels (k)-(m)]. Regions with $1/\gamma = 1$ reach the normal state sooner for lower values of the applied magnetic field than when $1/\gamma = 1.2$ is used. In the discussion of Fig. **5-13**, we show that new vortex configurations can be obtained with suitable changes in the anisotropy and the size of the defect. Here, only the anisotropy in the triangular defect changes from a value of $1/\gamma_T = 1.2$, where the superconductivity is enhanced (values of $1/\gamma > 1$) to a value of $1/\gamma_T = 0.8$, in which area the superconductivity is reduced. In addition, the vertices of the largest defect on the sample are in contact with

CASE 1

(a) H = 0.0, N = 0 | (b) H = 0.901, N = 13 | (c) H = 0.908, N = 30 | (d) H = 0.918, N = 72 | (e) H = 0.922, N = 72

(f) H = 0.926, N = 74 | (g) H = 0.969, N = 97 | (i) H = 1.005, N = 113 | (j) H = 1.010, N = 140 | (k) H = 1.024, N = 140

(l) H = 1.050, N = 210 | (m) H = 1.082, N = 210 | (n) H = 1.092, N = 233 | (o) H = 1.130, N = 233 | (p) H = 1.140, N = 274
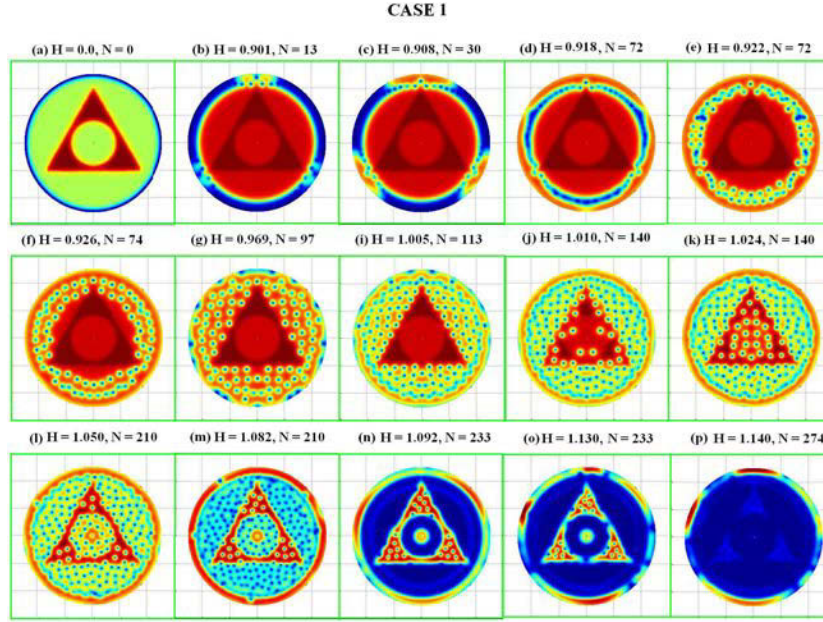
Figure 5-12: (Color online) Square modulus of the order parameter $|\psi|^2$ for a thin disk with $R_e = 25.25\xi$, $R_t = 0.8R_e$, $R_i = R_e/3$, $1/\gamma_T = 1.2$, $1/\gamma_C = 1.0$ and $1/\gamma_{Ext} = 1.0$. The shown vortex states are obtained by sweeping the magnetic field up in the considered field-range.

CASE 2

(a) H = 0.0, N = 0 | (b) H = 0.878, N = 3 | (c) H = 0.879, N = 4 | (d) H = 0.882, N = 33 | (e) H = 0.884, N = 33

(f) H = 0.885, N = 37 | (g) H = 0.886, N = 39 | (h) H = 0.888, N = 49 | (i) H = 0.889, N = 79 | (j) H = 0.958, N = 126

(k) H = 0.940, N = 132 | (l) H = 1.002, N = 164 | (m) H = 1.022, N = 187 | (n) H = 1.108, N = 258 | (o) H = 1.138, N = 275

Figure 5-13: (Color online) Contour plots of the Cooper-pair density for $R_e = 25.25\xi$, $R_t = R_e$, $R_i = R_e/2$, $1/\gamma_T = 0.8$, $1/\gamma_C = 1.0$ and $1/\gamma_{Ext} = 1.0$.
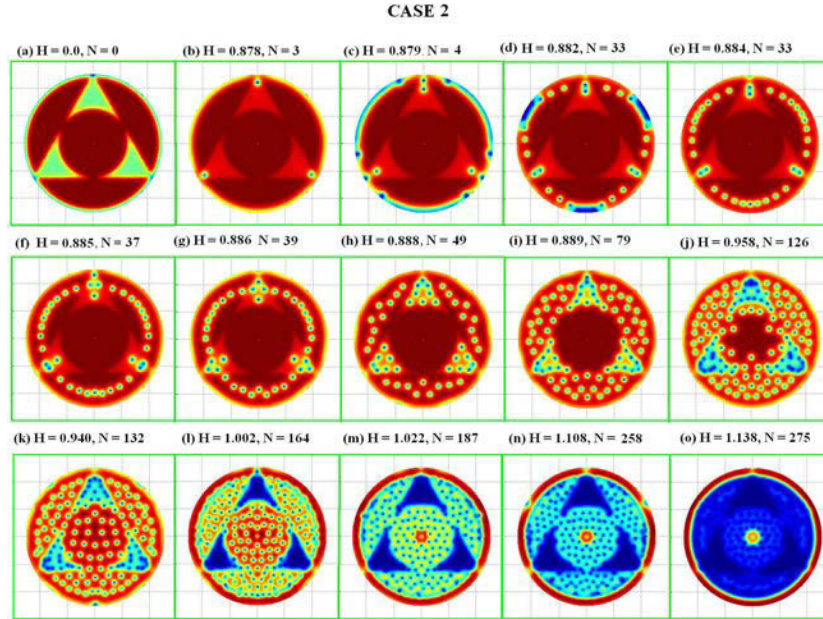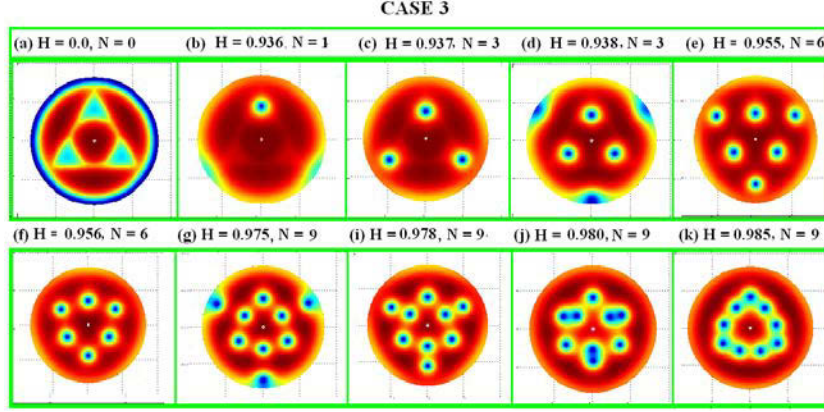
Figure 5-14: (Color online) Contour plots of the Cooper-pair density for $R_e = 8.25\xi$, $R_t = 0.8R_e$, $R_i = R_e/3$, $1/\gamma_T = 0.8$, $1/\gamma_C = 1.0$ and $1/\gamma_{Ext} = 1.0$.

its boundary, which did not happen in the previous analysis. In this case 2, the vortex entry into the defect is not through the triangle defect side, as takes place in case 1, because the vertices with anisotropy $1/\gamma_T = 0.8$ with weak superconductivity allow better conditions for vortex penetration into the disk, but also into the defect [see panel (b)]. This opens a new vortex configuration and pinning center. We can see in the snapshot of the order parameter [see panels (c)-(i)] that the vortices saturate the area of the defect first, before the rest of the disk, as we expect, due to the selected condition, but this also allows some regions to remain without flux entry for a higher applied magnetic field. Subsequently, increasing the magnetic field compresses vortices more toward the central defect, owing to the increasing Meissner currents at the sample boundaries, and finally the vortices penetrate into the region with anisotropy $1/\gamma_T = 1.0$ at $H = 0.958H_{c2}$ [see panel (j)]. In contrast to the previous case 1, the triangle defect reaches the normal state before the disk and the circular defect at the center of the superconducting sample [see panel (k)-(o)]. In Fig. **5-14**, we consider a reduction of the area of the entire sample, selecting a radius $R_e = 8.25\xi$ with conditions of the spatial distribution of the anisotropy similar to the previous case 2, but the vertices of the triangular defect are separated from the boundary of the superconducting disk. In summary, special vortex features are shown in Figs. **5-14** and Fig **5-15**, in which we considered a reduction of the area of the entire sample by selecting a radius $R_e = 8.25\xi$, with conditions similar to the spatial distribution of the anisotropy of the previous case 2, except that the vertices at the triangular defect are separated from the boundary of the superconducting disk. Additionally, in Fig **5-15** the triangular defect combines two halves with anisotropies $1/\gamma_T = 0.8$ (left half) and $1/\gamma_T = 1.2$ (right half). We can see in case 3 that the vortices penetrate through the points in the boundary near the vertices of the triangular defect, in which the superconductivity is reduced, similar to case 2 [see Fig. **5-14** panel (a)-(c)]. However, in this case the following vortices do not penetrate through the vertices; they do it through

the disk boundary in the direction of the sides of the triangular defect, due to the repulsion
exerted by the vortices already located in the vertices of the defect [see panel (D)]. These
three vortices finally enter and establish a minimal energy system configuration [see panel
(e)], created by the repulsion of the vortices initially in the defect and the shielding cur-
rents, which have a greater effect on the displacement and the final location of the vortices,
due to the reduction of the sample size, which is typical in mesoscopic samples, as we can
observe if we compare cases 2 and 3. We can also see in panel (f) that the increase of the
applied magnetic field moves the vortices towards the center until they adopt the triangular
form of the defect without penetrating the central defect and in this way give rise to the
entrance of three more vortices in the direction of the sides of the triangle formed by the six
previous vortices, due to the lower energy cost for entering in this direction rather than in
the direction of the vortices located in the vicinity of the disk boundary [panels (g) - (h)].
Finally, the screening currents force the vortices to adopt the shape of the triangular defects
at a higher applied magnetic field [panel (k)]. In Fig. **5-15**, we corroborate our analysis
by considering a superconducting sample with two anisotropies, $\gamma_T = 0.8$ and $\gamma_T = 1.2$ [see
panel (a)]. The first vortex penetrates the sample on the side of the disk with a reduction in
the superconductivity, and it has a greater area (bottom of the triangular defect) [see panel
(b)]. The next vortex avoids entering in the direction of the vortex previously anchored,
but also prefers access to the zone where the superconductivity is reduced. For this reason,
it makes its entry in the upper part of the triangular defect with $\gamma_T = 0.8$ [see panel (c)].
However, it is interesting to see that the next state does not show the input of the vortex in
the direction of the vertices of the defect area with anisotropy $\gamma_T = 1.2$, where the shield-
ing current is higher because there is a greater area with enhanced superconductivity, and
also as far as possible from the two previous vortices in the sample [see panel (e)]. As we
consequently expected, the defect with anisotropy $\gamma_T = 0.8$ reaches the normal state before
the region with anisotropy $\gamma_T = 1.2$. In Fig.**5-16**, we compare case 2 with case 5, changing
the area of both overlapped defects by considering a reduction of the radii from $R_i = R_e/2$
to $R_i = R_e/3$ and from $R_t = R_e$ to $R_i = 0.8R_e$, respectively. But the parameters related to
the anisotropy and the size of the sample is maintained. If we increase the applied magnetic
field under this configuration, the behavior is the same in which the vortex entrance occurs
through the vertices in the triangular defect and finally penetrates the central defect until
it reaches the normal state. Our results (shown in Fig.**5-16**) clearly demonstrated that the
change of the size of the defects does not appreciably disturb the behavior of the vortices and
their configurations in the different states. Nevertheless, we have to mention that there are
differences between the respective curves of magnetization, in which the jumps for the vortex
entrance occur at different magnitudes of the applied magnetic field, and at values similar
to the magnetization (cases 2 and 5). The free energy and supercurrent density also exhibit
a similar behavior, which shows the influence of the anisotropy selected for each mesoscopic
superconductor system selected for study (see Fig.**5-10**). Finally, in Fig. **5-17**, we compare
case 3 with case 6, changing the area of the circular defect by considering an increase in the
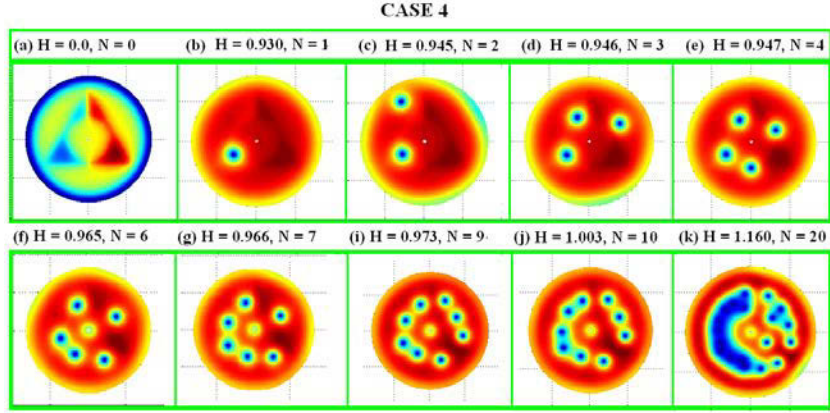
Figure 5-15: (Color online) Contour plots of the Cooper-pair density for $R_e = 8.25\xi(0)$, $R_t = 0.8R_e$, $R_i = R_e/3$, $1/\gamma_T = 0.8$ (left half of triangle), $1/\gamma_T = 1.2$ (right half of triangle), $1/\gamma_C = 1.0$ and $1/\gamma_{Ext} = 1.0$.

Figure 5-16: (Color online) Contour plots of the Cooper-pair density for selected vortex states for $R_e = 25.25\xi(0)$, $R_t = 0.8R_e$, $R_i = R_e/3$, $1/\gamma_T = 0.8$, $1/\gamma_C = 1.0$ and $1/\gamma_{Ext} = 1.0$.
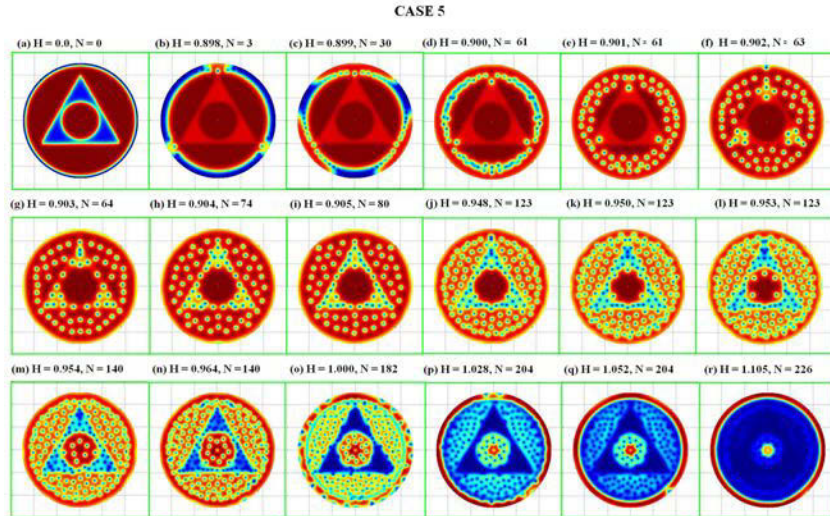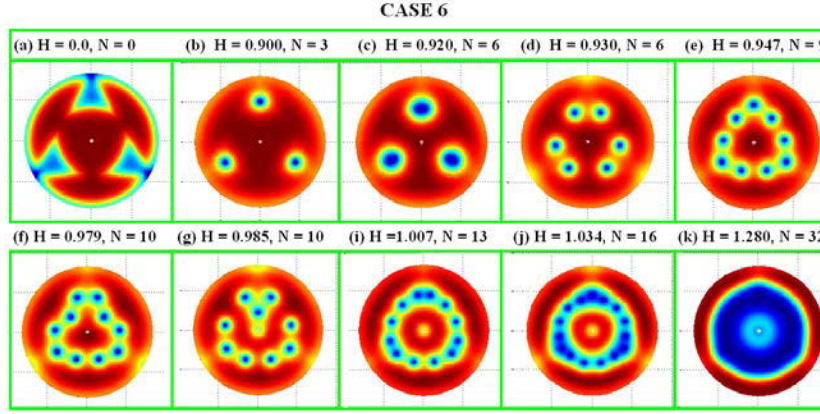
Figure 5-17: (Color online) Contour plots of the Cooper-pair density for selected vortex states for $R_e = 8.25\xi(0)$, $R_t = 0.8R_e$, $R_i = R_e/2$, $1/\gamma_T = 0.8$, $1/\gamma_C = 1.0$ and $1/\gamma_{Ext} = 1.2$.

radius from $R_i = R_e/3$ to $R_i = R_e/2$, as well as the anisotropy in the disk from $1/\gamma_{Ext} = 1.0$ to $\gamma_{Ext} = 1.2$ [panel (a)]. The increase of the anisotropy $1/\gamma_{Ext} = 1.2$ allowed two other vortices to penetrate through the vertices towards the area on the triangular defect after the first entry of vortices through the vertices [panel (b)], by completing two vortices at each corner of the triangle with anisotropy [panel (c)]. This did not occur in case 3, in which only one vortex penetrated through the vertices, while the rest did so in the direction of the sides of the triangular defect. Subsequently, the increase in the applied magnetic field separates the vortices by the repulsion generated by the imminent entrance of the vortices through each vertex, a behavior that shows a high-energy barrier that can confine the vortices to be situated on the defect, due to the influence of the anisotropy [panels (d),(e)]. Finally, we can see that the vortices continue entering through the points on the boundary disk in the direction of the vertices of the triangular defect until reaching the normal state [panels (f)-(k)]. All these complications of the defect geometry are interesting, because due to recent achievements in optics, it has become possible to exploit the interaction of light with superconductivity and create spatially periodic imprints on superconducting samples. Therefore, these findings open up avenues for future exploration of spatially engineered superconducting samples that allow achieving advanced functionalities. Also, it is possible to experimentally control the defect geometry and measurable properties of the vortex states.

Conclusions

We studied the properties of a mesoscopic superconducting thin disk with an array of overlapped triangular and circular defects with changes in T_c across the sample, which includes a spatially distributed anisotropy coefficient γ. Our first finding was that we showed the

great influence of the magnetization, free energy, and supercurrent density as a function of the anisotropy level and spatial distribution on the formation of geometrical defects, as well as on the changes in the size of the sample and on the triangular and circular defects. We found that the transitions to different vortex states can be suitably modified in order to obtain the desired states. Furthermore, we investigated the vortex configurations in the sample with two geometrical defects in order to establish a complex configuration of the spatial variation of the critical temperature T_c. We found that the energy barrier can be modified spatially in the sample by considering regions with lower/higher superconductivity and choosing anisotropy $(1/\gamma)$ greater than or less than 1, which can favor the entrance of the vortices into the defect or produce their repulsion. Therefore, this determines the competition, which results in the final vortex configuration, but with the help of the vortex-vortex interaction and the boundary of the sample.

5.4 Nanoscale superconducting condensate manipulation using a continuous wave laser

5.4.1 Addendum to the theoretical formalism

The superconducting structure exposed to a perpendicular magnetic field $\vec{H}$ that include regions of depleted superconductivity which is created by local heating, due to the system is affected by a continuous wave laser, it can be modeled by using a theoretical approach with the generalized time-dependent Ginzburg-Landau (TDGL) equation (Eq. 5-1)which is used to simulate the behavior of the superconducting condensate inside of pinning center (weak-superconducting regions) as well as in the rest of the sample. Where, the function $f(\vec{r})$ provides the regions where Ψ is depleted, which create the weak-superconducting for pinning center (or defect) with normal state $(f = 0)$ immersed in a superconducting state $(f = 1)$ at the rest of the sample, where its relation with the temperature is given through $f(\vec{r}) = \frac{(1-T_L/T_c)}{(1-T_s/T_c)}$, considering T_c as the critical temperature, T_L the temperature generated by CWL whereas T_s is the superconductor working temperature outside of the defect.

5.4.2 Cooper pair density

We studied the vortex structure of a superconducting film introducing artificial pinning centers changing locally the temperature of the sample, forming circular regions where an artificial defects is well established as we can see in Fig. **5-18**, as a strategy to trap quantum vortices and increase the value of applied magnetic that can be used until reach the normal state in the entire sample. It is well known that the regular triangular vortex lattice has the lowest energy in defect free superconductors, but the inclusion of defects where the superconductivity is diminished, the vortex-vortex repulsion starts to dominate in the sample. These competing interactions can be tuned controlling the number, size and shape
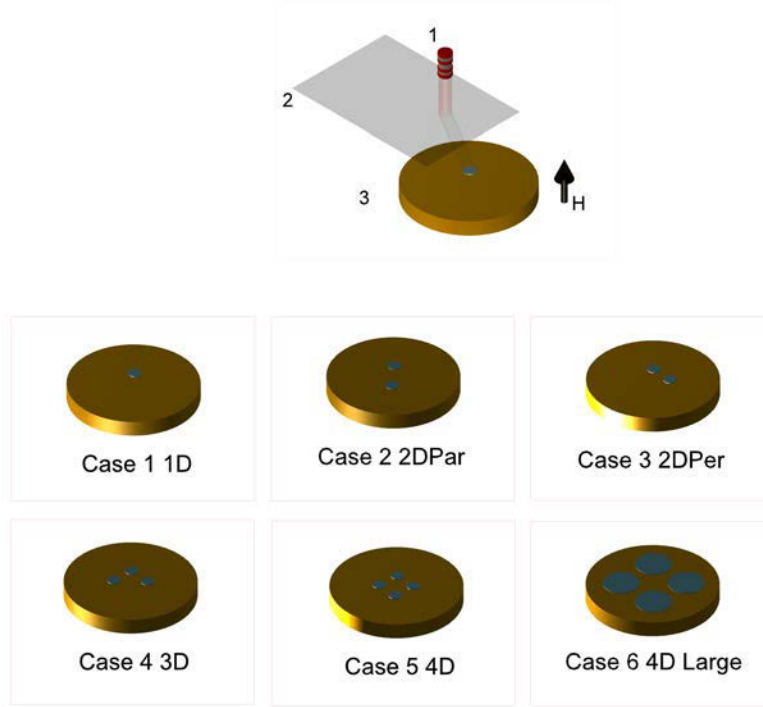
Figure 5-18: (Up) Suggested experimental setup to modify spatially the superconducting condensed, by using a 1. continuous wave laser (CWL) passing through a 2. mask to create the weakly-superconducting regions in the 3. sample with different sizes and shapes. (Down) Cases studied in this work: Case 1 (1D one defect), Case 2 (2DPar two defects parallel), Case 3 (2DPer two defects perpendiculars) Case 4 (3D three defects), Case 5 (4D four defects) and Case 6 (4D four defects larger)

of the defects which is possible to accomplish by using a CWL, as we showed in Fig. **5-19**, where the vortex configuration for selected values of applied magnetic field H_0 is showed, increasing the number and position of the defects for the experimental simulations. Following the panels for each case at the first snapshot with $H = 0.0$, we can see the normal regions generated locally by the CWL depicted by blue regions where the order parameter is $|\Psi|^2 \approx 0$ whereas the yellow one represents a value of Copper-pair density $|\Psi|^2 = 1$. Fig.**5-19** shows that the position of the defect encourages the entrance of the quantized flux in the vicinity of its location and subsequent entry of the vortices to the defect (see Case 1) until reaching its normal state at $H_0 \approx 1.380 H_{c2}$. This effect can also be evidenced by including an additional defect opposite to the center of the disk but as we expected the entry of the vortices is modified and also the vortex configurations obtained for each case. When we compare the obtained vortex configuration in each panel (Cases 1, 2, 3 and 4) at magnetic
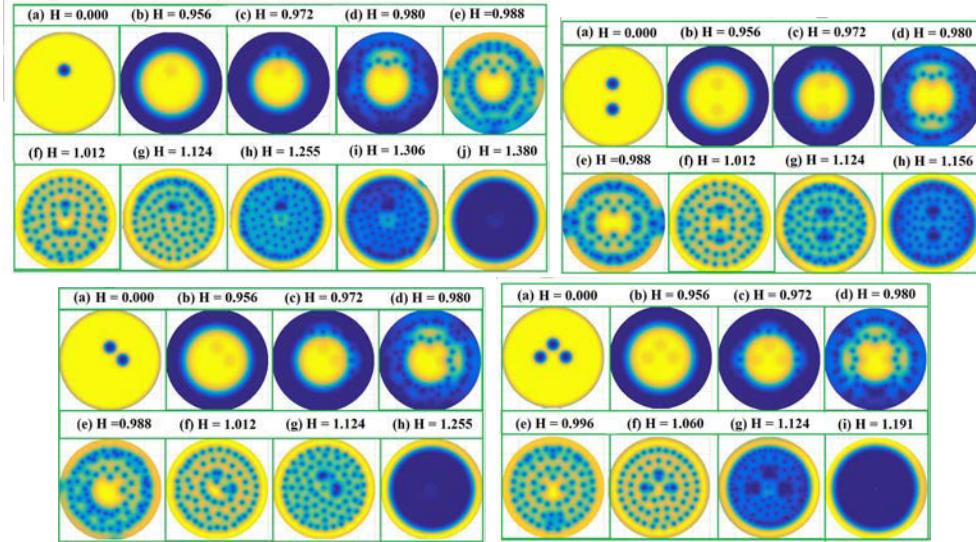
Figure 5-19: (Color online) Vortex configurations corresponding to selected states for following cases: Case 1 (1D one defect), Case 2 (2DPar two defects parallel), Case 3 (2DPer two defects perpendiculars) Case 4 (3D three defects).For each state, panels shows the Cooper-pair density of the vortices trapped in the weak-superconducting region formed where the CWL is pointing.

field $H_0 = 1.124H_{c2}$, we can see that the inclusion of a new defect increases the number of vortices from $N_{Case1} = 70$ to $N_{Case2} = 78$ (see Case 1 and Case 2), but for Cases 2 and 3 it is possible to see that at same value H_0 the position of the defects changes the number of vortices inside the sample $N_{Case2} = 78$ and $N_{Case3} = 72$. It is due to defects distribution that encourage the vortex penetration in two points at the boundary of the sample (up and bottom) [See Fig. **5-19**, Case 2 snapshot (d)], whereas the proximity between the defects could encourage the penetration only through one point [See Fig. **5-19**, Case 3 snapshot (d)]. Now, Fig. **5-19**, Case 4 snapshot (g) in which the inclusion of additional defect show a greater number of vortices inside the sample that almost a normal state is reached at the same value of applied magnetic field $H_0 = 1.124H_{c2}$ considered in the previous Cases. Next, we introduce a lattice of pinning centers which are formed by four defects and study their effect on the vortex configuration and critical parameters of the sample. The dimensions of the sample are the same as in Fig.**5-20**, but the radius of the defect in the Case 5 is $R = 4\xi$ whereas in Case 6 is changed to $R = 8\xi$. Knowing that the density of the superconducting Cooper-pair drops to zero inside the defects this favorate the vortex entry and with the increase of the size defects,the mutual repulsion of vortices is minimized into the sample and it encourage the vortex entry in the pinning centers, due to the strong screening (Meissner) currents running along the perimeter.
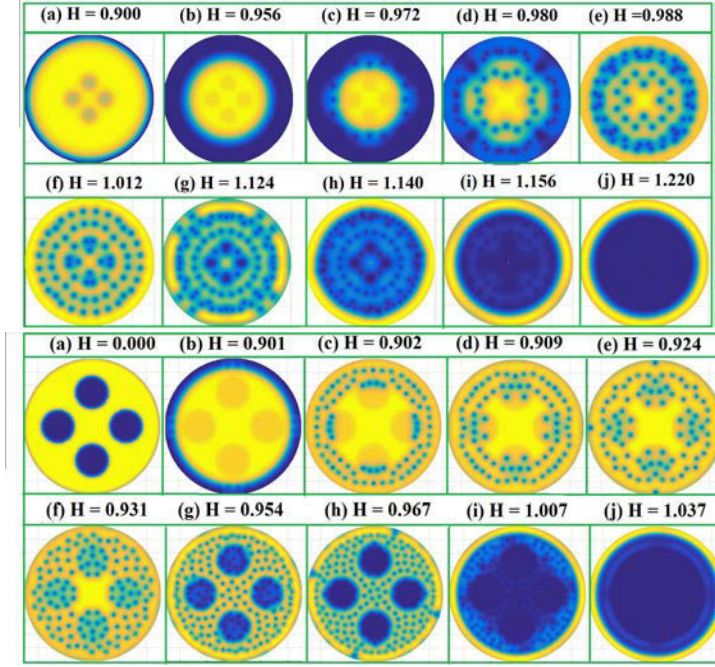
Figure 5-20: (Color online) Vortex configurations corresponding to increase the size of the defects. For each state, left/right panel shows the Cooper-pair density of the vortices trapped in the weak-superconducting region formed where the CWL is pointing for the considered cases: Case 5 (4D four defects) and Case 6 (4D four defects larger).

5.4.3 Magnetization and vorticity

The magnetization curves show corresponding discontinuities, as expected by using the theoretical approach the previous section we consider small superconducting disk with a circular defects distributed around the center with different sizes in several positions, generated by continuous wave laser. Therefore, in the process of sweeping up the applied magnetic field H_0, novel reactions of the material were found reflected in the differences where the jumps of the magnetization curves occurs comparing the Cases proposed in this study for greater values of the magnetic field, nevertheless, the behavoir of Meissner state that show the curves is the same until the first vortex entry (See Fig. **5-21** (a) and (b)) at $H_0 \approx 0,925$ where the sizes of the defects remains but the number of them as well as the positions change, which is reflected on the states at $H_0 \approx 0,972$ in Fig. **5-19** and snapshot (c) for every Case shows approximately the first vortex entry at same value of applied magnetic field, despite of the number of vortices entrance that change with the defects variations. The dimensionless magnetization, which is a direct measure of the expelled magnetic field from the sample, is defined as $\mathbf{M} = (\mathbf{h} - \mathbf{H_0})/4\pi$, where H_0 is the applied magnetic field and h is the magnetic field averaged over the sample and $\mathbf{h} = \nabla \times \mathbf{A}$, this expulsion depends on how much region
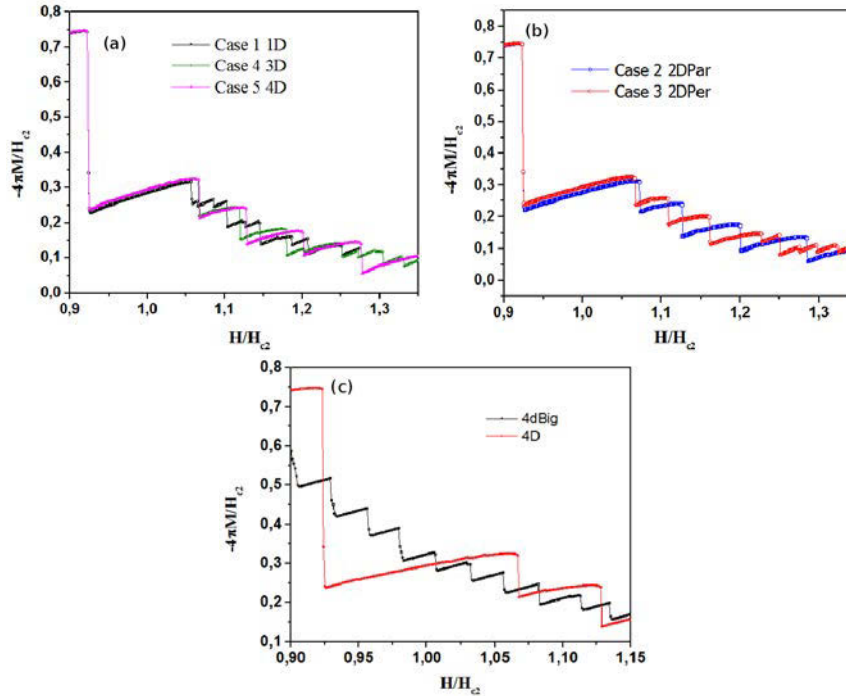
Figure 5-21: (Color online) Plot of the Magnetization as a function of the magnetic field for the cases compared on each of figures. (a) with Case 1 (1D one defect), Case 2 (2DPar two defects parallel) and Case 4 (3D three defects), (b) Case 2 (2DPar two defects parallel), Case 3 (2DPer two defects perpendiculars) and (c) Case 5 (4D four defects) and Case 6 (4D four defects larger).

of the sample is in the superconducting state, we see that for the case with major defects, the jumps are greater because this expulsion is smaller allowing a greater number of vortices to penetrate the sample [See red curve Fig. **5-21**]. On the other hand, we see that the smaller size of the defects causes a greater expulsion of the magnetic field causing a reduction in the number of vortices that the sample penetrates, resulting in smaller variations of the magnetization [See black curve Fig.**5-21**]. One of the most important contributions of this work focuses on the possibility of modifying the shape and size of the defect in the same superconducting sample without the need for a structural change due to the inclusion of metals, heavy ions, orifices, etc. In Fig. **5-22** we studied the magnetization in a superconducting sample with the inclusion of square defects [Fig. **5-22** (left)] and triangular [Fig. **5-22** (right)], in which the modification in the expulsion of the magnetic field can also be evidenced by including these changes. Fig. **5-22** shows that in both cases the transition from the Meissner state to the mixed state is achieved at approximately the same value of the applied magnetic field $H_0 = 1.03H_{c2}$ at point (b) of both curves, but the jump in the magnetization has a difference of 40%. Situation that is reflected also in the number of vortices that enter the sample as mentioned in the previous paragraph, but in this case is
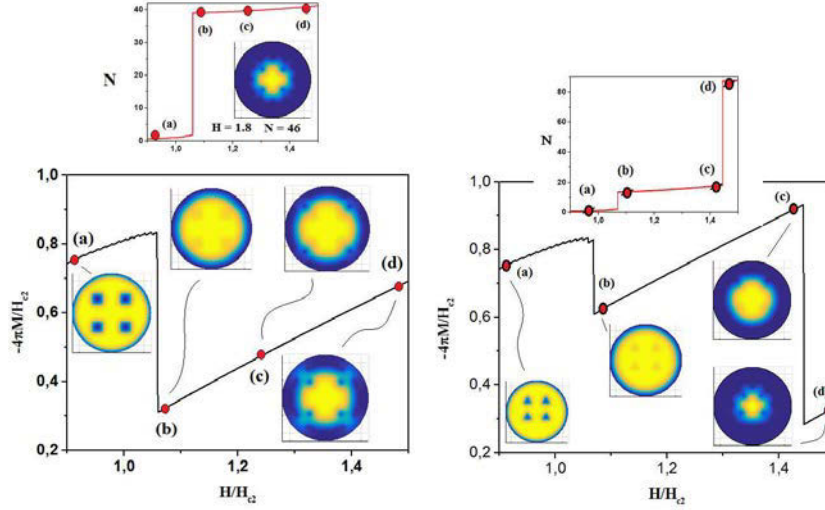
Figure 5-22: (Color online) Plot of the Magnetization and vorticity as a function of the magnetic field for two differents shapes of the defects. (Left) four square and (right) four triangular.

caused by the form of the defect, as we can see in the vorticity curves inset for each case [see Fig. **5-22** (left)], the number of vortices for the sample with square defects reaches almost $N = 40$ vortices, while in the case of triangular defects the value of the vorticity is $N = 19$ for the same $H_0 = 1.03 H_{c2}$ at point (b).

Conclusions

In summary, we have studied the superconducting array pinning of magnetic flux quanta by using a continuous wave laser (CWL) to obtain a nanoscale modulation of local temperature T. This creates an energy landscape for flux quanta, where the size and shape of weak-superconducting zones can be tuned over the same sample without any structural change even at any value of the applied magnetic field H_0. In addition to its fundamental interest, the possibility to manipulate flux quanta by designing the structure of superconducting condensate along the entire superconductor is relevant in view of applications. These include fluxtronic devices based on the controlled motion of flux quanta, for which the weak-superconducting zones is created also might be used for the fabrication of reconfigurable nanodevices based on versatility that offer the system proposed in this experimental simulation.

Publications.

The results presented in this chapter were published as:

- J. Barba-Ortega, J. D. González, and E. Sardella, *Complex Vortex Configuration in a Disk with a Higher/Lower Critical Temperature Superconducting Geometrical Central Defect*, Journal Low. Temp. Phys. **179**, 264 (2015).

- J. D. González, M. R. Joya and J. Barba-Ortega, *Induced Anisotropy by the Inclusion of Defects of Variable T_c in a Superconducting Disk*, Journal Low. Temp. Phys. **190**, 178 (2018).

- J. D. González, J. R. Bentrán and J. Barba-Ortega, *Weak links array generated by a continuous wave laser in a superconducting sample*, Optik - International Journal for Light and Electron Optics, **158**, 806 (2018).

6 Vortex matter in mesoscopic superconductor with nanoengineered thickness profile

We demonstrate the modulation of the superconducting condensate at nanoscale via control of the thickness over the surface. It yields a landscape for magnetic flux quanta due to the selected symmetry that allow, us to impose creation of vortex configurations, but also tune the critical parameters of the superconductor that can be effectively controlled. Our result suggests the possibility of modifying superconductivity of a thin film by exploiting well-controlled and thickness-dependent quantum size effects.

6.1 Introduction

Superconducting systems with artificial pinning centers have received much attention over the past decade. Due to the advances in lithographic techniques based on modern electron-beam and etching procedures one can design superconducting disks with different shapes and sizes of defects. These systems enable one not only to study possible vortex configurations, but also to get enough statistics to identify stable and metastable configurations of interacting vortices and consider the effect of the sample geometry on the final vortex state [61, 143]. These advances allow to propose almost any mesoscopic system for theoretical study and obtain their critical parameters, which determine the properties of the superconductor and its applications. This is of interest for fundamental physics, also for potential device applications in nanoelectronics [144, 145, 146, 147, 148]. The possibility to control the vortex density has made them one of the favorite experimental and theoretical systems for studies of the physics of solid state [149, 150, 92, 93, 82, 83, 84, 85, 151]. The configuration on the vortices in an external magnetic field is strongly influenced by the boundary conditions, we expect that different geometries of the central defects on the disk will generate different arrangements of vortices, allowing for the realization of exotic vortex configurations more stable than the conventional ones. In the case of a larger disk, the vortices are locate on a ring near the boundary, due to the confinement and Abrikosov-like lattice also may appear, but this configuration, is owing to the influence of sample geometry and it is diminished at a distance from the boundary [49].

The superconducting properties of the vortex state of samples with engineered manufactured defects as trench/holes or barrier/pillars have attracted a great deal of attention [152, 153]. The possibility to control the vortex density has made them one of the favorite experimental and theoretical systems for studies of the physics of solid state [82, 83]. It was observed that defects can strongly facilitate the control of vortices over the surface barrier and reduce the field penetration [88, 91]. Usually, pinning/anti-pinning centers and the Bean-Livingston surface barrier are considered to be competing effects that alternatively control the magnetic response in the vortex state. In previous works we studied the effect of weak circular, square and triangular trench on the vortex configurations in a circular geometry. We found that the lower and upper critical fields are independent of the geometry of the weak defect, due to weak pinning force. Also, we found that the vortex configurations are strongly influenced by the geometry of the defects on the sample [154, 155].

In this kind of heterostructures it is possible to demonstrate that the critical parameters of a superconductor can be manipulated and fine-tuned through nanostructuring [156]. Ghinobker $et.al$ predicts spontaneous generation of the magnetic flux inside the superconducting ring. Josephson weak links in the ring increase the magnitude of the spontaneously generated magnetic flux [157]. In the regime for conventional low temperature Type II superconductors, $\kappa > 1/\sqrt{2}$ samples with different geometries with/without structural/superficial defects surrounded by different materials have been studied theoretically [158]. The authors report a high dependence of the boundary conditions and the structural defects on the thermodynamics fields and superconducting electron density of the sample. Complicated pinning topologies of arrays of defects in superconducting micro-structures have been experimentally and theoretically studied. Several authors have shown that the critical magnetic fields, critical current and vortex configurations are dependent of the geometry/pinning force of the defects [159, 160, 161]. Kosterlitz and Thouless [162] have predicted that in two dimensional neutral superfluids a thermodynamic instability should occurs in which vortex-anti-vortex pairs spontaneously dissociate into free vortices, experiments on superfluid helium films apparently confirming this prediction [163]. V. R. Misko $et.al$ [160] found a thermodynamically stable vortex-antivortex pattern in mesoscopic type I superconducting triangles due to the change of the sign in the vortex-vortex and vortex-anti-vortex interaction forces when passing through the Bogomolny point ($\kappa = 1/\sqrt{2}$), combined with the condensate confinement by the boundary of the mesoscopic triangle.

The Bogomolny point $\kappa_c = 1/\sqrt{2}$ was introduced originally in string theories, where at critical temperature it marks the border between ideally diamagnetic bulk type-I superconductors and type-II ones that can host vortices. At this point the superconductivity exhibits properties different from the usual superconductors [164]. The possibility of modifying the properties of superconducting samples inserting structural defects in the superconductor or/and controlling the sample boundary conditions has made from nano and mesoscopics systems one of the more popular experimental and theoretical system for studies of the physics of solid state. Berdiyorov $et.$ al investigated the phase boundaries for square sam-

ples containing several anti-dots in the presence of a uniform perpendicular magnetic field, they found that the phase of these structures reveals an oscillatory behavior caused by the formation of vortex configurations in these pinning anti-dots. In previous works, we show that under an appropriate construction of the superconducting boundary, a type-II superconducting disc may behave like a type-I and that the thermodynamic critical fields, magnetization, free energy and vorticity, depend on the chosen boundary condition. The effect of the geometry of a square and triangular trench on the thermodynamical properties of a superconducting disk with a central hole was studied. Our results have shown that the vortex state depend strongly of the geometry of the trench at low magnetic fields. Finally, the superconducting state in a small Type II superconducting square with a central square pillar of different area was analyzed in a recent work. A novel vortex configurations as a function of magnetic field was found.

The study of superconducting properties in this kind of heterostrustures takes a particular importance for potential applications, such as the fabrication and development of microwave circuits, and SQUIDs [165, 166, 167]. In 2007, Brandt and Mikitik [168] studied what is known as the shaking effect, considering an inclined DC magnetic field and a small AC field applied parallel to the plane of a superconducting thin film. Thus, they obtained an anisotropic relaxation of the internal field and sheet currents over the sample. Several authors described the distribution of the internal field and the sheet currents in films shaped in the so-called SQUID geometry, employing some variations for the cross section of the sample [169, 170, 97]. The confinement on the superconducting condensate inside the samples can be controlled using the deGennes extrapolation length b in the boundary conditions described by Ginzburg-Landau theory (GL) [92, 93]. The GL theory has been proven to give a good account of the superconducting properties in samples of varies geometries, e.g, disks with finite height and spheres [171, 172], shells [173] on cone [174]. Experimentally was demonstrated that active and passive superconducting thin-film devices can be used as very sensitive tools for detecting motion and penetration of vortices in superconducting material and that the analysis of the local distribution of vortices in the devices can be used for optimization of device properties [175, 176, 177].

This chapter is organized as follows. Sec.6.1. Introduction. Addendum to the theoretical formalism is presented Sec.6.1.1. In Sec. 6.2. We solved the time dependent Ginzburg Landau (TDGL) equations for a large disk with radius $R_e = 26\xi$ in presence of a magnetic field and central defects are considered. The magnetization, magnetic induction, vorticity and Cooper pair density are calculated. We found an interplay between surface and strong pinning/anti-pinning centers and the vortices are arranged by the defect geometry, which vortex configuration more energetically stable and the sequential transition of different vortex states occurs with increasing magnetic field. In Sec. 6.3. We consider an interplay between surface and strong pinning/anti-pinning centers. We calculate the magnetization, free energy, vorticity and Cooper pair density for a thin disk with a central hole containing one pentagonal or hexagonal trench (or barrier). Also we consider the deGennes parameter $b \to \infty$ and $b = 0$.

In Sec. 6.4. We study the superconducting state for a mesoscopic sample with a central anti
pinning center (dot) in presence of a magnetic field applied perpendicular at this surface.
The goal of our work is found an interesting spontaneous anti-vortex states generation with
a posterior vortex-anti-vortex annihilation at determined magnetic field. In Sec. 6.5. We
study the vortex matter profile, Gibbs free energy and magnetization for a circle with a hole
at the center connected to the outside vacuum through a very thin slit with angular width.
We have also studied the influence of a metallic or superconducting material in contact
with the sample on the first vortex entry field of the superconducting sample. According to
angular width of the slit and the boundary conditions we show that the diamagnetic nature
of the sample can be considerably enhanced. Our results are summarized in each Section.

6.1.1 Addendum to the theoretical formalism

We consider a superconducting film (of thickness $d \ll \lambda, \xi$) with several geometrical shapes
in the presence of a perpendicular uniform magnetic field For the given system we solved
the nonlinear GL equation averaged over the sample thickness, which can be written in
dimensionless units in the following form [178, 179, 180, 181, 182, 147]:

$$\frac{\partial \psi}{\partial t} + \frac{1}{g} \left(i\boldsymbol{\nabla} + \mathbf{A}_0\right) \cdot g \left(i\boldsymbol{\nabla} + \mathbf{A}_0\right) \psi - \psi + \psi^3 = 0. \tag{6-1}$$

where $g(r, \theta)$ is just a function which describes the thickness of the sample. In this case,
the magnetic field can be taken nearly uniform inside the superconductor $\mathbf{H}_0 = \boldsymbol{\nabla} \times \mathbf{A}_0$,
so that second GL equation does not need to be solved. In Eq. (6-1) dimensionless units
were introduced as follows: $|\psi|$ is the order parameter in units of $\psi_\infty(T) = \sqrt{-\alpha(T)/\beta}$,
where $\alpha(T)$ and β are two phenomenological constants; lengths in units of the coherence
length $\xi(T)$; time in units of $t_0 = \pi\hbar/8K_BT_c$; $\mathbf{A}$ in units of $H_{c2}(T)\xi(T)$, where $H_{c2}(T)$ is
the second critical field, temperature in units of the critical temperature T_c, supercurrent
density $\mathbf{J} = \mathrm{Re}\left[\bar{\psi}(-i\nabla - \mathbf{A})\psi\right]$ in units of $J_0 = \hbar c^2/8\pi e\xi$; Gibbs free energy G in units of
$G_0 = H_{c2}^2 V/8\pi$, $\lambda(T)$ is the penetration depth.

6.2 Influence of 3D artificial defects on vortex lattice in a large mesoscopic superconductor

Let a thin superconducting disk of thickness d and radius $R_e = 26\xi \approx 1\mu m$, with $|z| < dg(r, \theta)$, for all (r, θ); $g(r, \theta)$ is a function which describes the thickness of the sample. However, in the former case, κ is replaced in the by the Ginzburg-Landau parameter $\kappa_{eff} = \kappa^2 \xi/d$.
Largest unit cells lengths were $a_r = R_e/N_r$ and $a_\theta = 2\pi/N_\theta$, taking $N_r = N_\theta = 128$ as
the number of cells in the r and θ directions respectively (polar coordinates). We take
$\kappa_{eff} = 0.8854$, which is a value for a thin disk of Nb with thickness $d \approx 45$ nm, where $\xi = 38$
nm, $T_c = 9.2K$, $\kappa = 1.02$, $\eta = 1$ and $T = 0$. Numerical limitations arise in the choice of

Figure 6-1: Layout of the studied sample: Superconducting disk with a central defect, hole (right) or barrier (left), for circular (up) or triangular (down) case. With a superconductor/vacuum interface.

the time step due to the forward-Euler treatment of the Ginzburg Landau equations. A practical rule for time step selection is:

$$\triangle t \leq \left[\frac{(a_r a_\theta)^2 \eta}{2(a_r^2 + a_\theta^2)}, \frac{a_r a_\theta)^2}{2(a_r^2 + a_\theta^2)\kappa^2}\right] \tag{6-2}$$

Then, we choose to increase the value of the applied magnetic field each $\triangle t = 0.01$.

Let us now turn to the presentation of the results that arise from the numerical solution of GL equation. We are interested only in the vortex configurations and the choice of geometrical defects is adequate for this purpose. The disk and circular defect areas are $A_D = 26^2 \xi^2 \pi = 2124\xi^2$, and $A_C = 7^2 \xi^2 \pi = 154\xi^2$ respectively; while the bisector of triangular defect is 6ξ with a area $A_T = 49\xi^2$. We consider $g(r, \theta) = 1$ everywhere, except at defects position in the disk which are simulated by using $g = 0.8$ for the hole and $g = 1.2$ for the barrier, see Fig. **6-1**. The issue here is to determine which geometric defect is the suitable to find the pinning or anti-pinning effect and its interplay with the applied magnetic field. It should be detectable through all the order parameter, the magnetic induction, and the magnetization. Initially, we analysis the magnetization versus the external applied magnetic field, the curves shown in Fig.**6-2** (up) for large disk with circular defects (barrier and hole) and thin disk, while triangular case is shown in Fig. **6-3**(up). Both samples exhibit the first clear jump at the field $H_0 = 1.0350H_{c2}(0)$ and $H_0 = 1.0309H_{c2}(0)$, respectively, corresponding to the first entrance of vortices into the sample. We can see that the value of the field for the first vortices entrance is approximately the same, while for the second vortex entry, we found differences in the location of peaks (see inset) in Fig. **6-2**(up) and Fig. **6-3**(up). Additionally, we can see despite the first vortex entry the field H_1 is almost the same value. The Fig. **6-2** (down) and Fig. **6-3** (down) shows differences in the number of vortices entering at $H_0 \approx 1.0329H_{c2}(0)$, snapshot (Insets) shows the values of vorticity for circular defects as follow $N = 135, 121, 116$ corresponding to the hole, thin disk and barrier defects, respectively. While for triangular defects, the snapshot show $N = 131$ and $N = 119$ for hole and barrier. It is possible to
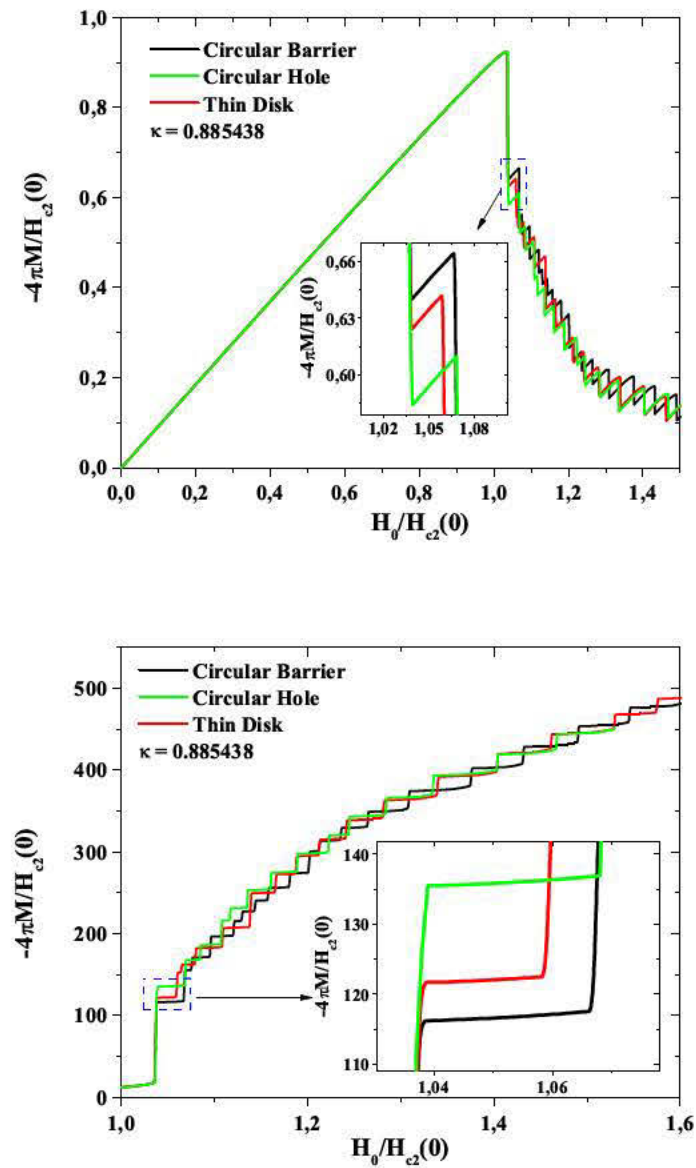
Figure 6-2: Magnetization curve (up) and vorticity N (down) as a function of the external applied magnetic field for a large disk with circular defects: hole (green curve), barrier (black curve), and thin disk (red curve). (Insets) Enlarged snapshot of the second entrance of vortices.
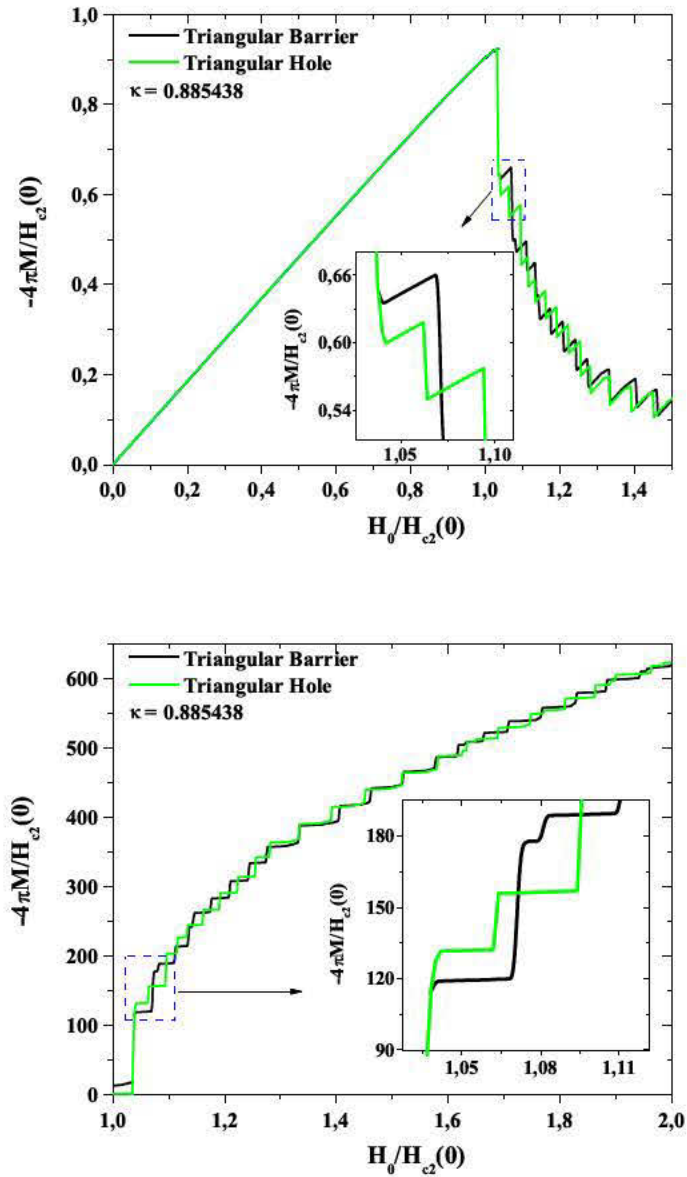
Figure 6-3: Magnetization curve (up) and vorticity N (down) as a function of the external applied magnetic field for a large disk with triangular defects: hole (green curve), barrier (black curve). (Insets) Enlarged snapshot of the second entrance of vortices.
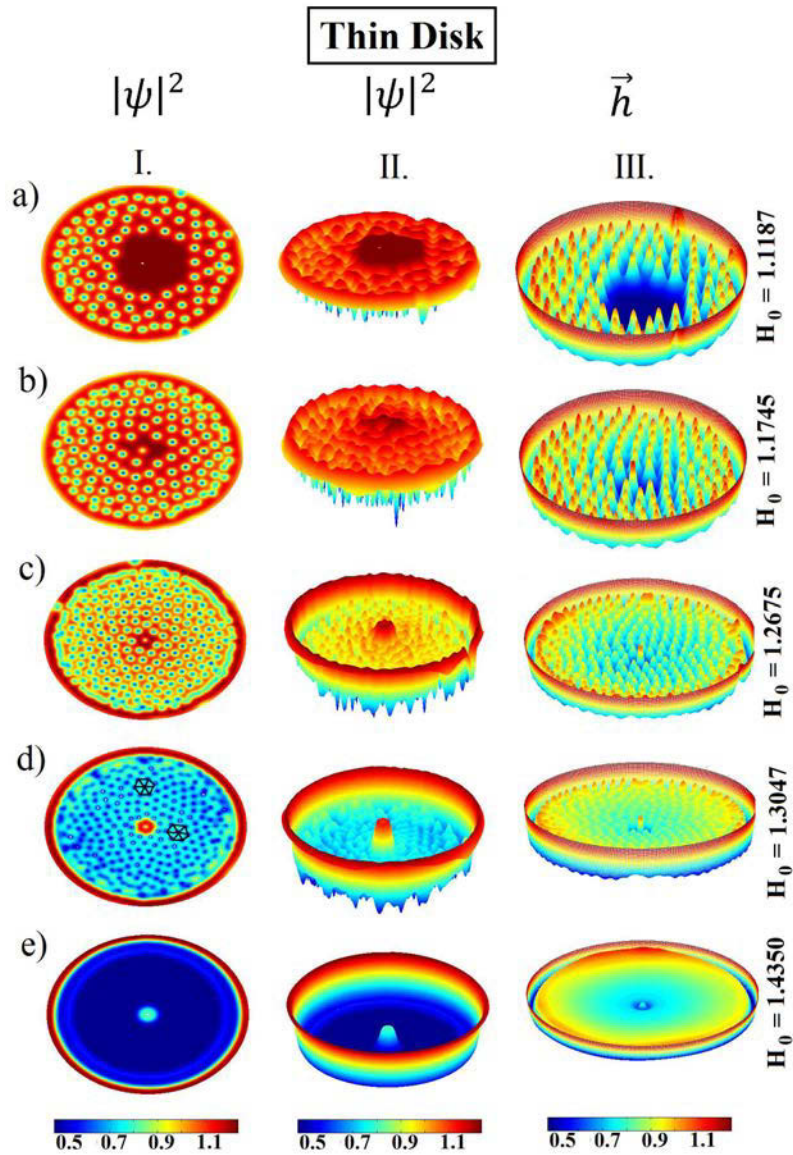
Figure 6-4: (Color online) The vortex structure in the indicated magnetic field for a thin disk with a central perforation with radius $r_0 = 0.31\xi(0)$. I. Square modulus of the order parameter $|\psi|^2$, II. Oblique view of $|\psi|^2$, III. Magnetic induction $\vec{h}$.

.

observe the correlation between the vorticity N and the defects used for this simulation, in which the value of N decrease, because the barrier defect generate greater opposition to the vortices entrance, while the opposite occur with the thin disk and hole defect.   It is well known that vortices nucleate at the boundary of the sample, additionally, the interaction among vortices, which are just nucleating at the surfaces form somewhat deformed lattice structures and Abrikosov lattice for some values of H_0, Fig. **6-4** column I line d).   The first and second columns in Figures **6-5**− **6-8** represent the cooper-pair density and the columns III are contour plots of the magnetic induction. Blue and/or red regions indicate high and/or low Copper pair density/induction, i.e. in Fig. **6-5** column II line c) in which the red color in the center of the barrier is degraded until blue on the bottom, as well the Copper pair density decrease similar to the magnetic induction in the column III line c). Fig. **6-5** and **6-6** shows the vortex configuration increasing the applied magnetic field and the differences when is barrier or hole circular the defect used in the numerical simulation. We find relevant differences in both cases, at $H_0 = 1.1187 H_{c2}$, shown in line a) the vortices are extended at larger area of the disk, including into the hole, comparing with the barrier case in which there is not vortices, thus, the pinning state is obtained first using a hole defect as we expected and, furthermore, in line b), $N_d = 10$ in the hole whereas none vortex has entered into the barrier, but the force of vortex-vortex interaction overcomes the repulsive force exerted by the barrier and the vorticity obtained is $N = 7$ (see Fig. 5 line c) with $H_0 = 1.3233 H_{c2}$), while in hole defect case $N = 15$ (see Fig. 6 line b) with $H_0 = 1.1615 H_{c2}$). The snapshot of the magnetic induction in both figures in line a) show that the blue color is centered on the disk and this confirm the Meissner effect on the circular defects, so its behavior is like type I superconductor. However, when the field reaches great values the vortices penetrate the defects and the peaks of magnetic induction can even be counted, so the defects reached its state as type II superconductor. For $H_0 = 1.3605 H_{c2}$ the line e) show a new vortex configuration into the barrier with $N_d = 14$, the vortices are positioned separately as much as possible and this is being located between the vortices, this due to the geometry of the circle and the lowest possible energy state that must be achieved by the system. On the other hand, in line e) (Fig. **6-6**) the hole defect is found in normal state, and the magnetic field has penetrated completely as we can see in the magnetic induction, in addition, Abrikosov lattice is found in this case at $H_0 = 1.3047 H_{c2}$. Notice the same behavior for barrier case in line b) at $H_0 = 1.2547 H_{c2}$. Finally, in line f) at $H_0 = 1.4163 H_{c2}$ the disk is completely in normal state (Fig. **6-6**), while a little central region remain in superconductor state (Fig. **6-5**) at $H_0 = 1.3977 H_{c2}$. In the following, we analyzed a superconducting disk with triangular defects and consider their area smaller than the circular defects discussed above. However, the pinning effect produce a different behavior in this case. Fig. **6-7** and **6-8** exhibit the vortex structure for barrier and hole in large disk, as shown in line a) at $H_0 = 1.0350 H_{c2}$, but we can see that in the defect barrier at $H_0 = 1.1187 H_{c2}$ there is no penetration of vortices while for the case hole at $H_0 = 1.0536 H_{c2}$ the vortices remain in the defect, spite of difference of values of magnetic field applied. Throughout the whole simulation, the pinning

Figure 6-5: (Color online) The vortex structure in the indicated magnetic field for a disk with a circular barrier centered. I. Square modulus of the order parameter $|\psi|^2$, II. Oblique view of $|\psi|^2$, III. Magnetic induction $\vec{h}$.

Figure 6-6: (Color online) The vortex structure in the indicated magnetic field for a disk with a circular hole centered. I. Square modulus of the order parameter $|\psi|^2$, II. Oblique view of $|\psi|^2$, III. Magnetic induction $\vec{h}$.

Figure 6-7: (Color online) The vortex structure in the indicated magnetic field for a disk with a triangular barrier centered. I. Square modulus of the order parameter $|\psi|^2$, II. Oblique view of $|\psi|^2$, III. Magnetic induction $\vec{h}$.
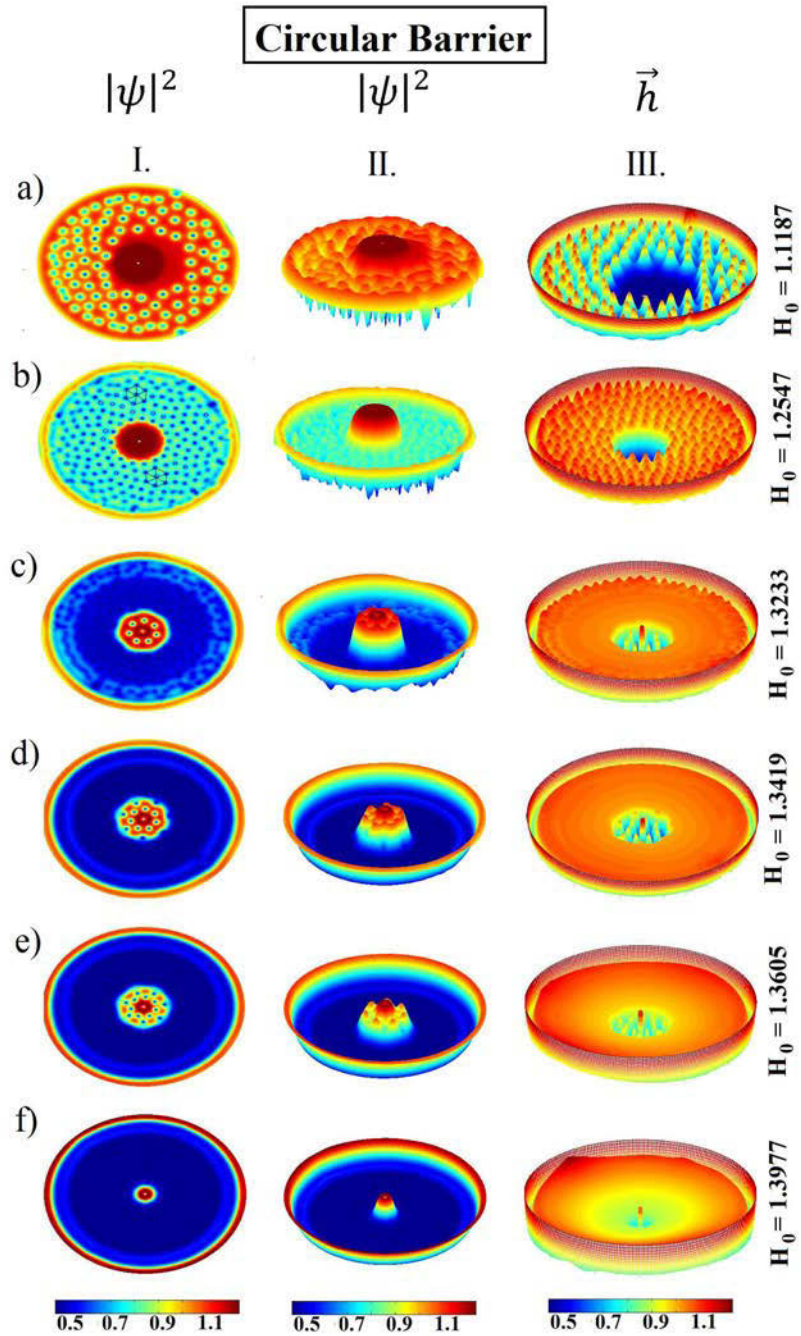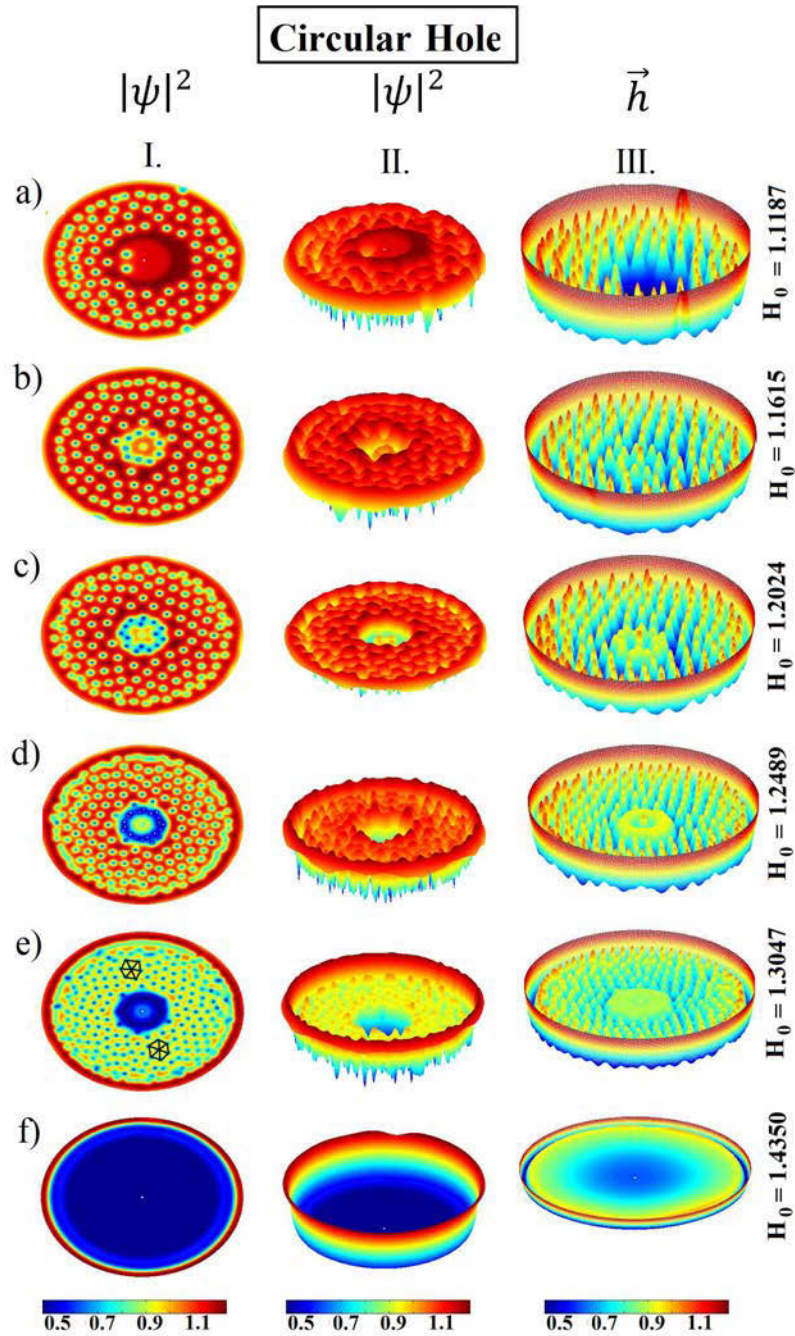
Figure 6-8: (Color online) The vortex structure in the indicated magnetic field for a disk with a triangular hole centered. I. Square modulus of the order parameter $|\psi|^2$, II. Oblique view of $|\psi|^2$, III. Magnetic induction $\vec{h}$.
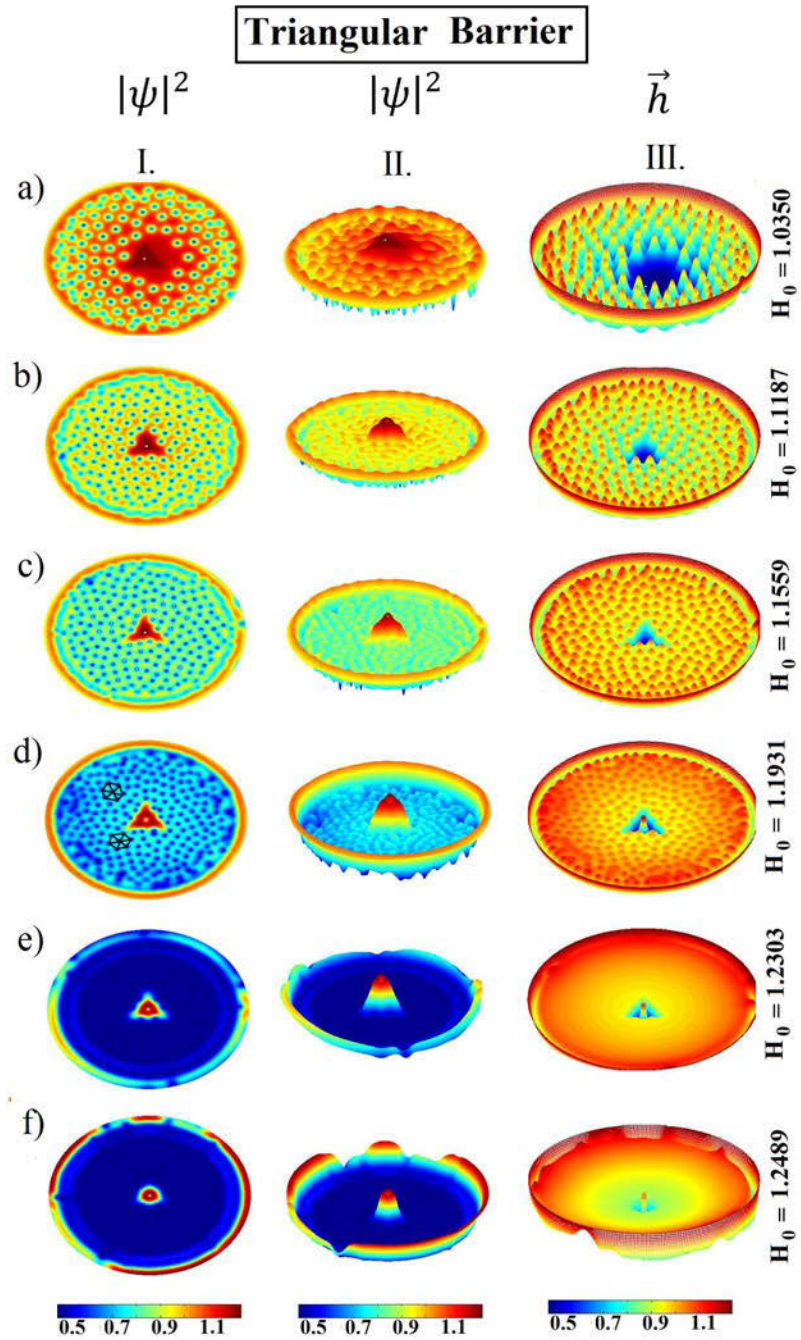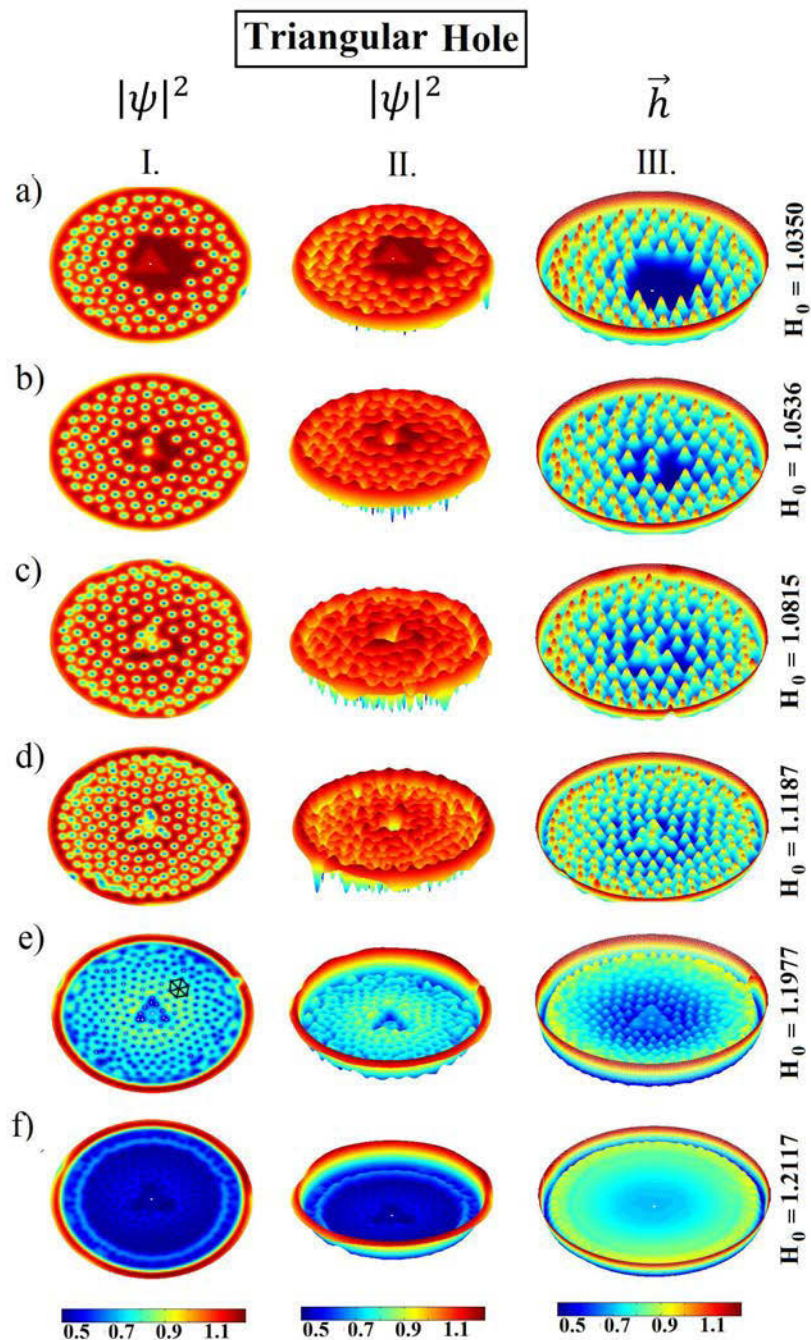
force is weaker than the pinning force of the barrier (See Fig. **6-7**). Finally, from b) until
f), the vortices do not penetrate the barrier as seen in the instantaneous density of Cooper
pairs and magnetization. In these lines is possible to see the entrance of the magnetic field
applied homogeneously from the edges of the barrier towards the center of the disk, without
quantized field entry is found. For triangular hole defect the vortices become pinned into
the defect due to "caging" effect, thus vortices are "caged" at the into the defect and form
a slightly distorted triangular structure due to the repulsive vortex-vortex interaction. By
increasing the applied magnetic field the number of vortices increase in the triangular defect
and it become to normal state with the rest of the disk.

Conclusions

We studied vortex configurations in a superconducting flat disk with topological defects in
the framework of the time dependent Ginzburg Landau theory. Our calculations shows that
numerous kinds of vortex lattice structures can be obtained, some of which have different
symmetries depending which defect were used. For circular barrier or hole defects, the
vortex lattice still exists with increasing the magnetic field, it gradually transforms into a
circular vortex configuration and larger density of vortices, clusters of vortices are particularly
favorable around the defects. To illustrate the transition between these vortex states we
present figures that shown the values of the applied magnetic field in which the vortices
entrance take place, as well as the number of vortices. Due to the influence of the shell
vortices and the boundaries conditions in the disk, a transition from Abrikosov-like vortex
lattice was obtained.

6.3 The case of poligonal trench/barrier

In this case, the magnetic field can be taken nearly uniform inside the superconductor $\mathbf{H}_0 = \nabla \times \mathbf{A}_0$, so that second GL equation does not need to be solved. We consider $g(r, \theta) = 1$ everywhere, except at pentagonal and hexagonal defects position in the disk which are
simulated by using $g = 0.5$ for the trench and $g = 1.5$ for the barrier. We simulate a
mesoscopic superconducting disk of radius $R = 10\xi(T)$ with a little central hole of radius
$r_i = 0.5\xi(T)$ (see Fig. **6-9**). We will assume either a superconductor/vacuum external
interface ($b \to \infty$) or the surface of the sample in a complete normal state ($b = 0$). Fig. **6-10** shows the (a) supercurrent density J (b) Magnetization $-4\pi M$, (c) Gibbs free energy G
and (d) vorticity N, calculated as a function of the applied magnetic field by taking $b = 0$.
The insects represent in (a) the supercurrent density, (b) the local field and (d) the phase of
order parameter (the phase allows to determine the number of vortices in a given region, by
counting the phase variation $\Delta \varphi$ in a closed path around this region. If the vorticity in this
region is N, then the phase changes by $2\pi N$, all of them at $H_0 = 0$). We simulated this disk
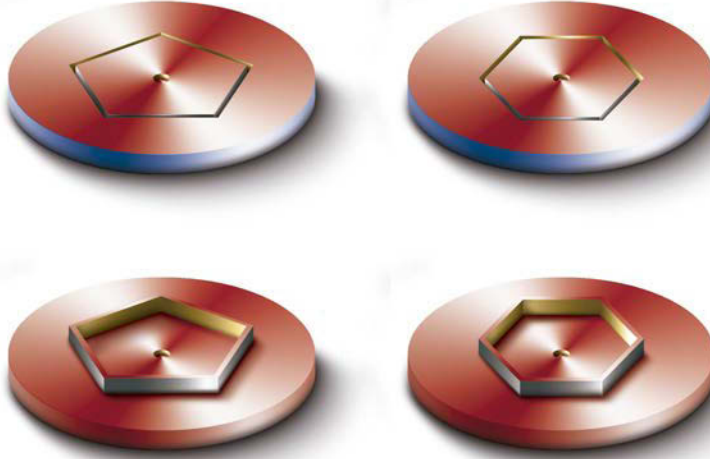
Figure 6-9: Layout of the studied sample: superconducting disk with a central hole and a pentagonal (left) or hexagonal (right) trench (up) or barrier (down). With a superconductor/vacuum interface ($b \to \infty$) (down) and the surface of the sample in a complete normal state ($b = 0$) (up).
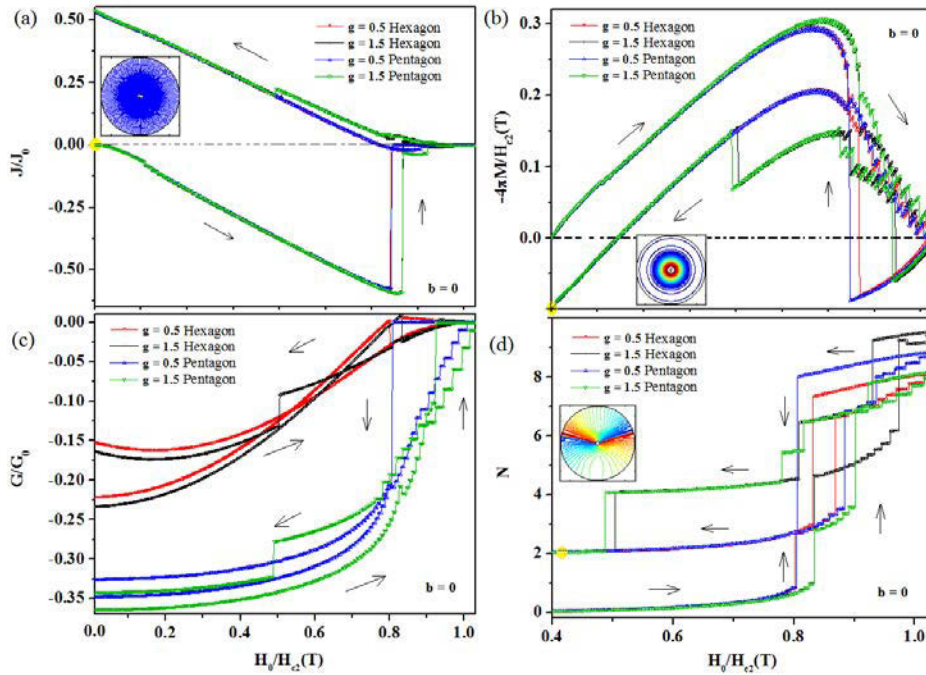
Figure 6-10: (Color online) a) Supercurrent J b) Magnetization $-4\pi M$, c) Gibbs free energy G and d) Vorticity N, as a function of the magnetic field for the disk with a pentagonal and hexagonal trench and barrier for $b = 0$.

with one internal pentagonal and hexagonal trench ($g = 0.5$) and barrier ($g = 1.5$) for $b = 0$. It is seen from these figures that the upper critical field H_{c3} is independent of the geometry and height of the defects in the disk. Moreover, the first vortex penetration field depends on the pinning or anti-pinning force of the defects, $H_{c1} = 0.802$ for trench and $H_{c1} = 0.835$ for barrier for both geometries. This means that the barrier repeals the first penetration than the trench, which was expected, but surprisingly, it does not depend on the the geometry used. The decrease in the Gibbs free energy for the disk with a barrier in the downward branch of the magnetic field is related to the fact that this barrier allows less vortices inside the sample. For both pentagonal and hexagonal cases the upper thermodynamical critical field H_{c3} occurs at the same value $H_{c3} = 1.03$ but in part of the downward branch of the magnetic field the vortex expulsion fields are different. Two vortices remain into the sample at zero magnetic field. In the inset of Fig. **6-10** (d) we have $\Delta\varphi = 4\pi$ due to the presence of the defect, but the final vortex transitions occur at different values of H_0 following a distinct dynamics for each case: $N = 4 \rightarrow 2$ occurs at $H_0 = 0.48$ for the pentagonal barrier, at $H_0 = 0.51$ for the hexagonal barrier, at $H_0 = 0.801$ in $N = 8 \rightarrow 2$ transition for the pentagonal trench and $H_0 = 0.85$ for the hexagonal trench in a $N = 7 \rightarrow 2$ vortex transition. With the barrier and trench we can control the number of vortices at zero magnetic field. In the insects of Figs. **6-10** (a,b) we can observe that the current streamlines and the local field at $H_0 = 0$ are independent of the type of defect and are symmetric with respect to the center of the disk. The jump in the critical current in the Fig. **6-10**(a) could be correlated to a "structural transition" in the system where the distribution of vortices is altered, This structural transition is accompanied by a local re-distribution of the flux inside the disk, or by the appearance of flux jump instabilities. As H_0 increases from zero (Fig. **6-10** (c)), the free energy of the screening currents increases with H_0 as expected until the first critical field H_{c1} is reached when two vortices penetrates the disk at the center. As H_0 is further increased, more vortices nucleate on the disk forming $N \rightarrow N + 1$ vortex transitions, is energetically more favorable for the next vortex to nucleate at the center of the disk than to form a hexagon or pentagon of six or five off-center vortices with a vortex at each vertex. This result agrees with those of other studies on the nucleation of vortices which showed that a central vortex would appear in the system. The entry of each vortex at successive critical fields is accompanied by a jump in the free energy. In previous works a similar study was performed using a disk with a circular, square and triangular ring-like trench of punctual defects. In Fig. **6-11** we depict the Magnetization and the contour plot of the order parameter (insects) as a function of the magnetic field for the disk with a pentagonal and hexagonal trench and barrier for $b = 0$ and $b \rightarrow \infty$. It can be clearly noticed that these curves have a series of discontinuities signaling that one or more vortices have entered or exited the sample. We can see from these figures that both, the first vortex penetration field and upper critical fields dependent on the boundary condition and on the height of the defects. We have $H_{c1} = 1.12$ and $H_{c3} = 1.8$ when we use $b \rightarrow \infty$ for all cases, whereas if we use $b = 0$, we have $H_{c1} = 0.802$ for trench, $H_{c1} = 0.835$ for barrier and $H_{c3} = 1.03$ for both geometries. In
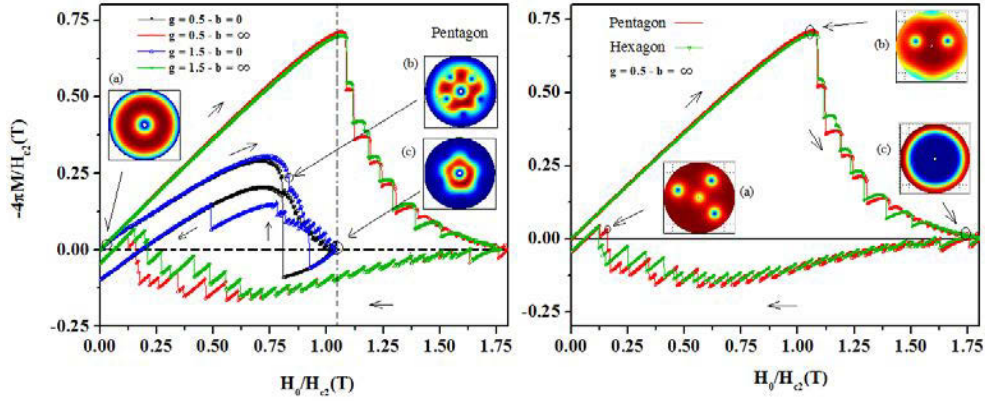
Figure 6-11: Plot of the Magnetization as a function of the magnetic field for the disk with a pentagonal and hexagonal trench and barrier for $b = 0$ and $b \to \infty$.

the insects of Fig. **6-11** we show the contour plot of the order parameter for several vorticity for $b = 0$ (left) and pentagonal defect: (a) at $H_0 = 0$, when the magnetic field is decreasing, the superconducting order parameter vanishes at the surface, which is a direct consequence of $b = 0$; (b) at $H_0 = 0.83$ for $g = 1.5$ we plot a non-stable state with $N = 3$ vortices, and we can appreciate that the shielding currents are nucleated at a distance of $\sim 15\%$ of the radius of the disk; (c) at $H_0 = 1.00$, closer to H_{c3}, the superconducting region obey a geometry of the defect. For the case $b \to \infty$ (right) and both pentagonal and hexagonal defects and by taking $g = 0.5$ we plot the order parameter: (a) at $H_0 = 0.23$ for a pentagonal case, when the magnetic field is decreasing, and we can see that the superconducting order parameter do not vanish at the surface, which is a direct consequence of $b \to \infty$; in this non-stable state we have $N = 3$ vortices and the surface barrier is larger than that that for the $b = 0$ case; (b) at $H_0 = H_{c1}$ we plot a non-stationary state with $N = 2$ vortices; and finally (c) at higher fields H_{c3}, when more vortices come in, the geometry of the sample will prevail, so that all vortices collapse at the center forming a giant vortex. An additional vortex only increases the vorticity of the giant vortex. The panels of Fig. **6-12** show several spatial pattern of the order parameter for a disk with a pentagonal barrier (up) and hexagonal trench (down) by using $b \to \infty$. Following the panels from the left to the right and from the top to the bottom, in this order, from (a,e) we can see that initially we have a Meissner state at $H_0 = 0$. Then, by increasing the magnetic field, in panels (b,f) five and eight (seven in the superconducting region and one in the center of the disk) vortices nucleate in the sample at $H_0 = 5.09$ and $H_0 = 1.14$ respectively. In (c) we have a giant vortex with $N = 32$ for the pentagonal barrier at $H_{c3} = 1.8$. Now, when the magnetic field is decreasing, at $H_0 = 1.09$ a pentagonal structure with $N = 5$ vortices (more two central vortices) is forming (panel g). Finally, for $H_0 = 0.0$, there are a giant central vortex with vorticity $N = 2$ for both pentagonal and hexagonal trenches (panels d,h).
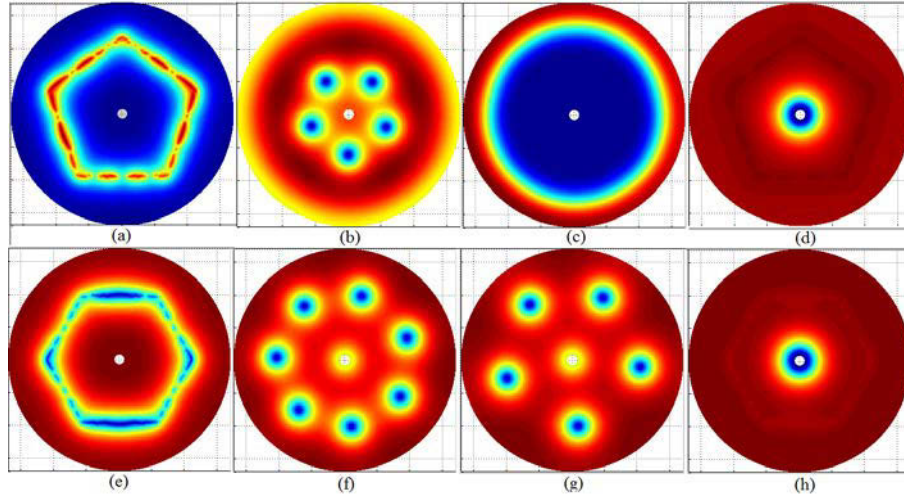
Figure 6-12: Spatial pattern of the order parameter for a disk with a pentagonal barrier (up) and hexagonal trench (down) by using $b \to \infty$.

Conclusions

We studied the effect of the geometry of a pentagonal and hexagonal trench and barrier on the thermodynamical properties of a mesoscopic superconducting disk with a central hole solving the time dependent Ginzburg-Landau equations. We take two values for the deGennes parameter $b = 0$, simulating a sample with its lateral surface in complete normal state and $b \to \infty$, simulating a usual superconducting/vacuum interface. Our results have shown that the lower thermodynamics field H_{c1} depend strongly of the chosen boundary condition and the nature of the defects and is independent of the geometry of the defects, whereas the upper magnetic field H_{c3} depend just on the boundary condition, that is, due to the force of the pinning (trench) and the anti-pinning centers (barrier) are high. We believe that these findings are relevant not only for groups working on or exploring the vortex state and manipulation of nanoengineered superconductors, but also for those studying confined systems where similar competing interactions take place.

6.4 Magnetic response of a structured mesoscopic superconductor

We consider $g(x, y) = 1$ everywhere, except at the tower position in the sample, where $g(x, y)$ is slightly larger than one. The passage from Eq. (6-1) requires an average of the original equations along the z direction by considering a film of thickness $a \ll \xi$. We simulate a superconducting sample of area $L^2 = 46^2\xi^2$ with a central tower of area $d^2 = 12^2\xi^2$. The height of the pillar and square are $a = 0.5\xi$. In Fig. **6-13** we illustrate the schematic view

of a large square superconductor with a tower on the top of it for (a) Dirichlet boundary condition and (b) Neumann boundary condition.
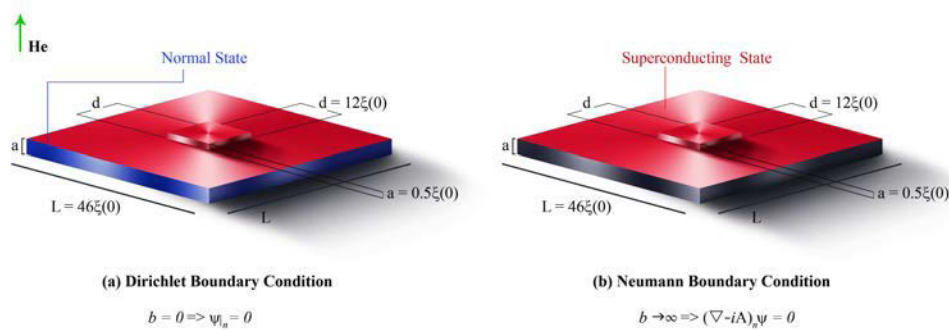
Figure 6-13: (Color online) Illustration of a large square superconductor with a tower on the top for two cases (a) Dirichlet boundary condition and (b) Neumann boundary condition.
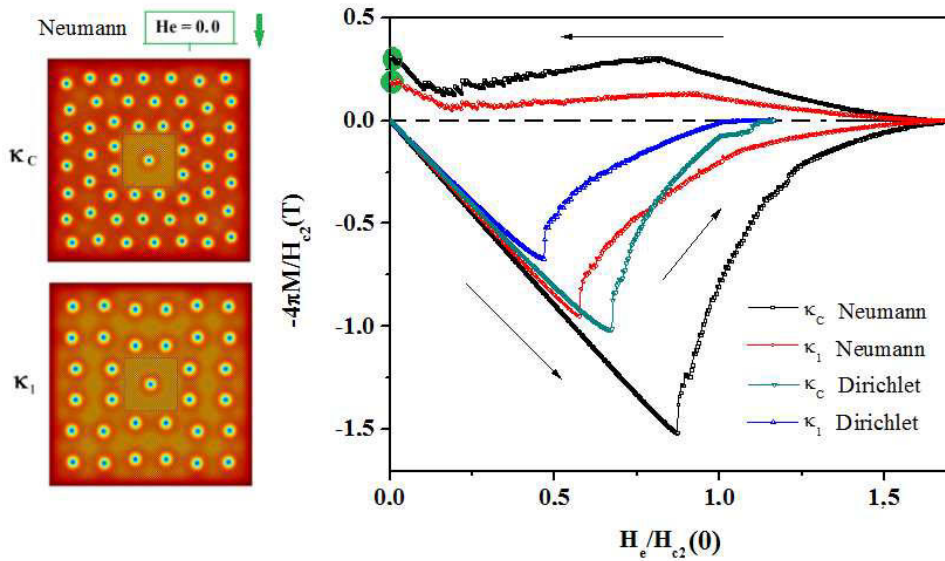
Figure 6-14: (Color online) Cooper pairs density at $H_e = 0.0$ (left) and Magnetization $4\pi M$ (right) for κ_1 and κ_c, $b = 0$ and $b \to \infty$.

Fig. **6-14** shows the density of Cooper pairs at $H_e = 0.0$ (left) and magnetization $4\pi M$ (right) for κ_c and κ_1, $b = 0$ and $b \to \infty$. In the Fig. **6-14** (left), the density of superconducting electrons at zero field in a downward branch of the magnetic field is plotted. There are
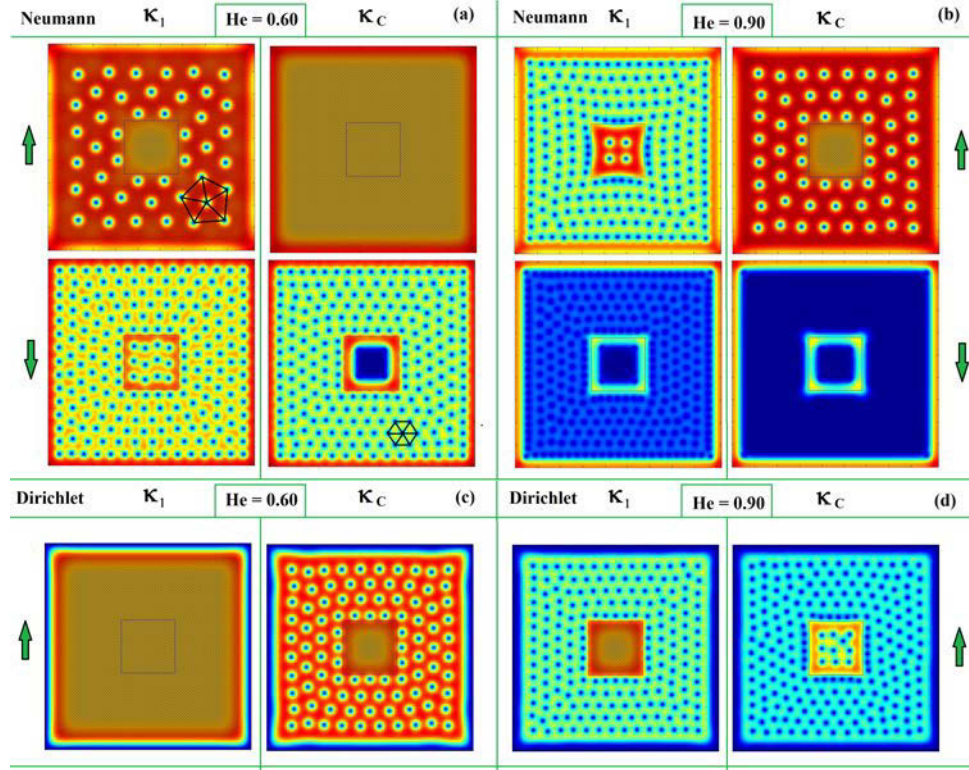
Figure 6-15: Cooper pair density $|\psi|^2$ for the indicated values of κ in the upward branch (arrow up) and the downward branch (arrow down) for the indicate magnetic field H_e.

$N = 33$ vortices into the sample for K_1, which $N = 1$ sit in the tower and $N = 32$ outside. For K_c, there are $N = 53$ vortices, which $N = 1$ sit in the tower and $N = 52$ outside. As we can see in the Fig. **6-14**(right) the lower and upper critical fields H_1 and H_2 are slightly dependent of the Ginzburg Landau parameter κ and strongly depends on the boundary condition. We have $H_2 = 1.657$ and $H_1 = 0.870$ for κ_c, $H_2 = 1.581$ and $H_1 = 0.576$ for κ_1, taking $b \to \infty$ (Neumann boundary condition); $H_2 = 1.119$ and $H_1 = 0.672$ for κ_c, $H_2 = 1.000$ and $H_1 = 0.466$ for κ_1, taking the Dirichlet boundary condition. The field barrier for the first penetration field alter significantly with variation of the κ and b parameters. A interesting characteristic in the downward branch of the magnetic field, is that the sample remains always in paramagnetic state for a superconductor/vacuum interface. Our simulations did not show any results physically possible decreasing the magnetic field in $b = 0$ case, it is an open problem that will be analyzed in a next paper. In Fig. **6-15** we plot the Cooper pairs density $|\psi|^2$ for $H_e = 0.600$ and $H_e = 0.900$ in the increasing and decreasing branches of the magnetic field for κ_1, κ_c and $b \to \infty$ in the upper panel of the figure, and for $b = 0$ just increasing branch of the applied filed in the lower panel. In the deceasing branch of the applied field, in Fig. **6-15** (middle panel) we can see that for κ_1, $b \to \infty$ and $H_e = 0.60$
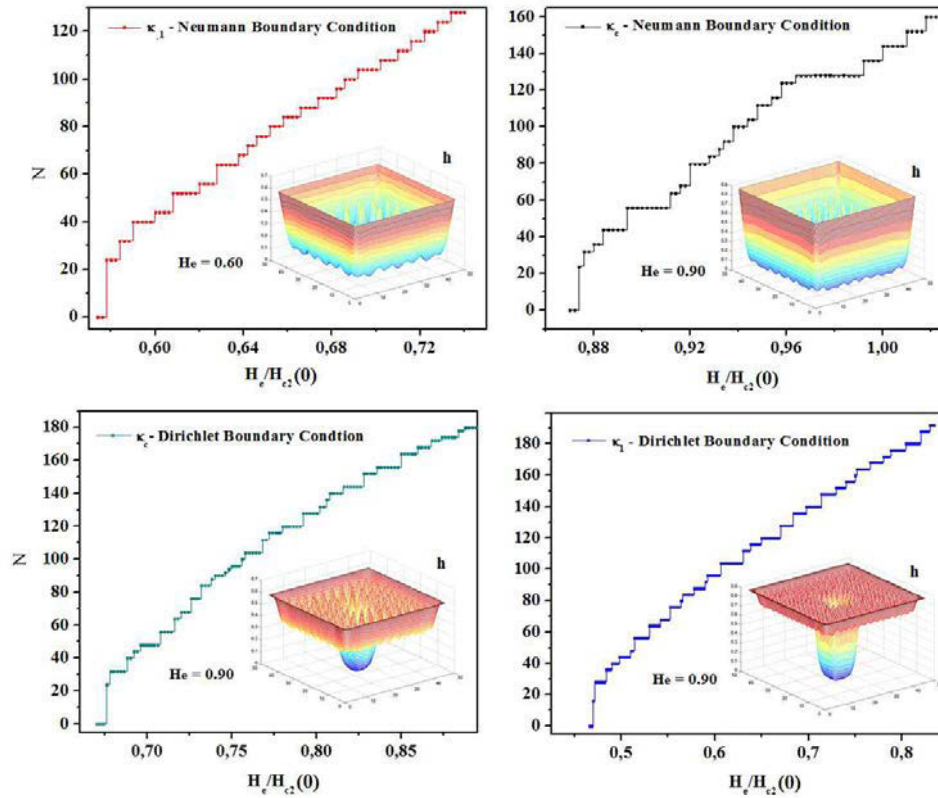
Figure 6-16: Illustration of the vorticity N in the upward branch of the magnetic field. (Insets) Snapshot of the Magnetic induction h for the indicate magnetic field H_e

we have a $N = 208$ state, $N = 12$ of them sit in the tower. The vortices inside the pillar set along lateral side of the inner square and not set along the diagonal, this is surprisingly, since vortex-vortex interaction is repulsive and the cross section of the pillar is large. In interesting to note that a vortex Abrikosov lattice is formed in several configurations. Now, in the increasing branch of the applied field, for $H_e = 0.90$, κ_1, $b \to \infty$ we have a $N = 212$ state, $N = 4$ of them sit in the tower, the vortex configuration is totally rearranged in square symmetry, still considering the decreasing branch of H_e, for the same case. In the decreasing branch of the applied field, for $H_e = 0.90$, κ_c, $b \to \infty$, the vortices are undistinguished and the sample is practically in normal state, but still a small region around the tower remain in superconducting state. In Fig. **6-16** we can see the number of vortices and the magnetic induction in these configurations at the indicate magnetic field.

Conclusions

We studied the effect of a square tower on the vortex configuration and magnetization of a large superconducting square sample solving the time dependent Ginzburg-Landau equations. We take two values for the Ginzburg Landau parameter $\kappa_1 = 1.0$, $\kappa_c \simeq 1/\sqrt{2}$ and two different boundary conditions $b = 0$ and $b \to \infty$. Our results have shown that the critical fields H_1 and H_2 depend of κ and b.

6.5 Superconducting state in a circular SQUID shaped mesoscopic film

The z-dependence of the order parameter is ignored if the system is a very thin film o f thickness $w << \xi$. In that case, κ is replaced by a Ginzburg-Landau parameter $\kappa_{eff}^2 = \kappa^2/(w/\xi$. The parameters used in our numerical simulations were: $\kappa_{eff} = 2.56$, which is a value for a film thickness $w \approx 6$ nm, assuming $\xi = 38$ nm and $\kappa = 1.02$). Largest unit cells lengths were $dr = 0.2$ and $d\theta = 2\pi/N_\theta$, taking $N_r = 32$ and $N_\theta = 128$ as the number of cells in the r and θ directions respectively (polar coordinates). The studied sample is circle of external radius $R_e = 12\xi$ with a central hole of radius $R_i = 6\xi$ connected to the outer rim through a very thin slit with angular width $d = 1\theta, 2\theta, 4\theta, 6\theta, 8\theta$, $(\theta = d\theta)$ (see Fig. **6-17** (a)). In the boundary conditions $(i\nabla + \mathbf{A}\psi \cdot \mathbf{n} = i\psi/b)$ we considered $b \to \infty$, $b = -2.45\xi$ and $b = 2.45\xi$, simulating superconducting/dielectric, superconducting/superconducting at higher critical temperature, and superconducting/metal interfaces respectively. Fig. **6-17**(b) shows the vorticity N as a function of magnetic field. Figs. **6-17** (c-d) show the magnetization as a function of the external applied magnetic field H_e, for (c) $d\theta = 2$, $b \to \infty$, $b = 2.45\xi$, $b = -2.45\xi$ and (d) $d/\theta = 1, 2, 4$, $b \to \infty$. We see that the magnetization curves present differences in the Meissner and multi-vortex states when the angular width of the slit varied, however at low magnetic fields all curves are very close each other. The sample becomes more diamagnetic with increasing θ and less diamagnetic when the sample is in contact with a metallic material ($b = 2.45\xi$). We observe that first vortex penetration field is $H_1 = 0.366$, with $N = 5$ and independent of θ. Between $0.579 \leq H_e \leq 0.848$ we have a regular vortex entrance for $11 \leq N \leq 23$ and $N \to N + 2$ vortex transitions, independently of θ. For higher magnetic fields $H_e \geq 0.879$ the vortex transitions are irregular and dependent of θ. In Fig. **6-18** (left) we show the Gibbs free energy for three different boundary conditions $b \to \infty$, $b = 2.45\xi$, and $b = -2.45\xi$. In the inset of the figure we present clearly the first vortex penetration field H_1. Notice that H_1 varies slowly with b parameter, the value of the energy at $H_1 = 0.440, 0.424, 0.412$ is $G = -0.251, -0.269, -0.276$ for $b = 2.45\xi, \infty, -2.45\xi$ respectively, the vortex entry is energetically more favorable for a system in contact with a superconductor with higher critical temperature. We see that the second vortex penetration field $H_2 = 0.484$ is independent of the boundary condition with
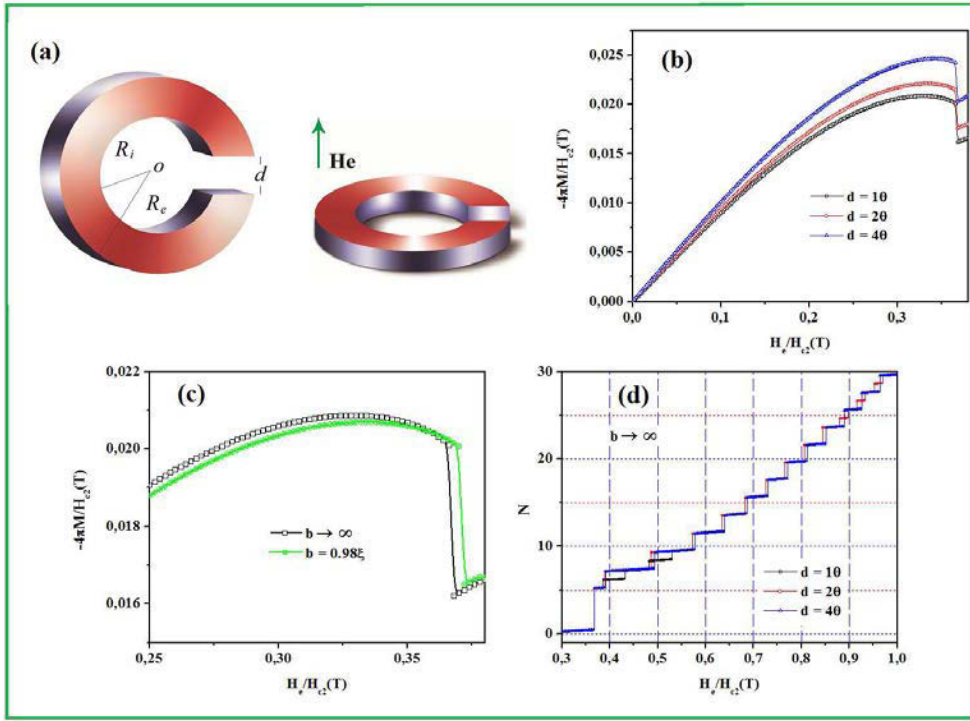
Figure 6-17: (a) 3D view of the studied sample. (b) Vorticity $N(H_e)$ as a function of the external applied magnetic field H_e, (c-d) Magnetization $-4\pi M(H_e)$, for $b \to \infty$, $b = \pm 2.45\xi$ and $d/\theta = 1, 2, 4$.

an energy equal to $G = -0.149$. In Fig. **6-18** (right) we found a linear behavior of the maximum of the magnetization $-4\pi M_{Max}$ as a function of d. The analytical fitted curve corresponds to $-4\pi M_{Max} \simeq 0.00126d + 0.0196$. The linear growth with d suggest that the smaller angular width of the slit makes the material less diamagnetic. The Fig. **6-19** we show the Cooper pair density at indicated magnetic field for $d/\theta = 1, 2, 4$ and $b = \infty$. A first multi vortex state $N = 5$ at $H_e = 0.379$ for all the samples and is independent of θ and b values. Note that, for the equilibrium configuration, the vortices obey the geometry of the sample. In Figs. **6-20** we the Cooper pair density in the absence of the magnetic field at $H_e = 0$ (upper panel), as well as $H_e = 0.452$ (lower panel) for $d = 2\theta$ and (left) $b = 2.45\xi$ (middle) $b \to \infty$ and (right) $b = -2.45\xi$. Note that, the superconductivity is enhanced (suppressed) in the boundary at $H_e = 0$ when a superconducting (metallic) material is in contact with the sample. An interesting result is that for our system $N_{b>0} < N_{b<0}$ at $H_e = 0.452$, while we expect that a superconducting/superconducting interface decrease the vorticity in the sample due to proximity effects of the Coopers pairs of the superconductor at higher critical temperature. There are two ingredients influencing on the formation of the lattice: the vortex-vortex interaction, which is repulsive and the vortex-surface interaction; this last one is related to the Lorentz force which pushes the vortex to the interior of the sample, once it has been nucleated. From this balance it will result the vortex state.
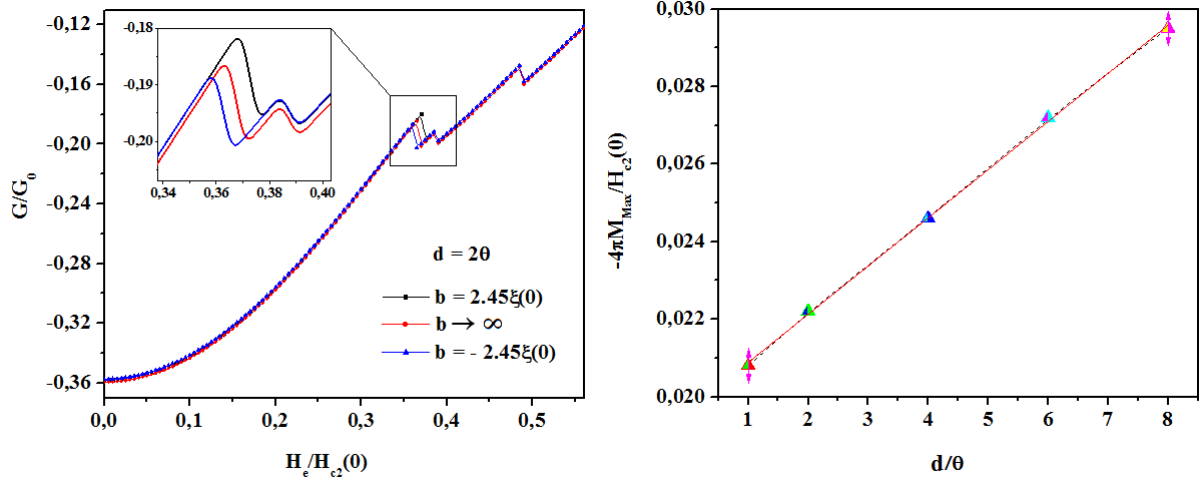
Figure 6-18: (left) Gibbs free energy $G(H_e)$ and (right) Maximum of the diamagnetic response $-4\pi M_{Max}(d)$, as a function of the applied magnetic field.
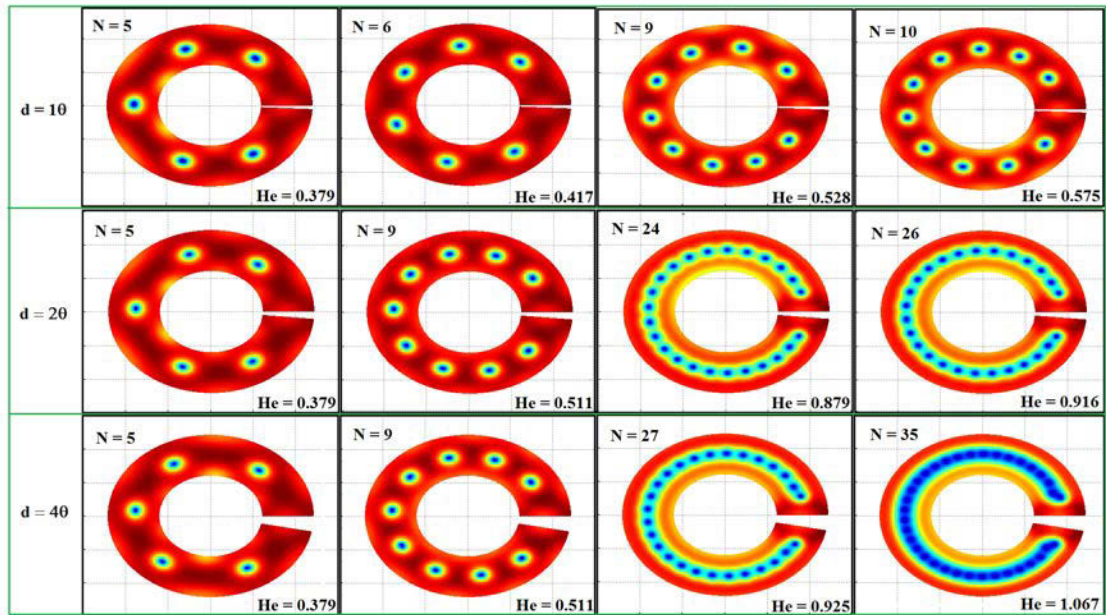
Figure 6-19: (Color online) Cooper pair density contour plots ($|\psi|^2$) at indicated magnetic field H_e and vorticity N for $d/\theta = 1, 2, 4$, $b = \infty$. Blue and red regions represent values of the modulus of the order parameter from 0 (normal state) to 1 (superconducting state).
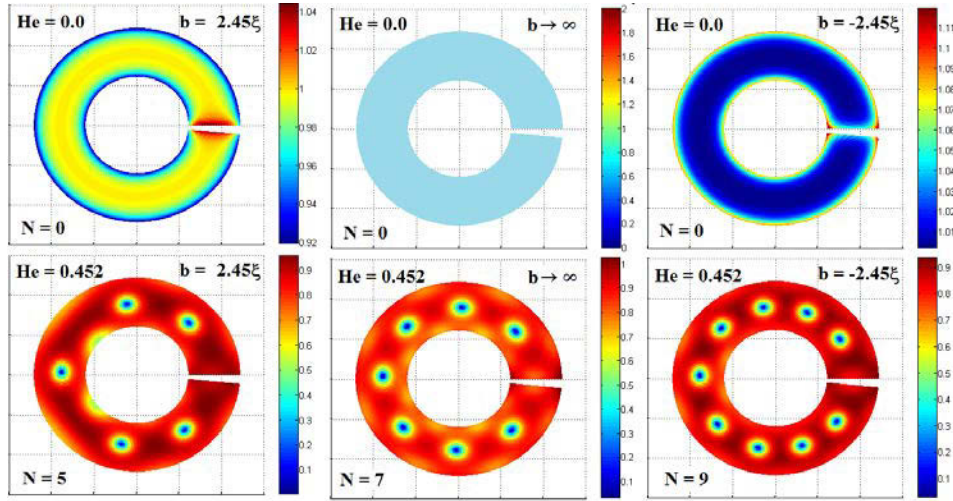
Figure 6-20: (Color online) The Cooper pair density ($|\psi|^2$) at indicated magnetic field and vorticity N for $d = 2\theta$ and (left) $b = 2.45\xi$ (middle) $b \to \infty$ and (right) $b = -2.45\xi$. Color map represents the modulus of the order parameter ($|\psi|^2$).

6.6 Conclusions

We demonstrated that the extrapolation deGennes parameter b for tunneling of Cooper pairs at the sample boundary and angular width θ of the slit in the Squid sample geometry play an important role in the magnetization and vorticity of the sample. The results presented in this paper included the linear behavior of the maximum of the magnetization as a function of the angular width of the slits corresponds to $-4\pi M_{Max} \simeq 0.00126d + 0.0196$. Another very interesting result is that for our system the first vortex penetration field and vorticity strongly depend on the boundary condition, e.g. $H_1(b < 0) < H_1(b > 0)$, and $N(b > 0) < N(b < 0)$ at $H_e = 0.452$, when is well know that a superconducting/dielectric interface should decrease the first vortex penetration field and vice-versa for the proximity to a superconductor. These results will be further analyzed in the next work.

Publications.

The results presented in this chapter were published as:

- J. D. González, M. R. Joya and J. Barba-Ortega, *Influence of short-range artificial defects in a mesoscopic flat disk on the Abrikosov state*, Int. Journal of Mod. Phys. B **28**, 1450227 (2014).

- J. Barba-Ortega, J. D. González, and E. Sardella, *Superconducting state of a disk with a pentagonal/hexagonal trench/barrier*, Journal Low. Temp. Phys. **174**, 96 (2014).

- J. Barba-Ortega, J. L. Aguilar and J. D. González, *Unconventional anti-vortex spontaneous generation in a superconducting microstructure*, Mod. Phys. Lett. B **29**, 1550070 (2015).

- J. Barba-Ortega, J. D. González and M. R. Joya *Magnetic profile in a nanostructured superconducting sample* , Mod. Phys. Lett. B **28**, 1450150 (2014).

- J. Barba-Ortega, J. L. Aguilar and J. D. González, *Superconducting state in a circular SQUID shaped mesoscopic film*, Modern Phys. Lett. B **28**, 1450230 (2014).

7 Lateral heterostructure of two superconductors

Two-component superconductivity is not limited to multiband/gap materials, but can also be realized by combining different superconductors in a hybrid heterostructure. We cover a multitude of possible two-component superconducting hybrids, realized either by combining two different materials, or using the same material with different levels of disorder and/or different thickness in two regions, where we hope that our findings will improve understanding of the involved processes and offer new pathways to superconducting quantum devices.

7.1 Introduction

The study of the superconducting mesoscopic samples received recently a lot of attention due to results obtained in the analysis of the properties of the superconductors and therefore their applications, which are determined by critical parameters, i.e. the critical fields (H_c, H_{c1}, H_{c2}, H_{c3}), the critical current j_c and the critical temperature T_c, those can be basically tuned by their intrinsics characteristic length scales: the coherence length (ξ), the length scale of the Cooper-paired electrons, and the London penetration length (λ), the length scale of magnetic field penetration into the superconductor. For application purposes is necessary to control these parameters.

Previous works focused on the effect of superconducting condensate strongly confined in small elements as a procedure to improve the critical properties. Researchers has found novels effects on confinement in mesoscopics disks [114, 46, 61, 47], and the contribution of symmetry [183] in comparing disks, squares [184], and triangles [145]. The individual vortices pierce the sample in direction of applied magnetic field forming vortex clusters in those mesoscopic systems, both theoretical and experimental, revealed multivortex Abrikosov-like states that tending to mimic the symmetry of the sample due to the repulsion with the surrounding screening (Meissner) currents, as well as depending on the details of the condensate confinement because edge currents may even compress the vortex lines in to a single bundle, often called giant vortex [185, 186, 187, 188, 189, 190, 191].

Recently, there has been growing interest in investigating nanostructured superconductivity that include topological superconductors which are analogs of the topological insulators. In these systems, the main proposals are focused on combining in proximity with a conventional superconductor [192] to use the transport properties, observed experimentally, in

transport measurements [161, 193] and scanning tunneling spectroscopy [194, 195]. This systems has been studied by using half-Heusler materials to offer multifuntional topological devices [196], due to its superconducting properties with low carrier concentration in electron transport measurements [197]. These measurements demonstrate that is possible to control the energy gaps, critical temperature and critical magnetic field in selected region as a result of creating of tailored nanostructured superconductors with complex superconductor materials quantum technology applications. This developments has reached new advances including the superconducting proximity effect in epitaxial graphene induced by a graphene-superconductor interface [1, 198]. From the point of view of numerical calculations have shown a lot of effects usually observed in nanostructured superconductors, resulting in complex vortex patterns when barrier or defects are included [199, 92, 200, 182, 180]. Similar behavior has also been simulated including anisotropy in the superconducting sample, through variation of T_c in different layer of the sample that leads to distinct vortex states and their free energy [201, 202, 203]. Another possibility for the non-conventional vortex structure can be obtained from multi-band superconductivity, since high temperature superconductor MgB_2 was observed in the experiments [204, 205, 16]. These multi-band systems are provided with two o more electronic condensates from Cooper paring in different bands of the material, and exhibit a variety of new and interesting phenomena with no counterpart in conventional single-component superconductors [206, 207, 208, 209]. One of most intriguing of these phenomena are related to the exotic vortex structures that can emerge in a two-component superconductor, because of the different length scales ξ_i at which the Cooper-pair density varies in each component [210, 211].

The study of mesoscopics superconductor has been widely studied because of the confinement present in the sample, therefore novel characteristics take place useful for advances to develop new technologies. For that reason, the 2D superconductivity has been investigated to find an insight into a variety of quantum phenomena, where the thermal evaporation and sputtering of metallic films allow to study most of the basic properties of 2D superconductors [212, 213]. Nevertheless, the methods for fabrication such as quantum phase transitions new discussions and studies in thin-film superconductors with thickness from 0.3nm to 10nm [214, 215, 216, 217, 22, 23]. In those days, new fabrications techniques, such as molecular beam epitaxy accompanied by surface or interface reconstruction processes, methods for the production of field-effect devices and mechanical exfoliation, were introduced into the field of 2D superconductors [26, 70, 29, 32, 218, 33, 34, 219, 220] and as a result, the crystallinity improved greatly, even in atomically thick samples. Therefore, the emerging 2D superconductors are increasingly as a platform for studying new physics. Furthermore, Based on the possibility of change the mean free path (l) using impurity-doping of superconductors techniques, represent a groundbreaking prospects in the, study of the effects of l that might exploit unique superconducting properties [221]. The modulation of superconductivity,can be obtained not only for choosing smaller superconducting lengths comparing with bulk superconducting length or considering several geometric shapes, but also whether strong local

doping effect can be produced over the superficial area of the superconductor.

The different phenomena associated with the hybrid combination with other superconductors show relevant effect such as the magnetic field-driven quantum phase transition take place electrostatically in superconducting interfaces among other effects [222, 223], but also a combination with low dimensional semiconductors offers a versatile ground for novel device concepts, such as supercurrent transistors, sources of spin-entangled electrons or nano-SQUIDS [224]. From a more basic point of view, these hybrid systems are interesting melting pots where various fundamental effects in condensed matter physics coexist. When superconductor is coupled to another superconductor to a very interesting phenomena take place, both condensates at the interface interact each other and the supercurrent can be modulated in this region. In this context, the modulated domain-wall superconductivity offers the possibility to control the strength of superconductivity at will. The underlying physics behind such hybrid device ultimately relies on which superconductors are selected to be coupled.

In the present contribution, we study the fundamentals properties and vortex matter of two-component superconductor, in which the quantity of each component is well know, choosing the parameter of the components desired as well as the geometry, amount, kind and distribution of each superconductor. In recent literature can be encountered that developing of theory for two-component superconductors is similar than two-band superconductors in which both can be described by following Ginzburg Landau (GL) energy density [206, 207, 208, 225, 226]. Nevertheless, by using the theory of two-band superconductor, it is not possible to determine the quantity of each superconducting condensate in the sample. In our work, we used the G-L formalism to study the hybrid superconducting samples, where the interaction between the two density of Cooper-pair occurs in the interface in soft manner and the wall domain in the interface is modulated through the fundamental parameters of each superconductor. This kind of superconducting sample has not been study up to now. Additionally, we used the G-L formalism in the dirty limit to simulate ultra thin superconducting samples, but also for selecting the local distribution of the mean free path on the superconductor.

In Sec. II, we show the derived G-L equations with the ratio of intrinsic parameters of superconductivity and procedure we used in the calculations. In Secs. III and IV, we analyze the results obtained for samples with two-component samples divided in two halves considering type II/type II and type I/type II. Further we discuss the issues concerning the distribution and configuration of vortices in the sample, but also the phase of the order parameter, density of supercurrent and magnetization. Our results are finally summarized in Sec. V.

This chapter is organized as follows. Sec.7.1. Introduction. Addendum to the theoretical formalism is presented Sec. 7.1.1. that include separately Sec. 7.1.1.1 Two-component superconductor: Hybrid superconductor and Sec. 7.1.1.2 Two-compnent superconductor: Ultra thin superconductor and electron mean free path variation. In Sec. 7.1.2 The mesoscopic superconductor comprising two different materials, laterally coupled, is simulated using time-

dependent GinzburgLandau theory, with included anisotropy of all parameters relevant for the behavior of the carriers involved in the formation of the superconducting condensate (such as critical temperature, penetration depth, coherence length, and Cooper-pair mass of each component. Sec. 7.1.3 and Sec. 7.1.4 In dirty limit, the anisotropy is also simulated via the variation of the electron mean free path in the corresponding part of the sample. We fully characterize the behavior of such samples in applied magnetic field, reflected in novel vortex matter and hybrid magnetic response uncharacteristic of any single-component system to date.

7.1.1 Addendum to the theoretical formalism

7.1.1.1 Two-component superconductor: Hybrid superconductor

We consider a two-component superconducting sample of thickness d more smaller than the two characteristic of lengths for a superconductor system, in such a way that the system is effectively two-dimensional. In this paper we will denote the two superconductors inside of the sample as S_1 and S_2, the quantities are scaled to the units that depend on the parameters of S_1. We implement the G-L theory by solving the equations obtained by minimizing the following energy functional:

$$\mathcal{F} = \sum_{i=1,2} \int dV [\alpha_i(0) \left(1 - \frac{T}{T_{ci}}\right) |\Psi|^2 + \frac{\beta_i}{2}|\Psi|^4 \quad + \quad \frac{1}{2m_i^*} \times \left| \left(-i\nabla - \frac{2e}{c}\mathbf{A}\right)\Psi \right|^2$$
$$+ \quad \frac{(\mathbf{H} - \mathbf{H}_a)^2}{8\pi}] \tag{7-1}$$

where $\mathbf{H}_a$ denotes the applied magnetic field, and $\mathbf{H}$ is the total local magnetic field, including the response of the superconductor, and where the index i represents either S_1 or S_2 depending on the location inside the volume V. We include the additional component scaling the functional to the parameters of S_1, with variables α_1, β_1 and m_1^*. We minimizing the Eq.(1), we obtain for the order parameter and vector potential,

$$-(1 - c_T t)\frac{1}{c_\xi}\psi + \frac{c_\lambda c_m^2}{c_\xi}|\psi|^2\psi + (-i\nabla - \mathbf{A})^2\psi = 0 \tag{7-2}$$

$$j_s = \kappa_1^2(\nabla \times \nabla \times (\mathbf{A} - \mathbf{A}_0)) = c_m \Re(\psi^*(-i\nabla - \mathbf{A})\psi) \tag{7-3}$$

with boundary condition:

$$\mathbf{n}.(-i\nabla - \mathbf{A})\psi|_{S_s} = 0 \tag{7-4}$$

where parameters are defined as $c_T = T_{c,1}/T_{c,2}$, $c_\xi = \xi_2^2(0)/\xi_1^2(0)$, $c_\lambda = \lambda_2^2(0)/\lambda_1^2(0)$, $c_m = m_1^*/m_2^*$ and $t = T/T_{c,1}$, where c_m, c_λ, c_ξ and c_T are equal 1 inside the S_1 material. The above equations are given in dimensionless form and distances are measured in units of

$\xi_1(0) = \sqrt{-\hbar^2/2m\alpha_1(0)}$, the temperature in units of the critical temperature of S_1 $(T_{c,1})$, the order parameter Ψ in units of $\Psi_{\infty,1} = \sqrt{-\alpha_1(0)/\beta_1}$, the vector potential in units of $A_{0,1} = c\hbar/2e\xi_1^2(0)$, the magnetic field in units of the upper critical field of S_1, $H_{c2,1} = c\hbar/2e\xi_1^2(0)$ and in the free energy in units of $F_0 = \alpha_1^2(0)/\beta_1$. The region in the sample where the additional superconductor is included to obtain a two-component superconducting thin film, can be directly modeled by changing the parameters c_T, c_ξ, c_λ and c_m, in other words, many types of two-component superconducting system can be studied tunning the parameter with the precision desired. We solve the coupled GL equations self-consistently using the link variable approach for a finite-difference representation of the order parameter and the vector on a uniform two-dimensional Cartesian space grid (x, y). Using the first GL equation, the order parameter will be calculated. The second GL equation will then in turn be used to find the supercurrent, and by Fourier transform of the supercurrent, the vector potential will be calculated to again be used as input into the first GL equation until a convergent solution for both ψ and $\mathbf{A}$ is found.

Physical parameters in two-component superconductors

In the analysis of the superconducting state of two-component superconductors, we have to consider the relation between the parameters in each materials, in order to describe correctly important physical quantities used to describe the vortex state such as the Gibbs free energy, magnetization, density of order parameter, superconducting current density and phase of order parameter. In what follows we will derive an expression for each kind of parameter used in superconductivity.
(A.1) The coherence lenght.
In S_1, $\xi_1^2(0) = -\hbar^2/m_1^*|\alpha_1(0)|$ whereas S_2, $\xi_2^2(0) = -\hbar^2/m_2^*|\alpha_2(0)|$

$$\frac{\xi_2^2(0)}{\xi_1^2(0)} = \frac{m_1^*|\alpha_1(0)|}{m_2^*|\alpha_2(0)|} \tag{7-5}$$

(A.2) The penetration lenght.
S_1, $\lambda_1^2(0) = \frac{m_1^*c^2\beta_1}{4\pi(e^*)^2|\alpha_1(0)|}$ and S_2, $\lambda_2^2(0) = \frac{m_2^*c^2\beta_2}{4\pi(e^*)^2|\alpha_2(0)|}$

$$\frac{\lambda_2^2(0)}{\lambda_1^2(0)} = \frac{m_2^*\beta_2|\alpha_1(0)|}{m_1^*\beta_1|\alpha_2(0)|} \tag{7-6}$$

Taking into account Eq.(5) we can obtain additional relation between coherence length and penetration length

$$\frac{\lambda_2^2(0)}{\lambda_1^2(0)} = \left(\frac{m_2^*}{m_1^*}\right)^2 \left(\frac{\beta_2}{\beta_1}\right) \left(\frac{\xi_2^2(0)}{\xi_1^2(0)}\right) \tag{7-7}$$

(A.3) Order parameter.

Using the Eq. 6 and the definition of the order parameter, we obtain:

$$\frac{\psi_{\infty,2}^2}{\psi_{\infty,1}^2} = \frac{m_2^*}{m_1^*}\frac{\lambda_1^2(0)}{\lambda_2^2(0)} \tag{7-8}$$

Additional relation for the order parameter is found in terms of c_λ, c_ξ and c_m, as well as the Ginzburg-Landau parameters β and α

$$\frac{\psi_{\infty,2}^2}{\psi_{\infty,1}^2} = \frac{1}{c_\lambda c_m} \tag{7-9}$$

$$\frac{\beta_1}{\beta_2} = \frac{c_\xi}{c_\lambda}\frac{1}{c_m^2} \tag{7-10}$$

$$\frac{\alpha_2}{\alpha_1} = \frac{c_m}{c_\xi} \tag{7-11}$$

7.1.1.2 Two-component superconductor: Ultra thin superconductor and electron mean free path variation

In order to simulate two-component superconductor in which the thickness change spatially, but also the mean free path Fig. **7-1**. The framework for our theoretical studies is the phenomenological Ginzburg-Landau (GL) theory. We used the expressions for GL coefficients α and β in the dirty limit, to include the variation l_e the electron mean free path in the sample, i.e.

$$\alpha(T) = -1.36\frac{\hbar}{2m^*\xi_0 l_\xi}\left(1 - \frac{T}{T_c}\right) \tag{7-12}$$

$$\beta = \frac{0.2}{N(0)}\left(\frac{\hbar^2}{2m^*\xi_0 l_e k_B T_c}\right)^2 = \frac{\beta_0}{l_\xi^2} \tag{7-13}$$

Where $l_\xi = \frac{l_e}{\xi}$ is the ratio of the electron mean free path and BCS coherence length. The dimensionless form of the GL equations can be written as follow:

$$(-i\nabla - \mathbf{A})\Psi = \left(\frac{1.367}{l_\xi} - \frac{1}{l_\xi^2}|\Psi|^2\right)\Psi \tag{7-14}$$

$$\frac{\lambda_0}{\xi_0}\nabla \times \nabla \times \mathbf{A} = -\frac{1}{2i}(\Psi^*\nabla\Psi - \Psi\nabla\Psi^*) + |\Psi|^2\mathbf{A} \tag{7-15}$$

Where the all lengths are scaled to ξ_0, penetration depth λ_0 is defined as $\lambda_0^2 = mc^2\beta_0/16\pi|a_0|e^2$, the vector potential $\mathbf{A}$ is expressed in $\phi_0/2\pi\xi_0$, and the order parameter is in units of $\Psi_0 = \sqrt{-\alpha/\beta}$. We consider a two-component superconducting sample of thickness d more smaller than the two characteristic of lengths for a superconductor system, in such a way that the system is sufficiently two-dimensional to assume the constant order parameter in

z-direction. But in the case that the sample has non-uniform thickness $d(x, y)$, Eq.(14) has to be expanded on the left side by the term $-i\frac{\nabla d(x,y,z)}{d(x,y,z)} \cdot (-i\nabla - \mathbf{A})$, as derived and used in Ref.[180]. Finally, we obtain our equation to be solve:

$$(-i\nabla - \mathbf{A})\Psi = \Psi\left(\frac{1.367}{l_\xi} - \frac{1}{l_\xi^2}|\Psi|^2\right) - i\frac{\nabla d(x,y,z)}{d(x,y,z)} \cdot (-i\nabla - \mathbf{A})\Psi \qquad (7\text{-}16)$$
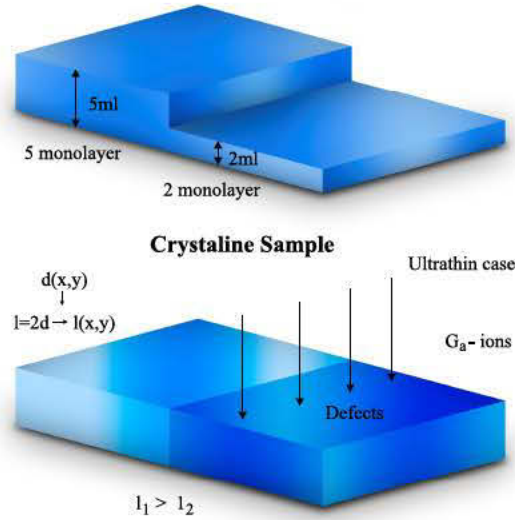
Figure 7-1: (Color online) The considered system: Ultra thin superconducting sample considering a variable thickness (up) and electron mean free path (down)

7.1.2 Mesoscopic sample made of two superconducting materials

In this thesis we will denote the two superconductors inside of the sample as S_1 and S_2, the quantities are scaled to the units that depend on the parameters of S_1. In what follows, we first consider a superconducting film of size $a = 2000nm$ and width of size $d = 5.5nm$ in the sample that is formed by niobium (Nb) and led (Pb) in each sides of the sample. The coherence length and the penetration depth for such a thin and diffusive superconductor take the effective values: $\xi_{eff} \approx 0.85\sqrt{\frac{\xi_0 l}{1-\frac{T}{T_c}}}$ and , $\lambda_{eff} \approx 0.65\lambda_0\sqrt{\frac{\xi_0}{l(1-\frac{T}{T_c})}}$ where the $\xi_0 = 80nm$ and $\lambda_0 = 50nm$ are, respectively, the coherence length and the penetration depth in the bulk for Pb, while for Nb the characteristics lengths are, $\xi_0 = 160nm$ and $\lambda_0 = 38nm$. The conditions chosen for the hybrid superconducting system allow to find in the sample the circulation of two screening currents in the interface that can be modified considering variations of the effective characteristic lengths (ξ_{eff}, λ_{eff}) including changes in the mean free path l, which can be modified in the sample by ion bombardment to reduce the electron mean-free path value. To begin with, we discuss variation of the magnetization in the sample
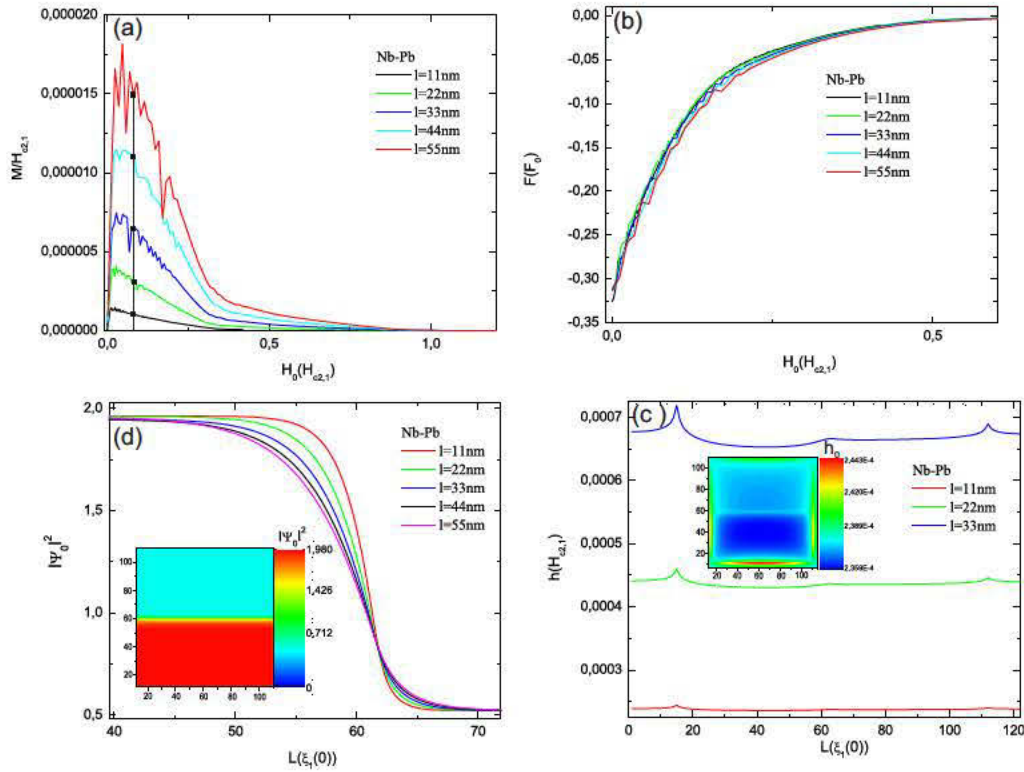
Figure 7-2: (Color online) (a) Magnetization and (b) Free energy of the sample versus the applied field for different values of the electron mean free path as well as the profile of (c) density of Cooper-pair density $|\Psi|^2$ and (d) magnetic field $\mathbf{h}_0$ as a function of the position

due to vortex entrance in both superconductor components, as illustrated in Fig.**7-2** (a), it presents a series of discontinuities, in which each jump signals the entrance of more vortices into the sample. This picture represents a profile which is not typical, as we know. In this work, the diamagnetic response of the sample in the Meissner state manifest as the magnetization of the sample, increasing with the applied magnetic field. When the vortices enter the sample, the magnetization decrease showing jumps, how it is expected in samples with only one component, but the results in two-component show that after one jump in which the magnetization decrease, in the next jump can increase.

In the case of Fig.**7-2** (a), this first jump in the magnetization, owing to the transition from the Meissner state to the mixed state, occurs through of the component (S2) in which the partial flux penetrate due to the diamagnetic energy cost of holding the field out is less. The magnetization reaches a value higher in the component (S1) in which after the first peak in the magnetization it is growing again [see Fig.**7-2** (a)red curve], we can see that the value of the magnetization on the second peak exceeds the first one implying that the diamagnetism is growing in the other component and the cost of the diamagnetic energy to maintain the magnetic field out is higher in S1 than S2.

The magnetization curves show a more pronounced or step-like jumps at the lower values of the applied magnetic field.This behavior of the transitions can be explained using the Eq. 7-9 in which the ratio of Cooper-pair density between S2 and S1, that depend of the parameters used in each component. Therefore, the transitions with large variations in the magnetization curve are produced in S1, whereas the small variations to S2. One consequence of simulating a superconducting sample with two components is that we obtain two upper critical magnetic fields. Thus S1 reach its normal state at a value of the applied field less than S2, therefore S1 takes properties as a metal and establish a Dirichlet boundary condition on this side of the sample meanwhile the others sides remain with Newman boundary conditions. This is reflected in the behavior of the magnetization curve [Fig.**7-2** (a)] which normally drop with approximately same slop but in some point it change and drop in a higher value of H_2. In this point the superconductor sample reach a rectangular shape due to only in one have remain in superconducting state. In Fig. **7-2** (a) shown the influence of the electron mean free path l on the magnetic behavior of the sample. The level of magnetization is strongly influenced by the variations of the l, which turns out smaller with the reduction of l. This follows from the fact that, the magnetization drop with l, and the condensate on each half of the sample change providing poor and better screening of the magnetic field depending of the selected conditions in the superconductors (S_1 and S_2), and when one of the condensates ceases, the first condensate experiences a large difference in the felt magnetic field, which in turn allows for a larger flux penetration and thus a lower diamagnetic response of the sample. However, the free energy is lower influenced by changes in the electron mean free path [See Fig. **7-2** (b)] Figs. **7-2** (c-d) show the Cooper-pair density and the magnetic field distribution, as a function of the position for different values of electron mean free path l at $H_0 \approx 0$ value of the applied magnetic field. It is possible to observe that exist a position near to the interface in the sample at which the variation of the l does not affect the value of the condensates neither on the Nb nor on the Pb [see curves at Fig. **7-2** (c)], that implies new characteristics that can be found in this kind of samples taking into account that l modified always the diffusion on every materials. The magnetic field distribution show peaks at the edge as it is expected for a square superconducting sample but inside additional peaks field the interface at $L \approx 62\xi_1(0)$ decrease selecting lower values of l [see Fig. **7-2** (d)], i.e. Inset of the same figure is possible to see the difference between the field distribution in both components (S_1 and S_2).

In Fig. **7-3** shows obtained vortex configuration for several values of l at the same value of $H_0 = 0.0817H_{c2}$, in which is observed a huge differences between the condensates on each half. As we know, the coherence length is the characteristic length scale over which the order parameter changes and it is therefore related with the size of vortex core. Therefore, it is intuitive that size of vortices will change when it penetrate from one superconductor to another, but additionally, the mean free path make a contribution in this sense due to it is related with the characteristics length of a superconductor. In consequence, we can see that the reduction of l can preserve the condensate for higher values of applied magnetic field
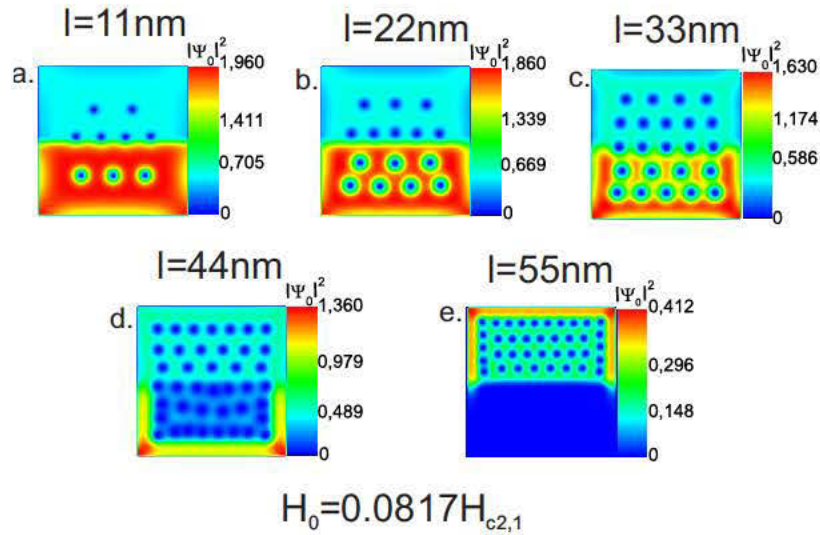
Figure 7-3: (Color online) (a-e) The contour plots of the Cooper-pair density of the hybrid superconducting sample immersed at the same applied magnetic field $H_0 = 0.0817$ different values of electron mean free path l.

[see Fig. 7-3 (a)] while for the same H_0 the superconductivity is quickly depreciated [see Fig. 7-3 (e)], which also produce a reduction of the vortex size as the l reduced. Finally, the hybrid superconductor can be considered a novel kind of superconducting system in which the main characteristic can be tuned to obtain the desired properties for any kind of use in electronic devices. In Figs. 7-4 show the behavior of the coherence length ξ and penetration depth λ for niobium and led whereas the electron mean free path is changed as well as between them. In thin films in the dirty limit $\xi_0 > l$ in which λ_0 and ξ_0 become dependent on l. The theory predicts that the coherence length is proportional to a square root of the electron mean-free path, $\xi \propto l^{1/2}$, as opposed to the increase of the penetration depth with decreasing:$l\lambda \propto l^{-1/2}$. However, in thin films, the effective penetration depth (λ_{eff}) might even be much larger.

7.1.3 Mesoscopic atomically-thin superconductors with spatially varied thickness

In this section, we investigate the influence of the variations of the thickness on the vortex configuration as well as free energy. Similar to the situation of the hybrid superconductor, the dimension of the sample are the same with side $a = 2000nm$ but only one half remains with thickness $d = 5.5nm$ while the other half take several lower values of d, where the vortices are confined in the thinner side of the sample, initially, in which the supercurrent is weaker and the vortices can enter first and move freely among the boundaries and the interface generated by the step-edge, interacting with each other repulsively.

Figs. 7-5 (a,b) show the free energy as a function of applied magnetic field and variation of
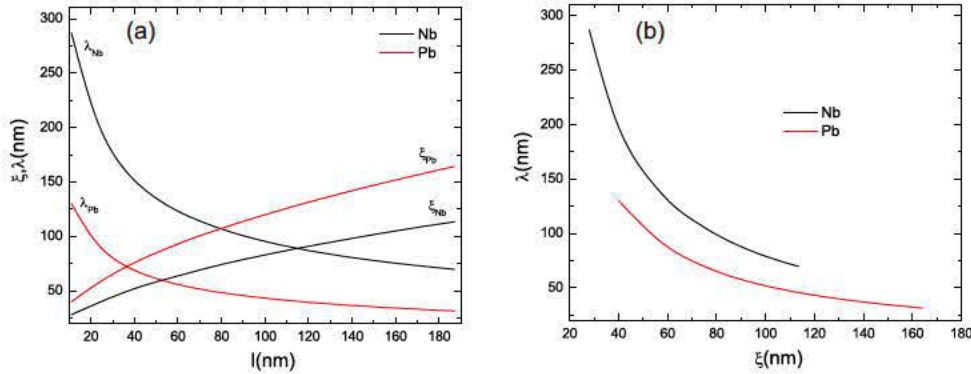
Figure 7-4: (Color online) characteristics lengths of a hybrid superconductor formed by niobium and led as a function of electron mean free path.

the thickness d as a function of the position. In all cases, the free energy of the Meissner state for the sample shown similar behavior for the different values d which is consequence of the lower screening barrier at the boundary obtained in the thinner section of the superconductor, therefore it bring on the enhanced penetration of the magnetic field, nevertheless, the first vortex enter is clearly modified due to changes on the interface where the step-edge generate a differences in the current density between both halves of the sample. Although the behavior of the peaks in each of the curves continues to occur for the different values of the applied magnetic field, they are very close to each other, which implies that the energy cost of the nucleation process is similar.
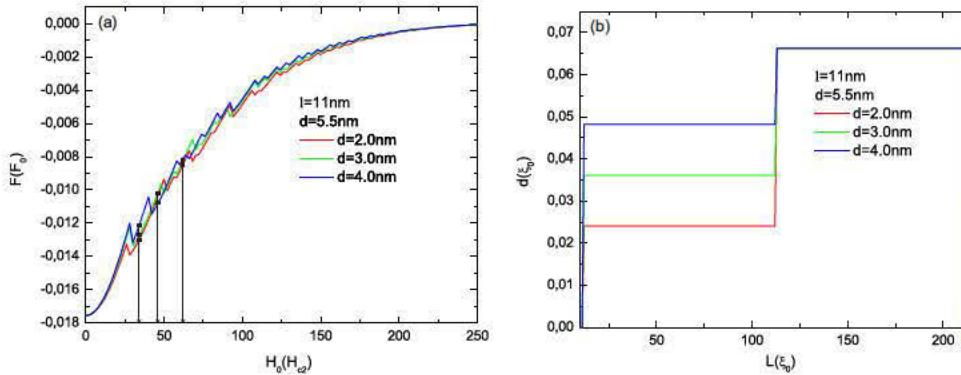
Figure 7-5: (Color online) (a) The free energy and magnetization as a function of the applied magnetic field H_0 of the superconducting sample with thickness $d/nm = 5.5$ in one half while several thickness $d/nm = 2.0, 3.0, 4.0$ on the other half (b). Vortex states are selected for different values of H_0 pointing for the arrows inset which correspond to the panels dispositions on Fig. **7-6**.

In Fig. **7-6** the vortex configuration reached on each halves for three considered values of H_0/H_{c2} is shown, in which can be appreciated the influence of the thickness in the behavior of the vortices. For the square sample the vortex states at $H_0 = 34H_{c2}$ it is possible to
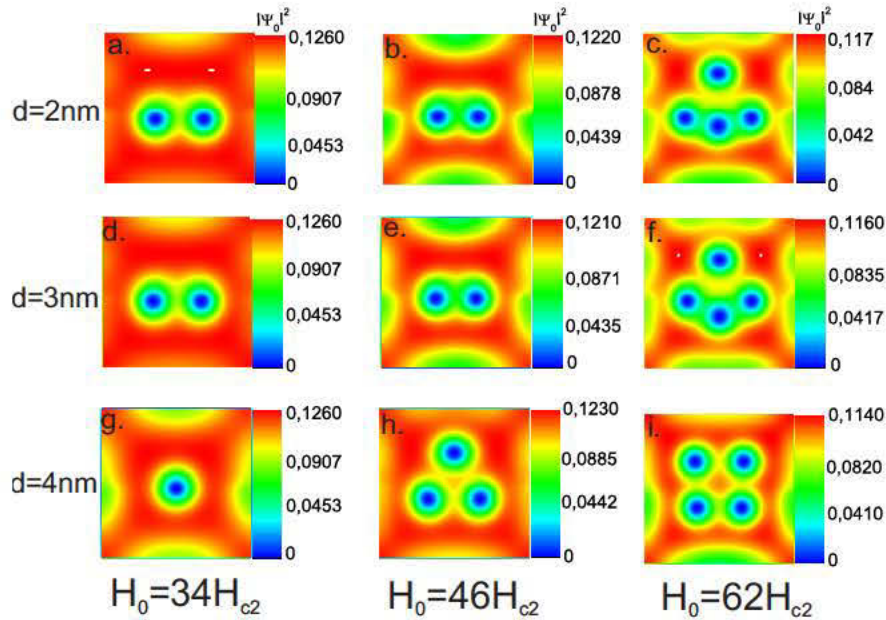
Figure 7-6: (Color online) (a-i) The Cooper-pair density plots for a superconducting thin sample with a step-edge generated by different thickness between both halves.

observe that only one vortex enter through the side with thickness $d = 4nm$ whereas for $d = 2nm, 3nm$ two vortices are sited in the same side. At $H_0 = 46H_{c2}$ and $H_0 = 62H_{c2}$ the difference remains to be one vortex in the entire superconducting sample, in this last case, we see that the effect caused by the repulsion between the vortices and the screening current provides enough energy to overcome the superconducting current at the interface getting the entrance of the vortices in the side of the sample with the thickness $d = 5.5nm$, while this does not occur for the case $d = 2nm, 3nm$ for which only one vortex can be entered.

7.1.4 Mesoscopic sample of one material with spatially different disorder

In this section, we investigate the influence of the electron mean free path (l) on the superconducting state in the square sample considering different cases such as a flat sample with two values of l on each halves, same value of l with two thickness on the sample and variations of l only in one half of the sample with two thickness. The systems proposed with the different configurations considering variations of the mean free path of the electron and the thickness, show the possibility to obtain results close to the experimental ones for this type of systems, in which the changes in thickness can be generated with the recent techniques of growth thin superconductors, as well as including the variations of the mean free path caused by the impurities of these systems when they are grown, as well as the inclusion at will of l through the implantation of heavy ions that modify the intrinsic properties of superconductor such as the coherence length ξ, current density and the magnetic field H_{c2}. In Fig. **7-7** shows
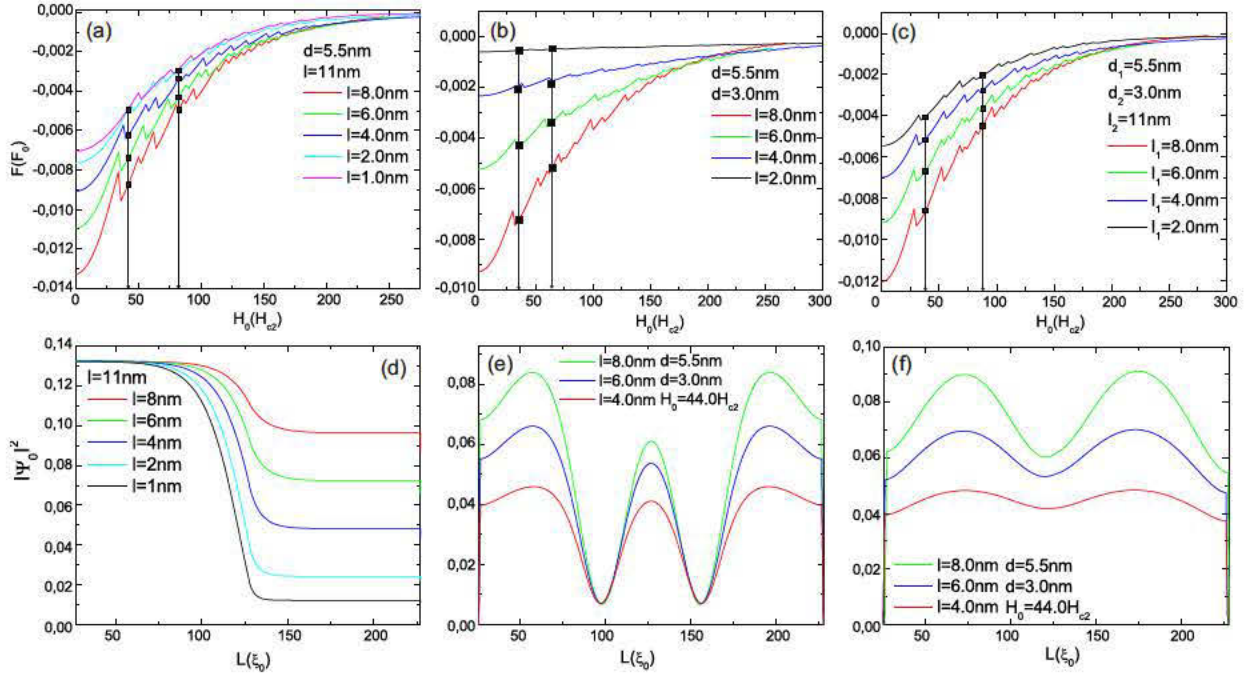
Figure 7-7: The free energy as a function of the applied magnetic field(a-c) and profile of
order parameter as a function of the position on the sample (d-f). (a) Flat
sample with thickness $d = 5.5nm$ and $l = 11nm$ in one half whereas l change
on the other half. (b) Thickness variation is included considering $d = 5.5nm$
in one half and $d = 3.0nm$ with changes of the l in the entire sample. (c)
Same thickness that (b) with $l = 11nm$ on the half where $d = 3.0nm$ and l is
changed on the half with $d = 5.5nm$. (d) Order parameter profile at $H_0 = 0.0$
for the case (a). (e) Order parameter for the case (b) at $H_0 = 44.0H_{c2}$ with
two vortices along the the interface whereas (f) is calculated perpendicular to
the interface.

the free energy as a function of H_0 a and variation of the order parameter as a function of
position of the mesoscopic superconducting square sample where the conditions of thickness
d and electron mean free path l will be changed on each half that we call h_1 and h_2, which
give us plenty information on the physical process in the superconductor. Fig. **7-7** (a) we
consider a flat sample with thickness $d = 5.5nm$ which show that the Meissner states curves
follow different values of the free energy, but also the value of H_0 at which the mixed state
is reached in the sample $H_0/H_{c2} = 36.0, 36.0, 40.0, 46.0, 52.0$ that clearly correspond to the
changes of $l/nm = 8.0, 6.0, 4.0, 2.0, 1.0$, respectively. In this figure, it is possible appreciate
the increase of energy of the sample considerably with the reduction of the electron mean
free path, then we can conclude that the superconducting condensate is depreciated with
the reduction of l.

This results is directly related to the two characteristics length of a superconducting sample:

Correlation length ξ and penetration depth λ in a magnetic field which depends on $l^{0.5}$ and $l^{-0.5}$ respectively. Therefore, the magnetic field in a superconductor is affected due to the increment of λ with the increases of concentration of impurities, but also a strong variation of the number of superconducting electrons, i.e. electrons linked in Cooper pairs with the decrease of ξ. This behavior is shown in Fig. **7-8** where two different kind of condensate are reached considering a spatial change of the electron mean free path. Therefore, the order parameter is modified through the sample as we can see in Fig. **7-7**(d), that show a reduction of value of $|\Psi_0|^2$ with the reduction of l, as we expected, according to the proportionality between the order parameter and penetration depth which is $|\Psi_0|^2 \sim 1/\lambda$.

Fig. **7-7**(b) show the free energy as a function of H_0 for a sample with thickness variation which is included considering $d = 5.5nm$ in h_1 and $d = 3.0nm$ in h_2, whereas the mean free path takes several values $l/nm = 8.0, 6.0, 4.0, 2.0$ over the entire superconducting sample. Additional case is studied including $d = 5.5nm$ with fixed $l = 11nm$ on h_1 while l takes several values only in h_2 with $d = 3nm$ [see Fig **7-7** (c)]. In Figs. **7-7**(b) and (c) the values of mean free path used are the same that considered in case of Fig. **7-7** (a), but due to the contribution of thickness a increment of energies can be notice in the huge separation among the curves in Fig. **7-7** (b), but also in Fig. **7-7** (c) despite of in this case the curves are closer. This behavior is a consequence of the dependence of λ and ξ on the thickness of Pb ultra thin sample. Using the equation for those lengths that include the mean free path, $\lambda_{eff} = 0.65\lambda_0\sqrt{\frac{\xi_0}{l(1-\frac{T}{T_c})}}$ and $\xi_{eff} = 0.85\sqrt{\frac{l\xi_0}{(1-\frac{T}{T_c})}}$ in which the thickness is included for a dirty superconductor $d << \xi_0$ considering $l = l_0/\xi_0$ and $l \approx 2d$ with $\xi_0/l \approx 1/d$ therefore $\lambda_{eff} \approx \lambda_0(\xi/d)^{1/2}$ and $\xi_{eff} \approx (\xi_0 d)^{1/2}$, it would occur if l were limited by surface scattering. The inclusion of thickness variation with mean free path clearly open two possibilities that are reflected in the curves of energy obtained in Figs. **7-7** (b) and (c), due to it can increase or decrease modifying d and l carefully, to have a interface which can be energetically disadvantageous, making length ξ greater than depth λ with the magnetic field already forced out, superconducting electron are reduced, and there is not sufficient energy gain obtained yet. In the case in which λ is larger than ξ, the magnetic field decreases smoothly and is forced out less faster than the electron forming pairs and the energy gain is obtained which is energetically advantageous.

In Fig. **7-8** the panels shows the obtained vortex configuration considering different values of applied magnetic field (H_0) where the vortices move, between h_1 in the upper half of the sample shown in every snapshot in Fig. **7-8** whereas h_2 cover the down part, over several conditions that include changes on thickness (d) and electron mean free path (l). In the figure **7-8** black panel, in which there is a superconductor with no change in the thickness d, while in h_1 it takes the value of $l = 11nm$ and in h_2 the mean free path varies $l/nm = 8.0, 6.0, 4.0, 3.0$. At low field $H_0 = 42H_{c2}$ we observe the first vortex enter only in h_1 where lower values of l has been considered than in h_2, indicative of the changes caused on the condensed of Cooper-pairs through the variations of l [See snapshots in the first column], but we can notice in Fig. **7-8** (g) that no vortex enters into the sample due to a large increase
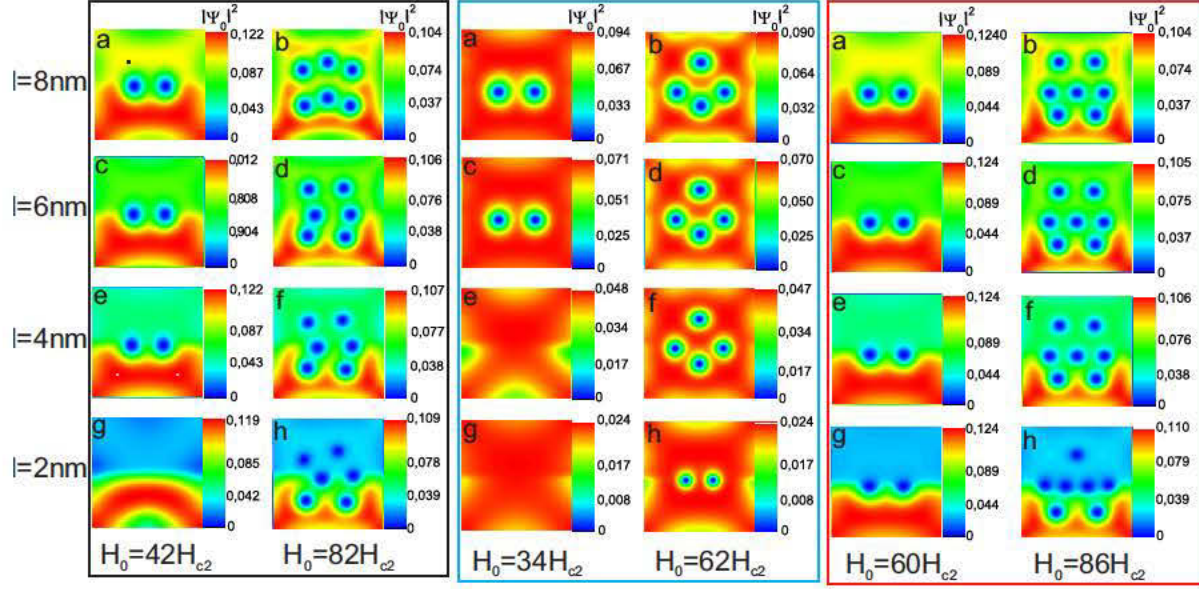
Figure 7-8: (Color online) The contour plots of the Cooper-pair density for selected different vortex states at certain values of applied magnetic field that show the vortices moving on the sample. (Black panel) Flat sample with thickness $d = 5.5nm$ and $l = 11nm$ in one half whereas l change on the other half. (Blue panel) Thickness variation is included considering $d = 5.5nm$ in one half and $d = 3.0nm$ with changes of the l in the entire sample. (Red panel) Same thickness that (blue panel) with $l = 11nm$ on the half where $d = 3.0nm$ and l is changed on the half with $d = 5.5nm$.

of impurity concentration with the reduction of mean free path until $l = 2.0nm$. In Fig. **7-8** on the second column is possible to appreciate the effect of the l over the influence on the movement of vortices toward the center compressing them increasingly, decreasing l, despite of the vortex-vortex repulsion at the same value of $H_0 = 82H_{c2}$.

In Fig. **7-8** blue panel, we include a change in the thickness considering $d = 5.5nm$ on h_1 and $d = 3.0nm$ on h_2, while the variations of l cover the entire sample. We can observe in the first column that the enter of the vortices is presented through h_2 where the sample is thinner, similar to that seen in the previous section for a particular case where $l = 11nm$ in the whole sample, but in this case we have considered lower values for l which an additional contribution due to the difference of thickness between h_1 and h_2 is obtained, as can be seen if we compare the snapshots in the Fig. **7-8** panels black and blue case (e), because in the first panel in h_1 with width $d = 5.5nm$ and $l = 4.0nm$ two vortices penetrated the sample, while this did not occur in the second panel with the same conditions of l and d on h_1. In the second column of the blue panel it is clearly shown, following the snapshots from top to bottom, as the reduction of l causes a decrease in vortex size, this is due to the relationship between the mean free path of the electron and the coherence length of, which is $\xi \approx l^{0.5}$.

The Fig. **7-8** red panel shown the Cooper pair density for a superconducting sample considering the following conditions of thickness and mean free path: $d = 3.0nm$ and $l = 11nm$ on h_2, while $d = 5.5nm$ and $l/nm = 8.0, 6.0, 4.0.2.0$ on h_1. In the first column in this figure, we can conclude that the effect of the l is greater than d, due to vortices enter through thicker half despite of the in the previous results shown on blue panel the vortices enter into the sample by the thinner side. This behavior can be also illustrated by the curves of the free energy on Figs. **7-5** and **7-7** in which the contributions of thickness to the changes to the energy are smaller than the mean free path. In the second column show the addiotonal contribution of l to the displacement of the vortices to the center of the sample, as it is possible to see in Fig. **7-8** panel (h) where large number of vortices are on the interface opposite to cases (b,d,f).

7.2 Conclusions

In the framework of the models discussed in this work, we study of the superconducting state of two-component mesoscopic square sample, where novel and rich magnetization curves, free energy and vortex configurations are obtained simulating two kind of ultra thin samples using niobium (Nb) and led (Pb). There has been much interest in such superconducting systems in which the number of degrees of freedom of the wave-function allows for emergent quantum effect that is otherwise unattainable in single-component superconductor. In this work, the two superconductors are simulated including anisotropies into the ultra thin sample which modifies the behavior of the carriers involved in the formation of the superconducting condensate which can be changed locally. The anisotropy in our first kind of two component superconducting samples studied in this paper, is considered including two superconductors on each half of the sample, a hybrid superconductor, which depends on the ratio of the sample parameters such as critical temperature c_T, penetration depth c_λ, coherence length c_ξ, electron mass c_m and the order parameters in each component which is tunable by ratio of this parameters that interact only in the interface between superconductors, and no the special boundary conditions is needed. In our work, the anisotropy is also modified including the variation of the electron mean free path in each half of the sample by using the expressions for GL coefficients α and β in the dirty limit whereas to simulate a sample in which the thickness does not uniformly vary, a additional term is included in the first GL equation to explore the recent development in the field of ultra thin superconductors and highlight the unprecedented physical properties of this systems in which we created a step-edge on each halve and a disrupt superconductivity is observed and also act as a barrier to improve the understanding of the processes in the interface superconductivity. This paper open the different possibilities for adapting the magnetic field penetration, coherent length, thickness and electron mean free path for a certain application taking into account that those components (Nb,Pb) are used commonly in the technological devices.

Publications.

The results presented in this chapter will be submitted:

- J. D. González, J. Barba-Ortega and M. V. Milošević, *Vortex matter in a two-component mesoscopic superconductor*, Phys. Rev. B (2018).

8 Summary

Due to quantum confinement, nanoscale superconductivity exhibits richer phenomena than bulk superconductivity. This will allow us to artificially design the electronic properties by changing the size and geometry of the superconductor, leading to the desired control and enhancement of superconductivity. Looking toward the future, we have shown theoretical and numerically is possible that having the ability to induce changes in the local structure and properties at the mesoscopic superconductor sample offers a useful quantum nanotechnology workbench to design superconducting nanostructures for investigating both fundamental interest and practical applications of quantum electronics.

In the present thesis, we theoretically investigated several aspects of nanoscale superconductivity of novel two-component superconductors by using the self-consistently the Ginzburg-Landau equations generalized that includes the GL coefficients α and β in the dirty limit whereas to simulate a sample in which the thickness does not uniformly vary, an additional term is included in the first GL equation to explore the recent development in the field of ultra thin superconductors and highlight the unprecedented physical properties of this systems in which we created a step-edge. It provides us with a great potential for applications in ultra-fast, power-saving electronic devices such as superconducting transistors and single-photon detectors.

In the introductory chapters of this thesis, I first reviewed historic events related to superconductivity. Further, different theoretical frameworks are presented, starting from phenomenological models of brothers London and Ginzburg and Landau, up to more sophisticated microscopic approaches, namely Bardeen-Cooper-Schrieffer model. In addition, In addition, The intrinsic properties of the superconductors and response to the applied magnetic field, as well as the behavior of the vortices is included in **Chapter 1**. In **Chapter 2** I described the basic numerical approaches that I have used to solve the Ginzburg-Landau equations. The central equations for order parameter and supercurrent are derived, where characteristic quantities, such as coherence length, penetration depth are explained. In **Chapter 3**, I exemplified some experimental results of the studied vortex matter with direct vortex imaging techniques. Experiments sensitive directly to the vortex magnetic field and with sufficient spatial resolution to resolve individual vortices. In addition, different experimental setups used to manipulate the vortex behavior through external means are presented, where particular attention is given to design of a pinning landscape and individual vortex manipulation

by a nearby magnetic or tunneling tip, or a laser beam.

In **Chapter** 4, We studied the effect of different negative values of the deGennes parameter in the thermodynamics properties for a small superconducting square of size $3\xi(0) \times 3\xi(0)$ in the presence of an applied external magnetic field by solving the coupled nonlinear Ginzburg-Landau equations. We considered the lateral surface of the sample in contact with a thin superconducting layer at higher critical temperature. Our results shows that a giant vortex state and multi-vortex state appear in the sample choosing a convenient value of $b < 0$ parameter, even for such small system. The vorticity, the local magnetic filed, Cooper pair density, magnetization and the phase of order parameter depend strongly of the chosen boundary condition. Also, the upper magnetic field H_{c3} grows when the values of the deGennes parameter decreases toward negative values. We present new results in this work such as the analytical dependence between the third critical field, maximum of the magnetization and b-parameter and a weak dependence of the first critical field as a function of the b-parameter.

In **Chapter** 5, We investigated theoretically the influences of the centered geometrical defects formed by higher/lower critical temperature superconducting sample on the vortex configuration in a thin superconducting disk. We calculated the magnetization, Cooper pair density, magnetic field, super-current density and free energy as a function of time for hexagonal and pentagonal defects. The vortex lattice was different in the two geometries used due to the fact that it tries to be adapt to the geometry of the sample. This influences considerably the stability range of the different vortex states. We also want to emphasize that the surface barrier generated by given $f(r, \theta)$ values, plays a crucial role for the pinning/anti-pinning effect, which not only accelerates the vortices to rush into the central area but also decelerates or even stops the vortex to escape from the defects due to the surface barrier. Additionally, We studied the properties of a mesoscopic superconducting thin disk with an array of overlapped triangular and circular defects with changes in T_c across the sample, which includes a spatially distributed anisotropy coefficient γ. Our first finding was that we showed the great influence of the magnetization, free energy, and supercurrent density as a function of the anisotropy level and spatial distribution on the formation of geometrical defects, as well as on the changes in the size of the sample and on the triangular and circular defects. We found that the transitions to different vortex states can be suitably modified in order to obtain the desired states. Furthermore, we investigated the vortex configurations in the sample with two geometrical defects in order to establish a complex configuration of the spatial variation of the critical temperature T_c. We found that the energy barrier can be modified spatially in the sample by considering regions with lower/higher superconductivity and choosing anisotropy $(1/\gamma)$ greater than or less than 1, which can favor the entrance of the vortices into the defect or produce their repulsion. Therefore, this determines the competition, which results in the final vortex configuration, but with the help of the vortex-vortex interaction and the boundary of the sample. Additionally, we have studied the supercon-

ducting array pinning of magnetic flux quanta by using a continuous wave laser (CWL) to obtain a nanoscale modulation of local temperature T. This creates an energy landscape for flux quanta, where the size and shape of weak-superconducting zones can be tuned over the same sample without any structural change even at any value of the applied magnetic field H_0. In addition to its fundamental interest, the possibility to manipulate flux quanta by designing the structure of superconducting condensate along the entire superconductor is relevant in view of applications. These include fluxtronic devices based on the controlled motion of flux quanta, for which the weak-superconducting zones is created also might be used for the fabrication of reconfigurable nanodevices based on versatility that offer the system proposed in this experimental simulation.

In **Chapter** 6, We studied vortex configurations in a superconducting flat disk with topological defects in the framework of the time dependent Ginzburg Landau theory. Our calculations shows that numerous kinds of vortex lattice structures can be obtained, some of which have different symmetries depending which defect were used. For circular barrier or hole defects, the vortex lattice still exists with increasing the magnetic field, it gradually transforms into a circular vortex configuration and larger density of vortices, clusters of vortices are particularly favorable around the defects. To illustrate the transition between these vortex states we present figures that shows the values of the applied magnetic field in which the vortices entrance take place, as well as the number of vortices. Due to the influence of the shell vortices and the boundaries conditions in the disk, a transition from Abrikosov-like vortex lattice was obtained. Moreover, structural defects that included geometrical shapes such as pentagonal and hexagonal trench and barrier on the thermodynamical properties of a mesoscopic superconducting disk with a central hole solving the time dependent Ginzburg-Landau equations. We take two values for the deGennes parameter $b = 0$, simulating a sample with its lateral surface in complete normal state and $b \rightarrow \infty$, simulating a usual superconducting/vacuum interface. Our results have shown that the lower thermodynamics field H_{c1} depends strongly on the chosen boundary condition and the nature of the defects and is independent of the geometry of the defects, whereas the upper magnetic field H_{c3} depends just on the boundary condition, that is, due to the force of the pinning (trench) and the anti-pinning centers (barrier) are high. We believe that these findings are relevant not only for groups working on or exploring the vortex state and manipulation of nanoengineered superconductors, but also for those studying confined systems where similar competing interactions take place. Using the bi-dimensional Ginzburg-Landau approach we have studied the vortex matter and local field distribution in a microscopic structure consisting of a square prism with a central square dot. We found that this system projects an interesting decrease in the vorticity even when the external applied magnetic field is increasing. This thermodynamically stable vortex-anti-vortex pattern could be due to the condensate confinement by the boundary of the mesoscopic microstructure. Also in this structure two values for the Ginzburg Landau parameter $\kappa_1 = 1.0$, $\kappa_c \simeq 1/\sqrt{2}$ and two different boundary conditions

$b = 0$ and $b \to \infty$ was considered. Our results have shown that the critical fields H_1 and H_2 depend of κ and b. We demonstrated that the extrapolation deGennes parameter b for tunneling of Cooper pairs at the sample boundary and angular width θ of the slit in the Squid sample geometry plays an important role in the magnetization and vorticity of the sample. The results includes the linear behavior of the maximum of the magnetization as a function of the angular width of the slits corresponds to $-4\pi M_{Max} \simeq 0.00126d + 0.0196$. Other very interesting result is that for our system the first vortex penetration field and vorticity strongly depends on the boundary condition, e.g. $H_1(b < 0) < H_1(b > 0)$, and $N(b > 0) < N(b < 0)$ at $H_e = 0.452$, when is well known that a superconducting/dielectric interface should decrease the first vortex penetration field and vice-versa for the proximity to a superconductor.

In **Chapter** 7, In the framework of the models discussed in this work, we studied the superconducting state of two-component mesoscopic square sample, where novel and rich magnetization curves, free energy and vortex configurations are obtained simulating two kind of ultra thin samples using niobium (Nb) and led (Pb). There has been much interest in such superconducting systems in which the number of degrees of freedom of the wave-function allows for emergent quantum effects that is otherwise unattainable in single-component superconductor. In this work, the two superconductors are simulated including anisotropies into the ultra thin sample which modifies the behavior of the carriers involved in the formation of the superconducting condensate which can be changed locally. The anisotropy in our first kind of two component superconducting samples studied in this work, is considered including two superconductors on each half of the sample, a hybrid supercon-ductor, which depends on the ratio of the sample parameters such as critical temperature c_T, penetration depth c_λ, coherence length c_ξ, electron mass c_m and the order parameters in each component which is tunable by ratio of this parameters that interact only in the interface between superconductors, and special boundary conditions is not needed. In our work, the anisotropy is also modified including the variation of the electron mean free path in each half of the sample by using the expressions for GL coefficients α and β in the dirty limit whereas to simulate a sample in which the thickness does not uniformly vary, a ad-ditional term is included in the first GL equation to explore the recent development in the field of ultra thin superconductors and highlight the unprecedented physical properties of this systems in which we created a step-edge on each halve and a disrupt superconductivity is observed and also act as a barrier to improve the understanding of the processes in the interface superconductivity. This work open the different possibilities for adapting the mag-netic field penetration, coherent length, thickness and electron mean free path for a certain application taking into account that those components (Nb,Pb) are used commonly in the technological devices.

Bibliography

[1] H. Baek, J. Ha, D. Zhang, B. Natarajan, J. P. Winterstein, R. Sharma, Paglione, J., Y. Kuk, N. B Zhitenev, and J. A. Stroscio. Creating nanostructured superconductors on demand by local current annealing. *Phys. Rev. B*, 92:094510, 2015.

[2] H. Kamerlingh Onnes. The resistance of pure mercury at helium temperatures. *Leiden Communications*, 122b:482, 1911.

[3] J. File and R. G. Mills. Observation of persistent current in a superconducting solenoid. *Phys. Rev. Lett.*, 10:93, 1963.

[4] W. Meissner and R. Ochsenfeld. Ein neuer effekt bei eintritt der supraleitf higkeit. *Naturwissenschaften*, 21:787, 1933.

[5] V. Ginzburg and L. Landau. *Zh. Eksp. Teor. Fiz.*, 20:1064, 1950.

[6] A. A. Abrikosov. On the magnetic properties of superconductors. *Sov. Phys. JETP*, 5:1174, 1957.

[7] L. P. Gor'kov. Microscopic derivation of the ginzburg-landau equations in the theory of superconductivity. *Sov. Phys. JETP*, 36:1364, 1959.

[8] J. Bardeen, L. N. Cooper, and J. R. Schrieffer. Theory of superconductivity. *Phys. Rev.*, 108:1175, 1957.

[9] J. G. Bednorz and A. K. Müller. Possible high-$_c$ superconductivity in the Ba-La-Cu-O. *Zeitschrift fur Physik B Condensed Matter*, 64:189, 1986.

[10] A. Schilling, M. Cantoni, J. D. Guo, and H.R. Ott. Superconductivity above 130 k in the Hg-Ba-Ca-Cu-O system. *Nature (London)*, 363:56, 1993.

[11] H. Maeda, Y. Tanaka, M. Fukutomi, and T. Asano. A new high-T_c oxide superconductor without a rare earth element. *Japanese Journal of Applied Physics*, 27:27, 1988.

[12] S. N. Putilin, E. V. Antipov, A. M. Abakumov, M. G. Rozova, K. A. Lokshin, D. A. Pavlov, Balagurov A. M., D. V. Sheptyakov, and Marazio M. Effect of fluorination and high pressure on the structure and properties of the Hg-bearing superconducting cu mixed oxides. *Physica C*, 338:52, 2000.

[13] L. Gao, Y. Y. Xue, F. Chen, Q. Xiong, R. L. Meng, D. Ramirez, C. W. Chu, J. H. Eggert, and H. K. Mao. Superconductivity up to 164K in $HgBa_2Ca_{m-1}Cu_mO_{2m+2+\delta}$ (m=1, 2, and 3) under quasihydrostatic pressures. *Phys. Rev. B*, 50:4260, 1994.

[14] Y. Maeno, H. Hashimoto, K. Yoshida, S. Nishizaki, T. Fujita, J. G. Bednorz, and F. Lichtenberg. Superconductivity in a layered perovskite without copper. *Nature (London)*, 372:532, 1994.

[15] T. M. Rice and M. Sigrist. Sr_2RuO_4 : An electronic analogue of 3He. *Journal of Physics: Condensed Matter*, 7:L643, 1995.

[16] J. Nagamatsu, N. Nakagawa, T. Muranaka, Y. Zenitani, and J. Akimitsu. Superconductivity at 39 k in magnesium diboride. *Nature (London)*, 410:63, 2001.

[17] P. C. Canfield and G. W. Crabtree. Magnesium diboride: Better late than never. *Physics Today*, 56:34, 2003.

[18] H. Hosono and Z.-A. Ren. Focus on iron-based superconductors. *Journal of Physics*, 11:025003, 2009.

[19] K. Ishida, Y. Nakai, and H. Hosono. To what extent iron-pnictide new superconductors have been clarified: A progress report. *Journal of the Physical Society of Japan*, 78:062001, 2009.

[20] D. B. Haviland, Y. Liu, and A. M. Goldman. Onset of superconductivity in the two-dimensional limit. *Phys. Rev. Lett.*, 62:2180, 1989.

[21] A. F. Hebard and M. A. Paalanen. Magnetic-field-tuned superconductor-insulator transition in two-dimensional films. *Phys. Rev. Lett.*, 65:927, 1990.

[22] Y. Liu and D. B. Haviland. Insulator to superconductor transition in ultrathin films. *Phys. Rev. B*, 47:5931, 1993.

[23] Y. Qin, C. L. Vicente, and J. Yoon. Magnetically induced metallic phase in superconducting tantalum films. *Phys. Rev. B*, 73:100505, 2006.

[24] T. Nishio, M. Ono, T. Eguchi, H. Sakata, and Y. Hasegawa. Superconductivity of nanometer-size Pb islands studied by low-temperature scanning tunneling microscopy. *Appl. Phys. Lett.*, 88:113115, 2006.

[25] D. Eom, S. Qin, M. Y. Chou, and C. K. Shih. Persistent superconductivity in ultrathin Pb films: a scanning tunneling spectroscopy study. *Phys. Rev. Lett.*, 96:27005, 2006.

[26] S. Qin, J Kim, Q. Niu, and C. K. Shih. Superconductivity at the two-dimensional limit. *Science*, 324:1314, 2009.

[27] T. Zhang, P. Cheng, W. Li, Y. Sun, G. Wang, X. Zhu, K. He, L. Wang, X. Ma, X. Chen, Y. Wang, Y. Liu, H. Lin, H. Jia, and Q. Xue. Superconductivity in one-atomic-layer metal films grown on Si(111). *Nat. Phys.*, 6:104, 2010.

[28] N. Reyren, S. Thiel, A. D. Caviglia, L. Fitting-Kourkoutis, G. Hammerl, C. Richter, C. W. Schneider, T. Kopp, and Ruet A. S. Superconducting interfaces between insulating oxides. *Science*, 317:1196, 2007.

[29] A. Gozar, G. Logvenov, L. Fitting-Kourkoutis, A. T. Bollinger, L. A. Giannuzzi, D. A. Muller, and I. Bozovic. Superconducting interfaces between insulating oxides. *Nature (London)*, 455:782, 2008.

[30] Q.Y. Wang, Z. Li, W. H. Zhang, Z. C. Zhang, J. S. Zhang, W. Li, H. Ding, Y.-B. Ou, P. Deng, K. Chang, and J. Wen. Interface-induced high-temperature superconductivity in single unit-cell fese films on $SrTiO_3$. *Chin. Phys. Lett.*, 29:37402, 2012.

[31] N. E. Staley, J. Wu, P. Eklund, Y. Liu, L. Li, and Z. Xu. Electric field effect on superconductivity in atomically thin flakes of $NbSe_2$. *Phys. Rev. B*, 80:184505, 2009.

[32] D. Jiang, T. Hu, Y. Lixing, Q. Li, A. Li, H. Wang, G. Mu, Z. Chen, and H. Zhang. $High - T_c$ superconductivity in ultrathin $Bi_2Sr_2CaCu_2O_{8+x}$ down to half-unit-cell thickness by protection with graphene. *Nat. Commun.*, 5:5708, 2014.

[33] Y. Cao, A. Mishchenko, G. L. Yu, E. Khestanova, A. P. Rooney, E. Prestat, A. V. Kretinin, P. Blake, M. B. Shalom, and C. Woods. Quality heterostructures from two-dimensional crystals unstable in air by their assembly in inert atmosphere. *Nano Lett.*, 15:4914, 2015.

[34] X. Xi, L. Zhao, Z. Wang, H. Berger, L. Forró, J Shan, and K. F. Mak. Strongly enhanced charge-density-wave order in monolayer $NbSe_2$. *Nat. Nanotechnol.*, 10:765, 2015.

[35] K. Ueno, S. Nakamura, H. Shimotani, A. Ohtomo, N. Kimura, T. Nojima, H. Aoki, Y. Iwasa and M. Kawasaki. Electric-field-induced superconductivity in an insulator. *Nat. Mater.*, 7:855, 2008.

[36] J. T. Ye, S. Inoue, K. Kobayashi, Y. Kasahara, H. T. Yuan, H. Shimotani and Y. Iwasa. Liquid-gated interface superconductivity on an atomically flat film. *Nat. Mater.*, 9:125, 2010.

[37] F. London and H. London. The electromagnetic equation of the supraconductor. *Proc. Roy. Soc.*, 49:71, 1935.

[38] L. N. Cooper. Bound electron pairs in a degenerate fermi gas. *Phys. Rev.*, 104:1189, 1956.

[39] L. D. Landau and E. M. Lifshitz. *Statical Physics.* Pergamon Press, Oxford, London, 1980.

[40] P. G. de Gennes. *Superconductivity of Metals and Alloys.* Benjamin, New York, 1966.

[41] M. Tinkham. *Introduction to superconductivity.* McGraw Hill, New York, 1975.

[42] A. A. Shanenko, M. V. Milošević, F. M. Peeters, and V. Vagova. Extended ginzburg-landau formalism for two-band superconductors. *Phys. Rev. Lett.*, 106:106, 2011.

[43] H. B. Nielsen and P. Olesen. A quantum liquid model for the QCD vacuum: gauge and rotational invariance of domained and quantized homogeneous color fields. *Nucl. Phys. B.*, 160:380, 1979.

[44] G. Stenuit, S. Michotte, J. Govaerts, and L. Piraux. Temperature dependence of penetration and coherence lengths in lead nanowires. *Supercond. Sci. Technol.*, 18:174, 2005.

[45] P. S. Deo, V. A. Schweigert, F. M. Peeters, and A. K. Geim. Magnetization of mesoscopic superconducting disks. *Phys. Rev. Lett.*, 79:4653, 1997.

[46] V. A. Schweigert, F. M. Peeters, and P. S. Deo. Vortex phase diagram for mesoscopic superconducting disks. *Phys. Rev. Lett.*, 81:2783, 1998.

[47] B. J. Baelus and F. M. Peeters. Dependence of the vortex configuration on the geometry of mesoscopic flat samples. *Phys. Rev. B*, 65:104515, 2002.

[48] Y. E. Lozovik and E. A. Rakoch. Energy barriers, structure, and two-stage melting of microclusters of vortices. *Phys. Rev. B*, 57:1214, 1998.

[49] L. R. E. Cabral, B. J. Baelus, and F. M. Peeters. From vortex molecules to the abrikosov lattice in thin mesoscopic superconducting disks. *Phys. Rev. Lett.*, 70:144523, 2004.

[50] L. Vagov, A. A. Shanenko, and F. M. Peeters. Superconductivity between standard types: Multiband versus single-band materials. *Phys. Rev. B.*, 93:174503, 2016.

[51] C. P. Bean and J. D. Livingston. Surface barrier in type-II superconductors. *Phys. Rev. Lett.*, 12:14, 1964.

[52] V. V. Schmidt. *The Physics of Superconductors: Introduction to Fundamentals and Applications.* Springer-Verlag, Berlin Heidelberg, 1997.

[53] G. S. Mkrtchyan and V. V. Schmidt. Interaction between a cavity and vortex in a superconductor of the second kind. *Sov. Phys. JETP*, 34:195, 1972.

[54] U. Essmann and H. Trauble. The magnetic structure of superconductors. *Sci. Am.*, 224:74, 1971.

[55] W. H. Kleiner, L. M. Roth, and S. H. Autler. The magnetic structure of superconductors. *Phys. Rev.*, 133:A1226, 1964.

[56] R. Kato, Y. Enomoto, and S. Maekawa. Effects of the surface boundary on the magnetization process in type-II superconductors. *Phys. Rev. B*, 47:8016, 1993.

[57] A. Schmid. A time dependent ginzburg-landau equation and its application to the problem of resistivity in the mixed state. *Phys. Kondens. Mater.*, 5:302, 1966.

[58] W. D. Gropp, H. G. Kaper, G. K. Leaf, D. M. Levine, M. Palumbo, and V. M. Vinokur. A time dependent ginzburg-landau equation and its application to the problem of resistivity in the mixed state. *J. Comput. Phys.*, 123:254, 1996.

[59] S. J. Bending. A time dependent ginzburg-landau equation and its application to the Local magnetic probes of superconductors. *Adv. in Phys.*, 48:449, 1999.

[60] I. V. Grigorieva. Magnetic flux decoration of type-II superconductors. *Supercond. Sci. Technol.*, 7:729, 1994.

[61] I. V. Grigorieva, W. Escoffier, J. Richardson, L. Y. Vinnikov, S. Dubonos, and V. Oboznov. Direct observation of vortex shells and magic numbers in mesoscopic superconducting disks. *Phys. Rev. Lett.*, 96:077005, 2006.

[62] P. E. Goa, H. Hauglinr, M. Baziljevich, E. Ilýashenko, P. Gamme, and T. Johansen. Real-time magneto-optical imaging of vortices in superconducting $NbSe_2$. *Supercond. Sci. Technol.*, 14:729, 2001.

[63] D. V. Denisov, D. V Shantsev, Y. M. Galperin and E. Choi. Onset of Dendritic Flux Avalanches in Superconducting Films. *Phys. Rev. Lett.*, 97:077002, 2006.

[64] R. B. G. Kramer, A. V. Silhanek, W. Gillijns, and V. V. Moshchalkov. Imaging the statics and dynamics of superconducting vortices and antivortices induced by magnetic microdisks. *Phys. Rev. X*, 1:021004, 2011.

[65] J. C. Loudon, C. J. Bowell, N. D. Zhigadlo, J. Karpinski and P. A. Midgley. Magnetic structure of individual flux vortices in superconducting MgB_2 derived using transmission electron microscopy. *Phys. Rev. B.*, 87:144515, 2013.

[66] M. J. G. Cottet, M. Cantoni and B. Mansart. Quantitative imaging of flux vortices in the type-II superconductor MgB_2 using cryo-Lorentz transmission electron microscopy. *Phys. Rev. B.*, 88:014505, 2013.

[67] N. Kokubo, S. Okayasu, A. Kanda and B. Shinozaki. Scanning SQUID microscope study of vortex polygons and shells in weak-pinning disks of an amorphous superconducting film. *Phys. Rev. B.*, 82:014501, 2010.

[68] A. Kremen, S. Wissberg, N. Haham, E. Persky, Y. Frenkel and B. Kalisky. Mechanical Control of Individual Superconducting Vortices. *Nano Lett.*, 16:1626, 2016.

[69] C. J. Chen. Origin of atomic resolution on metal surfaces in scanning tunneling microscopy. *Phys. Rev. Lett.*, 25:448, 1990.

[70] T. Zhang, P. Cheng, W. Li, Y. Sun, G. Wang, X. Zhu, K. He, L. Wang, X. Ma, X. Chen, Y. Wang, Y. Liu, H. Lin, H. Jia, and Q. Xue. Superconductivity in one-atomic-layer metal films grown on Si(111). *Nat. Phys.*, 6:104, 2010.

[71] C. Song, Y. Wang, P. Cheng, Y. Jiang, W. Li, and T. Zhang. Direct observation of nodes and twofold symmetry in FeSe superconductor. *Science*, 332:1410, 2011.

[72] I. Guillamon, H. Suderow, A. Fernández-Pacheco, J. Sesé, R. Córdoba, J. M. De Teresa, M. R. Ibarra and S. Vieira. Direct observation of melting in a 2-D superconducting vortex lattice. *Nat. Phys.*, 5:651, 2009.

[73] I. Guillamon, R. Córdoba, J. Sesé, J. M. De Teresa, M. R. Ibarra and H. Suderow. Enhancement of long-range correlations in a 2D vortex lattice by an incommensurate 1D disorder potential. *Nat. Phys.*, 10:851, 2014.

[74] J. Ge, V. N. Gladilin, J. Tempere, C. Xue, J. Devreese, J. Van de Vondel, Y. Zhou and V. V. Moshchalkov. Nanoscale assembly of superconducting vortices with scanning tunnelling microscope tip. *Nat. Commun.*, 7:13880, 2016.

[75] J. Ge, V. N. Gladilin, J. Tempere, C. Xue, J. Devreese, and V. V. Moshchalkov. Controlled Generation of Quantized Vortexâˆ’Antivortex Pairs in a Superconducting Condensate. *Nano Lett.*, 17:5003, 2017.

[76] I. S. Veshchunov, W. Magrini, S. V. Mironov, A. G. Godin, J.-B. Trebbia, A. I. Buzdin. Optical manipulation of single flux quanta. *Nat. Commun.*, 7:12801, 2016.

[77] J. Simonin. Surface term in the superconductive Ginzburg-Landau free energy: Application to thin films. *Phys. Rev. B*, 33:7830, 1986.

[78] W. P. Halperin. Quantum size effects in metal particles. *Rev. Mod. Phys.*, 58:533, 1986.

[79] Y. G. Sun and Y. N. Xia. Shape-controlled synthesis of gold and silver nanoparticles. *Science*, 298:2176, 2002.

[80] D. J. Harrison, K. Fluri, K. Seiler, Z. H. Fan, C. S. Effenhauser, and A. Manz. Micromachining a miniaturized capillary electrophoresis-based chemical analysis system on a chip. *Science*, 261:895, 1993.

[81] F. Baletto and R. Ferrando. Structural properties of nanoclusters: Energetic, thermodynamic, and kinetic effects. *Rev. Mod. Phys.*, 77:371, 2005.

[82] A. E. Koshelev and V. M. Vinokur. Suppression of surface barriers in superconductors by columnar defects. *Phys. Rev. B*, 64:64, 2001.

[83] D. S. Golubovic, V. M. Milosevic, F. M. Peeters, and V. V. Moshchalkov. Magnetically induced splitting of a giant vortex state in a mesoscopic superconducting disk. *Phys. Rev. B*, 71:180502, 2005.

[84] M. V. Milosevic and F. M. Peeters. Vortex-antivortex lattices in superconducting films with magnetic pinning arrays. *Phys. Rev. Lett.*, 93:267006, 2004.

[85] M. V. Milosevic and F. M. Peeters. Superconducting wigner vortex molecule near a magnetic disk. *Phys. Rev. B*, 68:024509, 2003.

[86] G. R. Berdiyorov, B. J. Baelus, M. V. Milosevic, and F. M. Peeters. Stability and transition between vortex configurations in square mesoscopic samples with antidots. *Phys. Rev. B*, 68:174521, 2003.

[87] M. V. Milosevic, G. R. Berdiyorov, and F. M. Peeters. Fluxonic cellular automata. *Appl. Phys. Lett.*, 91:212501, 2007.

[88] J. K. Gregory, M. S. James, S. J. Bending, C. J. van der Beek, and M. Konczykowski. Suppression of surface barriers for flux penetration in $Bi_2Sr_2CaCu_2O_{8+\delta}$ whiskers by electron and heavy ion irradiation. *Phys. Rev. B*, 64:134517, 2001.

[89] Y. A. Genenko, H. Rau, and S. V. Yampolskii. The bean-livingston barrier at a superconductor/magnet interface. *Journal of Physics: Condensed Matter*, 17:L93, 2005.

[90] R. G. Mints and I. B. Snapiro. Surface-barrier and magnetization relaxation in layered superconductors. *Phys. Rev. B*, 47:3273, 1993.

[91] E. Zeldov, A. I. Larkin, V. B. Geshkenbein, M. Konczykowski, D. Majer, B. Khaykovich, V. M. Vinokur, and H. Shtrikman. Surface-barrier and magnetization relaxation in layered superconductors. *Phys. Rev. Lett.*, 73:1428, 1994.

[92] J. Barba-Ortega, J. D. González, and E. Sardella. Superconducting state of a disk with a pentagonal/hexagonal trench/barrier. *J. Low. Temp. Phys.*, 174:96, 2014.

[93] J. Barba-Ortega, E. Sardella, and J. A. Aguiar. Superconducting boundary conditions for mesoscopic circular samples. *Supercond. Sci. Technol.*, 24:015001, 2011.

[94] P. N. Lisboa-Filho, A. L. Malvezzi, and E. Sardella. Minimum size for the occurrence of vortex matter in a square mesoscopic superconductor. *Physica B*, 403:1494, 2008.

[95] J. Barba-Ortega and J. A. Aguiar. De gennes parameter limit for the occurrence of a single vortex in a square mesoscopic superconductor. *Physica C*, 469:754, 2009.

[96] B. J. Baelus, S. V. Yampolskii, and F. M. Peeters. Superconducting properties of mesoscopic cylinders with enhanced surface superconductivity. *Phys. Rev. B*, 65:024510, 2001.

[97] F. Rogeri, P. Zadorosny, P. Lisboa, E. Sardella, and W. Ortiz. Magnetic field profile of a mesoscopic squid-shaped superconducting film. *Supercond. Sci. Technol.*, 26:075005, 2013.

[98] E. W. J. Straver, J. E. Hoffman, M. Auslaender, D. Rugar, and A. Kathryn. Controlled manipulation of individual vortices in a superconductor. *Appl. Phys. Lett.*, 93:172514, 2008.

[99] D. Larbalestier, A. Gurevich, D. M. Feldmann, and A. Polyanskii. Review article high-Tc superconducting materials for electric power applications. *Nature (London)*, 414:638, 2001.

[100] R. M. Scanlan, A. P. Malozemoff, and D. Larbalestier. Superconducting materials for large scale applications. *Proc. IEEE*, 92:1639, 2004.

[101] T. Haugan, P. N. Barnes, R. Wheeler, F. Meisenkothen, and M. Sumption. Addition of nanoparticle dispersions to enhance flux pinning of the $YBa_2Cu_3O_{7-x}$ superconductor. *Nature (London)*, 430:867, 2004.

[102] S. Kang, A. Goyal, J. Li, A. A. Gapud, P. M. Martin, L. Heatherly, J. R. Thompson, D. K. Christen, F. A. List, M. Paranthaman, and D. F. Lee. High-performance high-T_c superconducting wires. *Science*, 311:1911, 2006.

[103] J. E. Villegas, S. Savelev, F. Nori, E. M. Gonzalez, J. V. Anguita, R. Garcia, and J. L. Vicent. A superconducting reversible rectifier that controls the motion of magnetic flux quanta. *Science*, 302:1188, 2003.

[104] M. B. Hastings, C. J. Olson Reichhardt, and C. Reichhardt. Ratchet cellular automata. *Phys. Rev. Lett.*, 90:247004, 2003.

[105] M. Berciu, T. G. Rappoport, and J. Boldizsar. Manipulating spin and charge in magnetic semiconductors using superconducting vortices. *Nature (London)*, 435:71, 2005.

[106] C. Weeks, G. Rosenberg, and B. Seradjeh. Anyons in a weakly interacting system. *Nature (London)*, 3:796, 2007.

[107] C. J. Olson Reichhardt and M. B. Hastings. Do vortices entangle? *Phys. Rev. Lett.*, 92:157002, 2004.

[108] D. R. Nelson. Vortex entanglement in high-t_c superconductors. *Phys. Rev. Lett.*, 60:1973, 1988.

[109] G. Blatter, M. V. Feigelman, V. B. Geshkenbein, A. L. Larkin, and V. M. Vinokur. Vortices in high-temperature superconductors. *Rev. Mod. Phys.*, 66:1125, 1994.

[110] J. C. Wynn, D. A. Bonn, B. W. Gardner, Y. J. Lin, R. Liang, W. N. Hardy, J. R. Kirtley, and K. A. Moler. Limits on spin-charge separation from $h/2e$ fluxoids in very underdoped $YBa_2Cu_3O_{6+x}$. *Phys. Rev. Lett.*, 87:197002, 2001.

[111] J. E. Hoffman, E. W. Hudson, K. M. Lang, V. Madhavan, H. Eisaki, S. Uchida, and J. C.. Davis. Imaging quasiparticle interference in $Bi_2Sr_2CaCu_2O_{8+\delta}$. *Science*, 295:466, 2002.

[112] Y. Kafri, D. R. Nelson, and A. Polkovnikov. Unzipping vortices in type-II superconductors. *Phys. Rev. B*, 76:144501, 2007.

[113] O. Buisson, P. Gandit, R. Rammel, Y. Y. Wang, and B. Pannetier. Magnetization oscillations of a superconducting disk. 150:36, 1990.

[114] A. K. Geim, I. V. Grigorieva, S. V. Dubonos, J. G. S. Lok, J. C. Maan, A. E. Filippov, and F. M. Peeters. Phase transitions in individual sub-micrometre superconductors. *Nature (London)*, 390:259, 1997.

[115] S Pedersen, G. R. Kofod, J. C. Hollingbery, C. B. Sorensen, and P. E. Lindelof. Dilation of the giant vortex state in a mesoscopic superconducting loop. *Phys. Rev. B*, 64:104522, 2001.

[116] H. J. Fink, S. B. Haley, C. V. Giuraniuc, V. F. Kozhevnikov, and J. O. Indekeu. Boundary conditions, dimensionality, topology and size dependence of the superconducting transition temperature. 103:21, 2005.

[117] H. J. Fink and W. C. H. Joiner. Surface nucleation and boundary conditions in superconductors. *Phys. Rev. Lett.*, 23:120, 1969.

[118] V. K. Kozhevnikov, M. Van Bael, W. Vinckx, K. Temst, C. Van Haesendonck, and J. O. Indekeu. Surface enhancement of superconductivity in tin. *Phys. Rev. B*, 72:174510, 2005.

[119] D. G. Naugle, J. W. Baker, R. E. Allen, K. Temst, C. Van Haesendonck, and J. O. Indekeu. Evidence for a surface-phonon contribution to thin-film superconductivity: Depression of T_c by noble-gas overlayers. *Phys. Rev. B*, 7:3028, 1973.

[120] I. L. Landau, D. L. Shapovalov, and I. A. Parshin. Increase in the superconducting transition temperature of a thin film as a result of the deposition of a normal metals on its surface. *JETP Lett.*, 53:263, 1991.

[121] E. G. Astrakharchik and C. J. Adkins. Enhancement of superconductivity and observation of antilocalization in thin metal films by suppression of electron-interaction effects. *Journal of Physics: Condensed Matter*, 50:13622, 1994.

[122] I. N. Khlyustikov and M. S. Khaikin. Proximity effect and phase diagram of twinning-plane superconductivity in metalleic crystals. *JETP Lett.*, 36:198, 1982.

[123] M. V. Milošević, A. Kanda, S. Hatsumi, F. M. Peeters, and Y. Ootuka. Local current injection into mesoscopic superconductors for the manipulation of quantum states. *Phys. Rev. Lett.*, 103:217003, 2009.

[124] B. Maiorov, S. A. Baily, H. Zhou, O. Ugurlu, J. A. Kennison, P. C. Dowden, T. G. Holesinger, S. R. Foltyn, and L. Civale. Synergetic combination of different types of defect to optimize pinning landscape using $BaZrO_3$-doped $YBa_2Cu_3O_7$. *Nat. Mater.*, 8:398, 2009.

[125] J. L. MacManus-Driscoll, S. R. Foltyn, Q. X. Jia, H. Wang, A. Serquis, L. Civale, B. Maiorov, M. E. Hawley, M. P. Maley, and D. E. Peterson. Strongly enhanced current densities in superconducting coated conductors of $YBa_2Cu_3O_{7-x}+BaZrO_3$. *Nat. Mater.*, 3:439, 2004.

[126] C. Carballeira, V. V. Moshchalkov, L. F. Chibotaru, and A. Ceulemans. Multi-quanta vortex entry and vortex-antivortex pattern expansion in a superconducting microsquare with a magnetic dot. *Phys. Rev. Lett.*, 95:237003, 2005.

[127] J. S. Neal, M. V. Milošević, S. J. Bending, A. Potenza, L. San Emeterio, and C. H. Marrows. Competing symmetries and broken bonds in superconducting vortex-antivortex molecular crystals. *Phys. Rev. Lett.*, 99:127001, 2007.

[128] B. Rosenstein, I. Shapiro, and B. Y. Shapiro. Maximal persistent current in a type-ii superconductor with an artificial pinning array at the matching magnetic field. *Phys. Rev. B*, 81:064507, 2010.

[129] B. Rosenstein, I. Shapiro, and B. Y. Shapiro. Transport current carrying superconducting film with periodic pinning array under strong magnetic fields. *Phys. Rev. B*, 83:064512, 2011.

[130] C. Y. Liu, G. R. Berdiyorov, and M. V. Milošević. Vortex states in layered mesoscopic superconductors. *Phys. Rev. B*, 83:104524, 2011.

[131] C. H. Ahn, J. M. Triscone, and J. Mannhart. Electric field effect in correlated oxide systems. *Nature (London)*, 424:1015, 2003.

[132] C. H. Ahn, A. Bhattacharya, M. Di Ventra, J. N. Eckstein, C. D. Frisbie, M. E. Gershenson, A. M. Goldman, I. H. Inoue, J. Mannhart, and A. J. Millis. Electrostatic modification of novel materials. *Rev. Mod. Phys.*, 78:1185, 2006.

[133] S. Mathews, R. Ramesh, T. Venkatesan, and J. Benedetto. Ferroelectric field effect transistor based on epitaxial perovskite heterostructures. *Science*, 276:238, 1997.

[134] S. M. Wu, S. A. Cybart, P. Yu, M. D. Rossell, J. X. Zhang, R. Ramesh, and R. C. Dynes. Reversible electric control of exchange bias in a multiferroic field-effect device. *Nat. Mater.*, 9:756, 2010.

[135] S. Kakani and S. L. Kakani. Theoretical study of specific heat, density of states and free energy of itinerant ferromagnetic superconductor urhge. *J. Supercond. Novel Magn.*, 22:667, 2009.

[136] J. Mannhart, D. G. Schlom, J. G. Bednorz, and K. A. Muller. Influence of electric fields on pinning in $YBa_2Cu_3O_{7-\delta}$ films. *Phys. Rev. Lett.*, 67:2099, 1991.

[137] X. X. Xi, C. Doughty, A. Walkenhorst, C. Kwon, Q. Li, and T. Venkatesan. Effects of field-induced hole-density modulation on normal-state and superconducting transport in $YBa_2Cu_3O_{7-x}$. *Phys. Rev. Lett.*, 68:1240, 1992.

[138] J. Mannhart. High-T_c transistors. *Supercond. Sci. Technol.*, 9:0953, 1996.

[139] C. H. Ahn, S. Gariglio, P. Paruch, T. Tybell, L. Antognazza, and J. M. Triscone. Electrostatic modulation of superconductivity in ultrathin $GdBa_2Cu_3O_{(7-x)}$ films. *Phys. Rev. Lett.*, 68:1240, 1992.

[140] D. Matthey, N. Reyren, J. M. Triscone, and T. Schneider. Electric-field-effect modulation of the transition temperature, mobile carrier density, and in-plane penetration depth of $NdBa_2Cu_3O_{(7-delta)}$ thin films. *Phys. Rev. Lett.*, 98:057002, 2007.

[141] G. Berdiyorov, K. Harrabi, J. P. Maneva, and F. M. Peeters. Effect of pinning on the response of superconducting strips to an external pulsed current. *Supercond. Sci. Technol.*, 28:025004, 2015.

[142] G. Berdiyorov, A. R. de C. Romaguera, M. V. Milosevic, M. M. Doria, L. Covaci, and F. M. Peeters. Dynamic and static phases of vortices under an applied drive in a superconducting stripe with an array of weak links. *Eur. Phys. J. B*, 85:130, 2012.

[143] I. V. Grigorieva, W. Escoffier, V.R̃. Misko, B. J. Baelus, F. M. Peeters, L. Y. Vinnikov, and Dubonos. Pinning-induced formation of vortex clusters and giant vortices in mesoscopic superconducting disks. *Phys. Rev. Lett.*, 99:147003, 2007.

[144] K. Harada, O. Kamimura, H. Kasai, T. Matsuda, A. Tonomura, and V. V. Moshchalkov. Direct observation of vortex dynamics in superconducting films with regular arrays of defects. *Science*, 274:1167, 1996.

[145] V. V. Moshchalkov, H. Baert, V. V. Metlushko, E. Rosseel, M. J. Van Bael, K. Temst, R. Jonckheere, and Y. Bruynseraede. Magnetization of multiple-quanta vortex lattices. *Phys. Rev. B*, 54:7385, 1996.

[146] G. R. Berdiyorov, M. V. Miloŝević, and F. M. Peeters. Novel commensurability effects in superconducting films with antidot arrays. *Phys. Rev. Lett.*, 96:207001, 2006.

[147] S. Raedts, A. V. Silhanek, M. J. Van Bael, and V. V. Moshchalkov. Flux-pinning properties of superconducting films with arrays of blind holes. *Phys. Rev. B*, 70:024509, 2004.

[148] M. Lange, M. J. Van Bael, Y Bruynseraede, and V. V. Moshchalkov. Nanoengineered magnetic-field-induced superconductivity. *Phys. Rev. Lett.*, 90:197006, 2003.

[149] M. V. Milosevic, S. V. Yampolskii, and F. M. Peeters. Magnetic pinning of vortices in a superconducting film: The (anti)vortex-magnetic dipole interaction energy in the london approximation. *Phys. Rev. B*, 66:174519, 2002.

[150] J. Barba-Ortega, E. Sardella, J. Albino Aguiar, and F. M. Peeters. Non-conventional vortex configurations in a mesoscopic flat disk. *Physica C*, 487:47, 2013.

[151] H. T. Huy, M. Kato, and T. Ishida. Vortex states in de facto mesoscopic $Mo_{80}Ge_{20}$ pentagon plates. *Science*, 26:065001, 2013.

[152] J. Barba-Ortega, E. Sardella, and J. Albino Aguiar. Nucleation of superconductivity in a thin disk with a ring-like defect. *Mod. Phys. Lett. B*, 27:1350025, 2013.

[153] J. Barba-Ortega, J. Baron-Jaimez, and J. Albino Aguiar. Superconducting state of a perforated mesoscopic disk with a square or triangular trench. *Mod. Phys. Lett. B*, 27:1350115, 2013.

[154] J. Barba-Ortega, E. Sardella, and J. Albino Aguiar. Triangular arrangement of defects in a mesoscopic superconductor. *Physica C*, 485:107, 2013.

[155] J. Barba-Ortega, E. Sardella, and J. Albino Aguiar. Linear arrangement of metallic and superconducting defects in a thin superconducting sample. *Physica C*, 492:1, 2013.

[156] G. Teniers, V. Moshchalkov, L. Chibotaru, and A. Ceulemans. Vortex-antivortex patterns in mesoscopic superconductors. *Physica B*, 329:1340, 2003.

[157] M. Ghinovker, B. Ya. Shapiro, and I. Shapiro. Spontaneous magnetic-flux generation in superconducting ring. *Europhys. Lett.*, 53:2, 2001.

[158] E. Sardella and E. H. Brandt. Vortices in a mesoscopic superconducting disk of variable thickness. *Supercond. Sci. Technol.*, 23:025015, 2010.

[159] M. Motta, F. Colauto, W.Ã. Ortiz, J. Fritzsche, J. Cuppens, W. Gillijns, V. Moshchalkov, T. H. Johansen, A. Sanchez, and A. V. Silhanek. Enhanced pinning in superconducting thin films with graded pinning landscapes. *Appl. Phys. Lett.*, 102:212601, 2013.

[160] V. R. Misko and F. Nori. Magnetic flux pinning in superconductors with hyperbolic-tessellation arrays of pinning sites. *Phys. Rev. B*, 85:184506, 2012.

[161] W. J. Zhang, S. K. He, H. F. Liu, G. M. Xue, H. Xiao, B. H. Li, X. F. Wen, C. Z. Zhao, Qiu X. G., and V. V. Moshchalkov. Crossover behaviors in magnetoresistance oscillations for nb thin film with rectangular arrays of antidots. 99:37006, 2012.

[162] J. M. Kosterlitz and D. J. Thouless. Ordering, metastability and phase transitions in two-dimensional systems. 6:1181, 1973.

[163] D. J. Bishop and J. Reppy. Study of the superfluid transition in two-dimensional 4He films. *Phys. Rev. Lett.*, 40:1727, 1978.

[164] E. B. Bogomolny. Stability of classical solutions. *Sov. J. Nucl. Phys.*, 24:449, 1976.

[165] N. Klein. High-frequency applications of high-temperature superconductor thin films. *Rep. Prog. Phys.*, 65:1387, 2002.

[166] V. Sokolovsky, L. Prigozhin, and V. Dikovsky. Meissner transport current in flat films of arbitrary shape and a magnetic trap for cold atoms. *Supercond. Sci. Technol.*, 23:065003, 2010.

[167] H. J. M. Brake. Scenet roadmap for superconductor digital electronics. *Physica C*, 439:1, 2006.

[168] E. H. Brandt and G. P. Mikitik. Vortex shaking in superconducting platelets in an inclined magnetic field. *Supercond. Sci. Technol.*, 20:S111, 2007.

[169] E. H. Brandt. Thin superconductors and squids in perpendicular magnetic field. *Phys. Rev. B*, 72:024529, 2005.

[170] J. R. Clem and E. H. Brandt. Response of thin-film squids to applied fields and vortex fields: Linear squids. *Phys. Rev. B*, 72:174511, 2005.

[171] B. Xu, M. V. Miloŝević, and F. M. Peeters. Magnetic properties of vortex states in spherical superconductors. *Phys. Rev. B*, 77:144509, 2008.

[172] M. Doria, A. R. Romaguera, and F. M. Peeters. Effect of the boundary condition on the vortex patterns in mesoscopic three-dimensional superconductors: Disk and sphere. *Phys. Rev. B*, 75:064505, 2007.

[173] Q. Du. Numerical approximations of the ginzburg landau models for superconductivity. *J. Math. Phys.*, 46:095109, 2005.

[174] Y. Chen, M. Doria, and F. M. Peeters. Vortices in a mesoscopic cone: A superconducting tip in the presence of an applied field. *Phys. Rev. B*, 77:054511, 2008.

[175] A. K. Elmurodov, D. Y. Vodolazov, and F. M. Peeters. The break-up of the vortex structure in a mesoscopic wire containing a constriction. *Europhys. Lett.*, 74:151, 2006.

[176] R. Wordenweber, P. Lah, and P. Dymashevski. Magnetic flux in active and passive superconducting devices. *Physica C*, 369:141, 2002.

[177] R. Wordenweber and P. Selders. Reduction of low-frequency noise in high-T_c squids by artificial defects. *Physica C*, 366:135, 2002.

[178] M. V. Milosevic and R. Geurts. The ginzburg-landau theory in application. *Physica C*, 470:791, 2010.

[179] E. Sardella, P. N. L. Filho, and A. L. Malvezzi. Vortices in a mesoscopic superconducting circular sector. *Phys. Rev. B*, 77:104508, 2008.

[180] G. R. Berdiyorov, M. V. Milosevic, B. J. Baelus, and F. M. Peeters. Superconducting vortex state in a mesoscopic disk containing a blind hole. *Phys. Rev. B*, 70:024508, 2004.

[181] Q. Du and M. D. Gunzburger. A model for superconducting thin films having variable thickness. *Physica D*, 69:215, 1993.

[182] G. R. Berdiyorov, V. M. Misko, M. V. Milosevic, W. Escoffier, I. V. Grigorieva, and F. M. Peeters. Pillars as antipinning centers in superconducting films. *Phys. Rev. B*, 77:024526, 2008.

[183] L. Chibotaru, A. Ceulemans, V. Bruyndoncx, and V. V. Moshchalkov. Symmetry-induced formation of antivortices in mesoscopic superconductors. *Nature (London)*, 408:833, 2000.

[184] M. Morelle, G. Teniers, L. F. Chibotaru, A. Ceulemans, and V. V. Moshchalkov. Nucleation of superconductivity in a mesoscopic triangle. *Physica C*, 369:351, 2002.

[185] A. Kanda, B. J. Baelus, F. M. Peeters, K. Kadowaki, and Y. Ootuka. Experimental evidence for giant vortex states in a mesoscopic superconducting disk. *Phys. Rev. Lett.*, 93:257002, 2004.

[186] T. Cren, D. Fokin, F. Debontridder, V. Dubost, and D. Roditchev. Ultimate vortex confinement studied by scanning tunneling spectroscopy. *Phys. Rev. Lett.*, 102:127005, 2009.

[187] Y. X. Ning, C. L. Song, Y. L. Wang, X. Chen, J. F. Jia, Q. K. Xue, and C. Ma. Vortex properties of two-dimensional superconducting Pb films. *Journal of Physics: Condensed Matter*, 22:065701, 2010.

[188] T. Cren, L. Serrier-Garcia, F. Debontridder, and D. Roditchev. Vortex fusion and giant vortex states in confined superconducting condensates. *Phys. Rev. Lett.*, 107:097202, 2011.

[189] T. Tominaga, T. Sakamoto, T. Nishio, T. An, Eguchi T., Y. Yoshida, and Y. Hasegawa. Observation of vortex clustering in nano-size superconducting pb island structures by low-temperature scanning tunneling microscopy/spectroscopy. *J. Supercond. Novel Magn.*, 25:1375, 2012.

[190] B. Deloof, V. V. Moshchalkov, and L. F. Chibotaru. Quantum states and vortex patterns in nanosuperconductors. *Ann. Phys.*, 525:951, 2013.

[191] H. T. Huy, H. Shishido, M. Hayashi, T. Yotsuya, M. Kato, and T. Ishida. Direct observation of vortices by scanning squid microscope on small superconducting $Mo_{80}Ge_{20}$ circular disks. *Physica C*, 484:86, 2013.

[192] L. Fu and C. L. Kane. Superconducting proximity effect and majorana fermions at the surface of a topological insulator. *Phys. Rev. Lett.*, 100:096407, 2008.

[193] M. Veldhorst, M. Snelder, M. Hoek, T. Gang, V. K. Guduru, X. L. Wang, U. Zeitler, W. G. van der Wiel, A. A. Golubov, H. Hilgenkamp, and A. Brinkman. Josephson supercurrent through a topological insulator surface state. *Nat. Mater.*, 11:417, 2012.

[194] M. X. Wang, C. Liu, J. P. Xu, F. Yang, L. Miao, M. Y. Yao, C. L. Gao, C. Shen, X. Ma, X. Chen, Z. A. Xu, Y. Liu, S. C. Zhang, D. Qian, J. F. Jia, and Q. K. Xue.

The coexistence of superconductivity and topological order in the Bi_2Se_3 thin films. *Science*, 336:52, 2012.

[195] J. P. Xu, C. Liu, M. X. Wang, J. Ge, Z. L. Liu, Yang X., Y. Chen, Y. Liu, Z. A. Xu, D. Gao, D. Qian, S. C. Zhang, and J. F. Jia. Artificial topological superconductor by the proximity effect. *Phys. Rev. Lett.*, 112:217001, 2014.

[196] S. Chadov, X. Qi, J. Kbler, G. H. Fecher, C. Felser, Yang X., and S. C. Zhang. Tunable multifunctional topological insulators in ternary heusler compounds. *Nat. Mater.*, 9:541, 2010.

[197] N. P. Butch, P. Syers, K. Kirshenbaum, A. P. Hope, and J. Paglione. Superconductivity in the topological semimetal YPtBi. *Phys. Rev. B*, 84:220504, 2011.

[198] F. D. Natterer, J. Ha, H. Baek, D. Zhang, W. G. Cullen, N. B. Zhitenev, Y. Kuk, and J. A. Stroscio. Scanning tunneling spectroscopy of proximity superconductivity in epitaxial multilayer graphene. *Phys. Rev. B*, 93:045406, 2016.

[199] J. D. González, M. R. Joya, and J. Barba-Ortega. Influence of short-range artificial defects in a macroscopic flat disk on the abrikosov state. *Int. J. Mod. Phys. B*, 28:1450227, 2014.

[200] G. R. Berdiyorov, M. V. Milôŝević, and F. M. Peeters. Composite vortex ordering in superconducting films with arrays of blind holes. 11:013025, 2009.

[201] Y. Liu, G. R. Berdiyorov, and M. V. Milôŝević. Vortex states in layered mesoscopic superconductors. *Phys. Rev. B*, 83:104524, 2011.

[202] G. R. Berdiyorov, K. Harrabi, J. P. Maneval, and F. M. Peeters. Effect of pinning on the response of superconducting strips to an external pulsed current. *Supercond. Sci. Technol.*, 28:025004, 2015.

[203] J. D. González, J. Barón-Jaimez, and J. Barba-Ortega. Complex vortex configuration in a disk with a higher/lower critical temperature superconducting geometrical central defect. *J. Low. Temp. Phys.*, 179:264, 2015.

[204] F. Bouquet, R. A. Fisher, N. E. Phillips, D. G. Hinks, and J. D. Jorgensen. Specific heat of $Mg^{11}B_2$: Evidence for a second energy gap. *Phys. Rev. Lett.*, 87:047001, 2001.

[205] P. Szabó, P. Samuely, J. Kacmarcik, T. Klein, J. Marcus, D. Fruchart, S. Miraglia, C. Marcenat, and A. G. M. Jansen. Evidence for two superconducting energy gaps in MgB_2 by point-contact spectroscopy. *Phys. Rev. Lett.*, 87:137005, 2001.

[206] R. M. da Silva, M. V. Milôsević, D. Domínguez, F. M. Peeters, and J. Albino Aguiar. Distinct magnetic signatures of fractional vortex configurations in multiband superconductors. *Appl. Phys. Lett.*, 105:232601, 2014.

[207] J. C. Piña, C. C. de Souza Silva, and Milôsević. Stability of fractional vortex in a two-band mesoscopic superconductor. *Phys. Rev. B*, 86:024512, 2012.

[208] R. Geurts, M. V. Milôsević, and F. M. Peeters. Vortex matter in mesoscopic two-gap superconducting disks: Influence of josephson and magnetic coupling. *Phys. Rev. B*, 81:214514, 2010.

[209] L. Komendová, M. V. Milôsević, A. A. Shanenko, and F. M. Peeters. Different length scales for order parameters in two-gap superconductors: Extended ginzburg-landau theory. *Phys. Rev. B*, 84:064522, 2011.

[210] E. Babaev, L. D. Faddeev, and A. Niemi. Hidden symmetry and knot solitons in a charged two-condensate bose system. *Phys. Rev. B*, 84:100512, 2002.

[211] E. Babaev. Vortices with fractional flux in two-gap superconductors and in extended faddeev model. *Phys. Rev. Lett.*, 89:067001, 2002.

[212] A. Shalníikov. Superconducting thin films. *Nature (London)*, 142:74, 1938.

[213] M. Strongin and O. F. Kammerer. Superconductive phenomena in ultrathin films. *J. Appl. Phys.*, 39:2509, 1968.

[214] J. M. Graybeal and M. R. Beasley. Localization and interaction effects in ultrathin amorphous superconducting films. *Phys. Rev. B*, 29:4167, 1984.

[215] B. G. Orr, H. M. Jaeger, and A. M. Goldman. Local superconductivity in ultrathin Sn films. *Phys. Rev. B*, 32:7586, 1985.

[216] H. M. Jaeger, D. B. Haviland, A. M. Goldman, and B. G. Orr. Threshold for superconductivity in ultrathin amorphous gallium films. *Phys. Rev. B*, 34:920, 1986.

[217] H. M. Jaeger, D. B. Haviland, B. G. Orr, and A. M. Goldman. Onset of superconductivity in ultrathin granular metal films. *Phys. Rev. B*, 40:182, 1989.

[218] Y. Saito, T. Nojima, and Y. Iwasa. Highly crystalline 2D superconductors. *Nat. Rev. Mater.*, 2:16094, 2017.

[219] D. Costanzo, S. Jo, H. Berger, and A. F. Morpurgo. Gate-induced superconductivity in atomically thin MoS_2 crystals. *Nat. Nanotechnol.*, 11:339, 2016.

[220] C. K. Schiller. Angular dependence of the critical field of quenched thin pb and sn films. *J. Appl. Phys.*, 40:4179, 1969.

[221] S. Takahashi, M. Gabay, D. Jaccard, K. Shibuya, T. Ohnishi, M. Lippmaa, and J. M. Triscone. Local switching of two-dimensional superconductivity using the ferroelectric field effect. *Nature (London)*, 441:195, 2006.

[222] A. Buzdin. Hybrid devices: Mixing superconductivity and magnetism. *Nat. Mater.*, 3:751, 2004.

[223] J. Biscaras, N. Bergeal, S. Hurand, C. Feuillet-Palma, A. Rastogi, R. C. Budhani, M. Grilli, S. Caprara, and J. Lesueur. Multiple quantum criticality in a two-dimensional superconductor. *Nat. Mater.*, 12:542, 2013.

[224] S. De Franceschi, L. Kouwenhoven, C. Schonenberger, and W. Wernsdorfer. Hybrid superconductor-quantum dot devices. *Nat. Nanotechnol.*, 5:711, 2010.

[225] E. Babaev and M. Speight. Semi-meissner state and neither type-I nor type-II superconductivity in multicomponent superconductors. *Phys. Rev. B*, 72:180502(R), 2005.

[226] J. P. Wang. Stability of vortex in a two-component superconductor. *Phys. Rev. B*, 82:132505, 2010.

9 Curriculum Vitae

Jesús David González Acosta
Born on November 20th,1975
Santa Marta/Colombia

Education

- February 1995-August 2000: Lic. in Mathematics and Physics, Deparment of Education, Universidad del Magdalena, Santa Marta, Colombia.

- February 2001-August 2004: M. Sc in Physics, Universidad Industrial de Santander, Bucaramanga, Colombia.

- August 2011-May 2017: PhD. in Science-Physics, Universidad Nacional de Colombia-Sede Bogotá, Colombia and University of Antwerp, Antwerp, Belgium.

Research internship

- Condensed Matter Theory Group, at University of Antwerp, Belgium. Head of the group Prof. François Peeters, under supervision of Prof. Milorad Milošević.

Publications

Journal Articles in superconductivity

- *Superconducting state of a disk with a pentagonal/hexagonal trench/barrier*, J. Barba, **J.**

D. González and E. Sardella **Journal of Low Temperature Physics. 174**, 96 (2014). **ISSN**: 1573-7357.

- *Multi-vortex State Induced by Proximity Effects in a Small Superconducting Square*, J. Barba-Ortega, **J. D. González** and Edson Sardella **Journal of Low Temperature Physics 177**, 193 - 201 (2014). **ISSN**: 0022-2291.

- *Influence of short-range artificial defects in a macroscopic flat disk on the Abrikosov state*, **J. D. González**, J. Barba-Ortega and M. R. Joya **International Journal of Modern Physics B 28**, 1450227 (2014). **ISSN**: 0217-9792.

- *Magnetic profile in a nanostructured superconducting sample*, J. Barba-Ortega, **J. D. González** and M. R. Joya **Modern Physics Letters B 28**, 1450150 (2014). **ISSN**: 0217-9849.

- *Superconducting state in a circular SQUID shaped mesoscopic film*, J. Barba-Ortega, J. L. Aguilar and **J. D. González Modern Physics Letters B 28**, 1450230 (2014). **ISSN**: 0217-9849.

- *Complex Vortex Configuration in a Disk with a Higher/Lower Critical Temperature Superconducting Geometrical Central Defect*, **J. D. González**, J. Barón-Jaimez and J. Barba-Ortega **Journal of Low Temperature Physics 179**, 264275 (2015). **ISSN**: 0022-2291.

- *Unconventional anti-vortex spontaneous generation in a superconducting microstructure*, J. Barba-Ortega, J. L. Aguilar and **J. D. González Modern Physics Letters B 29**, 1550070 (2015). **ISSN**: 0217-9849.

- *Effects of size, deGennes and Ginzburg-Landau parameters on the magnetic susceptibility of an isotropic superconductor*, C. A. Aguirre, **J. D. González** and J. Barba-Ortega **Journal of Low Temperature Physics 182**, 51-60 (2016). **ISSN**: 0022-2291.

- *Induced Anisotropy by the Inclusion of Defects of Variable T_c in a Superconducting Disk*, **J. D. González**, M. R. Joya and J. Barba-Ortega, **Journal of Low Temperature Physics 190**, 178-190 (2018). **ISSN**: 0022-2291.

- *Weak links array generated by a continuous wave laser in a superconducting sample*, **J. D. González**, J. R. Bentrán and J. Barba-Ortega, **Optik - International Journal for Light and Electron Optics**, **158**, 806 (2018). **ISSN**: 0030-4026.

- *Quantized magnetic flux in a disk with a defect with different critical temperature*, **J. D. González**, O. J. Gaona and J. Barba-Ortega **Journal of Low Temperature Physics** Under review: Submission ID: JLTP-D-18-00001, (2018).

- *Topologically trapped vortex in inhomogeneous condensate*, **J. D. González**, M. R. Joya and J. Barba-Ortega **Physics Letters A** Under review, (2018).

- *Theoretical proposal for temperature dependence of deGennes extrapolation parameter: Ginzburg-Landau approach*, J. Barba-Ortega, M. R. Joya and **J. D. González**, **Physica C: Superconductivity and its applications** Under review, (2018).

Journal Articles in cooperations with related topics

- *Effect of potential shape on density of states for a light-hole exciton in a microtube of AlGaAs/GaAs*, **J. D. González**, M. R. Joya and J. Barba-Ortega. **Modern Physics Letters B. 28**, 1450013 (2014). **ISSN**: 0217-9849.

- *Theoretical study on density of states for heavy-hole exciton in a microtube of GaAs/AlGaAs*, **J. D. González**, M. R. Joya and J. Barba-Ortega, **Physica E 62**, 118-122 (2014). **ISSN**: 1386-9477.

- *Raman spectroscopy as a versatile tool for studying of explicit contribution of anharmonicity*, M. R. Joya, **J. D. González** and J. Barba-Ortega. **Journal of Nonlinear Optical Physics & Materials 23**, 1450051 (2014). **ISSN**: 0218-8635.

- *Anharmonicity Study of Semiconductors and Metallic Nanotubes by Inelastic Spectroscopy*, M. R. Joya, **J. D. González** and J. Barba-Ortega. **Fullerenes, Nanotubes and Carbon Nanostructures 23**, 566-571 (2014). **ISSN**: 1536-383X.

- *Neutral donor in a bilayer spherical semiconductor quantum dot*, **J. D. González**, M. R. Joya and J. Barba-Ortega **International Journal of Modern Physics B 29**, 1550228 (2015). **ISSN**: 0217-9792.

Proceedings on Journal of Physics: Conference Series

- *Numerical solution of the time-dependent Ginzburg-Landau equation for a superconducting mesoscopic disk: Link variable method*, J. Barba-Ortega, and **J. D. González**, M. R. Joya. **410**, 012008 (2013). **ISSN**: 1742-6596.

- *Computational simulation of vortex matter in Type-II mesoscopics superconductors*, J. Barba-Ortega, and **J. D. González**, M. R. Joya, **410**, 012009 (2013). **ISSN**: 1742-6596.

- *Giant-vortex state induced by negatives values of deGennes parameter in a mesoscopic square*, **J. D. González**, J. L. Aguilar and J. Barba-Ortega. **480**, 012040 (2014). **ISSN**: 1742-6596.

- *Shubnikov state in complex geometry Type-II Technetium device*, **J. D. González**, J. L. Aguilar and J. Barba-Ortega. **574**, 012159 (2015). **ISSN**: 1742-6596.

- *Ferromagnetic/superconducting interface in a hybrid nanoscopic disc*, **J. D. González**, J. L. Aguilar and J. Barba-Ortega. **574**, 012141 (2015). **ISSN**: 1742-6596.

- *3D electromagnetic simulation of spatial autoresonance acceleration of electron beams*, V. D. Dugar-Zhabon, **J. D. González** and E. Orozco. **687**, 012077 (2016). **ISSN**: 1742-6596.

- *Anisotropy included in a nanoscale superconductor: Theoretical development*, O. J. Gaona, **J. D. González** and J. R. Beltrán. **935**, 12070 (2017). **ISSN**: 1742-6596.

- *Electrons acceleration in a TE_{113} cylindrical cavity affected by a static inhomogeneous magnetic field*, V. E. Vergara, **J. D. González**, J. R. Beltrán and E. Orozco. **935**, 012076 (2017). **ISSN**: 1742-6596.

Supervision of master students during Ph.D studies

- *Energía de enlace del estado base y densidad de estados de una D_0 en un nanotubo cilíndrico con diferentes formas de potencial y campo magnético axial*, Fredy José Rondano Lobo, (2013).

- *Espectro de fotoluminiscencia de un exitón confinado en un microtubo de GaAs/AlGaAs con doble pozo y diferentes formas de potencial*, Adolfo David Barrios De la Ossa, (2015).

- *Estudio teórico de la configuración de vórtice en superconductores mesoscópico con diferente temperatura crítica*, Oscar Javier Gaona Cruz, (2018).

- *Simulación computacional de los efectos de un campo electrostático sobre un haz de electrones en condiciones de autoresonancia ciclotrónica espacial.*, Victor Emilio Vergara Díaz (Current student).

- *Unconventional vortex states in nanoscale superconductors due to optical manipulation Cooper-pair condensate.*, Angélica María Valencia Rodríguez, (Current student).

Professional service

- Referee for Nanoscale Research Letters.Springer.5-year Impact Factor-3.196.

Conferences

- **3rd International Conference on Multi-Condensate Superconductivity and Superfluidity in Solids and Ultra-cold Gases**, Trieste, Itlay (may 14th-18th 2018)- Poster entitled: *Vortex matter in a two-component mesoscopic superconductor.*

- **4th International meeting of researchers in materials and technology plasma**, Santa Marta, Colombia (may 23th-26th 2017): Oral presentation: *Vortex state in nano-structured systems superconductor-superconductor and superconductor-metal.*

- **27th International Conference on Low Temperature Physics**, Buenos Aires, Argentina (August 6th-13th 2014) - Poster entitled: *Pinning/anti-pinning effects of a circular and triangular hole/barrier on the fluxoid in a thin mesoscopic disk.*

- **3rd International Conference on Mathematical Modeling in Physical Sciences**, Madrid, Spain (August 28th-31th 2014) - Poster entitled: *Superconducting state in a circular SQUID shaped mesoscopic film.*

- **31st International Conference on the Physics of Semiconductors**, Zurich, Switzerland (July 29th-August 3rd 2012) - Poster entitled: *Effect of magnetic field and soft potential barrier on off-axis donor binding energy in a nanotube with two quantum wells.*